Université catholique de Louvain
École Polytechnique de Louvain
Earth and Life Institute

Université de Liège
Faculté des Sciences
Département d'Astrophysique,
Géophysique et Océanographie

Modelling storm surges in the Scheldt-North Sea continuum under present and future climate conditions

Doctoral dissertation presented by

Ny Riana Randresihaja

in partial fulfillment of the requirements for the degree of

Doctor in Engineering Science
and
Doctor in Sciences

Thesis committee:

Prof. Emmanuel Hanert (Supervisor)	UCLouvain, Belgium
Prof. Marilaure Grégoire (Supervisor)	ULiège, Belgium
Dr. Olivier Gourgue	Royal Belgian Institute of Natural Sciences, Belgium
Prof. Xavier Fettweis	ULiège, Belgium
Prof. Emil Stanev	Helmholtz-Zentrum Hereon, Germany
Dr. Jonathan Lambrechts (Secretary)	UCLouvain, Belgium
Prof. Marnik Vanclooster (President)	UCLouvain, Belgium

Louvain-la-Neuve, November 2026

It was the best of times, it was the worst of times,
it was the age of wisdom, it was the age of foolishness,
it was the epoch of belief, it was the epoch of incredulity,
it was the season of Light, it was the season of Darkness,
it was the spring of hope, it was the winter of despair,
we had everything before us, we had nothing before us,
we were all going direct to Heaven, we were all going direct the other way
in short, the period was so far like the present period, that some of its noisiest authorities insisted on its being received, for good or for evil, in the superlative degree of comparison only.

— Charles Dickens, *A Tale of Two Cities* (1859)

Abstract

Estuaries amplify storm surges as they converge inland, towards cities and ports. The surge response of the Scheldt estuary, which leads to the port of Antwerp, has rarely been studied with the estuary and the adjacent sea resolved in a single domain. In this thesis, we use the depth-averaged version of the multiscale model SLIM, on one unstructured mesh extending from the shelf break to the tidal channels of the upper Scheldt, to study storm surges along this continuum under present and future atmospheric forcing. Over 2016–2020, the configuration reproduces the M2 tide within 5.2 % in amplitude up to the Scheldt upstream, the currents with correlations of at least 0.90, and the non-tidal residual with root-mean-square errors of 9 to 14 cm from the open shelf to Bath, with no loss of skill across the mouth; skill decreases upstream, where the tide reaches about 20 minutes early. For Storm Xaver (2013), refining the regional atmospheric model MAR from 30 to 2 km improves the simulated peak water level by about 20 % in the upper estuary, whereas the forcing interval matters only at 2 km: spatial resolution controls the estuarine surge, and a 5 km forcing offers a nearly equivalent, cheaper alternative. We then follow a storyline approach under SSP3-7.0 and simulate 65 extreme surge events over 2033–2096, holding mean sea level and bathymetry at present-day values. The estuary amplifies positive and negative surges by a similar factor, 1.5 to 1.7 between the mouth and Antwerp, for every track type with more than four storms; the track instead shapes the sign and form of the surge. A quarter to a third of the events combine both signs, yet the two are not mirror images: the estuary increases the cumulative intensity of the surge but not of the drawdown. This thesis provides a single-domain representation of the Scheldt–North Sea continuum.

Acknowledgements / Remerciements

"I've heard it said. That people come into our lives for a reason..."
— For Good, *Wicked*

Au début de ma thèse, on m'a dit : « La thèse, ce n'est pas un sprint, c'est un marathon. » Et ça tombe bien : j'ai commencé la course à pied plus ou moins au début de la thèse et j'ai couru des marathons depuis, et je peux donc faire le parallèle entre les deux.

Pour le coaching, je voudrais d'abord remercier Emmanuel et Marilaure, sans qui cette thèse n'aurait pas eu lieu et sans qui je n'aurais donc jamais pris mon dossard. Vous avez su instaurer un climat de confiance qui m'a accompagnée durant ces cinq années. Merci pour votre patience et vos précieux conseils, qui m'ont constamment poussée à approfondir ma réflexion, ainsi que pour votre grande bienveillance, qui m'a permis de grandir humainement tout au long de cette aventure, et surtout pour votre positivité à toute épreuve qui m'a aidée à croire et à persévérer dans les moments les plus durs.

I would like to express my sincere gratitude to the members of my defence committee: Jonathan Lambrechts, Olivier Gourgue, Xavier Fettweis, Emil Stanev and Marnik Vanclooster. Thank you for your time, your insightful feedback, and for guiding me during the private defence. Your benevolence throughout this discussion gave me confidence.

Puis, tout au long de la course, viennent les supporters et leurs encouragements. Je tiens à remercier chaleureusement de l'ensemble de ces personnes.

Lauranne, avec qui j'ai pris le départ et fait un bout de chemin, nous nous sommes énormément soutenues et tu es devenue une véritable amie, je te souhaite le meilleur pour la suite de ton voyage.

Merci aussi à Insaf, Sacha et Constance pour nos amitiés et tout ce que nous avons partagé.

Cette épreuve a aussi compté son lot de ravitaillements, toujours en bonne compagnie. D'abord au bureau B.315, à la porte toujours ouverte, dont les membres ne manquaient jamais de motivation pour des pauses sucrées ou des verres en afterwork ; merci à toutes celles et ceux qui s'y sont succédé pour les échanges et les discussions. Il y a aussi eu des ravitos avec l'équipe SLIM pour les réunions du vendredi, les tartes, couques et autres douceurs sucrées en provenance de la réserve. De manière plus festive, il y a eu les soupers de Noël, les afterworks et les team-buildings avec le pôle ELIE. Et enfin, avec l'équipe extended MAST et sa tradition des goûters d'anniversaire « surprises » et des sorties aux marchés de Noël.

Des remerciements spéciaux à ceux qui m'ont accompagnée pendant quelques sorties de course à pied : d'abord Barbara à LLN sur la neige, dans le froid ou au soleil sur la cyclostrade, c'étaient de véritables bulles d'air dans nos quotidiens respectifs ; et Loïc entre le Chili et la Pologne, peut-être enfin un jour en Bretagne ?

Et une pensée à Jasmine un rayon de soleil sans qui ELIE tournerait moins bien.

Merci à ma famille et à mes amis proches. À Leila et Magalie pour votre amitié solide et fidèle depuis bientôt deux décennies. Merci à Margaux, Maïté, Lara, Ariane et Aline. Vos encouragements ont été précieux. À Anne-France et Olivier de toujours vous préoccuper de mon bien-être et de m'avoir soutenue cette dernière année.

À Ony d'être toujours là et d'être à l'écoute, merci encore pour ce câlin après le marathon de Gand, il me réchauffe encore le cœur. Et à Hery et Noa pour votre présence.

À Maman et Papa : vous m'avez toujours poussée à donner le meilleur de moi-même dans chacune de mes courses, et merci pour

toutes les opportunités que vous m'avez offertes depuis toujours dans la vie.

À PA : merci pour ta présence indéfectible dans tous les moments, les hauts comme les bas. Merci de me suivre dans mes idées : après tout, entre « viens, on fait un marathon », « viens, on fait un master » et « viens, on se marie », il n'y a que quelques lettres qui diffèrent. Le fameux « mur du trentième » était costaud pour moi, mais ton soutien émotionnel l'a été bien davantage.

Merci à tous·tes, je franchis cette ligne d'arrivée grâce à chacun·e d'entre vous.

Contents

Abstract v

Acknowledgements / Remerciements vii

Contents xi

List of acronyms and abbreviations xiii

1 Introduction 1
- 1.1 Why study estuary-sea continua ? . . . 1
- 1.2 Storm surges across the estuary–sea continuum . . . 2
- 1.3 The Scheldt–North Sea continuum . . . 5
- 1.4 Modelling storm surges across a multi-scale continuum . . . 11
- 1.5 Research questions and outline . . . 16

2 Multiscale hydrodynamic modeling of the Scheldt-North Sea continuum 21
- 2.1 Hydrodynamic model . . . 22
- 2.2 Model setup for the Scheldt–North Sea continuum . . . 27
- 2.3 Hydrodynamics validation . . . 32
- 2.4 Discussion and conclusion . . . 41

3 How atmospheric forcing resolution impacts storm surge model results: insights from Xaver Storm in the North Sea-Scheldt estuary continuum 47
- 3.1 Introduction . . . 47
- 3.2 Materials and methods . . . 49
- 3.3 Results . . . 51

3.4 Discussion 65
3.5 Conclusion 70

4 Future storm surges in the Scheldt North Sea continuum 71
4.1 Introduction 71
4.2 Material and Methods 73
4.3 Results 90
4.4 Discussion 101
4.5 Conclusion 113

5 Conclusions and perspectives 117
5.1 Conclusion 117
5.2 Contribution to the model development 120
5.3 Perspectives for future works 120
5.4 Final thoughts 123

6 Appendices 125
6.1 Appendix to Chapter 2 125
6.2 Appendix to Chapter 3 136
6.3 Appendix to Chapter 4 142

Bibliography 151

List of acronyms and abbreviations

BPNS	Belgian Part of North Sea
CERRA	Copernicus European Regional ReAnalysis
CFL	Courant-Friedrichs-Lewy
CMEMS	Copernicus Marine Service
CMIP6	Coupled Model Intercomparison Project Phase 6
DG	Discontinuous Galerkin
ECMWF	European Centre for Medium-Range Weather Forecasts
ERA5	ECMWF Reanalysis v5
ESM	Earth System Model
FCA	Flood Control Area
FEM	Finite Element Method
FVM	Finite Volume Method
GCM	Global Climate Model
GEOGloWS	Global Earth Observation for Global Water Sustainability
GPU	Graphics Processing Unit
MAE	Mean Absolute Error
MAR	Modèle Atmosphérique Régional

NAO	North Atlantic Oscillation
NAP	Normaal Amsterdams Peil
PCS	Physical Climate Storyline
RCM	Regional Climate Model
RMSE	Root Mean Square Error
SLIM	Second-generation Louvain-la-Neuve Ice-ocean Model
SSP	Shared Socioeconomic Pathway
SWE	Shallow Water Equations
TPXO	TOPEX/Poseidon Global Ocean Tide Model
VNSC	Flemish-Dutch Scheldt Commission
WD	Wetting and Drying
ZDI	Zeebrugge Dam Instrument

Chapter 1

Introduction

1.1 Why study estuary-sea continua ?

Estuaries and their adjacent coasts act as transition zones between land and sea and occupy a vanishingly small fraction of the planet, yet few environments carry higher importance than them. They make up barely 2% of the global land area and host more than 15% of the world's population, a share projected to grow by a further 9–13% by 2100 (Cosby et al., 2024; Merkens et al., 2016; McGranahan et al., 2007). Their strategic location has historically supported human settlement, offering proximity to fresh water and fertile alluvial land. They host key global industries including fisheries, aquaculture, tourism, energy production, and ports (Kapetsky, 1984; Klein et al., 2004; Flambard et al., 2019). These regions also serve as major corridors for international trade, linking continents through dense maritime networks. Per unit area, estuaries and coastal regions rank among the most valuable ecosystems on Earth, valued at roughly 29,000 \$ ha^{-1} yr^{-1}—more than one order of magnitude above the ~660 \$ ha^{-1} yr^{-1} of the open ocean (Costanza et al., 2014).

Behind this human and economic footprint lies a system of considerable Earth-system importance: the exchanges of water, sediment, and biogeochemical elements from which estuarine ecosystem services ultimately derive. As the interface between land and sea, estuaries and their coastal seas mediate these exchanges in both directions (Milliman et al., 2011). Seaward, they deliver freshwater and essential nutrients (C, N, P, Si) that fuel primary production and benthic–pelagic coupling on continental margins (Turner et al., 2003; Carstensen et al., 2015); landward, oceanic forcing regulates salinity intrusion, stratification, and mixing, shaping estuarine circulation, residence times, and habitat structure (Mohammed et al., 2018). From this interplay arises a suite of ecosystem services on which coastal populations depend—nutrient retention, carbon sequestration, shoreline stabilisation, waste treatment, and the attenuation of floods and storm surges (Barbier et al., 2011). These benefits, however, are increasingly threatened.

The openness to land and sea that makes estuaries and coastal zones so valuable also leaves them among the most exposed environments on Earth, facing a compounding set of natural and anthropogenic pressures. Among these, storm surges pose the most acute threat to coastal communities and ecosystems (Nicholls et al., 2007): they have claimed close to one million lives worldwide since 1900 (Bouwer et al., 2018), and between 1979 and 2014 roughly 1.3% of the world's population was exposed to a 1-in-100-year surge-driven flood, with economic exposure reaching into the trillions of US dollars (Muis et al., 2016; Nicholls, 2006).

These risks are particularly high in funnel-shaped estuaries modified for navigation, where the convergent geometry can amplify a surge as it propagates inland, so that inland areas are exposed to higher water levels than the open coast (Talke et al., 2021). The Scheldt–North Sea continuum, shared between Belgium and the Netherlands, is one such system and region of interest of this thesis.

1.2 Storm surges across the estuary–sea continuum

Understanding this hazard begins with the surge itself. A storm surge is a temporary anomaly in sea level driven by the passage of an

extratropical or tropical storm, principally through wind stress at the sea surface and horizontal gradients of atmospheric pressure (Flather, 2001). It takes the form of a long gravity wave, up to several kilometres in wavelength depending on the size and translation speed of the storm, that usually passes as a single wave raising or lowering the sea surface (Flather, 2001). Because its wavelength far exceeds the water depth, the surge is a barotropic response whose first-order dynamics are described by the depth-integrated shallow water equations, with the atmospheric forcing balanced by bottom friction.

A surge may take the form of a positive surge, an abnormal rise in water level above the predicted astronomical tide, or a negative surge, an anomalous drawdown below it and typically persist from a few hours to two or three days. The atmosphere forces the sea through the friction force of the wind on the sea surface, expressed as the wind stress, and through the atmospheric pressure gradient force, which produces the inverse-barometer effect. The surge results from the balance of these forcings with the barotropic pressure gradient force due to the sea-surface slope, the Coriolis force and the bottom friction. In a positive surge, the low pressure raises the water surface while the wind stress drives the elevated water landward. Negative surges arise from the inverse mechanism: strong offshore-directed winds push water away from the coast, exposing intertidal areas, lowering navigable depths, and disrupting port access (Jensen et al., 2022; Pugh, 1987). Extratropical cyclones, which dominate the mid-latitudes, generate surges over broad areas with comparatively modest peaks, whereas tropical cyclones produce more intense but more localised effects (Von Storch et al., 2008; Flather, 2001).

As it reaches the coast, the surge is amplified by the geometry of the sea floor and shoreline. Shallow coastal regions are especially exposed because of their depth: the wind set-up scales inversely with water depth—a given wind stress raises the sea surface more over a shallow shelf than over deep water—and a surge propagating into shallower water is further amplified by shoaling, as the decreasing depth compresses its energy into a thinner column (Pugh, 1987; Flather, 2001). The amplification is sharpest where the coastline itself converges, such as in the southern North Sea (Koopmann, 1962; Corkan, 1948; Jelgersma et al., 1995).. In a funnel-shaped estuary the

convergent geometry amplifies a surge of either sign as it propagates inland: to the shoaling already at work, the converging banks add further lateral constriction (funnelling), and together they concentrate the surge in the narrowing, shallowing reaches (Jay, 1991; Friedrichs et al., 1994), so that a positive surge grows landward and can exceed the level reached at the open coast (Talke et al., 2021) while the same funnelling deepens a negative-surge drawdown. Bed friction opposes this growth, dissipating energy and distorting the surge waveform into a tide-like asymmetry (Dronkers, 1986).

In shallow seas, the surge and the tide do not simply add up. Both travel through the same water and feel the same depth and bottom friction, so that tidal and wind-driven motions cannot be treated separately (Jacob et al., 2017). Three effects follow. At high tide the water is deeper, so the wind raises the sea surface less. Where tidal currents are strong and reverse with each tide, they reduce the work done by the wind on the water (Jacob et al., 2017). And a surge, by deepening the water, makes the tidal wave travel faster and arrive earlier (Prandle et al., 1978; Horsburgh et al., 2007). Part of the non-tidal residual, the observed level minus the predicted tide, can therefore come from this shift of the tide rather than from the weather. As a result, surge peaks in the North Sea occur mostly on the rising tide and rarely at high water (Horsburgh et al., 2007). For flood risk, the skew surge, the difference between the observed and predicted high water, is a better measure, because it is largely independent of the tide (Williams et al., 2016); adding tide and residual as if they were independent can overestimate extreme sea levels by up to 30 % (Arns et al., 2020). In estuaries, the tide is itself distorted by bottom friction and non-linear advection as it moves over the tidal flats and toward the head of the estuary (Stanev et al., 2014), so the surge propagates on an asymmetric tide and its interaction with it changes along the channel (Familkhalili et al., 2020). This is why Chapter 4 reports both the surge residual and the skew surge, and uses the timing of the residual relative to the tide as a diagnostic of the interaction.

These surges carry serious consequences that differ. A positive surge floods low-lying land, overtopping flood defences and inundating the hinterland, with socioeconomic impacts that persist long after the waters recede—more so where it coincides with heavy

rainfall or high river discharge, giving compound flooding (Marcos et al., 2019). A negative surge instead exposes intertidal and subtidal margins and can cut navigable depths in the narrow-margin channels below the thresholds required for deep-drafted vessels (Jensen et al., 2022; Pugh, 1987). The destructive potential of these events spans the globe, from tropical cyclones such as Katrina, which caused around 1,100 fatalities in New Orleans, to the extratropical windstorms that reach the low-lying coasts of north-western Europe (Muis et al., 2016).

1.3 The Scheldt–North Sea continuum

1.3.1 The North Sea

The North Sea is one of the busiest maritime basins in the world, bordered by seven countries and fed by numerous rivers (Fig. 1.1.a). The basin connects to the Atlantic Ocean through the English Channel in the south and the Norwegian Sea in the north. With an average depth of approximately 90 m and a maximum exceeding 800 m in the Norwegian Trench (Sündermann et al., 2011), it occupies a partially enclosed position on the northwestern European continental shelf that gives rise to a distinctive and complex physical environment. Its dynamics emerge from the interplay of three broad categories of forcing—oceanic, atmospheric and continental—and of their interactions.

From an oceanic perspective, the North Sea is too small to generate significant tides independently. Its tides are co-oscillations driven by the Atlantic Ocean, which enter the basin mainly through the northern opening and, to a lesser extent, through the English Channel (Sündermann et al., 2011). The dominant constituents are semi-diurnal, with M_2 accounting for roughly 80% of the tidal energy (Sündermann et al., 2011). As the tidal wave propagates southward into the shallower and narrower Southern Bight, it is amplified by shoaling and convergence, which results in the largest tidal ranges of the basin along the Belgian, Dutch and German coasts.

Atmospheric forcing over the region is largely controlled by the North Atlantic Oscillation (NAO), a large-scale pattern defined by fluctuations in the pressure difference between the Azores high and

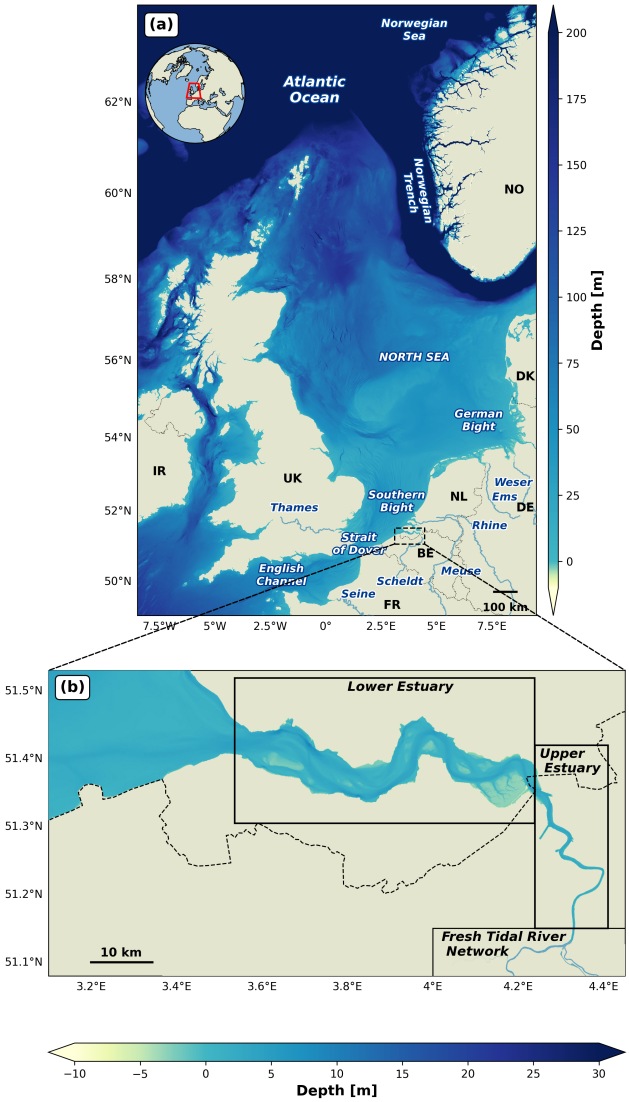

Figure 1.1: (a) The North Sea and its adjacent regions. The color gradient indicates water depth from shallow coastal areas to deeper offshore regions, the major river contributors to the North Sea are shown in blue with key geographic features labeled for reference and a small globe in the top left corner indicating the extent of the main map with a red rectangle. **(b)** Detailed bathymetric map of the Scheldt Estuary, highlighting the separation between the Lower Estuary, the Upper Estuary, and the freshwater tidal river network.

the Icelandic low (Hurrell et al., 2009). During NAO's positive phase, stronger westerlies drive a predominantly cyclonic wind-driven circulation over the North Sea (de Vries et al., 1995; Sündermann et al., 2011) and, at interannual to decadal timescales, are associated with increased extratropical cyclone activity (Hurrell et al., 2009). These cyclones generate the storm surges of the basin. A positive surge develops when low-pressure systems and strong northerly to north-westerly winds push water against the coast (de Vries et al., 1995; Weisse et al., 2012), whereas a negative surge develops when south-easterly gales drive water offshore (Jensen et al., 2022). Because the Southern Bight is shallow and funnel-shaped, both types of surge are amplified towards its coasts. Consequently, the German Bight and the Dutch and Belgian coasts rank among the most surge-exposed areas of the basin.

Continental forcing enters the basin mainly through river discharge. The largest contributions come from the Rhine–Meuse delta (long-term mean of about 2900 m^3/s), the Elbe (870 m^3/s), the Weser (330 m^3/s), the Humber (250 m^3/s), the Scheldt (120 m^3/s) and the Thames (65.5 m^3/s) (OSPAR Commission, 2000; Kwadijk et al., 2016). River discharge also bears on the surge hazard: the storms that generate surges often bring heavy rainfall that increases river flow, so high discharge and surge can coincide and lead to compound flooding (Khanal et al., 2019; Klerk et al., 2015).

These forcings do not act independently. At the basin scale, they drive a broadly cyclonic, counter-clockwise residual circulation (Otto et al., 1990; Sündermann et al., 2011). Moreover, because the basin is shallow and tidally energetic, wind and tide interact non-linearly through bottom friction (Jacob et al., 2017). The water level reached during a storm therefore differs from the sum of the astronomical tide and the surge, as it depends on the tidal phase at which the surge occurs. Surge and tide consequently need to be resolved together along the continuum.

1.3.2 The Scheldt estuary

The Scheldt estuary lies in the southwestern Netherlands and northwestern Belgium (Fig. 1.1.b), formed by the Scheldt River, which

originates in northern France and discharges into the Southern Bight of the North Sea. The river flows some 355 km from France to the North Sea at Vlissingen, with the Port of Antwerp, one of Europe's largest, near its head. Circulation is dominated by a macrotidal semidiurnal tide, whose influence extends some 160 km inland to the sluices at Gent (Nihoul et al., 1978). The estuary narrows and shoals landward, its width declining from roughly 5 km at Vlissingen to about 60 m near Gent and its depth from about 15 m to 7 m at the same location.

The estuary is a convergent, multi-channel system with two to three main channels separated by shoals, over a total area of 310–370 km^2 and is bordered by extensive mud and sand flats, about 35% of which are intertidal. This convergent, shallowing geometry amplifies a surge as it travels landward, while the intertidal flats store part of the surge volume and dissipate its energy, attenuating the peak upstream (Smolders et al., 2015). Dredging and a century of embankment have reduced this intertidal area and raised the tidal range (Wang et al., 2019). The morphology of the estuary keeps evolving under dredging, embankment and sea-level rise. This thesis focuses on the response of the continuum to the atmospheric forcing, the bathymetry is held at its present-day state in all simulations, so that the differences between simulations can be attributed to this forcing alone.

The Scheldt is a tide-dominated, generally well-mixed estuary whose salinity intrusion shifts seasonally over the three classical zones of the tidal river (Meire et al., 2005; Baeyens, 1998). Its discharge is rain-fed and varies strongly with season, from winter high flow to summer low flow (Fig. 1.3), yet even at its winter peak it remains small compared with the tidal and surge volumes (Meire et al., 2005). A storm surge arriving in the estuary is a barotropic response to a long wave arriving from the North Sea, and the strong winds and high water levels of the storm enhance vertical mixing and break down any stratification.

1.3.3 Surge history and flood management

A few extreme events have shaped the region's history: the Great North Sea flood of 1953, the Gale of 1976, and Storm Xaver in 2013 (Gerritsen, 2005; Wadey et al., 2015; Meyer et al., 2023). The 1953 flood

remains the defining event. A severe extratropical cyclone coincided with spring tides and drove total water levels of up to 6 m above mean sea level along the Dutch and Belgian coasts (Gerritsen, 2005; Rossiter, 1954), a surge of return period of order 1-in-4000 years. It inundated low-lying areas of the Netherlands, Belgium, and the United Kingdom (Fig. 1.2), caused over 2,500 deaths and displaced tens of thousands (Rossiter, 1954; Jonkman et al., 2012). Two days before the positive surge, pronounced negative-surge drawdowns halted navigation in the southern North Sea (Burlace, 1986; Jensen et al., 2022). This is an early illustration of the two-sided surge hazard central to this work.

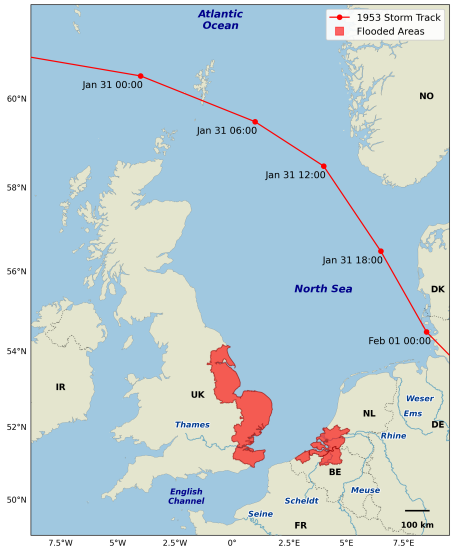

Figure 1.2: Storm track and flood extent of the 1953 North Sea storm surge event. Data for the flooded area were retrieved from Rijkswaterstaat (Paprotny, 2025).

Flood management in the region has responded to these events, shifting from hard engineering toward ecosystem-based defence (Morris et al., 2018; Sutton-Grier et al., 2015; Vitale et al., 2025). After the 1953 storm, the Netherlands built the Delta Works, a system of dams, sluices and storm-surge barriers designed for return periods of 1-in-4,000 to 1-in-10,000 years (Watson et al., 1990; Gerritsen, 2005). Belgium's Flemish government answered the 1976 gale with the Sigma Plan, combining higher dikes, controlled flood areas and a storm-surge

barrier. The barrier was abandoned as too costly, and management moved toward a more integrated flood-risk strategy (Vitale et al., 2025; Vikolainen et al., 2015). Protection now rests on dikes designed for a 1-in-4,000-year flood and on Flood Control Area (FCA) that lower the peak upstream (Cox et al., 2006; Smolders et al., 2015). These polders fill through sluices to store part of the surge. Some, since 2005, operate under a controlled reduced tide that also fosters intertidal habitat (Cox et al., 2006); their representation in the model is discussed in Chapter 2.

During Storm Xaver in 2013, flood areas and restored marshes measurably lowered surge height upstream (Smolders et al., 2020). Intertidal wetlands attenuate surges: they add friction, store water and dissipate energy over vegetation (Smolders et al., 2015; Stark et al., 2015). They also partly offset the historical loss of habitat (Meire et al., 2005). This dual function has made the Sigma Plan a reference for ecosystem-based adaptation in north-western Europe (Temmerman et al., 2013).

The estuary and its flood risks are shared between Belgium and the Netherlands, so their management is inherently transnational. Successive treaties on the Western Scheldt frame joint monitoring, shared modelling and harmonised flood-defence strategies. These are coordinated through bodies such as the Flemish-Dutch Scheldt Commission (VNSC), so that decisions on one side of the border account for their consequences on the other (van Buuren et al., 2010; Slinger, 2023). This coordination only grows in importance under climate change.

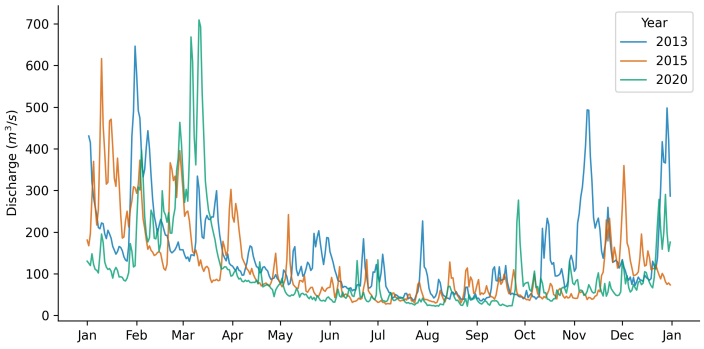

Figure 1.3: Evolution of river discharge at the Belgian-Dutch border for the years 2013, 2015, and 2020. Data were retrieved from SchkeldeMonitor, a portal providing information and data products on the Scheldt Estuary (ScheldeMonitor Team & VNSC Werkgroep Onderzoek & Monitoring, 2020).

1.4 Modelling storm surges across a multi-scale continuum

Sea levels and their extremes have been studied for nearly two centuries (Lubbock, 1836). Numerical prediction followed in the 1960s. Depth-averaged finite-difference formulations of the shallow water equations then made it possible to compute surge propagation over a shelf (Welander, 1961; Heaps, 1969). The depth-averaged formulation and its coupling to an atmospheric model both date from that period, and both still underpin operational surge forecasting (Kohno et al., 2018). What has changed since is the discretisation of the domain, the resolution of the atmospheric forcing and the available computational resources.

Historically, river and ocean modelling communities operated largely in isolation. This separation limits the representation of river-sea exchanges, and it has been identified as a key source of uncertainty in coastal models globally (Breitburg et al., 2018; Lewis et al., 2019). Seamless modelling of the river, estuary and coastal ocean within a single framework is therefore needed to capture the multi-scale nature of these interactions (Haidvogel et al., 2017). For storm surges, these scales range from tens of meters within estuaries to hundreds of

kilometers across continental shelves, and from hours to several years in time. Recent modeling efforts have started to bridge this gap.

The choice of the hydrodynamic model is discussed in the following section, followed by its atmospheric forcing.

1.4.1 Hydrodynamic modeling of the estuary-sea continuum

Two approaches represent storm surges in coastal regions: data-driven and physics-based models. Data-driven models predict hydrodynamic variables from historical observations, using statistical or machine-learning methods (Tadesse et al., 2020; Cid et al., 2016; Schaffer et al., 2025). They are computationally efficient and suited to near-real-time forecasting (Ayyad et al., 2022). Their dependence on training data, however, limits their ability to generalize to extreme events outside the observed record (Tadesse et al., 2020; Ayyad et al., 2022). Hybrid approaches coupling the two are increasingly explored (Ayyad et al., 2022). Physics-based models instead solve the governing equations of fluid motion. They are more expensive to run, but they remain valid under conditions that have not been observed, such as future atmospheric conditions. They are the reference for operational models (Kohno et al., 2018) and form the framework of this dissertation.

Both the three-dimensional (3D) baroclinic and the two-dimensional (2D) depth-averaged formulations rest on the hydrostatic assumption, which is valid where horizontal scales greatly exceed vertical scales (Cushman-Roisin et al., 2011). They differ in whether they resolve the vertical structure of the flow, and this is what guides the choice of vertical discretization. 3D models represent estuarine physics more completely, but they are more expensive and have more demanding boundary conditions. They are therefore warranted only when the vertical structure is dynamically important: in strongly stratified regions, in dense coastal vegetation where profile drag and dissipation affect the surge, or when baroclinic effects from salinity and temperature gradients influence storm surge and compound flood simulations (Ye et al., 2020; Lapetina et al., 2015). The Scheldt is a generally well-mixed estuary (Meire et al., 2005), where a surge behaves primarily as a barotropic response. Its vertical structure is

therefore not dynamically important for the surge, and the depth-averaged Shallow Water Equations (SWE) formulation is adopted here. This formulation is also the standard in operational surge modeling (Dube et al., 2010). The accuracy of a depth-averaged model then depends mainly on the parametrization of bottom friction and atmospheric forcing (Weaver et al., 2009; de Vries et al., 1995; Zheng et al., 2013; Huybrechts et al., 2010).

Regions of freshwater influence (ROFIs), such as the Rhine plume along the Dutch coast, are the main exception to the vertical homogeneity of the southern North Sea: there, the freshwater input creates a tidally modulated stratification and a sheared vertical velocity profile (Simpson, 2012). These features control the transport of the freshwater and its constituents, but their effect on the surge is of second order. During storms, wind and wave mixing homogenises the water column over most of the Rhine ROFI (Simpson et al., 1993), and comparisons between depth-averaged and three-dimensional surge models show differences in peak surge of the order of 5%, comparable to the uncertainty in the bottom friction and vertical mixing parameterisations (Weaver et al., 2009; Zheng et al., 2013). A depth-averaged formulation therefore suffices for the water levels studied here, but would not for the transport of salt, sediment or nutrients.

The horizontal discretization sets how the model spans the scales of the continuum, from the estuarine channels to the open shelf. It is therefore a central modeling choice. One option is to keep these scales separate, with grids of different resolution. Nested structured grids embed higher-resolution grids within coarser ones (Ivanov et al., 2020; Debreu et al., 2012; Marta-Almeida et al., 2013). In both cases, an interface is placed on the path of the surge, where the surge is still forced by the wind and interacts with the tide (Horsburgh et al., 2007; Jacob et al., 2017). The rigid layout of structured grids also struggles to represent the complex coastal geometries specific to estuarine regions (Hasan et al., 2016; Nudds et al., 2020). The alternative is a single unstructured mesh with Finite Element Method (FEM) or Finite Volume Method (FVM), such meshes let the resolution vary continuously across the domain. They concentrate computational effort in geometrically complex or dynamically active regions, and

keep a coarser resolution offshore, where bathymetry and flow vary over larger spatial scales. This flexibility makes unstructured models particularly well-suited to represent estuary–sea continua (Zhang et al., 2023; Nudds et al., 2020).

Several unstructured models have been widely applied to storm surge and estuarine simulations: FVCOM (Tasnim et al., 2014; Deb et al., 2020), ADCIRC (Luettich et al., 1999; Westerink et al., 2008), SCHISM (Zhang et al., 2016; Hsiao et al., 2021), SLIM (Lambrechts et al., 2008; Sampurno et al., 2022), Delft3D (Lesser et al., 2004; Xu et al., 2024), and TELEMAC (Hervouet, 2007; Gourgue et al., 2015; Benoit et al., 2002). These models differ in their discretisation method. Finite-volume schemes conserve mass and momentum locally and handle advection-dominated flows robustly, but they are sensitive to mesh quality (Chen et al., 2003). Continuous finite-element schemes achieve higher-order accuracy and tolerate anisotropic elements, but they require stabilisation for advection-dominated problems. The Discontinuous Galerkin (DG) finite-element method combines the local conservation of finite-volume schemes with the higher-order accuracy and geometric flexibility of finite-element schemes, at the cost of a larger number of degrees of freedom (Kärnä, 2012). The solution is computed element by element, and elements communicate only through numerical fluxes at their interfaces, so the method is also highly parallelisable (Cockburn et al., 2000). Second-generation Louvain-la-Neuve Ice-ocean Model (SLIM), the model used in this thesis, is built on the DG finite-element method on unstructured meshes (Lambrechts et al., 2008; de Brye et al., 2010). This choice is suited to the continuum. It provides the geometric flexibility to resolve the estuarine channels within the same domain as the shelf. It also provides the local conservation and robustness required for the advection-dominated flows over the intertidal flats. Unstructured-mesh models have historically carried a higher computational cost than their structured counterparts. The parallel structure of the DG method, however, makes it well suited to Graphics Processing Unit (GPU) architectures, which have substantially reduced this cost and made such models competitive for long-term applications (Dong et al., 2025; De Le Court et al., 2026).

1.4.2 Atmospheric forcing under present and future climate

Storm-surge models are forced at the sea surface by near-surface wind and atmospheric pressure, from which the wind stress is parameterised. These fields come from atmospheric models of different types, from global products down to the regional models used to reach the finer scales of coastal regions. Global reanalyses combine a model with observations to reconstruct the past atmosphere consistently over several decades. Regional reanalyses apply the same approach over a smaller domain, at a finer resolution. Regional climate models solve the atmospheric equations over a limited domain, driven at their boundaries by a coarser product. Their resolution can be adapted to the problem, but they inherit the errors of this driving product. Reanalyses are constrained by observations, but they tend to underestimate extreme winds (Molina et al., 2021). The resolution of these products typically ranges from a few to tens of kilometers (Dinapoli et al., 2020; Chen et al., 2023a). This is far coarser than estuarine-sea models. Small-scale atmospheric processes that the forcing does not resolve cannot be recovered by a finer mesh.

To represent future condition, hydrodynamic models rely on Global Climate Models (GCMs), such as the ones available under Coupled Model Intercomparison Project Phase 6 (CMIP6) Earth System Models (ESMs), to provide wind and pressure fields. Standard GCM resolutions are typically 100 km or coarser. They are insufficient to capture the localized pressure gradients and fine-scale coastal wind patterns that drive severe storm surges (Roberts et al., 2020; Mizuta et al., 2017). Two main strategies bridge this scale mismatch. Parametric wind profiles reconstruct the intense, near-symmetric pressure and wind fields of cyclones from a limited set of synthetic track parameters (Holland, 1980; Deppermann, 1947). They are highly effective for tropical cyclones, but poorly suited to the complex, asymmetric structure of the extratropical storms that dominate the North Sea (Loridan et al., 2015; Done et al., 2020). Dynamical downscaling is therefore preferred. It uses a Regional Climate Model (RCM) driven by a GCM to reach finer scales (5 km to 50 km) (Pringle et al., 2021; Yasuda et al., 2014; Woth, 2005). Recent global efforts have pushed this approach further, forcing surge models

with high-resolution climate ensembles such as the 25 km CMIP6 HighResMIP ensemble (Muis et al., 2023). This ensemble improves the representation of extratropical-cyclone structure relative to standard-resolution CMIP6 models, yet it still underestimates cyclone wind intensity (Priestley et al., 2022b).

Under future climate, the atmospheric forcing of the surge will itself change—one of two partly independent pathways by which climate change alters the surge hazard. The first pathway, sea-level rise, does not act through the atmosphere but by raising the baseline water level, it is projected to be the dominant driver of increasing extreme sea-level frequency this century (Vousdoukas et al., 2018; Oppenheimer et al., 2019), with end-of-century projections largest for the North Sea, approaching one meter under high-emission scenarios (Calafat et al., 2022; Vousdoukas et al., 2016; Kirezci et al., 2020). The second pathway, which does involve the atmospheric forcing, is the evolution of the meteorological surge, as storm tracks and wind fields change (Vousdoukas et al., 2017). Extratropical cyclones draw their energy from the meridional temperature gradient. Anthropogenic warming perturbs this gradient in opposite directions near the surface and in the upper troposphere (Screen et al., 2010; Shaw et al., 2016). Projections consistently indicate an eastward extension of the winter storm track into north-western Europe (Zappa et al., 2013; Harvey et al., 2020; Priestley et al., 2022b). This response is superimposed on strong internal variability, notably the NAO (Menéndez et al., 2010). It therefore remains considerably more uncertain and model-dependent (Weisse et al., 2012). This thesis addresses the second pathway: sea-level rise is held fixed so that the atmospheric contribution to the surge can be isolated (Chapter 4).

1.5 Research questions and outline

The overall objective of this dissertation is to represent storm surges through the full Scheldt–North Sea continuum under both present and future atmospheric forcing. Three gaps stand in the way, and each leads to a research question.

1.5.1 Resolving the continuum in a single domain for storm surges

Storm surges are therefore a major hazard for the Scheldt–North Sea continuum. Global surge reanalyses do not adequately resolve tidal interactions and estuarine dynamics (Muis et al., 2016). Other studies focus on neighbouring North Sea estuaries (Stanev et al., 2016; Pein et al., 2023; Grabemann et al., 2020). Studies that resolve the Scheldt in detail typically treat it in isolation, and single-domain applications, including earlier SLIM configurations, have addressed contaminant transport and biogeochemistry but not extreme water levels (de Brye et al., 2010; Gourgue, 2011; Patil et al., 2024). This thesis applies such a single-domain configuration of SLIM to storm surges along the Scheldt–North Sea continuum. Its GPU implementation (De Le Court et al., 2026) makes multi-year runs and large sets of storm simulations affordable at estuarine resolution, which previous configurations could not sustain. This leads to our first question:

- How accurately does a single-domain configuration reproduce the height and the timing of the tide and the storm surge from the open North Sea to the upper Scheldt estuary?

1.5.2 Impact of the resolution of the atmospheric forcing in the model results

The resolution required to reproduce the surge inside an estuary, as opposed to the open coast, remains poorly constrained. Previous studies disagree on whether the spatial or the temporal resolution of the forcing matters most (Weaver et al., 2016; Agulles et al., 2024). This leads to our second question:

- How does the spatial and temporal resolution of the atmospheric forcing affect the simulated storm surge along the continuum?

1.5.3 Future storm surges

Most surge projections in the region rely on coarse models that leave the inner continuum unresolved (Woth et al., 2006; Weisse et al., 2005;

Vousdoukas et al., 2016; Calafat et al., 2022), and negative surges remain far less documented than positive surges. We focus on the atmospheric component of future conditions, and global-mean sea-level rise is not included in the model. This leads to our third question:

- What do future extreme storms reveal about positive and negative storm surges along the Scheldt–North Sea continuum under a high-emission scenario?

We answer these questions in three chapters, one for each question.

Chapter 2 presents the modeling framework based on SLIM, the model is validated from 2016 to 2021, a period sufficient to capture intra-annual and interannual variability in tidal dynamics, river discharge and meteorological forcing with a focus on a storm during this period.

Chapter 3 investigates the sensitivity of storm surge predictions to the resolution of atmospheric forcing, simulations are performed with SLIM and one-way forced with the atmospheric model Modèle Atmosphérique Régional (MAR) (Fettweis et al., 2013) at spatial resolutions ranging from 2 km to 30 km and temporal resolutions from 15 minutes to 6 hours, applied to the hindcast of Storm Xaver in December 2013 in the region. This analysis identifies an optimal atmospheric forcing resolution to model surge in the region, with particular attention to the contrasting behavior of open-sea and estuarine stations. This chapter has been published in *Regional Studies in Marine Science* (Randresihaja et al., 2026).

Chapter 4 applies the modelling framework to future climate conditions under the SSP3-7.0 scenario. Using a Physical Climate Storyline (PCS) approach, plausible future extreme storm events are dynamically downscaled with MAR and simulated with SLIM to characterise how different typologies of storm tracks will alter the full spectrum of surge dynamics from positive to negative surges across the Scheldt–North Sea continuum by the end of the 21st century.

Finally, Chapter 5 synthesises the main findings of the three preceding chapters, reflecting on the implications of the model results, the limitations of the modeling approach, and perspectives for future research.

Supporting publications

Included in this thesis

Randresihaja N. R., Gourgue O., Alaerts L., Fettweis X., Lambrechts J., De Le Court M., Grégoire M., and Hanert E. (2026). How atmospheric forcing resolution impacts storm surge model results: Insights from Storm Xaver in the North Sea-Scheldt estuary continuum, *Regional Studies in Marine Science*, 96, doi: 10.1016/j.rsma.2026.104919

Other publications

Alaerts L., Lambrechts J., **Randresihaja N. R.**, Vandenbulcke L., Gourgue O., Hanert E., and Grégoire M. (2025). "An integrated high-resolution bathymetric model for the Danube Delta system". Earth System Science Data, 17.7, pp. 3125–3140. doi: 10.5194/essd-17-3125-2025.

Lecart M., Dobbelaere T., Alaerts L., **Randresihaja N. R.**, Mohammed A. V., Vethamony P., and Hanert E. (2024). "Land reclamation and its consequences: A 40-year analysis of water residence time in Doha Bay, Qatar". *PLoS One*, 19.1. doi: 10.1371/journal.pone.0296715

Alaerts L., Lambrechts J., De Le Court M., **Randresihaja N. R.**, Vandenbulcke L., Gourgue O., Hanert E., and Grégoire M. (2026). The Danube Delta: How do floodplains impact the Danube-Black Sea continuum? [Manuscript in preparation]

Grégoire M., Vandenbulcke L., Chevalier S., Choblet M., Drozd I., Grailet J. -F., Ivanov E., Macé L., Verezemskaya P., Yu H., Alaerts L., **Randresihaja N. R.**, Mangeleer V., de Noordhout G. M., Capet A., Meulders C., Mouchet A., Munhoven G., and Soetaert K. (2026). The BiogeochemicAl Model for Hypoxic and Benthic Influenced areas: BAMHBI v1.0, *Geoscientific Model Development*, 19.5, pp. 2137-2175, doi:10.5194/gmd-19-2137-2026

Chapter 2

Multiscale hydrodynamic modeling of the Scheldt-North Sea continuum

Modelling storm surges along the Scheldt–North Sea continuum requires a domain that spans the open shelf and the estuarine channels at widely different resolutions. This chapter addresses the first research question with the depth-averaged version of SLIM, whose solver, explicit Wetting and Drying (WD) scheme and GPU implementation are prior developments within the research group (De Le Court et al., 2026). My contribution lies in the application of this model to storm surges along the continuum. I configured, forced and validated it within a single unstructured mesh, from the open shelf to the upper estuary, and extended it to continuous multi-year simulations at estuarine resolution. This application was also among the first to use the early versions of the GPU implementation within SLIM and of the explicit WD scheme, which I tested and helped debug on a large, realistic domain. I first describe the model (Section 2.1) and its set-up for the period 2016–2020 (Section 2.2), then validate it against tides, currents, residual circulation, water levels and the surge of Storm

Ciara (Section 2.3), and finally discuss its relevance for storm-surge modelling (Section 2.4).

2.1 Hydrodynamic model

The hydrodynamic simulations presented in this thesis are performed in the framework of the Second-generation Louvain-la-Neuve Ice-ocean Model (SLIM, `www.slim-ocean.be`), developed at UCLouvain to simulate flows from the river to the coastal ocean. SLIM discretises the governing equations with the DG FEM on unstructured meshes (de Brye et al., 2010). Owing to this unstructured discretisation, the element size can vary widely within the same domain, which allows the open shelf, the coastal zone and the narrow estuarine channels to be represented together. As a storm surge is mainly a barotropic response of the water column to the wind stress and the atmospheric pressure gradients, we use the two-dimensional depth-averaged version of the model, SLIM2D, which solves the barotropic shallow-water equations. This choice is suitable for the Scheldt, which is a well-mixed estuary where the vertical density gradients have a negligible influence on the momentum balance (Patil et al., 2024; Sampurno et al., 2022). In addition, the wetting-and-drying algorithm implemented in SLIM2D allows the surge to propagate over the intertidal flats, tidal marshes and floodplains, which store part of the surge volume. Finally, the recent multi-GPU implementation of the model reduces the computation time of a one-month simulation to a few hours (De Le Court et al., 2026), which makes the multi-year, high-resolution simulations used in this thesis possible. In what follows, we present the governing equations of SLIM2D and their parameterisations.

2.1.1 Main equations

SLIM2D solves the barotropic shallow-water equations. The mass-conservation (continuity) equation reads

$$\frac{\partial \eta}{\partial t} + \underbrace{\nabla_h \cdot (H\mathbf{u})}_{1} = 0, \tag{2.1}$$

$$\frac{\partial (H\mathbf{u})}{\partial t} + \underbrace{\nabla_h \cdot \frac{H\mathbf{u}\,H\mathbf{u}}{H}}_{2} = \underbrace{-f\,\mathbf{e}_z \times H\mathbf{u}}_{3} \underbrace{- g\,H\,\nabla_h \eta}_{4} \underbrace{- \frac{g}{(\gamma H)^2} |H\mathbf{u}|\,H\mathbf{u}}_{5} + \underbrace{\nabla_h \cdot (H\kappa \nabla_h \mathbf{u})}_{6} + \underbrace{\frac{\boldsymbol{\tau}_s}{\rho}}_{7} \underbrace{- \frac{H}{\rho} \nabla_h p_{\mathrm{atm}}}_{8}, \tag{2.2}$$

where Eqs (2.1) and (2.2) are the mass-conservation and the momentum equations, respectively, and "1" – divergence of depth-integrated velocity "2" – momentum advection, "3" – Coriolis force, "4" – barotropic pressure gradient, "5" – bottom friction, "6" – horizontal diffusion, "7" – wind surface stress, "8" – atmospheric pressure gradient. The model is initialised at rest, $H\mathbf{u} = (0, 0)\ \mathrm{m^2\,s^{-1}}$; the initial free-surface elevation is given in Section 2.2.2. The meaning of all variables and parameters is given in Table 2.1.

The bottom stress is parameterized with a quadratic drag law using the Chézy–Manning–Strickler coefficient $\gamma = H^{1/6}/n$, where n is the Manning roughness coefficient.

Horizontal viscosity. Subgrid turbulent motions are represented through the Smagorinsky (1963) non-linear parameterisation of the horizontal eddy viscosity κ.

$$\kappa = C_S^2 A \|S\| = C_S^2 A \sqrt{2\left(\frac{\partial u}{\partial x}\right)^2 + 2\left(\frac{\partial v}{\partial y}\right)^2 + \left(\frac{\partial u}{\partial y} + \frac{\partial v}{\partial x}\right)^2}, \tag{2.3}$$

where $C_S = 0.1$ is the dimensionless Smagorinsky coefficient, A [$\mathrm{m^2}$] is the area of the triangular element and $\|S\|$ [$\mathrm{s^{-1}}$] is the norm of the strain-rate tensor.

The wind surface stress is computed as

$$\boldsymbol{\tau}_s = \rho_{\mathrm{air}}\, C_w \|\mathbf{u}_{10}\|\, \mathbf{u}_{10}. \tag{2.4}$$

To account for sea-surface roughness at high wind speeds (the spume effect, where intense winds tear droplets from wave crests and limit the momentum transfer), C_w saturates at large $\|\mathbf{u}_{10}\|$ (Powell et al., 2003; Donelan

Table 2.1: Variables and parameters used in the governing equations (2.1) and (2.2).

Symbol	Description	Units
t	Time	s
∇_h	Horizontal gradient operator	m^{-1}
η	Free-surface elevation above reference level	m
h	Still-water depth (bathymetry)	m
$H = h + \eta$	Total water-column height	m
$\mathbf{u} = (u, v)$	Depth-averaged horizontal velocity vector	$\mathrm{m\,s}^{-1}$
$H\mathbf{u}$	Depth-integrated momentum (flux)	$\mathrm{m}^2\,\mathrm{s}^{-1}$
$f = 2\Omega \sin\Phi$	Coriolis parameter	s^{-1}
Ω	Earth's angular velocity	s^{-1}
Φ	Latitude	rad
$\mathbf{e}_z$	Unit vector in the vertical direction	–
g	Gravitational acceleration	$\mathrm{m\,s}^{-2}$
$\gamma = H^{1/6}/n$	Chézy–Manning–Strickler coefficient	$\mathrm{m}^{1/2}\,\mathrm{s}^{-1}$
n	Manning roughness coefficient	$\mathrm{s\,m}^{-1/3}$
κ	Horizontal eddy viscosity	$\mathrm{m}^2\,\mathrm{s}^{-1}$
$\boldsymbol{\tau}_s$	Wind surface stress	$\mathrm{N\,m}^{-2}$
ρ	Water density	$\mathrm{kg\,m}^{-3}$
p_{atm}	Atmospheric pressure at the sea surface	Pa
$\mathbf{u}_{10}$	Wind velocity at 10 m above the surface	$\mathrm{m\,s}^{-1}$
ρ_{air}	Air density ($1.25\,\mathrm{kg\,m}^{-3}$)	$\mathrm{kg\,m}^{-3}$
C_w	Wind drag coefficient	–

et al., 2004; Holthuijsen et al., 2012; Curcic et al., 2020). We adopt the piecewise parameterisation of Flather (1976):

$$C_w = \begin{cases} 0.565 \times 10^{-3} & \text{if } \|\mathbf{u}_{10}\| \le 5\ \mathrm{m\,s}^{-1}, \\ \left(-0.12 + 0.137\,\|\mathbf{u}_{10}\|\right) \times 10^{-3} & \text{if } 5 < \|\mathbf{u}_{10}\| \le 19.22\ \mathrm{m\,s}^{-1}, \\ 2.513 \times 10^{-3} & \text{if } \|\mathbf{u}_{10}\| \ge 19.22\ \mathrm{m\,s}^{-1}. \end{cases} \tag{2.5}$$

This drag coefficient depends only on the wind speed. For a given wind, however, a young, steep sea is rougher than a developed sea and takes more momentum from the wind. Eq. (2.5) represents an average sea state and ignores this dependence. At the scale of the North Sea, most

of the wave effect on the surge can nevertheless be recovered with such a coefficient (Mastenbroek et al., 1993). The direct forcing of waves on the water column, through breaking (wave set-up) and wave–current interactions, is not represented: it requires coupling a wave model and can be larger in coastal areas during extreme events (Staneva et al., 2016). The sea surface temperature, through which the ocean also feeds back on the atmosphere (Lewis et al., 2019), plays no direct role in a barotropic surge. Since the same parameterisation is used in all simulations, these omissions bias the absolute surge levels more than the differences between runs on which Chapters 3 and 4 rely.

We tested the linear law of Smith et al. (1975) against the piecewise form of Flather (1976); the two give similar surge levels over the domain, and we retain the Flather parameterisation because its saturation above $19.22\,\mathrm{m\,s^{-1}}$ prevents the drag from growing unbounded at storm wind speeds. Nor does Eq. (2.5) represent the dependence of the air–sea momentum transfer on the stability of the atmospheric boundary layer (Smith, 1988): cold air over a warmer sea, as in winter, enhances the drag, whereas warm air over a cooler sea, more frequent in spring and summer, reduces it. Part of this effect is carried by the forcing, since MAR derives its near-surface wind from a surface layer based on Monin–Obukhov similarity theory (Gallée et al., 1994). The effect on the drag also weakens as the wind strengthens: at $10\,\mathrm{m\,s^{-1}}$, the drag coefficient varies by up to about 30 % between stable and unstable conditions, but by only about 3 % at $25\,\mathrm{m\,s^{-1}}$ (Smith, 1988), so that it matters least during storms.

2.1.2 Wetting and drying

In shallow coastal and estuarine systems, the tide periodically exposes and re-floods the intertidal flats, marshes and shoals. Consequently, some mesh elements become dry at low tide and wet again during the flood. As the total water depth H approaches zero, the bottom-friction and advection terms of Eq. (2.2) diverge, and a dedicated WD algorithm is therefore needed to ensure the stability of the model.

With an explicit scheme, the solution at the new time level is computed in one step from the known state at level n. The time step is then bounded by the Courant-Friedrichs-Lewy (CFL) condition, $\Delta t \leq C\,\Delta x/(|\mathbf{u}| + \sqrt{gH})$, where C is the Courant number, which for a DG scheme decreases with the polynomial order, and Δx is a characteristic length of the element, such as the inradius $2A/P$ of a triangle of area A and perimeter P. In drying areas, the gravity-wave speed $\sqrt{gH}$ decreases, but two difficulties arise. First, as H tends to zero, the velocity $\mathbf{u} = H\mathbf{u}/H$ can become very large and locally violate the CFL condition. Second, an element can lose more water in one time step than it

actually contains, which leads to negative water depths. Reducing the global time step to avoid both problems would make large, multi-year simulations prohibitively expensive.

To overcome these difficulties, the explicit scheme is combined with a thin-film approach, in which a minimum water depth H_{thin} is maintained at every node, so that dry elements remain in the computation (Medeiros et al., 2013). At each time step, three corrections are applied: the outgoing fluxes of nearly dry elements are limited to the water volume available above H_{thin}, the water is redistributed within partially dry elements, and the momentum is limited so that the Froude number remains below one. In this way, the global time step is set by the CFL condition in the wet part of the domain, that is, by the smallest wet elements, rather than by the drying areas. The complete algorithm is detailed in Appendix 6.1.1.

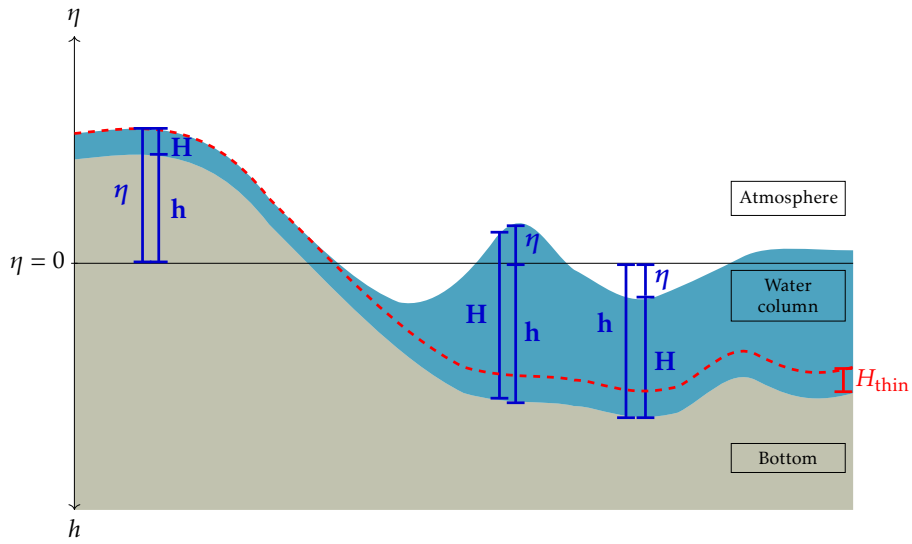

Figure 2.1: Schematic representation of the water column components and vertical reference considered for the shallow water equations (2.1) and (2.2). The blue area represents the water column where $H(x,y,t) = h(x,y) + \eta(x,y,t)$ is the total water depth; $\eta(x,y,t)$ is the free surface elevation positive upward, $h(x,y)$ is the bathymetry positive downward, the two latter are measured compared to the reference level ($\eta = 0$). Three configurations of the water level are illustrated in dark blue: (*left*) $h < 0$ and the water depth is constrained to a minimum level represented with the dashed red line $H = H_{\text{thin}}$; (*centre*) $h > 0$ and $\eta > 0$; (*right*) $h > 0$ and $\eta < 0$.

The equations are integrated in time with an explicit Runge–Kutta scheme at a fixed time step of $\Delta t = 0.1\,\text{s}$. As mentioned above, the constraint imposed

by the drying areas on the CFL condition (Section 2.1.2) has historically motivated the use of implicit WD formulations in SLIM (Kärnä et al., 2011; Le et al., 2020). The recent multi-GPU implementation of the model (De Le Court et al., 2026) compensates for this cost and makes explicit time stepping affordable for multi-year, high-resolution simulations.

2.2 Model setup for the Scheldt–North Sea continuum

The depth-averaged SLIM2D model is configured for the Scheldt–North Sea continuum.

2.2.1 Model domain

The model domain, shown in color in Fig. 2.2, covers the Scheldt estuary and the adjacent North Sea, extending offshore to the edge of the continental shelf—its northern open boundary following the 200 m isobath—and southwestward into the English Channel. Extending the domain to the shelf break provides coherent open boundaries and fully resolves offshore storm surge generation (de Brye et al., 2010). The unstructured mesh, generated with the Seamsh Python library and GMSH (Geuzaine et al., 2009), comprises approximately 2×10^6 triangles. Element size is dictated by local bathymetry and distance to the coast, transitioning from 2 km at the 200 m isobath down to 50 m along the estuarine channels and 20 m over shallow flats (Fig. 2.2.b).

Upstream of the Scheldt estuary, the freshwater tidal network attenuates the incoming tidal wave and delivers river discharge. Resolving its meandering geometry at full resolution would increase the computational cost. Unlike previous SLIM applications in the region that relied on 1D-2D coupling, the present setup uses a single 2D unstructured mesh over the entire domain. Following Kolokythas et al. (2021), the natural geometry of the upstream tributaries is replaced by straight, prismatic channels where the flow is essentially unidirectional. This schematization preserves the upstream tidal attenuation in the estuary without compromising the coastal and the solution in the lower estuary. Its effect on the local wind set-up is discussed in Section 2.4.

The model bathymetry is interpolated onto the mesh from datasets prioritized by resolution: AGENTSCHAP MDK (2021, 10 m) in the upper estuary, Rijkswaterstaat (2021, 20 m) in the lower estuary and coastal zone, and EMODNet (2021, 115 m) over the continental shelf (Fig. 2.2a). All datasets are referenced to the Normaal Amsterdams Peil (NAP) vertical datum. Because a detailed topography is irrelevant for an idealized channel,

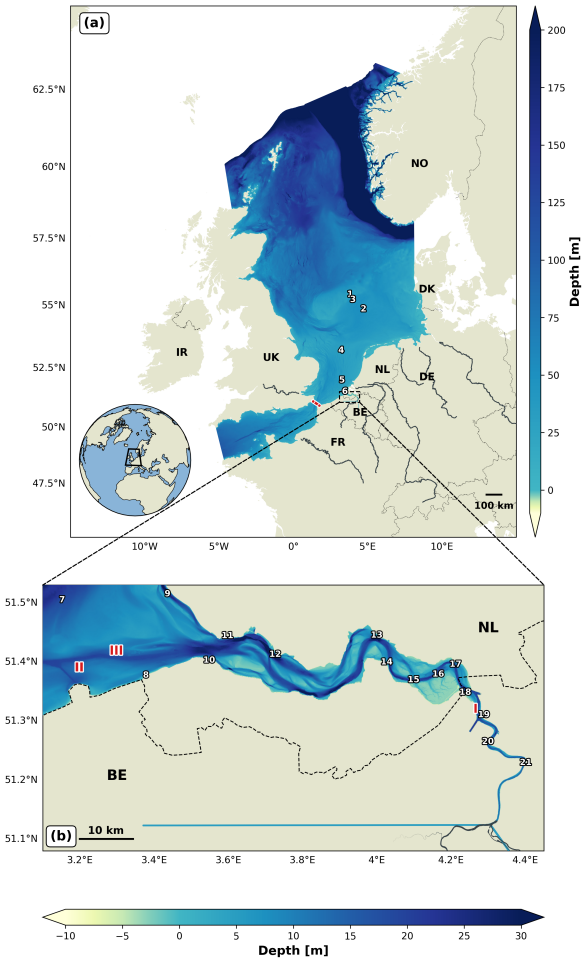

Figure 2.2: Map of the full model domain. **(a)** Bathymetry in coloured scale. Grey lines show rivers draining into the North Sea, included in the model as boundary inputs and the red line represents the Strait of Dover. **(b)** Close-up view of the Scheldt Estuary model bathymetry in coloured scale; grey lines show the Scheldt. White numberes denote the tide-gauge stations: (1) Platform A12, (2) F3 platform, (3) Platform F16-A, (4) K13a platform, (5) Euro Platform, (6) Lichteiland Goeree, (7) Vlakte van de Raan, (8) Cadzand, (9) Westkapelle, (10) Breskens Veerhaven, (11) Vlissingen, (12) Gat van Borssele, (13) Hansweert, (14) Walsoorden, (15) Baalhoek, (16) Schaar van de Noord, (17) Bath, (18) Prosperpolder, (19) Fort Liefkenshoek, (20) Kallosluis Schelde, (21) Antwerpen Loodsgebouw. Red markers in Roman numerals in panel (b) indicate the validation points for water velocity (I) Lillo-Meetpaal, (II) Scheur Wielingen (MP4) and (III) Bol Van Heist (MP3).

a constant mean depth of 7 m is assigned to these reaches which is the average depth of the upstream tributaries.

The natural intertidal flats and marshes are part of the mesh, including Saeftinghe, a natural marsh close to the Belgian-Netherlands border; the flood control areas and restored intertidal areas of the Sigma Plan are not. The consequences for the simulated surge are discussed in Section 2.4.

2.2.2 Open-boundary and river forcing

Model boundary conditions integrate marine, fluvial, and atmospheric forcings (Table 2.2). At the open shelf, tidal elevations and velocities reconstructed from 21 constituents (including M2, S2, N2, K2, K1, O1, P1, Q1) via the 1/30° TOPEX/Poseidon Global Ocean Tide Model (TPXO) (v9.5) (Egbert et al., 1994) are superimposed with daily-averaged residual fields from the Copernicus Marine Service (CMEMS) North West European Shelf reanalysis (0.111° × 0.067°). Freshwater discharges are prescribed at the landward boundaries. For the Scheldt, 10-minute observed discharges are retrieved from the Schelde Monitor Portal and applied at the tail of the schematized tributaries. To accurately capture residual coastal circulation (Gourgue et al., 2009; Ivanov et al., 2020), hourly discharges from the Thames, Seine, Meuse, Rhine, Humber, Weser, and Elbe are also imposed using Global Earth Observation for Global Water Sustainability (GEOGloWS) data (Hales et al., 2025). The 10 m wind $\mathbf{u}_{10}$ and atmospheric pressure p_{atm} (Eqs. 2.4–2.5) for the five-year hindcast are prescribed using the Copernicus European Regional ReAnalysis (CERRA) regional reanalysis (Table 2.2). CERRA is selected as it currently provides the highest spatial resolution available for a continuous atmospheric reanalysis over the domain, downscaling the ERA5 global product to 5.5 km over Europe and assimilating additional regional observations (Schimanke et al., 2021). Simulations are initialized with zero water velocities and a free-surface elevation $\eta = \max(-h + H_{\mathrm{thin}}, 0)$, which ensures the minimum water depth H_{thin} across the domain.

2.2.3 Model calibration

Bottom friction controls tidal propagation and dissipation across the domain. Roughness is the only free parameter of the model: all other inputs—bathymetry, open-boundary tides and atmospheric forcing—are fixed from data, and a single Manning value is assigned per morphological zone. The spatially varying Manning coefficient n was calibrated by a systematic parameter sweep (15 June–31 July 2013). The target variable is the water-level time series at the 15 tide gauges, summarised in a normalized Taylor diagram through the ratio of standard deviations $\sigma_m^* = \sigma_m/\sigma_o$ and the correlation R

Table 2.2: Summary of hydro-meteorological boundary conditions, imposed variables, and their treatment in the model.

Boundary	Variable	Treatment	Source
Open ocean (shelf)	Elevation (η)	Flather	TPXO9.5 + CMEMS
	Depth average velocity ($\mathbf{u}$)	Flather	TPXO9.5 + CMEMS
River inflows	Discharge (Q)	Flather	Schelde Monitor GEOGloWS
Sea surface	Wind ($\mathbf{u}_{10}$), pressure (p_{atm})	Surface source terms	CERRA
Closed boundaries	Normal flow ($\mathbf{u}\cdot\mathbf{n}=0$)	No-penetration	–
		(weak no-slip)	–

(Section 2.2.4). A configuration is judged "good enough" when the zonal Taylor statistics cluster at the reference point ($\sigma_m^* \approx 1$, R maximal) and the water-level errors fall within the shelf-and-estuary tolerance bands of Williams et al. (2017); beyond that point, further adjustment of n no longer improves the statistics at the gauges.

The optimal configuration yields a normalized standard deviation σ_m^* near unity at the 15 tide gauges (Fig. 2.3). Expressed in $\mathrm{s\,m^{-1/3}}$, the calibrated values are 0.025 in the North Sea and the Western Scheldt (tested range: 0.020–0.026), 0.012 between Bath and Antwerp (range: 0.008–0.015), and 0.080 over intertidal marshes (range: 0.060–0.100) (Kolokythas et al., 2021; Wamsley et al., 2010; Stark et al., 2017). These optima reproduce the zonation of previous models of the Scheldt (Kolokythas et al., 2021; Smolders, 2016). In the schematized upper estuary, the roughness is prescribed at 0.040 from the literature (Kolokythas et al., 2021) rather than optimised, because a detailed effective roughness is not meaningful for an idealised prismatic channel.

Using a high bottom friction as a proxy for marshes underestimates the drag where the water is shallower than the vegetation, but this approach is physically sound for storm surges that fully submerge the vegetation canopy. The roughness upstream of Bath may explain the residual over-amplification of the tide at Antwerpen Loodsgebouw (Section 2.3.3). This over-amplification could not be detected by a calibration on raw elevations: the correlation R ignores amplitude errors, and σ_m^* lumps all constituents and the non-tidal signal into a single number, so that an error on one constituent can stay hidden. Constituent-guided calibration of the reaches upstream of Bath is left for future work.

We calibrated over a summer period without storms, so the tidal signal at the gauges is controlled by bottom friction rather than by the atmospheric forcing. Calibrating during storms would have let the Manning coefficient absorb errors in the wind forcing—such as the underestimation of extreme winds by reanalyses (Chapter 3)—so it would no longer represent the bed

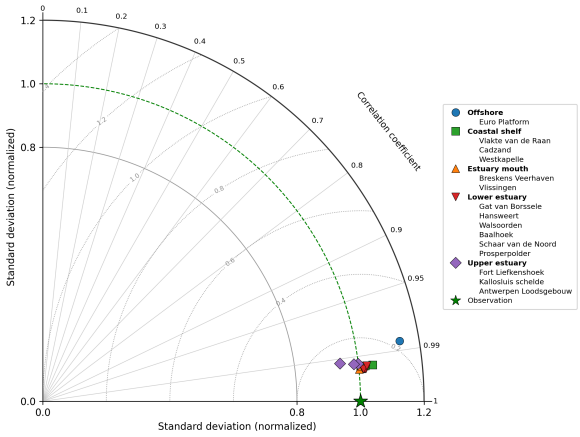

Figure 2.3: Normalized Taylor diagram summarizing model performance at 15 tide gauges over the calibration period (15 June–31 July 2013). Stations are categorized by morphological zone. (green star is the observation, $\sigma_m^* = 1$, $R = 1$).

alone. The six-week window spans three spring–neap cycles, enough to separate the main semi-diurnal constituents. The calibrated configuration was then used unchanged over five years including winters (Section 2.3) and the February 2020 sequence. The Manning law also makes the drag decrease with depth, so the effective friction adapts to the higher storm water levels.

2.2.4 Model skill metrics

Model skill is quantified by comparing simulated and observed time series station by station. For a pair of series of N points, with o_i the observation, m_i the corresponding model value and an overbar denoting the temporal mean, we report the Pearson correlation coefficient R, the bias $\overline{m} - \overline{o}$, the root mean square error $\mathrm{RMSE} = \left[N^{-1} \sum_{i=1}^{N} (m_i - o_i)^2\right]^{1/2}$ and the ratio of standard deviations σ_m/σ_o. The ratio σ_m/σ_o and R are shown in the normalized Taylor diagrams used for calibration (Chapter 2.2.3), in which the distance to the reference point is the centred RMSE, i.e. the RMSE once the bias is removed. Tidal skill is assessed on harmonic constants rather than on the raw signal: constituents are extracted by least-squares harmonic analysis fitted independently on each series, and reported as relative amplitude error and phase lag for elevation, and as semi-major axis, ellipticity, inclination and phase of the tidal ellipse for currents. The tidal prediction obtained from

the fit of each series is subtracted from that same series to yield its non-tidal residual surge, so that model errors on the tide do not contaminate the simulated residual. High and low waters are detected on both series and paired, which gives the level error and the phase error at each extremum.

Acceptance criteria follow the shelf-and-estuary guidance of Williams et al. (2017). Water levels are required to lie within 0.10 m in the North Sea, 0.30 m in the upper estuary, and 0.20 m in the lower estuary by interpolation between the two; the timing of high and low waters within 15 min on the coast and at the mouth of the estuary, and within 25 min at its head; currents within $0.20\,\mathrm{m\,s^{-1}}$ or 10 % to 20 % of the measured speed, with a directional bias below 10° on the shelf and 15° in the estuary. The compliance rate quoted hereafter is the fraction of paired extrema falling inside the corresponding band.

Because the model and the tide gauges do not share the same vertical datum, each simulated series is shifted to the observed mean level over the validation period. Mean levels are therefore not compared, and every bias quoted below is relative to that adjustment.

2.3 Hydrodynamics validation

The 2016–2020 hindcast is evaluated against an observational dataset entirely independent from the calibration phase (Section 2.2.3). Model skill is assessed across five distinct metrics: tidal harmonics, current velocities, mean residual transport through the Dover Strait, total water levels (Fig. 2.2) and non-tidal residuals during the February 2020 Ciara storm.

2.3.1 Tides

North Sea circulation is primarily tide-driven, and the M2 and S2 constituents dominate the tide. The model reproduces the large-scale structure of this tide. It resolves the four established M2 amphidromic systems (Fig. 2.5.a) (Proudman et al., 1924; Otto et al., 1990; Stanev et al., 2014; Prandle et al., 1978). It also captures the tidal amplification along the funnel-shaped Scheldt estuary (Fig. 2.5.b) (Wang et al., 2019). Along the continuum, the mean absolute amplitude error is $3.2 \pm 3.0\,\%$ for M2 and $3.9 \pm 2.0\,\%$ for S2, and the mean absolute phase error is $5.7 \pm 2.9°$ and $6.1 \pm 2.6°$, respectively; the amplitudes and phases at each gauge are given in Table 6.1.1 (Appendix 6.1).

The nature of the error changes along the continuum. Offshore, it is mainly an amplitude error: at the six offshore platforms, the mean M2 phase error is only $-0.4°$, whereas the amplitude is overestimated by 3.4 % on average, and up to 11 % where the amplitude is about 0.5 m (Fig. 2.4, Table 6.1.1). In the estuary, it is mainly a phase error. The model does not lag

the observations: it leads them, by 5° at Vlakte van de Raan and by 10° (about 20 min) at Kallosluis, whereas the amplitude error stays between −5 and +2 %. Averaged over the 14 gauges from Vlakte van de Raan to Kallosluis, the phase error therefore carries about 0.24 m of the complex M2 error, against 0.04 m for the amplitude.

The growing lead shows that the tidal wave travels too fast in the estuary. M2 takes about 96 min to travel from Vlakte van de Raan to Kallosluis in the model, against 107 min in the observations. S2 shows the same structure (Fig. 2.4b), so this error is a property of the propagation rather than of one constituent. This lead mainly affects low waters (Fig. 2.4c). High waters remain within about 8 min of the observations from Breskens to Kallosluis. Low waters arrive 4 to 8 min early near the mouth, and 14 to 21 min early from Hansweert upwards. The simulated tide therefore rises too slowly and falls too fast. As a result, the model underestimates the asymmetry of the tide in the estuary. Between Hansweert and Kallosluis, the relative phase $2\varphi_{M2}-\varphi_{M4}$ (Friedrichs et al., 1988) is −2 to 14° in the observations and 19–25° lower in the model. The strength of the overtide is nevertheless correct: the ratio A_{M4}/A_{M2} is reproduced (0.04–0.07), and the mean M4 amplitude error is +7 % in the lower estuary and −7 % in the upper estuary (Table 6.1.2).

Because the lead is concentrated at low water, the shallowest stage of the tide, it points to depth-dependent processes, such as the effective channel depth or the friction at low tide, rather than to the overall level of roughness: a uniform increase of n would also damp amplitudes that are already correct. The low roughness between Bath and Antwerp (Section 2.2.3) is a likely contributor, because the calibration on raw elevations is hardly sensitive to phase: the correlation R changes by less than 2 % for a phase error of 10°. Separating these contributions would require a cost function that also weights the phase or the currents, as in the Scaldis model (Vanlede et al., 2015).

The M2 constituent dominates tidal currents across the domain (Fig. 2.6.a-c). Channel confinement strongly modulates this flow towards the estuary: the ratio of the semi-minor to the semi-major axis decreases in magnitude from about -0.20 at the coastal piles to -0.001 in the estuary. The model captures this spatial evolution.

The model also reproduces the sense of rotation of the tidal current ellipse. At the coastal piles, the observed and simulated ellipticities are both negative: the current vector turns clockwise over the tidal cycle. In the estuary, the flow is nearly rectilinear and the ellipticity is close to zero. The sense of rotation of a current ellipse is a local property, set on the shelf by the bathymetry and by the reflection of the tide on the coast (Pugh, 1987). It is distinct from the counter-clockwise propagation of the tide around the amphidromic points of the North Sea (Fig. 2.5.a), which describes how the phase of the elevation travels across the basin.

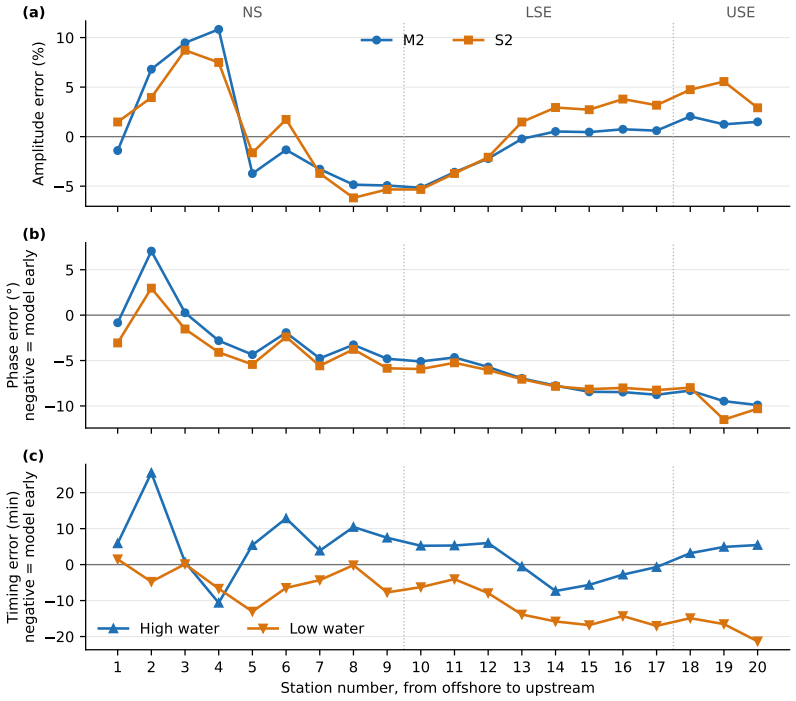

Figure 2.4: Model error along the continuum, for stations 1–20 of Fig. 2.2, from offshore to upstream. **(a)** Relative amplitude error of M2 and S2. **(b)** Phase error of M2 and S2 (2016–2020). **(c)** Mean timing error of high and low waters. Dotted lines separate the North Sea (NS), lower (LSE) and upper (USE) estuary. Negative phase and timing errors mean that the model is early.

The simulated velocity magnitudes are close to the observations. Semi-major axes deviate by only 1.0 % at Scheur Wielingen and 3.3 % at Lillo Meetpaal. Major-axis orientations are within 3.2° at these stations, and phase differences stay below 13 min across the domain. Over 2016–2020, the correlation between simulated and observed along-axis velocities reaches 0.98 at the coastal piles and 0.90 in the estuary, and the dominant current directions match within 22.5° (Fig. 6.1.4, Appendix 6.1).

Bol van Heist is the exception, with a simulated ellipse 11% weaker and rotated by 9.7°. Part of this deficit comes from comparing depth-averaged velocities with single-point measurements in a sheared water column, as the full profile is unavailable. At Lillo Meetpaal, where two cells allow a representative vertical average, using only the upper cell overestimates the

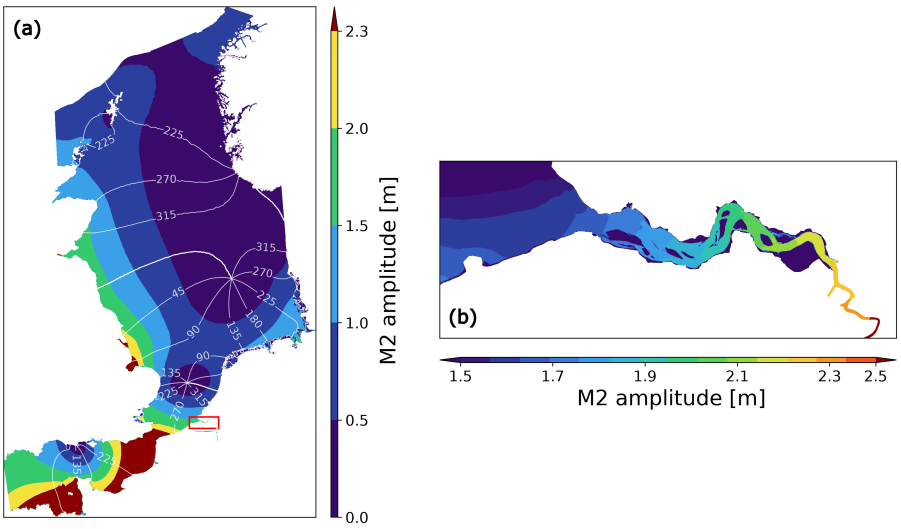

Figure 2.5: (a) Co-tidal lines (phase in degrees) and co-range chart (amplitude in m) of the M2 tidal constituent, showing the amphidromic points as resolved by the model, from north to south: one off the southern tip of Norway, one at the eastern tip of Dogger Bank, one in the centre of the Southern Bight and one near the coast of southern England in the English Channel. **(b)** Modelled amplitude of the elevation for the M2 constituent [m] in the upper and lower Scheldt Estuary. The amplitude increases along the river axis. The stations are separated between zones NS = North Sea, LSE = Lower Scheldt estuary, USE = Upper Scheldt estuary.

M2 semi-major axis by 7%. Single-cell measurements could thus explain roughly half of the deficit at Bol van Heist, whereas the 9.7° inclination difference reflects a genuine local discrepancy (Ivanov et al., 2020).

2.3.2 Residual transport

The simulated annual mean residual transport through the Dover Strait (0.114 Sv) agrees closely with historical estimates (Salomon et al., 1993; Ivanov et al., 2020). It consists of a permanent tidal contribution, about one third of the mean and directed towards the North Sea, modulated by wind stress (Fig. 2.7).

The 2016–2020 hindcast shows a stronger seasonal contrast and a wider interannual spread than the reference periods. Monthly means frequently reverse into a net flow towards the English Channel.

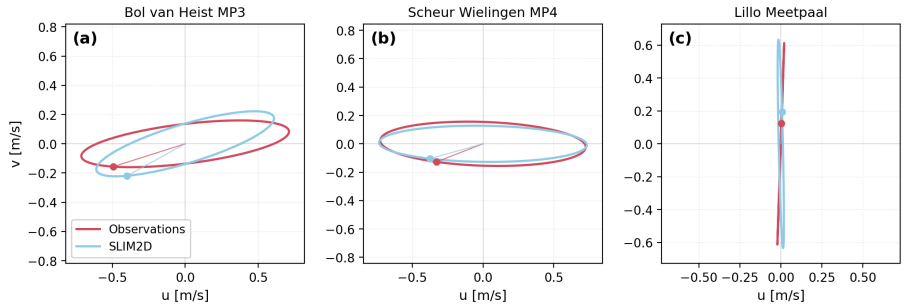

Figure 2.6: Tidal currents ellipse from the coastal shelf to the estuary. Observed (red) and simulated with SLIM (blue) tidal ellipses are compared at (a) Bol van Heist, (b) Scheur Wielingen, and (c) Lillo Meetpaal. Radial lines indicate the phase (velocity vector at $t = 0$). Stations locations are given in Fig. 2.2

This stronger variability reflects the atmospheric conditions of the period. Anomalously strong south-southwesterly storm sequences, such as those of January 2016 and February 2020 (Kendon et al., 2021), drive the positive extremes (up to 0.45 Sv monthly). Conversely, persistent anticyclonic blockings force north-northeasterly winds that reverse the net flow, as in spring 2020 (Ionita et al., 2020; Kendon et al., 2021) and October 2018 (Kendon et al., 2019).

The model thus responds consistently to atmospheric forcing, from persistent blockings to severe storms, and remains stable over the five-year period. Part of this residual stems from tidal rectification, the mean flow that oscillatory tidal currents generate through their non-linear interaction with bottom friction and topography (Zimmerman, 1978). On the northwest European shelf, this tidal contribution shapes the residual circulation, in particular through the English Channel, the Dover Strait and the southern North Sea (Tinker et al., 2022). The wind-driven part acts on shorter timescales and varies in direction (Holt et al., 2008), consistent with the monthly reversals of the 2016–2020 transport. Both contributions are included in the validated transport, but they are not separated here.

2.3.3 Water elevation

High and low waters are reproduced with mean errors of at most 11 cm across the domain (Table 2.3). The scatter of these errors increases upstream, from ±9 cm at the offshore platforms to ±23 cm at Antwerpen, following the natural amplification of the tidal range. Correlations are lower offshore (e.g., 0.801 at Platform A12), where the tidal signal is below one metre.

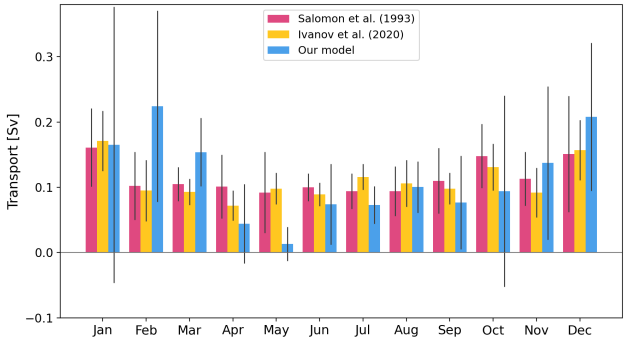

Figure 2.7: Monthly residual transport through the Dover Strait: the estimate of Salomon et al. (1993) (pink, 1983–1991), the simulation of Ivanov et al. (2020) (yellow, 2006–2008) and our model results (blue, 2016–2020). Error bars denote the interannual standard deviation; negative values indicate flow towards the English Channel.

The mean errors on high and low waters remain within the tolerances of Williams et al. (2017) in every zone: at most 9 cm in the North Sea (tolerance 0.10 m), 11 cm in the lower estuary (0.20 m) and 7 cm in the upper estuary (0.30 m). We assess their statistical significance with a 95 % confidence interval that accounts for the serial correlation of successive errors. Given the hundreds of extrema available at each station, this interval is narrow, about 1 cm, so that even small mean errors are significant: this is the case at three quarters of the stations for high waters and at nearly all stations for low waters. Thus, the significance of these errors reflects the length of the record rather than a substantial bias in the model. The remaining offset is small and consistent across stations: the model slightly underestimates the tidal range, with high waters a few centimetres low and low waters a few centimetres high, in line with the amplitude deficit of about 5 % in Table 6.1.1.

The non-tidal residuals are well reproduced from the open sea to Bath (Fig. 2.8), with correlations of 0.729 to 0.893 and RMSEs of 9 to 14 cm.

The performance decreases in the Upper Scheldt Estuary, where RMSEs rise from 15 cm at Prosperpolder to 20 to 21 cm further upstream and correlations drop to 0.736. This decrease is driven by freshwater discharge and complex channel geometry rather than by sampling resolution, since the observed sub-hourly variance accounts for less than 1 % of the total.

The accuracy of the model remains stable under severe meteorological forcing. During Storm Ciara (9–11 February 2020), absolute peak errors stay between 1 and 11 cm. These errors show no systematic spatial bias

(correlation with estuarine distance 0.15) and remain within the baseline standard deviation of each station (Table 2.3).

Antwerpen Loodsgebouw has the lowest low-water correlation (0.813) and the largest scatter (±23 cm). This anomaly may stem from an over-amplification of the tide in a reach whose roughness was calibrated on raw elevations only (Section 2.2.3): the modelled M2 amplitude at this station is 2.41 m, against 2.23 m observed, an excess of about 8 % (Table 6.1.1). Future upstream zonation should incorporate constituent-guided metrics (de Brye et al., 2010).

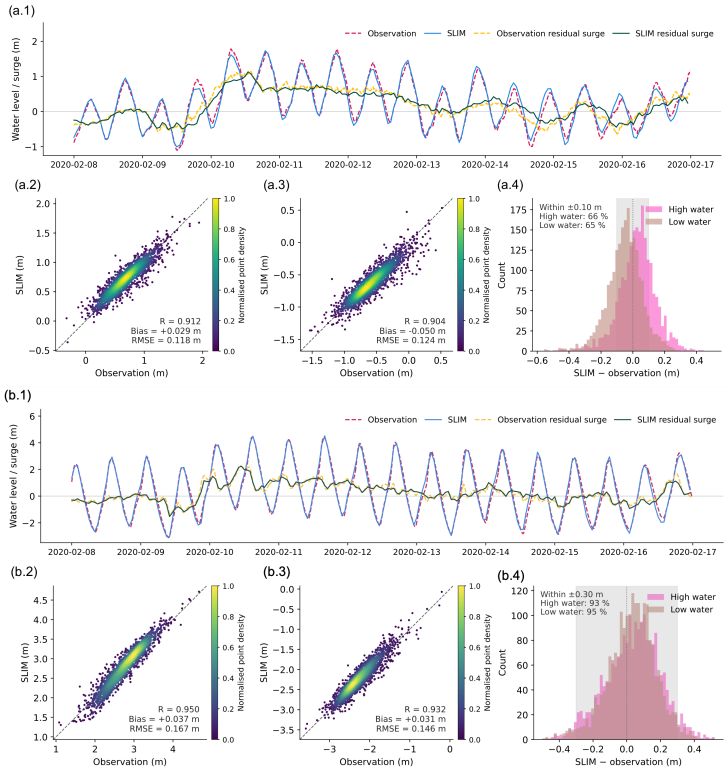

Figure 2.8: Validation of SLIM2D water levels at (a) K13a platform (North Sea) and (b) Prosperpolder (upper estuary). The model series is shifted to the observed mean level over the period, so the biases quoted are relative to that adjustment. **(1)** Water level during the February 2020 storm sequence, which includes storms Ciara (10 February) and Dennis (15–16 February), for the observations and for SLIM, with the residual surge of each series superimposed. The tidal prediction is fitted separately on each series by least squares over 35 harmonic constituents, so that each residual isolates its own non-tidal component. **(2)** Modelled against observed high waters and **(3)** low waters over the full period, coloured by point density normalised within each panel; the dashed line is the 1:1 line. **(4)** Distribution of the model–observation difference at both extrema. The grey band is the tolerance recommended by Williams et al. (2017) for the zone of the station, $\pm 0.10\,\mathrm{m}$ in the North Sea (a) and $\pm 0.30\,\mathrm{m}$ in the upper estuary (b), and the annotation gives the proportion of extrema falling inside it.

Table 2.3: Validation of SLIM2D at high tide (HW), low tide (LW) and on the non-tidal residual surge. The *Ciara* column gives the absolute error on the residual surge peak during storm Ciara (9–11 February 2020); NA marks a station where a gap in the observation record prevents the peak from being identified.

		High water		Low water		Residual surge		
No	**Station**	R	Level error (cm)	R	Level error (cm)	R	RMSE (cm)	Ciara (cm)
1	Platform A12 (NS)	0.801	$+1 \pm 12$	0.802	0 ± 12	0.729	12	6
2	F3 platform (NS)	0.895	$+3 \pm 9$	0.864	-4 ± 9	0.843	9	2
3	Platform F16-A (NS)	0.891	$+6 \pm 10$	0.879	-5 ± 10	0.830	10	4
4	K13a platform (NS)	0.912	$+3 \pm 11$	0.904	-5 ± 11	0.832	11	1
5	Euro Platform (NS)	0.922	-4 ± 11	0.895	$+2 \pm 12$	0.868	11	4
6	Lichteiland Goeree (NS)	0.936	-3 ± 11	0.906	$+3 \pm 12$	0.881	11	7
7	Vlakte van de Raan (NS)	0.955	-5 ± 12	0.927	$+4 \pm 13$	0.862	12	2
8	Cadzand (NS)	0.958	-9 ± 12	0.936	$+8 \pm 13$	0.878	12	3
9	Westkapelle (NS)	0.957	-6 ± 12	0.931	$+8 \pm 12$	0.883	12	2
10	Breskens Veerhaven (LSE)	0.961	-11 ± 12	0.940	$+9 \pm 12$	0.888	12	2
11	Vlissingen (LSE)	0.960	-6 ± 12	0.940	$+7 \pm 12$	0.890	12	4
12	Gat van Borssele (LSE)	0.959	-2 ± 13	0.940	$+5 \pm 13$	0.893	12	2
13	Hansweert (LSE)	0.952	$+6 \pm 14$	0.939	$+5 \pm 13$	0.889	13	1
14	Walsoorden (LSE)	0.951	$+4 \pm 15$	0.933	$+3 \pm 14$	0.890	13	1
15	Baalhoek (LSE)	0.954	$+2 \pm 15$	0.935	$+6 \pm 14$	0.887	13	NA
16	Schaar van de Noord (LSE)	0.955	$+1 \pm 15$	0.918	$+2 \pm 15$	0.882	14	2
17	Bath (LSE)	0.953	$+2 \pm 15$	0.933	$+6 \pm 14$	0.879	14	11
18	Prosperpolder (USE)	0.950	$+4 \pm 16$	0.932	$+3 \pm 14$	0.868	15	6
19	Fort Liefkenshoek (USE)	0.918	$+3 \pm 21$	0.916	$+4 \pm 17$	0.792	21	9
20	Kallosluis Schelde (USE)	0.934	$+5 \pm 19$	0.890	$+1 \pm 19$	0.786	21	7
21	Antwerpen Loodsgebouw (USE)	0.923	$+2 \pm 23$	0.813	$+7 \pm 23$	0.736	20	9

2.4 Discussion and conclusion

2.4.1 Tide

The tide provides a first test of surge propagation, since both are long waves that follow the same path from the shelf into the estuary. The model resolves the four M2 amphidromic systems of the North Sea and the amplification of M2 from 1.48 m at Vlakte van de Raan to 2.19 m at Kallosluis. The amplitude errors stay within 5.2 % between the mouth and Kallosluis (Table 6.1.1). This suggests that the balance between estuarine convergence and bottom friction, which controls the amplification of a long wave, is adequately represented.

The main defect of the configuration lies in the propagation speed, not in the amplitude. The tidal wave travels about 10 % too fast in the estuary: the M2 lead grows from 5° at the mouth to 10° (about 20 min) at Kallosluis. This lead mainly concerns low waters, which arrive 14 to 21 min early in the upper reaches, whereas high waters remain within about 8 min. Such a pattern points to depth-dependent processes at low tide, such as the effective channel depth or the low-water friction, whose respective contributions dedicated sensitivity runs could separate.

The overtides are represented with larger errors, but these errors have limited consequences. The mean amplitude errors of M4 and M6 are 12 % and 13 %, with phase errors of 3.4° and 8.2° (Table 6.1.2). The ratio A_{M4}/A_{M2} is reproduced in the estuary, but the underestimated tidal asymmetry may limit the representation of tide–surge interaction in the shallowest reaches, where this interaction is strongest (Horsburgh et al., 2007).

The errors on water levels are acceptable in the estuary, but stricter tolerances are not fully met at sea. 89 % of paired extrema fall within the 0.30 m tolerance of Williams et al. (2017) in the upper estuary, and 80 % within the 0.20 m tolerance in the lower estuary. In the North Sea, this proportion falls to 59 %, because the 0.10 m tolerance is comparable with the 9–13 cm scatter of the errors. Since extrema combine tidal and non-tidal errors, we consider this scatter acceptable for a study of surges, whose peaks are reproduced within 11 cm. The timing of the extrema meets the corresponding tolerances throughout the estuary. The mean timing error of high and low waters stays within about 6 min at Vlissingen, at the mouth, and reaches at most about 21 min for the low waters at Kallosluis, within the 25 min allowed at the head (Fig. 2.4c). At sea, it exceeds the 15 min tolerance only for the high waters at the F3 platform, by about 10 min, where the M2 amplitude is small (0.23 m).

2.4.2 Surge

The model also responds correctly to atmospheric forcing, at both the basin and the station scale. The monthly transport through the Strait of Dover reverses during the blocking episodes of October 2018 and spring 2020, and peaks during the storm sequences of January 2016 and February 2020 (Fig. 2.7). The non-tidal residual is reproduced with correlations of 0.73–0.89 and Root Mean Square Errors (RMSEs) of 9–14 cm from the open shelf to Bath (Table 2.3). During Storm Ciara, peak errors range from 1 to 11 cm and show no trend along the estuary. As bottom roughness was calibrated over a storm-free summer period, these scores are an independent test of the surge response. The hindcast runs continuously over 2016–2020, but the surge peak is evaluated on a single storm.

The level of low waters is reproduced with an accuracy similar to that of high waters (Fig. 2.8), which supports the use of the model for negative surges in Chapter 4. However, their timing is less accurate, so the results of that chapter are more reliable for low-water levels than for their exact time of occurrence.

2.4.3 Comparison with other models

These results are comparable with those of other models of the region. The high-resolution 3D ROMS model of Ivanov et al. (2020) reproduces M2 at twelve gauges of the Southern Bight and the eastern English Channel with a mean amplitude error of $-3.5 \pm 14.1\,\%$ and a mean phase error of $2.2 \pm 9.8°$, the amplitude error ranging from $-26\,\%$ at Harwich to $+32\,\%$ at Hoek van Holland. Our mean absolute errors are $3.2 \pm 3.0\,\%$ and $5.7 \pm 2.9°$ (Table 6.1.1). At the three gauges common to both studies, the amplitude errors are similar at the mouth of the estuary (-5.5 and $-5.9\,\%$ for ROMS at Vlakte van de Raan and Vlissingen, against -3.4 and $-3.5\,\%$ here), whereas ROMS overestimates the amplitude at Euro Platform by 13 %, against an underestimate of 4 % here. ROMS has smaller phase errors at the mouth (0 to 1°, against a lead of about 5° here), consistent with the too-fast propagation of the tidal wave identified above. Both models also reproduce the annual residual transport through the Strait of Dover, 0.111 Sv for ROMS and 0.114 Sv here, against 0.114 Sv in the 2D model of Salomon et al. (1993). Ivanov et al. (2020) compare the tidal ellipses only qualitatively and do not evaluate storm surges, so the comparison cannot be extended to these quantities.

The calibrated Manning coefficients follow the zonation of the 2D Scaldis-Coast model (0.022 at sea, 0.012 between Bath and Antwerp, 0.04 in the schematized reaches; Kolokythas et al., 2021), with a higher value over the intertidal areas. For water levels, studies comparing 2D and 3D simulations

of storm surges in estuaries report similar peak levels, differences appearing mainly after the peak, when vertical shear and residual stratification influence the evolution of the water level (Weaver et al., 2009; Zheng et al., 2013; Ye et al., 2020) (see also Huybrechts et al., 2010). For the surge itself, our residual RMSEs of 9 to 14 cm from the open sea to Bath lie between those of two reference models. They exceed the 6.4 cm of the operational 2D model DCSMv6 at 13 Dutch coastal stations over 2007 (Zijl et al., 2013), and remain below the 15 to 26 cm of the 3D GETM model in the German Bight during Storm Xaver, with and without wave coupling; run in 2D, the same model reached 39 cm (Staneva et al., 2016). These figures are indicative only, since the periods, the stations and the surge heights differ, the Xaver surge reaching about 2.5 m in the German Bight. The main difference with 3D, wave-coupled North Sea models lies in the processes rather than in the formulation: during Storm Xaver, coupling a wave model raised the surge by about 30 % in the German Bight (Stanev et al., 2016; Staneva et al., 2016), an effect that our configuration represents only through the drag coefficient.

2.4.4 Limitations

The references used in this validation also have their own limits. Tide gauges and model are compared after adjusting their mean levels, so the absolute mean level is not validated. At Bol van Heist, single-cell current measurements are compared with depth-averaged velocities, which explains about half of the local deficit.

Several model choices limit the results in specific ways. Upstream of Prosperpolder, residual RMSEs reach 20–21 cm, probably because the roughness of these reaches was calibrated on raw elevations, which are insensitive to phase errors and to errors on a single constituent (Section 2.2.3). Marsh roughness is weakly constrained by summer tides, since marshes flood mainly at spring high water and their vegetation is sparser in winter.

Replacing the meandering tributaries by straight channels can affect the local wind set-up during a surge, since set-up scales with the fetch aligned with the wind: a reach aligned with the wind overestimates it, one across the wind underestimates it. The effect is expected to be minor. These inland reaches experience much weaker winds than the open sea, are short and shallow, and their surge level is set by the barotropic wave from the North Sea and by the tide rather than by local wind. The good agreement at the upstream gauges supports this.

The Sigma Plan, Flanders' flood-protection programme for the Scheldt, combines dike reinforcement with controlled flood areas (FCAs) and tidal-marsh restoration; the FCAs lower the upstream surge peak by temporarily storing part of the surge volume (Smolders et al., 2015; Smolders et al.,

2020). Our configuration resolves the *natural* intertidal storage—the flats and marshes covering about 35 % of the estuarine area—as part of the domain, so the storage-driven attenuation of the lower estuary is captured, including that of Saeftinghe, a natural marsh of the Western Scheldt outside the Sigma Plan and the largest remaining intertidal area of the estuary (about 3000 ha) (Smolders et al., 2015), which lowered the Xaver high water by about 10 cm around Antwerp (Smolders et al., 2020). The engineered FCAs are not: they fill through inlet and outlet sluices, and these control structures, which set the storage actually available during an event, are absent from the mesh. The intertidal areas restored under the Sigma Plan are not represented either. One of the largest, Kruibeke–Bazel–Rupelmonde (about 600 ha), opened in 2017, after Storm Xaver. Omitting this storage biases the upstream peak high, by an amount bounded by Smolders et al. (2020), who found that the FCAs active in 2013 cut the Xaver surge by up to about 0.5 m around 150 km from the mouth, but left it unchanged downstream of 110 km. The bias is therefore local to the upper estuary and of order a few decimetres; it is conservative for flood levels.

Wind waves are not represented. In the North Sea, most of their effect on surges can be recovered through a higher sea surface roughness (Mastenbroek et al., 1993), but it can be larger in shallow coastal areas, as during Storm Xaver (Section 2.4.3). Their contribution in the Scheldt estuary remains to be quantified.

2.4.5 Conclusion

This chapter asked how accurately a single-domain configuration of SLIM2D reproduces the height and the timing of the tide and the storm surge from the open North Sea to the upper Scheldt estuary. Up to Kallosluis, the model reproduces the mean levels of high and low waters within about a decimetre and, in the estuary, their timing within about twenty minutes. The M2 amplitude error averages 3.2 % and stays within 5.2 % between the mouth and Kallosluis. The non-tidal residual is reproduced with RMSEs of 9–14 cm from the open shelf to Bath and 15–21 cm in the upper estuary, and the surge peak of Storm Ciara within 1–11 cm. Timing is the weaker of the two: the M2 phase leads by up to 10° (about 20 min) at Kallosluis.

The choice of a single domain is supported by these results. It removes the interface that 1D–2D or nested configurations introduce at the estuary mouth, and the residual errors remain of the same order on the shelf and in the lower estuary (Table 2.3). The transition from the sea to the estuary therefore does not appear to degrade the solution.

Within these limits, the configuration answers the research question for the part of the continuum where the following chapters draw their conclusions, from the open sea to Kallosluis, with low waters as the least

accurate in time. The aim of this chapter was to assess the model itself, so the atmospheric forcing was not examined. The CERRA reanalysis at 5.5 km remains a source of uncertainty that the hydrodynamic model cannot resolve by itself. Chapter 3 quantifies how the resolution of this forcing affects the simulated surge during Storm Xaver.

Chapter 3

How atmospheric forcing resolution impacts storm surge model results: insights from Xaver Storm in the North Sea-Scheldt estuary continuum

This chapter is based on the following published article:
Randresihaja N. R., Gourgue O., Alaerts L., Fettweis X., Lambrechts J., De Le Court M., Grégoire M., and Hanert E. (2026). How atmospheric forcing resolution impacts storm surge model results: Insights from Storm Xaver in the North Sea-Scheldt estuary continuum, In: Regional Studies in Marine Science, 96, doi: 10.1016/j.rsma.2026.104919

3.1 Introduction

Simulating processes along the estuary–sea continuum is challenging because of the range of scales involved, from tens of metres within estuaries to hundreds of kilometres across the continental shelf (Marchesiello et al., 2001; Lewis et al., 2019). Estuaries have long been under-represented in coastal models, while estuarine models rarely extend over the adjacent shelf

(Marchesiello et al., 2001). Multiscale models now bridge this gap, and have improved the understanding of storm surges along the land–sea continuum, of their sensitivity to model parametrisations and of their main forcing mechanisms (Garzon et al., 2016; Yang et al., 2020).

Despite these advances, certain aspects of the land-sea continuum modeling remain poorly understood. One issue is how the spatial and temporal resolution of atmospheric forcing influences storm surge simulations in complex topographic systems, such as estuaries. Although atmospheric conditions are the primary drivers of storm surge dynamics, the finer resolution of estuarine-sea models is generally not matched by the spatial resolution of the atmospheric forcing, with the latter typically operating on scales of tens of kilometers (Dinapoli et al., 2020; Chen et al., 2023a). Small-scale processes such as localized wind patterns, frontal systems, and pressure gradients are not resolved in coarse-resolution atmospheric data. As a result, these unresolved processes within estuaries can introduce errors in the simulated surge dynamics, impacting factors like the timing, peak intensity, and spatial distribution. Additionally, atmospheric models themselves vary in quality, and no single reanalysis product captures all events perfectly. This variability can introduce regional biases and uncertainties in storm surge model outputs, particularly in complex topographic systems (Lorenz et al., 2023).

In the context of the Scheldt estuary-sea continuum, existing models of the river system tend to simplify or exclude the influence of North Sea conditions on estuarine dynamics. A few two-dimensional (2D) models of the Scheldt extend into the nearby North Sea, but they focus on eco-hydrodynamics (Vanderborght et al., 2007; de Brye et al., 2010; Arndt et al., 2011). Other studies have modeled this land-sea continuum under storm surge conditions, but they have mostly focused on the mitigating effects of retention areas (Smolders et al., 2015). No existing research has specifically examined how variations in atmospheric forcing resolution impact storm surge behavior across this continuum.

The North Sea, on the Northwestern European Continental Shelf (NWCS) and connected to the Scheldt (Fig. 3.1), is highly exposed to storm surges, which its shallow bathymetry amplifies along the coasts of Belgium, the Netherlands and Germany (Sündermann et al., 2011), and which are expected to intensify under climate change (Woth et al., 2006). Previous studies have explored how different atmospheric forcing models affect storm surge simulations across the NWCS, with findings highlighting the importance of high spatio-temporal resolution in capturing surge magnitude and duration accurately (Muller et al., 2014; Meyer et al., 2023; Ridder et al., 2018; Agulles et al., 2024). However, those studies mainly focused on coastal regions and have largely neglected the specific complexities of estuarine dynamics.

In this chapter, we assess how the spatial and temporal resolution of atmospheric forcing influences storm surge simulations across the Scheldt–North Sea continuum. A multiscale coastal ocean model is forced with a high-resolution atmospheric model at several spatial and temporal resolutions during the extratropical Storm Xaver, which hit the region on December 5–6, 2013 (Fig. 3.2.a). After validating both models against in situ data, we evaluate the sensitivity of the simulated surge to the resolution of the forcing, with a focus on the estuary.

3.2 Materials and methods

3.2.1 Model set up

The model domain covers the Scheldt Estuary and the adjacent North Sea, extending offshore to the edge of the continental shelf—its northern open

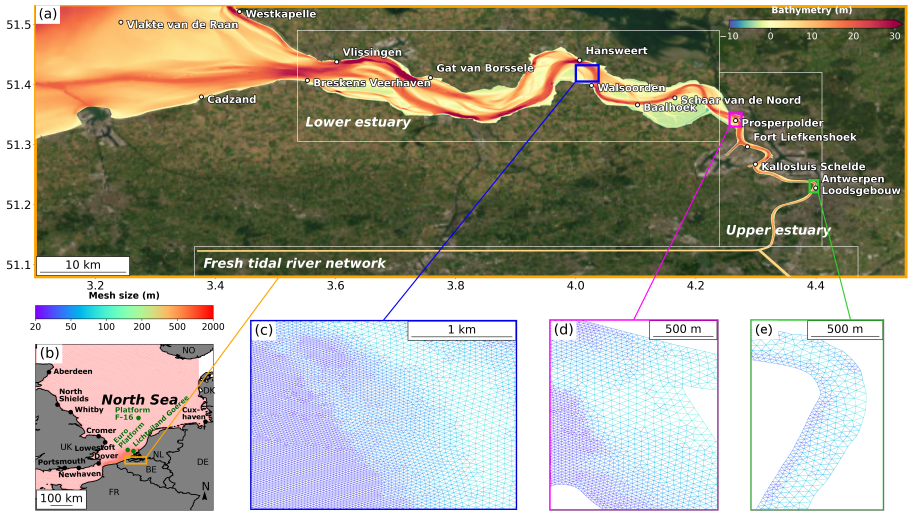

Figure 3.1: Model computation domain covering the Scheldt and North Sea region. The upper panel (a) displays the bathymetry of the Scheldt estuary, with the basemap ESRI (2025). The white rectangles outline the tidal zones of the estuary and the freshwater tidal river network is represented by artificial linear channels. Lower panels show the unstructured mesh configuration with (b) large view across the North Sea and (c-e) close-up views at three distinct locations on the Scheldt estuary. The dots in (a-b) mark validation points for the hydrodynamic model, colors in (b) differentiate coastal (black) and offshore (green) validation stations.

boundary following the 200 m isobath—and south-westward into the English Channel (Fig. 3.1). The mesh and the bottom friction follow the baseline model of Chapter 2, but the Storm Xaver simulation was run with an earlier version of the configuration and is validated separately below (Table 3.2). Only the elements specific to this chapter are presented here.

A one-month simulation was conducted with SLIM2D from November 20 to December 20, 2013, with a five-day spin-up phase excluded from validation to eliminate transient effects from the model's initial conditions.

We use MAR (Gallée et al., 1994; Fettweis et al., 2013) to simulate the atmospheric circulation over November and December 2013 at five different spatial resolutions: 2 km, 5 km, 10 km, 20 km and 30 km (Fig. 3.2.b-f). This enables a comparison of the effect of spatial resolution in atmospheric forcing, from (sub)-regional to global scale resolutions. The 30 km resolution matches the European Centre for Medium-Range Weather Forecasts (ECMWF) Reanalysis (ERA5) dataset scales (Hersbach et al., 2020) which was used as 6 hourly forcing of the MAR simulations. The sea surface temperature from ECMWF Reanalysis v5 (ERA5) is prescribed in MAR over the North Sea temperature, wind, humidity as well as surface pressure from ERA5 are used at the lateral boundaries of the five MAR integration domains centered over the studied area. The atmospheric pressure and near-surface wind speed computed with MAR for all spatial resolutions, are available at a 15 min time resolution. To assess the influence of the temporal resolution, we downscale the MAR output time to hourly, 3-hourly, and 6-hourly intervals by averaging, while maintaining constant spatial resolutions. Averaging preserves the overall evolution of wind and pressure during the storm and avoids the temporal aliasing of sub-sampling, as in prior hydrodynamic modelling studies (Cucco et al., 2019) and in reanalysis products such as ERA5, whose coarser products are derived by averaging (Hersbach et al., 2020). The bathymetry and the oceanic and river forcings are those of Chapter 2 (Table 2.2).

All MAR integrations use the same physical parameterisations, so that the grid spacing is the only setting that differs between them. This isolates the effect of resolution from that of model tuning, but the parameterisations are not scale-aware: schemes designed for coarser grids, in particular for convection and for the boundary layer, may lose part of their validity at the finest resolutions, which may contribute to the degradation of the wind from 5 to 2 km (Section 3.4).

3.2.2 Model-data comparison

Model results are compared with observations at the stations of Fig. 3.1, using the skill metrics of Section 2.2.4 (correlation coefficient R, bias, RMSE and

standard deviation σ), completed here by the mean absolute error, MAE = $N^{-1}\sum_{i=1}^{N}|m_i - o_i|$, and the normalized RMSE, NRMSE = RMSE/σ_o, where o_i and m_i are the observed and modelled values of a series of N points. Water elevation data were obtained from Rijkswaterstaat, which provides continuous 10 min observations along the Scheldt estuary. Wind speed and atmospheric pressure observations come from two sources: the Flemish Banks Monitoring Network on the Belgian Continental Shelf, Meetnet Vlaamse Banken, at a 10 min resolution, and the Global Historical Climatology Network hourly (GHCNh) dataset maintained by NOAA, which provides hourly observations from fixed land-based stations operated by various meteorological agencies (Fig. 3.2.a). These datasets are used to validate the atmospheric forcing. The ability of the hydrodynamic model to simulate the sea-level peak is assessed with the error on the highest water elevation during the storm surge. Water elevation or sea level refers to the barotropic sea level, including both tidal and surge components.

3.3 Results

3.3.1 The atmospheric model

The atmospheric model is first validated at all the stations of Fig. 3.2, then at the Zeebrugge Dam Instrument (ZDI) station, the westernmost station of the Scheldt region, between the mouth of the estuary and the coast (Fig. 3.2.b).

Multiple validation points

At 2 and 5 km (Fig. 3.2.c–f), MAR resolves finer details of the wind speed, particularly over land, where the topography induces localized wind patterns. Over the open sea, wind speeds are higher but more homogeneous. At 10 to 30 km (Fig. 3.2.g–l), these fine-scale variations are increasingly lost.

The normalized Taylor diagram, which includes all the observation stations depicted in Fig. 3.2.(a-b) highlights consistent patterns in the performance of MAR wind speed simulations across different spatial and temporal resolutions (Fig. 3.3.a). Simulations with finer spatial resolutions (2 km and 5 km) and shorter temporal intervals (15 min and 1 h) tend to cluster closer to the observation point, indicating better agreement with observed wind speed in terms of variability and correlation. Among these, the 5 km resolution consistently outperforms all other configurations. In contrast, simulations using coarser spatial resolutions (20 km and 30 km) and longer temporal outputs (3 h and 6 h) are located farther from the observation point, reflecting a systematic decrease in performance associated with lower

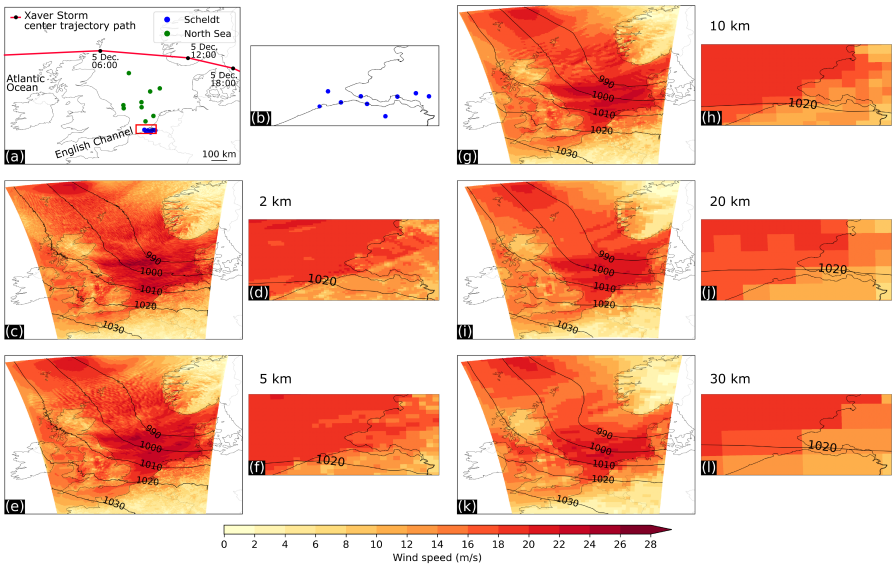

Figure 3.2: (a-b) Storm Xaver's central low-pressure trajectory over the North Sea and surrounding areas, showing its path on December 5, 2013, with time stamps in UTC. The storm path is indicated by a red curve; blue and green dots represent atmospheric data validation stations for the Scheldt estuary and North Sea, respectively. Panels (c–l) display snapshots of 10 m wind speed magnitude and sea level pressure contours at 12:00 UTC on December 5, 2013, as simulated by the MAR atmospheric model at varying spatial resolutions. These resolutions range from (c-d) 2 km, (e-f) 5 km, (g-h) 10 km, (i-j) 20 km, to (k-l) 30 km, each resolution includes an inset focusing on the Scheldt estuary and adjacent coastal areas.

correlation and underestimated variability. Clear regional contrasts are also apparent: simulations over the Scheldt region tend to align more closely with observations, while those over the North Sea show comparatively weaker agreement. This discrepancy between these two areas is largely due to the fact that the wind in the North Sea is measured at 30-50 m above sea level (a.s.l.) on oil platforms and not at 10 m a.s.l. as simulated with MAR.

For atmospheric pressure (Fig. 3.3.b), the markers of all spatial resolutions cluster together: unlike wind speed, the pressure is barely sensitive to the grid spacing. Temporal resolution matters slightly more, as the 15 min and 1 h outputs have slightly higher correlations and standard deviations closer to the observations than the 3 h and 6 h outputs. This lower sensitivity likely reflects the smoother, more spatially coherent nature of the pressure field.

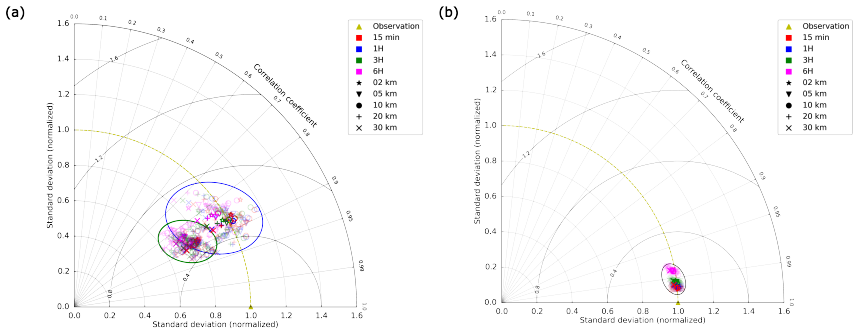

Figure 3.3: Normalized Taylor diagram of the MAR simulation for (a) wind speed at 10 m and (b) sea level atmospheric pressure, comparing simulations across different spatial resolutions, indicated by marker type, and temporal resolutions, indicated by color. Semi-transparent markers show individual validation stations, while bold markers represent regional centroids for weather stations located in (a) the Scheldt (blue ellipse) and the North Sea (green ellipse) regions and (b) all the weather stations (black ellipse) as defined in Figure 3.2(a–b).

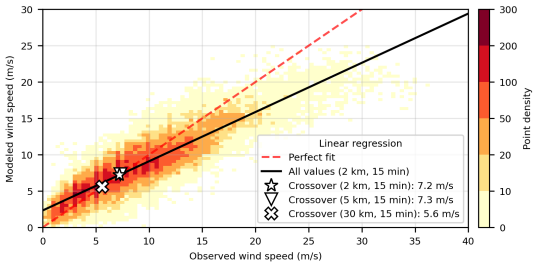

Figure 3.4: Density distribution of observed and modeled 10 m wind speeds, with observations (x-axis) and atmospheric model outputs at 2 km and 15 min resolution (y-axis). The solid black line shows the linear regression fit across all values of data points. The dashed red line represents the reference line of a perfect fit (model = observation). White markers indicate the crossover points, intersections between the reference line and the regression lines of the wind speed distributions for MAR simulations at 2 km (star), 5 km (triangle), and 30 km (cross) spatial resolutions, all at 15 min temporal resolution. These points represent the wind speed thresholds where the model shifts from overestimating to underestimating observed values.

The distribution of wind speed values when comparing observation and model results reveals a clear regime shift between low and high wind speed conditions (Fig. 3.4). Based on model outputs at 2 km spatial and 15 min temporal resolution, the model tends to overestimate wind speeds under low-wind conditions and increasingly underestimates them at higher observed wind speeds. For this finest resolution, this transition occurs at a crossover point of 7.2 m/s, defined by the intersection of the model's global linear fit with the perfect agreement reference line. Beyond this threshold, the discrepancy between model and observation widens with increasing wind speed, pointing to a saturation effect in the model response. For instance, at an observed wind speed of 30 m/s, the model simulates only 22 m/s—an underestimation of about 30%. This regime shift pattern remains consistent across all other spatial and temporal resolutions tested. The corresponding regression functions and crossover points are provided in Appendix 6.2.1. Notably, an improvement of 7–8% is observed in the slope of the linear fit when comparing the finest spatial resolutions (2 km and 5 km) with the coarsest (30 km), under the same 15 min temporal resolution. This reduced slope at coarser scales also results in a lower crossover point, further emphasizing the scale-dependent nature of the regime shift (Fig.3.4).

Single validation point

The atmospheric model MAR effectively reproduces the variability in atmospheric pressure and wind speed at ZDI during the simulated period (Fig. 3.5), as shown by comparisons between MAR simulations with a 2 km spatial resolution and 15 min temporal resolution. During the analysis period, three distinct peaks in wind speed and corresponding drops in atmospheric pressure occurred. The first event, on November 28, corresponds to Storm Oskari; the second, on December 6, to Storm Xaver; and the third, on December 18, to Storm Bernd. Notably, among the three events, only Storm Xaver generated a significant storm surge in the region. In contrast, although Storm Bernd caused a more substantial drop in atmospheric pressure at the observation site, its relatively weaker associated wind speeds were insufficient to trigger a storm surge event.

Table 3.1 gives the error metrics at ZDI for each resolution. As the exact height of the pressure sensor is unknown, the pressure bias due to the elevation difference with MAR (sea level) is removed, and the centred RMSE (**CRMSE!**) is reported instead of the RMSE. At a fixed 15 min resolution, the wind RMSE ranges from 2.1 m/s (2 and 10 km) to 2.4 m/s (5 and 20 km) and the pressure **CRMSE!** from 2.0 hPa (5 km) to 2.9 hPa (20 km), without a monotonic dependence on the grid spacing. At a fixed 2 km resolution, coarsening the output from 15 min to 6 h raises the wind RMSE from 2.1 to

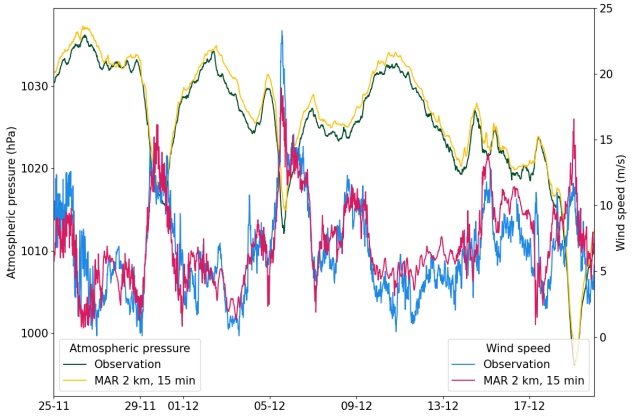

Figure 3.5: Wind speed and atmospheric pressure at Zeebrugge Dam Instrument (ZDI) from November 25 to December 20, 2013, showing observations in green for atmospheric pressure and blue for wind speed, alongside MAR atmospheric model outputs at 2 km and 15 min resolution, represented in yellow for atmospheric pressure and red for wind speed.

2.3 m/s and the pressure **CRMSE!** from 2.4 to 2.8 hPa, and lowers the wind correlation from 81.8 to 78.5 %. The wind correlation lies between 78.0 % (20 km) and 83.5 % (5 km), and the pressure correlation stays above 98 % in all configurations. These differences remain small: the largest spread between resolutions, 0.3 m/s for wind and 0.9 hPa for pressure, is well below the standard deviation of the observations (3.5 m/s and 7.5 hPa), and the NRMSE stays between 60 and 68 % for wind and between 26 and 39 % for pressure. At this station, the sensitivity of MAR to resolution is therefore modest.

3.3.2 Ocean model validation during storm surge

The time series analysis comparing model outputs and tide gauge observations shows that the model accurately reproduces the tidal cycles at the different stations (Fig. 3.6). There is a slight overestimation of the tidal high and low water by typically around 0.1 m. This overestimation is also visible in the comparison of the dominant tidal constituent M2 between the observations and the model results (Table 3.2). However, these deviations are relatively minor compared to the tidal range of about 6 m, and overall, the stations show a good representation of the tidal dynamics. Error metrics further indicate the model's robustness (Table 3.2). The RMSE values within the Scheldt estuary range from 0.21 m at Westkapelle and

Table 3.1: Statistics for wind speed and atmospheric pressure with different MAR spatial and temporal resolutions at Zeebrugge Dam Instrument (ZDI), the most western weather station on Fig. 3.2.b, from November 25 to December 20, 2013.

MAR spatial and temporal resolutions	Wind speed			Atmospheric pressure		
	RMSE (m/s)	NRMSE (%)	Correlation (%)	CRMSE (hPa)	NRMSE (%)	Correlation (%)
2 km, 15 min	2.1	60.5	81.8	2.4	32.7	99.6
5 km, 15 min	2.4	66.9	83.5	2.0	26.4	99.6
10 km, 15 min	2.1	60.7	80.3	2.7	36.1	99.6
20 km, 15 min	2.4	68.4	78.0	2.9	39.0	99.5
30 km, 15 min	2.2	61.6	80.2	2.5	33.6	99.3
2 km, 1 h	2.1	60.9	82.6	2.6	35.3	99.6
2 km, 3 h	2.2	61.6	81.6	2.6	35.1	99.4
2 km, 6 h	2.3	64.4	78.5	2.8	36.9	98.4

Breskens Veerhaven to 0.30 m at Antwerpen Loodsgebouw, corresponding to areas with tidal amplitudes of approximately 4 m. Stations exhibiting the largest RMSE values also display the largest phase differences with respect to the observed M2 constituent. This suggests that part of the RMSE originates from a slight time lag in the modeled tide, leading to discrepancies when comparing different phases of the tidal cycle. Such phase shifts may stem from uncertainties in bottom-drag parameterization or from small inaccuracies in the bathymetry. Stations far from the estuary show higher RMSEs, up to 0.97 m at Dover. At these stations the M2 phase differs from the observations by 22 to 35° (about one hour), whereas it stays within 5° at the other stations of Table 3.2. An offset this close to one hour may reflect a time-reference mismatch between these gauge records and the model rather than a propagation error, but this has not been established. These stations are excluded from the Taylor-diagram analysis below. The tide of this simulation also differs from that of the 2016–2020 hindcast, as discussed in Section 2.3.1. Overall, the bias and Mean Absolute Error (MAE) values remain close to zero, and correlation coefficients—consistently above 99% in the Scheldt and over 85% elsewhere, which demonstrate a strong linear relationship between modeled and observed water levels. This high correlation highlights the model's capability in accurately capturing water elevation dynamics, particularly within the Scheldt estuary, the main area of interest in this study.

3.3.3 Storm surge simulation sensitivity to atmospheric model resolution

The validation across different temporal and spatial resolutions reveals two distinct clusters corresponding to the Scheldt estuary and the offshore North

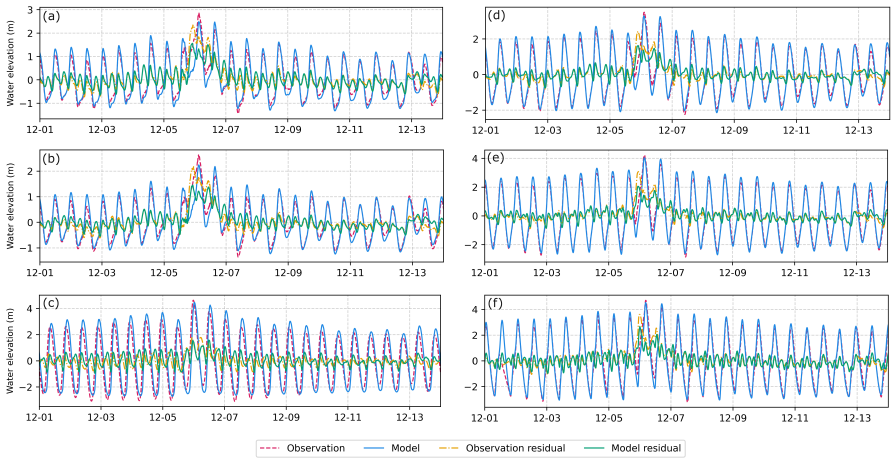

Figure 3.6: Time series of sea surface elevation from December 1st to December 15th, 2013, at six locations, on the offshore and coastal North Sea stations (a) Lichteiland Goeree, (b) Euro Platform, (c) Dover; and Scheldt estuary stations: (d) Vlakte van de Raan, (e) Hansweert, and (f) Antwerpen Loodsgebouw. Results are shown as simulated by SLIM using MAR atmospheric forcing with 2 km spatial and 15 min temporal resolution (blue), compared against observed sea surface elevation (red). Detided (residual) elevations are also shown for both the observations (orange) and model outputs (green).

Sea stations (Fig. 3.7). To ensure clarity and maintain readability, only those validation points, i.e. stations in the Scheldt represented by black dots in Fig. 3.1.a and offshore North Sea stations represented by green dots in Fig. 3.1.b were included in the analysis, while other coastal stations, where no specific calibration was applied, were excluded. For both regions, the position of the centroid of the model performance in the Taylor diagram improves as the temporal resolution of the atmospheric forcing becomes finer, and the best results are obtained with 15 min temporal resolution. The Scheldt cluster appears more compact and lies closer to the observational reference point, indicating that the model performs more accurately and consistently in this confined estuarine environment. Within this group, simulations at 5 km spatial resolution show the best alignment with observations, mirroring the behavior observed in the atmospheric forcing validation over the Scheldt (Fig. 3.3.a). Concerning the spatial resolution, the best results over the North Sea are obtained with the 2 km resolution of atmospheric forcing.

The comparison of simulations using atmospheric forcing at different spatial resolutions, while maintaining a fixed temporal resolution, indicates

Table 3.2: Error metrics for water elevation and principal tidal constituent M2 amplitude and phase for various stations along the Scheldt estuary (top) and other locations in the domain (bottom), from November 25 to December 20, 2013.

Station	RMSE [m]	Correlation [%]	MAE [m]	Bias [cm]	$M2_{obs}$ [m]	$M2_{mod}$ [m]	$M2_{obs}$ [°]	$M2_{mod}$ [°]
Vlakte van de Raan	0.22	98.5	0.17	0.05	1.42	1.58	18.03	17.40
Cadzand	0.22	98.7	0.17	0.02	1.61	1.73	21.08	21.93
Westkapelle	0.21	98.6	0.16	0.00	1.47	1.59	25.51	24.70
Breskens Veerhaven	0.21	98.8	0.16	-0.00	1.67	1.77	29.70	29.48
Vlissingen	0.22	98.8	0.17	-0.00	1.67	1.80	31.52	32.19
Gat van Borssele	0.23	98.9	0.17	-0.08	1.76	1.90	38.13	37.80
Hansweert	0.24	99.0	0.18	-1.73	1.93	2.08	52.16	51.86
Walsoorden	0.24	99.0	0.19	-1.87	1.97	2.14	54.81	54.04
Baalhoek	0.24	99.0	0.19	-2.17	2.02	2.19	58.55	57.69
Schaar van de Noord	0.24	99.1	0.19	-2.32	2.05	2.22	60.95	60.43
Prosperpolder	0.26	99.1	0.19	-2.56	2.09	2.27	64.70	64.35
Fort Liefkenshoek	0.25	99.1	0.19	-2.87	2.15	2.30	67.21	65.86
Kallosluis Schelde	0.26	99.0	0.20	-9.81	2.19	2.34	69.13	67.29
Antwerpen Loodsgebouw	0.30	98.7	0.23	-12.06	2.22	2.36	75.65	70.91
Platform F16-A	0.16	94.9	0.12	0.02	0.50	0.56	180.27	183.49
Euro Platform	0.21	95.6	0.16	0.01	0.69	0.83	26.46	28.16
Lichteiland Goeree	0.23	96.3	0.17	0.00	0.82	0.99	40.55	41.71
Cuxhaven	0.54	89.9	0.44	-0.37	1.37	1.19	313.55	335.81
Cromer	0.68	84.4	0.57	1.71	1.51	1.48	158.56	188.84
Dover	0.97	86.6	0.80	-1.04	2.23	2.48	303.47	331.30
Lowestoft	0.40	81.3	0.32	0.58	0.67	0.68	227.88	263.35
Newhaven	0.92	87.7	0.82	-1.07	2.23	2.49	293.58	322.18
North Shields	0.64	88.0	0.54	-0.38	1.57	1.67	59.51	87.27
Portsmouth	0.66	85.9	0.59	-0.93	1.40	1.67	299.50	328.75
Whitby	0.67	87.3	0.57	-0.14	1.63	1.70	75.09	103.82

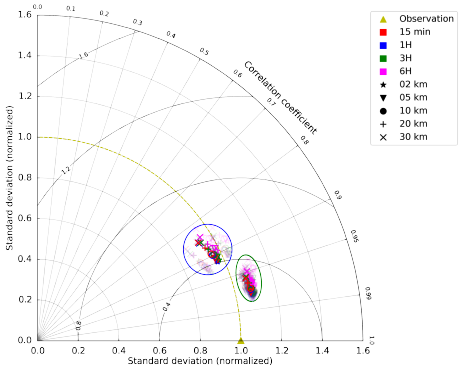

Figure 3.7: Normalized Taylor diagram of sea surface elevation simulated by SLIM when forced by different spatial resolutions, indicated by marker type, and temporal resolutions, indicated by color. Semi-transparent markers show individual validation points; bold markers represent regional centroids for stations near the Scheldt estuary (blue ellipse) and the offshore North Sea (green ellipse) regions as defined in Figure 3.1(a–b).

that the best results are achieved with the 2 km resolution when modeling the peak of water elevation (Fig. 3.8). The performance of the modeled peak water level declines as the spatial resolution of atmospheric forcing decreases. Along the Scheldt estuary, the finer spatial resolution consistently outperforms other resolutions in modeling the maximum water elevation, hereafter referred to as the peak water level, particularly in upstream stations (Fig. 3.8). The results of 5 km and 10 km resolutions are close to the accuracy of the 2 km forcing, whereas coarser resolutions of 20 km and 30 km yield poorer results. As a result, there is 20% improvement in peak water levels estimation between the simulations forced at 2 km and 30 km resolution in upstream regions like Antwerpen Loodsgebouw and Kallosluis Schelde.

The comparison of the simulations obtained by forcing the hydrodynamic model SLIM with MAR at different temporal resolutions and fixed spatial resolution shows that the best results are obtained with the 15 min resolution. However, the impact of the temporal resolution of the atmospheric forcing on the peak water levels is obvious only at the finest 2 km spatial resolution (Fig. 3.9.a). The temporal resolution of the atmospheric forcing appears to have an almost negligible impact on the quality of model simulations when the spatial resolution is coarser (Fig. 3.9.b). At 5 km resolution (Fig. 3.9.b), the scatter of points across different temporal resolutions shows comparable performance across most stations, with no evident advantage for higher temporal resolution. Similarly, coarser spatial resolutions ranging from 10 to 30 km (not shown here) exhibit behavior comparable to the 5 km resolution. The results suggest that the temporal resolution of the atmospheric forcing only has an impact on the model's performance when the spatial resolution is finer than 5 km. However, this effect likely depends on factors such as the characteristics of the surge, its duration or peak number, and the size and shape of the estuary. For Storm Xaver, the storm propagation speed had a strong impact on the surge characteristics (Wei et al., 2019). The results presented here apply to the Scheldt, a narrow and confined estuary. In contrast, larger systems with broader channels and multiple branches may respond less sensitively to high temporal resolution due to their wider cross-sections, longer response times, and different balances between tidal and river discharge influences.

At a fixed 15 min temporal resolution, the deviation in peak water level, defined as the difference between the maximum water elevations of two simulations, grows as the spatial resolution of the forcing coarsens (Fig. 3.10). Between the 2 and 5 km forcings, it stays mostly within ±10 cm (Fig. 3.10.a–b). With the 10, 20 and 30 km forcings (Fig. 3.10.c–h), it grows in magnitude and extent, exceeding 10 cm over the lower estuary and approaching 40 cm in its centre with the 30 km forcing. The lower estuary and the adjacent coast

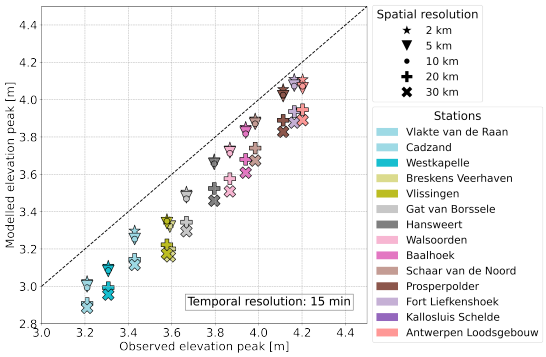

Figure 3.8: Comparison of peak water levels between simulation (y-axis) and observation (x-axis) at various stations and spatial resolution, using MAR atmospheric forcing fixed at a 15 min temporal resolution. Different symbols indicate spatial resolutions of the atmospheric forcing (ranging from 2 km to 30 km), and colors correspond to specific coastal stations as shown in the legend. The dashed line represents perfect agreement between model predictions and observations. The best agreement between model and observations is achieved for the largest storm surge peaks and the finest spatial resolution.

are the most sensitive; the open North Sea, farther from the funnel-shaped estuary, shows smaller but still noticeable deviations.

At a fixed 2 km spatial resolution, the peak water levels of the simulations forced at 1, 3 and 6 h differ by about ±10 cm from those of the 15 min simulation (Fig. 3.11). As for spatial resolution, the area of large deviations widens as the forcing coarsens, in the Scheldt estuary (Fig. 3.11.b, d, f) and even more in the North Sea (Fig. 3.11.a, c, e). The sign of the deviation also splits the domain: the 15 min forcing yields higher peaks in the Scheldt estuary and the North Sea, and lower peaks in the English Channel.

The hydrodynamic model results agree better with observations at upstream stations, where surge levels are highest. This holds true across different temporal and spatial resolutions of the atmospheric forcing. Stations such as Prosperpolder and Antwerpen Loodsgebouw exhibit slightly greater discrepancies in peak water levels, as evidenced by scatter markers deviating further from the diagonal line at coarser atmospheric resolutions. These deviations become more pronounced as resolution of atmospheric forcing decrease, as shown in Figs. 3.10 and 3.11. At the most upstream stations, temporal resolution exerts a substantial influence on peak water elevations, with observed differences of up to 15 cm between simulations forced at 15 min and 6 h temporal resolution (Figs. 3.9.a and 3.11). Spatial resolution has

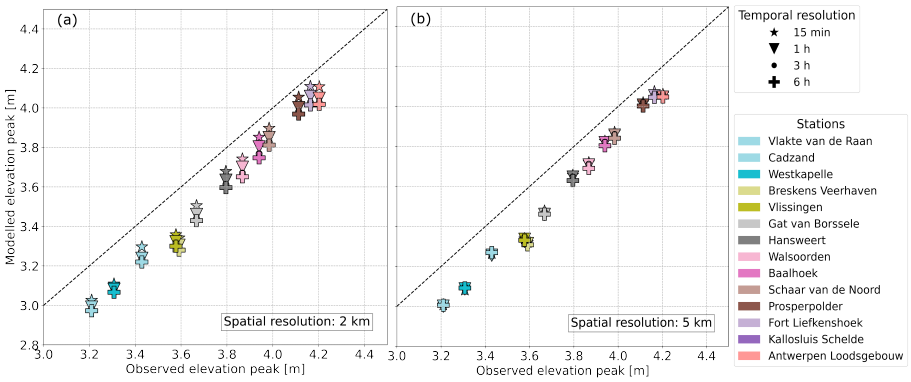

Figure 3.9: Same as Fig. 3.8 for various temporal resolutions of the atmospheric forcing with spatial resolution fixed at (a) 2 km, (b) 5 km. Symbols represent the different temporal forcing resolutions, ranging from 15 min to 6 h. A finer spatial resolution of 2 km (a) demonstrates significant improvement with increased temporal resolution compared to the coarser spatial resolution of 5 km (b).

an even greater impact, causing peak water levels deviations of up to 30 cm between 2 km and 20 km resolutions (Figs. 3.8 and 3.10) at those stations.

The timing of the storm surge is largely unaffected by the resolution of the atmospheric forcing, as peak water levels occur nearly simultaneously across most of the domain, regardless of the spatial or temporal resolution of the forcing. Peak water levels across different spatial and temporal resolutions display a time variation mostly around 0 min of deviation with a range within ± 10 min (Fig. 3.12 and Appendix Fig. 6.2.1). Both spatial and temporal scales exhibit similar patterns. The higher values of deviation appear as patchy regions in the estuary and coastal areas. These regions become larger as spatial or temporal resolution of the atmospheric forcing becomes coarser, particularly in the estuary, but they stay in the limited range of 10 min. Also in the estuary, a large time variation, with blue and red patches, can be seen in the region with tidal marshes.

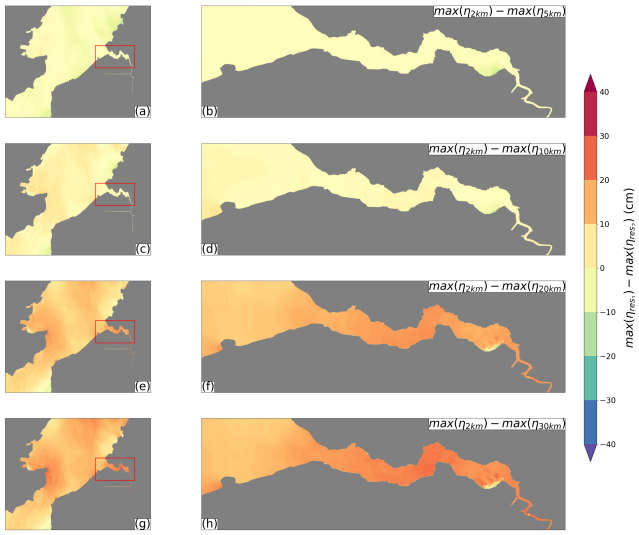

Figure 3.10: Difference in maximum water elevation between simulation results at 2 km atmospheric forcing resolution and those at (a-b) 5 km, (c-d) 10 km, (e-f) 20 km, and (g-h) 30 km forcing resolutions. The temporal resolution of the atmospheric forcing is fixed at 15 min for all simulations. The left panels depict the coastal North Sea, while the right panels present close-up views of the Scheldt estuary.

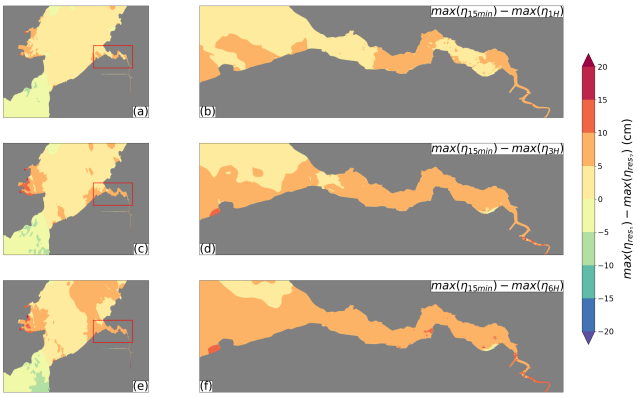

Figure 3.11: Difference in maximum water elevation between simulation results at 15 min atmospheric forcing resolution and those at (a-b) 1 h, (c-d) 3 h, (e-f) 6 h forcing resolutions. The spatial resolution of the atmospheric forcing is fixed at 2 km for all simulations. The left panels depict the coastal North Sea, while the right panels present close-up views of the Scheldt estuary.

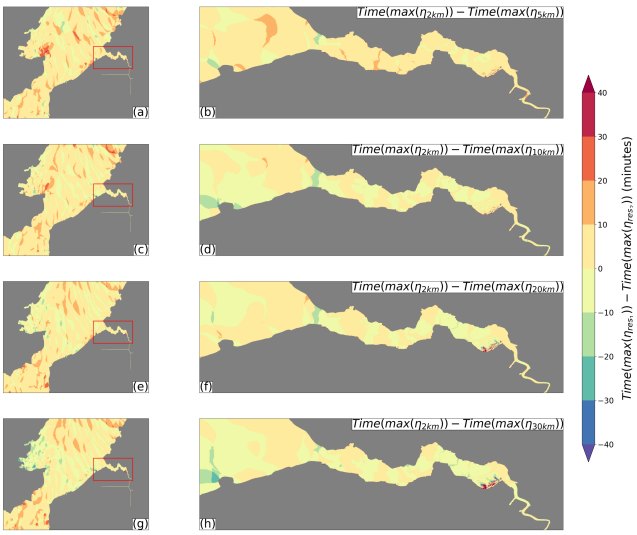

Figure 3.12: Timing differences in peak water levels during the storm surge between the reference simulation with 2 km resolution, and simulations with coarser spatial resolution: (a-b) 5 km, (c-d) 10 km, (e-f) 20 km, and (g-h) 30 km resolution, and a fixed temporal resolution of fixed to 15 min. The color scale indicates the deviation in peak timing from the reference, measured in minutes. The left panels depict the coastal North Sea, while the right panels present close-up views of the Scheldt estuary.

3.4 Discussion

Forcing a multiscale hydrodynamic model with atmospheric fields at spatial resolutions from 2 to 30 km and temporal resolutions from 15 min to 6 h shows that the simulated storm surge of Storm Xaver in the Scheldt estuary–sea continuum is sensitive to both. The model reproduces the event with errors comparable to those of other studies of the region (Plancke et al., 2020; Gourgue et al., 2015). A finer spatial resolution improves the simulated peak surge, whereas coarser resolutions underestimate it; the temporal resolution matters only at the finest spatial resolution. Spatial resolution is therefore the more important of the two for the peak surge in the estuary.

The improved performance of the modeled surge in estuarine regions can be linked to enhanced representation of atmospheric forcing at higher spatial and temporal resolutions. Refining the atmospheric forcing from 30 to 5 km improves the simulated wind at the offshore and coastal stations, where the RMSE decreases and the correlation increases (Fig. 3.3.a, Table 6.2.2). Over land, the improvement is less systematic: at four inland stations of the Scheldt (Marollegat, Hoofdplaat, Hansweert and Westdorpe), the 30 km forcing yields a lower RMSE than the 5 and 2 km forcings, although the correlation remains higher at finer resolution. Refining further from 5 to 2 km degrades the wind at nearly all stations (15 of 16). The wind is therefore best represented at 5 km, whereas the surge peak in the estuary is best represented at 2 km (Section 3.3.3). Given the lower sensitivity of atmospheric pressure accuracy to resolution (Fig. 3.3.b), except when the temporal resolution is at its coarsest, and the fact that storm surges in the North Sea are primarily wind-driven (Plüß et al., 2001), this discussion focuses exclusively on wind speed. The degradation at 2 km is likely related to the hydrostatic assumption of MAR: at this resolution, vertical accelerations are no longer negligible in convective cells and near the coastline, and the hydrostatic approximation reaches the limit of its validity. Parameterisations that are not scale-aware (Section 3.2.1) and grid-scale noise (Russell et al., 2019) may add to this effect. The 2 km forcing nevertheless gives the best surge peaks in the estuary, which suggests that the finer representation of the coastline and of the land–sea contrast outweighs the degradation of the wind at the stations. The finer forcing also reduces the underestimation of strong winds (Fig. 3.4 and Table 6.2.1), which strengthens the momentum transferred to the sea and the surge that enters the estuary.

The gain from 5 to 2 km remains modest, however: the simulated peaks differ little (Fig. 3.10), while the 2 km forcing requires roughly four times the computing resources of the 5 km forcing, because of both the denser grid and the shorter time step. In practice, a one-month 2 km MAR simulation over our

domain takes more than a week. The 5 km resolution is therefore a practical and nearly as effective alternative for many applications.

The sensitivity of the modelled surge to the forcing resolution agrees with previous studies (Weaver et al., 2016; Agulles et al., 2024). Agulles et al. (2024) found temporal resolution more important than spatial resolution, for spatial scales of 1.5–25 km, temporal resolutions from hourly to daily, and decades of surges along the European coastline. Our results point the other way for an estuary at finer scales, as did those of Weaver et al. (2016) for a cold-front surge in the Indian River Lagoon, Florida. The relative importance of the two resolutions thus depends on the scale and characteristics of the system, and possibly on the atmospheric data source: the hourly, 31 km ERA5 forcing (Hersbach et al., 2020) that gave the best results for Agulles et al. (2024) leads here to an underperforming surge model in the estuary.

The atmosphere acts on the hydrodynamic model only through the friction force of the wind, expressed as the wind stress, and the atmospheric pressure gradient force (Sections 1.2 and 2.1.1). The pressure is barely sensitive to the resolution of the forcing, so the coupling process degraded by a coarser forcing is the transfer of momentum through the wind stress. At 10 to 30 km, the Western Scheldt is narrower than a grid cell of the atmospheric model and is classified as land. The wind over it is therefore computed with the roughness of land and is underestimated. Coarser grids also smooth the mesoscale wind maxima. Since the stress is quadratic in the wind speed and the drag coefficient of Flather (1976) is constant at storm wind speeds, a 30 % underestimate of the wind halves the stress. The ocean does not transmit this deficit linearly. The wind set-up scales inversely with the depth, which varies with the tide, and the bottom friction couples the wind-driven and tidal currents, so that wind and tide do not add up in shallow tidal areas (Horsburgh et al., 2007; Jacob et al., 2017). The response to a weaker forcing therefore concentrates where these interactions are strong, as in the Scheldt estuary. Since the forcing is one-way and waves are not represented, feedbacks of the sea state and of the surface currents on the wind stress are not included.

The benefit of better representing the atmospheric data in storm surge modeling is not specific to estuaries and can also include larger regions. For example, in the Western Baltic Sea, Lorenz et al., 2023 showed that the coarse resolution of atmospheric models such as ERA5 is also insufficient to resolve wind speeds correctly, leading to an underestimated peak water level. The determination of an appropriate spatial resolution for atmospheric forcing is ultimately dependent on the specific processes and scales being modeled. For coastal storm surge dynamics, which typically unfold over several hours and tens of kilometers, atmospheric forcing at such spatial scales may suffice (Agulles et al., 2024; Meyer et al., 2023; Muller et al., 2014; Ridder et al.,

2018). However, our results indicate that these standard resolutions may be inadequate for modeling storm surges in complex topographic and smaller-scale regions such as estuaries. In those settings, finer-scale forcing is required to capture the local dynamics that drive the surge intensity. Furthermore, as demonstrated in our study, even some offshore areas benefit from higher-resolution atmospheric data, which yields a more realistic representation of wind and hence improves surge model results.

The ERA5 fields that drive MAR at its lateral boundaries likely contribute to the underestimated surge. ERA5 is known to underestimate wind speeds, especially during extreme events (Molina et al., 2021), and this deficit can propagate into MAR and reduce the momentum transferred to the ocean; a higher resolution only partly corrects it. At the offshore stations closer to the storm track and to the open boundary, MAR nevertheless produces stronger and more realistic winds than ERA5 (Appendix 6.2.1). The lateral forcing of MAR is also only 6-hourly. A higher boundary frequency can improve rapidly evolving storms in regional atmospheric models, but not consistently (Vemuri et al., 2022), and its storage, input/output and runtime costs were deemed impractical given the already long simulations. The quality of the MAR fields thus remains bounded by that of its external forcing.

The flood control areas and restored intertidal areas of the Sigma Plan are not represented in the hydrodynamic model (Section 2.2.1), whereas the natural flats and marshes are, including Saeftinghe, the largest remaining intertidal area of the estuary (about 3000 ha) (Smolders et al., 2015). During Storm Xaver, Saeftinghe lowered the high water by about 10 cm around Antwerp, and the flood control areas by up to about 0.5 m about 150 km from the mouth, but not downstream of 110 km (Smolders et al., 2020). The attenuation that acts on the validation stations, which end near Antwerp, about 90 km from the mouth, is therefore represented, and the missing flood control areas act farther upstream. Their absence can only raise the simulated peak there, so it cannot explain the underestimation of the surge peaks. Since all simulations share the same geometry, the missing storage affects them alike, and the comparison between forcing resolutions is little affected.

Refining the forcing further raises the question of its cost and benefit, for both the atmospheric and the hydrodynamic model. The 2 km, 15 min forcing gives the best simulated peak surge, though not always the most accurate atmospheric fields. In time, finer outputs are unlikely to help: the surge takes about two hours to travel along the estuary, from Vlakte van de Raan at 15:40 to Antwerp at 17:50 on December 6, eight times the 15 min step, and atmospheric fluctuations shorter than the hydrodynamic response time of the estuary would mainly add noise and amplify uncertainties.

In space, refining beyond about 2 km would require a non-hydrostatic atmospheric model, at a cost that grows at least fourfold with each halving of

the grid spacing. A local bias correction of the wind would be a cheaper way to improve the forcing. A finer forcing would also call for a finer hydrodynamic mesh, whose coarsest elements were matched here to the 2 km forcing. A finer mesh can improve the hydrodynamics (Saint-Amand et al., 2023), but at a much higher cost and with diminishing returns unless the bathymetry and the physical parameters are equally detailed. The optimal trade-off between accuracy and computational resources remains to be identified.

The timing of the peak surge is nearly insensitive to the forcing resolution, with deviations within ±10 min, which suggests that it is set by other factors, mainly the tide. Surge maxima in the North Sea occur predominantly on the rising tide (Horsburgh et al., 2007), and during Storm Xaver the peak coincided with high tide. Through the non-linear interaction between tide and surge (Ferrarin et al., 2012; Wahle et al., 2022), this synchronisation likely locked the timing of the peak in all simulations.

As with any modelling study, our approach has limitations. First, the 2D model does not represent vertical density gradients. The Scheldt estuary and its coastal zone are well mixed by the strong tide (Chapter 1), and stratification, which can occur during high river discharge, is absent during surges, when the oceanic input dominates over the river flow (Van Damme et al., 2005; Smolders et al., 2020). In comparable estuaries, 2D and 3D models reproduce the peak surge with similar accuracy, the advantage of 3D models appearing mainly during the post-surge relaxation (Ye et al., 2020; Lapetina et al., 2015). The 2D approach is therefore appropriate for the peak surge, and it allows a finer horizontal mesh than a 3D model at the same cost.

Another limitation is the representation of vegetation through an increased bottom friction. This simplification underestimates friction where the water depth is less than the vegetation height, as in the Scheldt marshes, where plants grow up to one metre; the patchy timing differences over the marshes (Fig. 3.12) may reflect it. In reality, the drag exerted by vegetation should remain constant regardless of depth, whereas our model reduces it as the depth increases. Methods such as that of Baptist et al. (2007) account for the full drag of vegetation and would improve storm surge simulations in marshlands, where vegetation mitigates extreme weather impacts (Hu et al., 2015).

The spatial resolutions compared here come from separate MAR integrations, whereas the temporal resolutions are obtained by averaging the output of a single run. A difference between two spatial resolutions therefore combines three contributions: the representation of the fields on a coarser grid, the response of the model's dynamics and parameterisations to the grid spacing, and the internal variability of each integration, i.e. the random deviations that each run develops inside its domain. With a single integration

per resolution, this internal variability cannot be separated from the effect of resolution. The second contribution changes the mean state of the model even with unchanged physics (Boer et al., 1988; Pope et al., 2002), and it is part of any forcing produced at a given resolution. The present design thus answers the practical question of which atmospheric resolution is needed to force the hydrodynamic model, but it does not attribute the differences to the grid alone. The internal variability of a regional model is constrained by its lateral boundaries and is weakest in winter, under a strong synoptic flow and over small domains (Giorgi et al., 2000; Alexandru et al., 2007; Lucas-Picher et al., 2008; Hong et al., 2014). It is therefore expected to be small for Storm Xaver, consistent with peak water levels occurring within ±10 min at all resolutions (Figs. 3.12 and 6.2.1). It may nonetheless be of the same order as the smallest differences found here, those between the 2 and 5 km forcings. Aggregating the 2 km fields onto the coarser grids would isolate the effect of the grid, and a small ensemble of 2 km runs with perturbed initial conditions would measure the internal variability. The temporal axis already follows the first design: averaging a single forcing removes a frequency band without changing the mean, as in Jacob et al. (2017), who showed that the ocean response to such a change concentrates where wind and tide interact non-linearly.

Finally, because of the high computational cost of resolutions from 20 m to 2 km for the hydrodynamic model and of 2 km for the atmospheric model, this study is limited to a single storm surge event, one of the highest recorded in the region (Rucińska, 2019). The validation period is also short: the model is validated here over a single one-month window around Storm Xaver rather than over the multi-year record of Chapter 2, so the results are event-specific. This is a common trade-off in high-resolution surge modelling—the cost of kilometre-scale forcing and fine meshes confines such studies to short windows and single events—that cheaper GPU computing is gradually easing. The surge also depends strongly on the storm itself: track deviations of 20–50 km, the translation speed of the storm, the bathymetry and the coastline geometry change how effectively the wind piles up water (Colle et al., 2015; Weisberg et al., 2006; Warder et al., 2021; Hussain et al., 2017; Rego et al., 2010; Orton et al., 2020). In the North Sea, a more southerly or a slower storm than Xaver would likely raise the surge in the Southern North Sea and in the Scheldt (Warder et al., 2021; Wei et al., 2019). Chapter 4 examines how the surge response varies across a panel of storms with different tracks.

3.5 Conclusion

With a focus on the Scheldt estuary during Storm Xaver, one of the largest North Sea surges of the past 60 years, this chapter shows that the resolution of the atmospheric forcing matters for storm surge modelling along the estuary–sea continuum. Spatial resolution matters more than temporal resolution: refining the forcing from 30 to 2 km improves the simulated peak water level by about 20 % in the upper estuary, whereas the temporal resolution matters only at 2 km. The 2 km, 15 min forcing gives the best peaks, and the 5 km forcing is a nearly as effective and four times cheaper alternative. The timing of the peak is insensitive to the resolution and is likely set by the tide. Global products at about 30 km, such as the ERA5 reanalysis and the operational forecasts of the ECMWF Integrated Forecasting System, are therefore too coarse to resolve the surge in the estuary. As climate change and sea-level rise are expected to intensify storm surges (Woth et al., 2006), balancing forcing resolution and computational cost will be key to both forecasting and long-term planning.

Chapter 4

Future storm surges in the Scheldt North Sea continuum

4.1 Introduction

Projections of North Sea storm surges have focused on how their magnitude changes at the coast, and found the meteorological contribution to be uncertain and strongly model-dependent (Woth, 2005; Sterl et al., 2009; Gaslikova et al., 2013; Vousdoukas et al., 2017). Most do not resolve estuarine dynamics, so how an extreme storm acts along a river–sea continuum, from the open shelf to the head of an estuary, remains poorly known.

Inside an estuary, the surge propagates as a long wave. In a convergent channel, the balance between convergence and friction determines whether a long wave is amplified or damped landward, as for the tide (Friedrichs et al., 1994; Savenije et al., 2008), and depth, convergence and river flow modulate the landward evolution of the surge in the same way (Familkhalili et al., 2022; Talke et al., 2021). In the Elbe, projected extreme water levels rise fastest in the upper estuary (Pein et al., 2023).

On the shelf, the storm track is a first-order control on the surge. The 1953 surge was generated mainly by sustained northerly winds over the southern North Sea (Flather, 1984), the intensity and direction of the wind set the surge

frequency at the Dutch and Belgian coasts (Bijl, 1997), and the track geometry sets the spatial footprint of surge extremes around the UK and Irish coasts (Camus et al., 2024). Physically plausible changes in track and propagation speed can produce surges far exceeding observed maxima (Horsburgh et al., 2021; Wei et al., 2019), and reconstructions of historical storm tides in the German Bight show the same sensitivity to track orientation and timing (Meyer et al., 2023; Grabemann et al., 2019).

Negative surges have received much less attention. They were documented early in the southern North Sea (Geelhoed, 1973; Burlace, 1986), but a systematic meteorological characterisation exists only for the Elbe, where strong south-easterly gales drive the extreme low waters (Jensen et al., 2022). Negative surges are also a concern in other regions of the world (Conte et al., 2013; Cheng et al., 2019). Beyond the peak value, the shape of the surge hydrograph and its timing relative to the tide matter for coastal management. Along the Dutch coast, more than half of the observed event types carry several peaks, and surge peaks occur preferentially on the rising and low tide (Pupic Vurilj et al., 2025), as tide–surge interaction predicts (Horsburgh et al., 2007). These characterisations exist for observed positive surges on the open coast, but not for negative surges, and not along an estuary.

In the Scheldt, process-based modelling has quantified the effects of sea-level rise on its century-scale hydro- and morphodynamic evolution, on dredging strategies and on flood management plans (Röbke et al., 2025; Broekx et al., 2011), but no study has characterised the positive and negative surges that extreme storms drive along the Scheldt–North Sea continuum. This gap motivates the central research question of this chapter: what do future extreme storms reveal about positive and negative storm surges along the Scheldt–North Sea continuum under a high-emission scenario? The chapter examines how the surge evolves from the open sea to the head of the estuary, how the storm track modulates it, and how surge and drawdown combine within an event and relative to the tide.

To address this question, we adopt a PCS approach, which constructs physically self-consistent, plausible unfoldings of specific weather or climate events rather than probabilistic projections (Shepherd et al., 2018; Baldissera Pacchetti et al., 2023; Baulenas et al., 2023). We identify 31 future storms exceeding the severity of windstorm Xaver (Section 4.2.4), downscale them with MAR (Gallée et al., 1994) over 25 continuous simulation windows, and use the resulting fields to force SLIM. Screening the simulated response then re-admits 34 more localized surge episodes (Section 4.2.4), yielding a panel of 65 surge events. Each event is characterised by the magnitude, duration, intensity and shape of its surge and drawdown hydrographs, and by their timing relative to the tide, at 26 gauges from the open sea to Antwerp.

The chapter thus describes the response of the continuum to a set of plausible extreme storms; it does not project how this response evolves over the century. For the same reason, since the tidal phase at which a storm arrives is arbitrary in the panel, the timing relative to the tide is used to test the tide–surge interaction of the model chain rather than to project a future change.

4.2 Material and Methods

4.2.1 Area of interest

The model domain covers the Scheldt Estuary and the adjacent North Sea, extending offshore to the edge of the continental shelf—its northern open boundary following the 200 m isobath—and south-westward into the English Channel (Fig. 4.1). The mesh design, bathymetry, bottom friction and validation of this configuration are those of the baseline model presented in Chapter 2; only the elements specific to the storyline set-up are presented here.

The atmospheric forcing driving the hydrodynamic simulations is provided by MAR over a larger domain (Fig. 4.1a), extending further north and west than the SLIM domain. This larger extent allows the regional atmospheric model to spin up its own mesoscale dynamics upstream of the area of interest, rather than inheriting boundary artefacts directly at the North Sea coast. Rivers draining into the southern North Sea and into the Scheldt outside the estuary itself (Fig. 4.1a) are included as boundary inputs only, prescribed as present-day climatological monthly means rather than as explicitly resolved reaches.

4.2.2 Storyline rationale

The representation of future windstorms follows a physical climate storyline (PCS) approach (Shepherd et al., 2018). A storyline is a self-consistent, physically plausible unfolding of a weather or climate event, increasingly used as an alternative to probabilistic projection for investigating plausible high-end scenarios (Sillmann et al., 2021). The approach is closely related to scenario analysis as used across disciplines to expose the vulnerabilities of a system under plausible alternative conditions; the term storyline is preferred here because scenario is reserved in climate science for emission trajectories. Although positive and negative surges are often treated separately, they are two responses of the same forcing: the wind-and-pressure field that raises water at the coast on one flank of a depression lowers it on the other. The storms are therefore selected once, on their atmospheric severity, and their

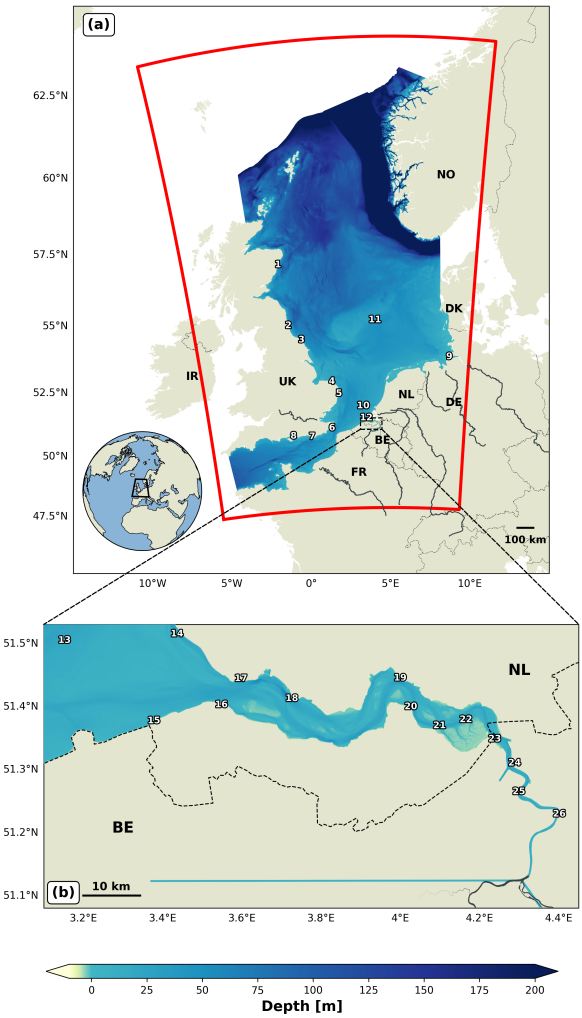

Figure 4.1: Map of the study domain. **(a)** Bathymetry of the discretised domain used in SLIM (colour scale), with the red outline indicating the larger domain used for the atmospheric model MAR. Grey lines show rivers draining into the North Sea, included in the model as boundary inputs. The black box in the inset globe indicates the extent of panel (a). **(b)** Close-up view of the Scheldt Estuary; grey lines show the Scheldt and its tributaries in the upstream region. Numbered markers denote the stations used, (1)–(12) in panel (a) and (13)–(26) in panel (b): (1) Aberdeen, (2) North Shields, (3) Whitby, (4) Cromer, (5) Lowestoft, (6) Dover, (7) Newhaven, (8) Portsmouth, (9) Cuxhaven, (10) Euro Platform, (11) Platform F-16, (12) Lichteiland Goeree, (13) Vlakte van de Raan, (14) Westkapelle, (15) Cadzand, (16) Breskens Veerhaven, (17) Vlissingen, (18) Gat van Borssele, (19) Hansweert, (20) Walsoorden, (21) Baalhoek, (22) Schaar van de Noord, (23) Prosperpolder, (24) Fort Liefkenshoek, (25) Kallosluis Schelde, (26) Antwerpen Loodsgebouw.

surge is interrogated for both signs — the negative surges analysed here are those produced by the same track-diverse set of events selected for their positive-surge potential, rather than a separately assembled catalogue.

The storyline varies a single factor, the atmospheric forcing consistent with the driving ESM, and holds the global-mean sea level, the bathymetry and the bottom friction at their present-day values (Section 4.2.4). Three reasons motivate this choice. First, it isolates the contribution of future storms, which remains unknown along the Scheldt, whereas the effects of sea-level rise on the estuary have already been modelled (Röbke et al., 2025; Broekx et al., 2011). Second, the events of the panel span 2033–2096: adding the global-mean rise would give each event a different baseline, rising over the century, and the comparisons between zones, track types and decades would mix this rise with the response to the storm. Third, raising the mean level on the present-day bathymetry, without the morphological adjustment of the intertidal flats and marshes, would not be self-consistent either. The surge residual is therefore read as the atmospheric contribution on the present-day mean sea level. To first order, the rise adds to it; the interactions between mean sea level, tide and surge, which reach about 10 to 15 cm on the European shelf, are discussed in Section 4.4.5.

4.2.3 Climate scenario

Future conditions are taken from the Shared Socioeconomic Pathway (SSP) SSP3-7.0 of CMIP6 (IPCC, 2021), a medium-to-high pathway reaching a radiative forcing of $7.0\,\mathrm{W\,m^{-2}}$ and a global-mean warming of about 3.6 °C by 2100. The scenario serves here only to provide physically plausible extreme storms. A high-end pathway suits a study of the upper envelope of plausible surge hazard (Harrison et al., 2019), and SSP3-7.0 is preferred to SSP5-8.5, increasingly regarded as less plausible for near-term emissions (Shiogama et al., 2023; Hausfather et al., 2020). Its "regional rivalry" narrative is discussed in Section 4.4.6.

4.2.4 Modelling chain

The modelling chain links global climate projections to estuarine-scale surge dynamics through four sequential steps (Fig. 4.2). First, an existing multi-decadal ensemble of the regional atmospheric model MAR (v3.14; Grailet et al. 2025; Brajkovic et al. 2025) is analysed both to select a driving CMIP6 ESM and to detect candidate future storms (Step 1). Following Brajkovic et al. (2025), we refer to the six driving models of this ensemble as CMIP6 Earth System Models (ESMs); only their physical atmospheric fields enter the chain.

Second, the selected ESM drives a dedicated MAR run over the full Scheldt–North Sea domain—which the original Belgium-centred ensemble does not resolve—producing the 5 km surface wind and sea-level-pressure fields for each retained storm (Step 2). These fields are then imposed as surface forcing on SLIM, which resolves the resulting surges across the continuum (Step 3). Finally, the simulated surge residuals are screened post hoc to include additional surge episodes that the atmospheric detection missed (Step 4; Section 4.2.4).

Regional climate-impact studies select driving ESMs beforehand for two reasons. Firstly, individual CMIP6 models vary widely in how well they capture historical storm tracks. Secondly, downscaling cannot correct a parent model with biased circulation. The regional model simply inherits the large-scale flow at its boundaries. The driving ESM is therefore selected on its demonstrated fidelity to the observed extreme-tail climatology at the location of interest (Step 1.1), consistent with the model-screening step routinely applied in EURO-CORDEX-based impact assessments (Sobolowski et al., 2023).

The atmospheric detection of Section 4.2.4 does not decide on its own which events enter the panel. Its severity threshold is anchored to a physical reference event, windstorm Xaver (2013), rather than to a return period estimated from a short historical record (Horsburgh et al., 2021), but wind and pressure at a single point are an imperfect proxy for the basin-integrated surge response (Befort et al., 2015). Basin-scale coherence is therefore screened separately (stage **(iii)**), and surge episodes identified directly from the simulated response are re-admitted (Section 4.2.4). This response-first logic follows Nguyen et al. (2025), and reflects the fact that event-based and response-based approaches can rank the same storms differently (Sanuy et al., 2020).

Step 1.1: ESM selection

ESM selection starts from an existing MAR ensemble, from which a single driving ESM is retained on its historical-climatology fidelity. The wind-speed and sea-level-pressure fields used for ESM selection and event detection are drawn from the long-term MAR ensemble originally produced for a study of extreme precipitation over Belgium (Brajkovic et al., 2025). It comprises six MAR-ESM runs (1980–2100), i.e. MAR driven by six distinct CMIP6 ESMs, together with the reference run MAR-ERA5 (1980–2010); all runs are performed at 5 km horizontal resolution and follow the EURO-CORDEX recommendations (Sobolowski et al., 2023). Each run is named after its driving ESM: MAR-EC3, for instance, denotes MAR driven at its lateral boundaries by EC-Earth3-Veg (Table 4.1).

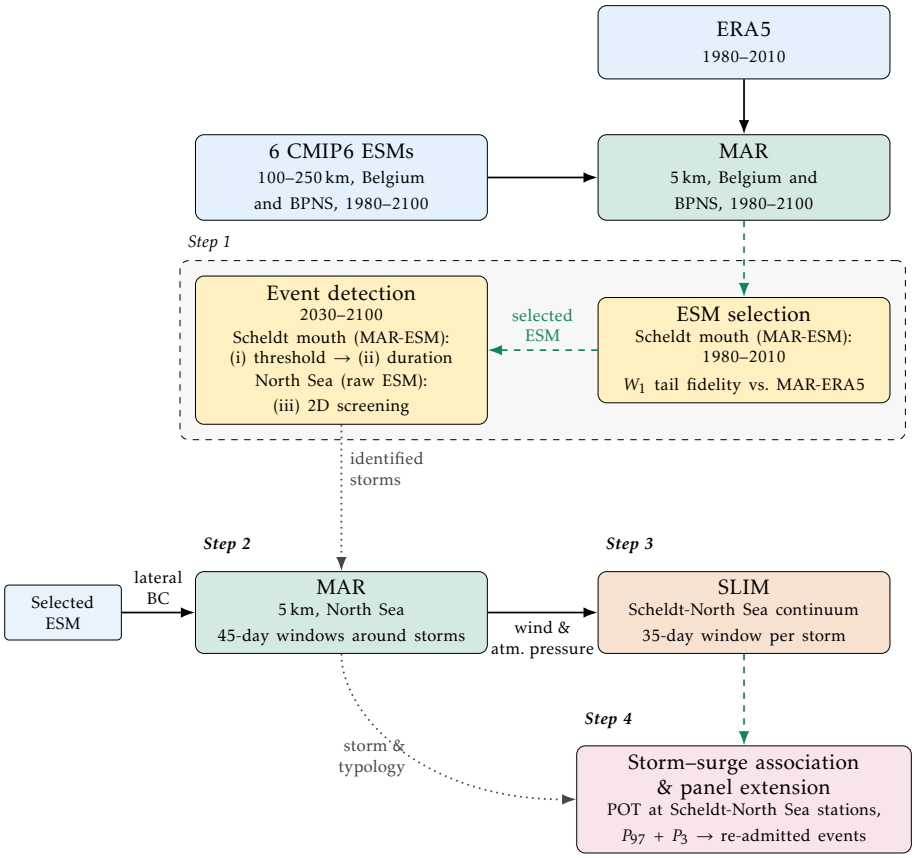

Figure 4.2: Flow chart of the atmospheric models and their outputs, from the CMIP6 ensemble and ERA5 (blue) to the MAR atmospheric forcing used by the hydrodynamic model SLIM (orange), and onward to the storm–surge association (pink). **Step 1** (dashed box) first selects a driving ESM (right yellow box) from a tail-fidelity analysis of the MAR-ESM runs at the Scheldt-mouth point, using the existing Belgium and Belgian Part of North Sea (BPNS) MAR ensemble, then detects candidate storms through a three-stage pipeline (left yellow box); selection and stages (i)–(ii) use the MAR-ESM fields at the Scheldt-mouth point, stage (iii) extends to the North Sea scale using the raw, un-downscaled fields of the selected ESM. **Step 2** re-runs MAR over the full North Sea basin at $5\,\mathrm{km}$, driven at its lateral boundaries by the selected ESM, for 45-day windows around the retained storms. **Step 3** forces SLIM with the resulting $10\,\mathrm{m}$ wind and sea-level-pressure fields over a 35-day window. **Step 4** applies a peaks-over-threshold criterion to the surge residual (P_{97} and P_3) to identify additional surge events and add them to the panel, then classify each event, through the track of its depression, into distinct typologies. Solid arrows denote model forcing at the boundaries (ESM → MAR, ERA5 → MAR, MAR → SLIM); dashed teal arrows denote analysis or post-processing; the dotted grey arrow denotes transmission of the identified storm list (Step 1 → Step 2).

Their transient climate response (TCR; Table 4.1) ranges from 1.33 K for MAR-NOR to 2.62 K for MAR-EC3; it is reported only to show the diversity of the ensemble, the driving ESM being selected on its historical fidelity.

Table 4.1: The six CMIP6 ESMs (ensemble member r1i1p1f1) used to force MAR at its lateral boundaries in Brajkovic et al. (2025), with their native atmospheric horizontal resolution, transient climate response (TCR), and the acronym used here for the corresponding MAR-ESM run. ERA5, which provides the present-day reference run (MAR-ERA5), is listed for comparison.

ESM	Native horiz. res. (km)	TCR (K)	MAR-ESM run
MIROC6	∼250	1.55	MAR-MIR
NorESM2-MM	∼100	1.33	MAR-NOR
MPI-ESM-1-2-HR	∼100	1.66	MAR-MPI
EC-Earth3-Veg	∼100	2.62	MAR-EC3
CMCC-CM2-SR5	∼100	2.09	MAR-CMC
IPSL-CM6A-LR	∼250	2.32	MAR-IPL
ERA5	∼31	—	MAR-ERA5

The ESM retained to force MAR for the future simulations is the one whose MAR downscaling best reproduces the statistical climate of MAR-ERA5 over the historical period (1980–2010), evaluated at a point near the mouth of the Scheldt (3.45° E, 51.45° N) for 10 m wind speed and sea-level pressure. The comparison is made between two downscaled products of identical resolution—a given MAR-ESM and MAR-ERA5—to isolate the fidelity of the driving ESM from that of the downscaling configuration. It relies on a distributional comparison, which measures agreement across all statistical moments in the variable's physical units (Vissio et al., 2020), with emphasis on the distribution tails since the application targets extremes.

Tail fidelity is quantified with the first-order Wasserstein distance,

$$W_1 = \int_0^1 \left| F^{-1}_{\mathrm{ESM}}(q) - F^{-1}_{\mathrm{ERA5}}(q) \right| \mathrm{d}q,$$

where F^{-1} is the quantile function and q the quantile level. Consistent with the relative thresholds used in the projections and with the peaks-over-threshold (POT) framework (Coles, 2001), W_1 is evaluated on the exceedances above each series' own P99 for wind speed and below its own P1 for pressure. These two tails are targeted because extreme surges arise from the combination of strong winds and deep low-pressure systems.

The six MAR-ESM runs are also compared with MAR-ERA5 over the full distribution, with four metrics per variable (Table 4.3), computed against MAR-ERA5 over 1980–2010 for 10 m wind speed and sea-level pressure. For each variable, $\Delta\mu = \bar{x}_{\text{model}} - \bar{x}_{\text{ERA5}}$ is the mean bias; $D = \sup_x |F_{\text{model}}(x) - F_{\text{ERA5}}(x)|$ is the Kolmogorov–Smirnov statistic, the maximum absolute difference between the two empirical cumulative distributions; and $S = \sum_i \min\left(Z_{\text{model},i}, Z_{\text{ERA5},i}\right)$ is the Perkins Skill Score, the cumulative overlap between the two histograms over shared bins i (equal to 1 for identical distributions and to 0 for fully disjoint ones). W_1^{P99} and W_1^{P1} are the first-order Wasserstein distances defined above, evaluated on the model and reference peaks-over-threshold exceedances above the wind P99 and below the pressure P1, respectively — the quantities plotted in Fig. 4.5.

For each metric the simulations are ranked relative to one another (by increasing $|\Delta\mu|$, D and W_1, and by decreasing S); the final rank is the ordinal of the mean of these per-metric ranks, so that it rewards balanced performance across both variables and can be reproduced directly from the table. This rank-averaging assigns equal weight to every metric and is purely ordinal, expressing relative standing within the ensemble rather than an absolute level of skill.

Step 1.2: Identification of future extreme events

The detection starts from a single point because the existing MAR ensemble covers only Belgium and the Belgian part of the North Sea and therefore provides no basin-wide fields at 5 km: the first two stages are evaluated at an offshore reference point at the Scheldt mouth (3.45° E, 51.45° N). Two elements then bring in basin-scale information: the coherence of the wind field over the whole North Sea, evaluated on the fields of the driving ESM (stage iii), and the surge response simulated at the 26 stations of the domain, which re-admits additional episodes (Step 4). The three stages of the atmospheric detection are described below.

(i) Point-scale threshold detection. Future extreme-wind candidates are identified from the hourly 10 m wind-speed and sea-level-pressure series of the selected MAR-ESM at the Scheldt-mouth point (3.45° E, 51.45° N). Using the ERA5 reference over 1980–2010, the severe windstorm Xaver (4–7 December 2013) was characterised by its peak wind speed, which corresponds to approximately four standard deviations above the historical mean and about 1.26 times the 99th percentile (P99) of the historical distribution of the hourly wind speed. These severity ratios were transferred to each simulation: a timestep was identified as extreme when its wind speed simultaneously exceeded four

standard deviations above the model's historical mean and 1.26 × P99 of the model's historical distribution at the Scheldt-mouth point. The factor 1.26 is not a tunable parameter but an empirical measurement: it is the ratio of Xaver's observed peak 10 m wind speed to the P99 of the ERA5 1980–2010 distribution at the reference point. Transferring this ratio—rather than the absolute wind speed—to each model's own historical distribution anchors "extreme" to a fixed physical severity relative to each model's own climatology, so that a model running systematically windy or calm is held to its own P99 scaled by the same Xaver factor. This neutralises inter-model wind biases. A secondary low-pressure condition ($p <$ P1, Xaver-scaled) confirms that each wind extreme is embedded in a genuine synoptic low; being rarely binding (removing fewer than 2% of the wind-selected hours), it serves a diagnostic rather than a selective role.

(ii) Point-scale duration screen. Events identified at stage **(i)** are clustered in time, and a candidate is retained only if the Scheldt-mouth wind speed stays above the extreme threshold (stage **(i)**) for at least 3 h. This is a lower bound on the forcing duration required to drive a fully developed surge, following the 3 h to 4 h minimum reported by Reef et al. (2018) in the Wadden Sea, a semi-enclosed North Sea basin under a Xaver-like storm. We adopt a deliberately conservative form of this criterion: the forcing duration is the contiguous time spent above the extreme wind threshold (1.26 × P99), a stricter measure than the wind-stress-envelope event duration of Reef et al. (2018).

(iii) Basin-scale coherence screening. Because point-scale criteria cannot guarantee the synoptic development of a windstorm, candidates are evaluated for spatiotemporal coherence over the full North Sea basin using the raw ESM fields, whose domain—unlike that of the Belgium and BPNS MAR ensemble—covers the entire basin. A candidate is retained only if its storm system completes a full transit of the basin: the track must enter, cross, and exit the North Sea domain while maintaining a contiguous extreme-wind footprint (wind speed above 25 m s^{-1} sustained for at least 2 h) (Fenoglio-Marc et al., 2015). This screening is applied *before* any hydrodynamic simulation, and the full-transit requirement acts as an a-priori kinematic proxy for the sustained, basin-wide momentum transfer that surge generation requires. Storms that stall within the basin, remain locally confined, or complete only a partial transit—however intense at the Scheldt-mouth point—are discarded at this stage, at the cost of excluding configurations that could nonetheless force a short-lived or spatially confined surge; that cost is

discussed in Section 4.4.6. The criterion was also designed with the track classification of Section 4.2.5 in mind. That classification identifies a storm by the latitude at which its track crosses the 8°E meridian; a storm that crosses the whole basin reaches this meridian, whereas a storm that stalls or remains confined may never reach it and would have no class. The typology itself is assigned to the retained tracks after the selection, but the transit requirement ensures that it is defined for all of them.

Application to historical storms. We apply stages **(i)**–**(ii)** to the MAR-ERA5 series over 1980–2010, using the ten most severe windstorms of the Extreme Wind Storms (XWS) catalogue (Roberts et al., 2014) as a reference. The method captures nine of these ten storms: Jeanett, Kyrill, Daria, Vivian, the Great Storm of 1987, and the storms of November 1984, December 1993, and 13 and 23 January 1993. Their peak wind speed ranges from 20.8 to 24.6 $\mathrm{m\,s^{-1}}$, above the 20.1 $\mathrm{m\,s^{-1}}$ threshold, which they exceed for 3 to 10 h. Only Anatol (December 1999), which mainly struck Denmark, is missed: its wind speed reaches 19.4 $\mathrm{m\,s^{-1}}$ at the Scheldt mouth. Stage **(iii)** is not evaluated here because it requires basin-wide fields. The criteria also hold beyond the reference period and beyond windstorms. Applied to major surge storms of the southern North Sea over 1940–2023, with the same thresholds, they retain the 1953 flood, the reference event for coastal defence in the region (Gerritsen, 2005), with 5 h above the threshold, the storm of January 1976 (3 h) and the windstorms Ciara (2020) and Eunice (2022). Calibrated on a single storm, the thresholds thus retain independent severe storms over eight decades. Two storms are not retained. For Britta (2006), this is consistent with the focus of the panel: its surge peaked on the coast between the northern Netherlands and Germany (Kettle, 2018) and remained moderate at the Scheldt mouth. Tilo (2007) is a genuine miss: it produced at Vlissingen the sixteenth highest water level since 1900 (Rijkswaterstaat, 2007), while the winds at the Scheldt mouth stayed below the threshold, a configuration discussed in Section 4.4.6.

Step 2: High-resolution MAR simulation

The events retained in step 1 are re-simulated with MAR at 5 km over the full Scheldt–North Sea domain (Fig. 4.1), an extent that the Belgium-centred ensemble of Section 4.2.4 does not cover. The two runs share the same 5 km horizontal resolution, the same driving ESM and the same downscaling configuration, and differ only in the geographical extent of the integration domain. Around each retained windstorm event, a 45-day MAR window is simulated, of which the first 10 days serve as atmospheric spin-up. The

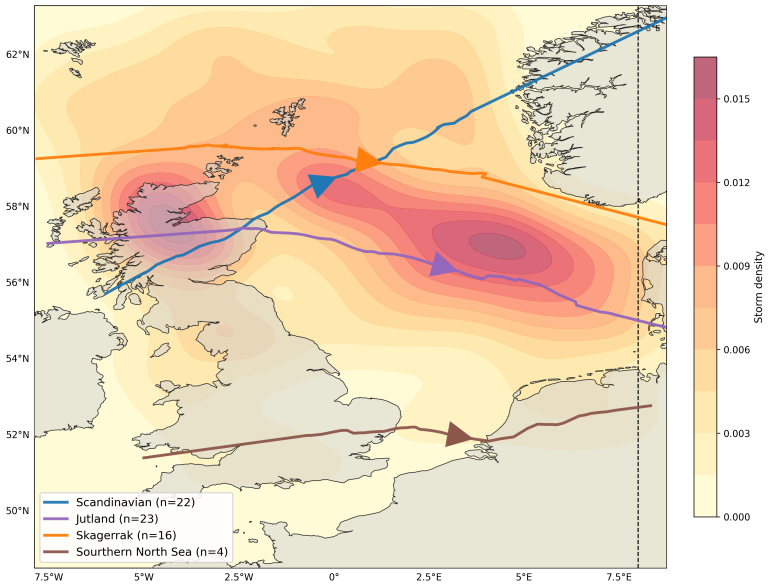

Figure 4.3: Mean storm track per typology over the North Sea basin for the 65 surge events of the panel ($n = 22$ Scandinavian, $n = 23$ Jutland, $n = 16$ Skagerrak, $n = 4$ Southern North Sea), overlaid on the kernel density estimate of tracks. The dashed vertical line marks the 8 °E meridian used by Prügel (1942), Petersen et al. (1991), and Meyer et al. (2023) to define storm typologies. Tracks do not reach the figure boundary because of the extent of the MAR domain shown in Fig. 4.1a.

MAR simulations provide hourly outputs, and the 10 m wind and sea-level-pressure fields are used to force the hydrodynamic model.

Step 3: Hydrodynamic simulation

The hydrodynamic processes of the region are simulated with SLIM in its 2D depth-integrated configuration with the WD and GPU configuration (Lambrechts et al., 2008; De Le Court et al., 2026) (Chapter 2). Each simulated window spans 35 days: the first five days are treated as spin-up and excluded from analysis, and the hydrodynamic run itself starts once the atmospheric forcing has completed its own ten-day spin-up.

The 10 m wind and sea-level-pressure fields produced by the dedicated MAR run (Section 4.2.4) are imposed at the free surface. The wind drives a surface stress following the piecewise drag formulation of Flather (1976), while the atmospheric-pressure gradient is used directly in the momentum

equations. Both the wind-setup and inverse-barometer contributions to the surge are thereby represented in the hydrodynamic model, the two mechanisms that drive storm-surge generation in this shallow, semi-enclosed basin.

At the open lateral boundaries, SLIM applies a Flather condition, prescribing the external sea-surface elevation and normal velocity to propagate in the domain (Carter et al., 2007). The elevation combines the astronomical tide, 21 constituents from the OSU TPXO9.5 global tidal model Atlas (1/30° resolution; Egbert et al. 1994) — with the monthly-mean sea-surface height, which like depth-averaged residual currents is obtained from the ESM provided through CMIP6, i.e. the regional dynamic sea level (the CMIP6 **`zos`** field, whose global mean is zero by construction; Gregory et al. 2019). Taking elevation and velocity consistently from the same ESM keeps the boundary dynamically coherent and carries the slow evolution of regional sea level landward up to the estuaries within the domain.

By contrast, the global-mean thermosteric component of sea-level rise (**`zostoga`**) is not added, and shoreline geometry, bathymetry and the Manning coefficient are held at their present-day values (Chapter 2). This design focuses the analysis on the response to the ESM-consistent atmospheric forcing and regional ocean state, in line with the storyline logic of Section 4.2.2. The quantity analysed is therefore the surge residual, not the total water level; what adding the global-mean rise would change is discussed in Section 4.4.5.

River inflow at the upstream boundaries of Scheldt and other river mouths in the North Sea are prescribed from climatological monthly means.

Step 4: Storm–surge association and panel extension

The final step of the modelling chain links the detected storms to their simulated hydrodynamic response. For each event retained through stages **(i)**–**(iii)**, SLIM's outputs (Section 4.2.4) are associated with the corresponding storm record, joining the typology assigned in Section 4.2.5 to the surge residual computed at every station (Section 4.2.6).

This joined dataset is then screened for additional surge events that the atmospheric criteria do not capture. Because stages **(i)**–**(iii)** retain events on point-scale wind and pressure alone, they can overlook episodes whose forcing falls short of the extreme-wind threshold at the Scheldt mouth yet still drives a locally significant surge. Two cases arise. In the first, a secondary low develops within the simulation window of a retained storm without itself clearing the point-scale threshold. In the second, the wind speed sampled at the single Scheldt-mouth point understates the forcing integrated over the

basin, so that a storm producing a substantial surge elsewhere in the domain fails the point-scale criteria altogether (Befort et al., 2015).

Following the storyline principle that inclusion is governed by simulated surge response rather than atmospheric rarity (Section 4.2.2), a peaks-over-threshold approach is applied directly to the surge residual $r(t)$ at each station. Episodes whose station-specific residual exceeds the local 97th percentile (r_{p97}) or falls below the local 3rd percentile (r_{p3}) — both computed over the full set of simulations — are flagged as additional positive or negative surge events and re-admitted to the panel, even when the originating storm does not clear stages **(i)**–**(iii)**. Because these episodes lie within simulation windows already available in Step 3, the extension requires no further MAR or SLIM runs.

Every re-admitted episode is attributed to the depression that drives it and classified on its own track: the depression driving it is identified in the ESM fields, its trajectory across the basin is extracted, and the same 8°E crossing criterion is applied as to the atmospherically detected events (Section 4.2.5). We call *surge event* a simulated surge episode together with the track of the depression that drives it, and *panel* the 65 surge events retained: 31 produced by the detected storms and 34 re-admitted from the simulated response. The panel is the unit of all the analyses that follow.

4.2.5 Storm track typology

Over the past decades, several storm classification schemes based on cyclone tracks have been proposed and discussed in the literature (e.g., Prügel, 1942; Petersen et al., 1991; Gerber et al., 2016). Broadly, the storm events that drive the storm-tide hazard in the southern North Sea fall into two main groups: a North-West (or Scandinavia) type and a West to South-West (or Jutland) type.

The retained events are classified into four storm typologies according to the track of the storm across the North Sea basin. The first three follow the classical scheme introduced by Prügel (1942) and later formalised by Petersen et al. (1991), applied since in North Sea storm-surge studies (Meyer et al., 2023). This scheme distinguishes storms by the latitude at which their track crosses the meridian 8°E:

- the **Jutland** type (55°–57°N);
- the **Skagerrak** type (57°–60°N);
- the **Scandinavian** type (60°–65°N).

For the present study a fourth class is added: the **Southern North Sea** type, comprising storms crossing the meridian near 52°N, south of the Jutland band, which approach the Scheldt from the west rather than transiting north

of the basin. The addition extends the classifying variable rather than the scheme: these storms have a well-defined 8°E crossing latitude, which simply falls below the range covered by Petersen et al. (1991), whose three bands were calibrated on the German Bight, some 4° of latitude further north. The class is small — four events of the sixty-five — and is retained for attribution rather than for statistical power: assigning these storms to the nearest band would credit the Jutland type with an approach geometry that is not its own, and would do so in the comparisons where the typology carries its only significant contrast (Section 4.3.4).

The typology discretises what is fundamentally a continuous track geometry. Each retained track is therefore also reduced to five scalar descriptors, listed in the event catalogue: the net zonal displacement Δlon and net meridional displacement Δlat — the signed longitude and latitude differences between the final and initial positions of the track over its North Sea transit (eastward and northward positive), so that a storm curving back on itself carries a small net displacement regardless of the path length travelled — together with the track-onset latitude φ_0, the mean track latitude, and the basin-transit duration (Table 6.3.3).

4.2.6 Surge metrics

Stations. The hydrodynamic response to each of the atmospheric events is characterised at the 26 gauges of Fig. 4.1, grouped into two analytical zones. The zones are defined geographically. A Scheldt zone gathers the 14 gauges of the estuary and its mouth, from Vlakte van de Raan to Antwerpen Loodsgebouw (gauges 13–26), and samples the estuarine response along the tidal river. An open North Sea zone gathers 11 coastal and offshore gauges of the shelf, along the British coast from Aberdeen to Portsmouth and on the Dutch shelf (gauges 1–12 except Cuxhaven), and samples the open-shelf, pre-estuarine response. Comparing the two zones therefore measures how the estuary modifies the surge it receives from the shelf. Cuxhaven is retained in the dataset but assigned to neither zone: located at the mouth of the Elbe, it carries that estuary's own amplification and cannot serve as an open-shelf baseline; including it changes the results, as shown in Appendix 6.3.4.

The simulated future hydrographs cannot be compared with observations. They are therefore read at the gauges where the model chain was evaluated against the observed water levels of Storm Xaver (Chapter 3), so that the metrics are read where its skill under storm conditions is documented. This plays the role that observed records play in hydrograph analyses of historical events (Pupic Vurilj et al., 2025), and that validation plays when hydrographs are built from model hindcasts (Dullaart et al., 2023). They cover the continuum from the open shelf to the head of the estuary, with 14 gauges in

the Scheldt, but sample the rest of the basin unevenly, the German Bight being represented by Cuxhaven alone; the North Sea zone is therefore an open-sea reference for the Scheldt rather than a sample of the whole basin.

Tide and surge residual. As in recent analyses of non-tidal residuals along the Dutch coast (Pupic Vurilj et al., 2025), we separate the simulated total water level at each station and for each event into an astronomical tide, obtained by harmonic analysis with UTide (Codiga, 2011), and a surge residual $r(t)$, on which we focus. In a macrotidal setting, this residual includes the meteorological surge and part of its interaction with the tide (Section 1.2); the skew surge, computed alongside it, is less sensitive to this interaction (Williams et al., 2016). The aim is to compare the events with one another, through the characteristics of the surge they drive, and the residual puts all events and track types on a common basis. Total water levels, which ultimately determine flooding, are therefore not addressed here (Section 4.4.5). Unlike these studies, the thresholds that delimit surge and drawdown are computed over the simulated panel rather than over a continuous record, so the hydrograph descriptors compare the events of the panel with one another and do not give their frequency of occurrence.

The astronomical tide is prescribed at the open boundary for the model dates, whereas the atmospheric forcing comes from a free-running climate simulation whose dates do not correspond to actual weather. The tidal phase at which a simulated storm passes is therefore arbitrary, and the simulated total water levels cannot be interpreted as such. We keep the tide in the simulations because it controls the depth, friction and wetting and drying through which the surge propagates in this macrotidal estuary (Prandle et al., 1978; Horsburgh et al., 2007; Familkhalili et al., 2020; Smolders et al., 2015), but we analyse only the surge residual, not total water levels (Section 4.4.5). The timing of the surge relative to the tide is used only as a diagnostic of tide–surge interaction (Section 4.2.6): because the tidal phase at which a storm arrives is arbitrary, a systematic clustering of surge peaks at one tidal phase reflects the interaction rather than a chance coincidence of storm and tide.

Event windows. Here, the surge hydrograph denotes the simulated time series of the surge residual $r(t)$ at a station during an event, and the drawdown hydrograph its negative part. The term is used in the same sense for observed non-tidal residuals (Pupic Vurilj et al., 2025) and for modelled surge and storm-tide series (Dullaart et al., 2023). To describe the whole surge hydrograph rather than its extremes alone, each of the 65 events is given an analysis window at every gauge. Following Pupic Vurilj et al. (2025), who delimit observed surge events with a low threshold to capture their full

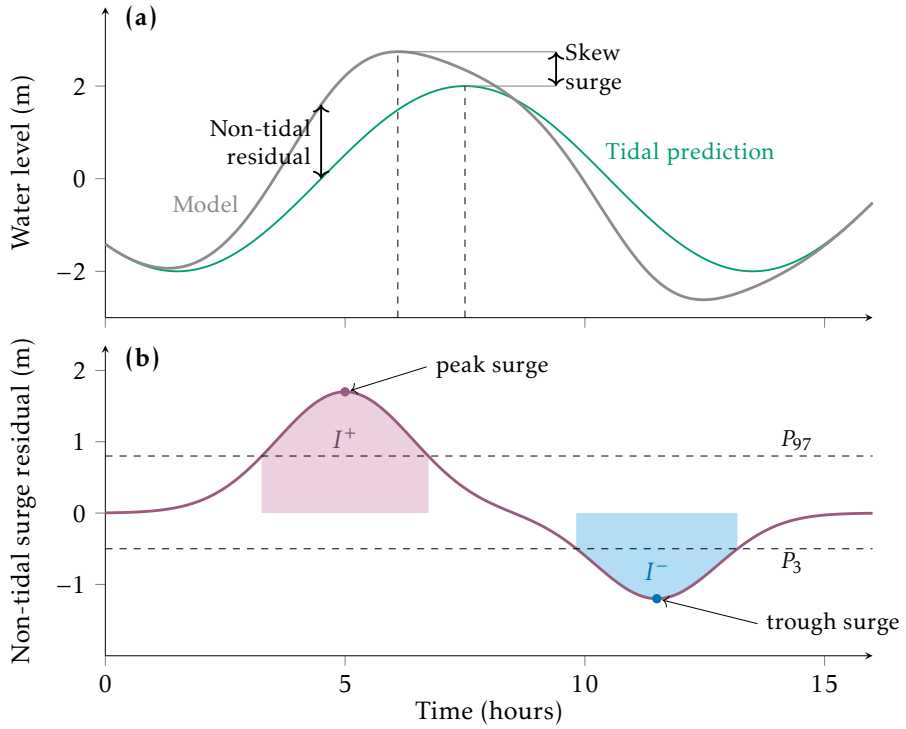

Figure 4.4: Schematic definition of the surge metrics (Section 4.2.6). **(a)** Modelled total water level versus predicted tide, showing the instantaneous residual and the skew surge (height difference of the paired extremes). **(b)** Non-tidal surge residual with peak/trough surge, the r_{P97}/r_{P3} thresholds, and the cumulative intensities I^+/I^- shaded in color.

development, the window starts 12 h before the start of the event and ends 48 h after its end. It is then extended by up to 48 h on either side, until the 12-hour running mean of the residual returns between its 30th and 70th percentiles. When two events follow each other closely, each hour is attributed to the nearer event, so that the windows of consecutive events do not overlap; when two simulation windows overlap in time, each hour is taken from the simulation in which it lies furthest from the window edges, so that no event is counted twice. The resulting windows last 77 h in median (interquartile range 62 h to 91 h).

Event metrics. Three metrics are computed for each event (Fig. 4.4) which are defined as:

- the **surge amplitude**: the extreme value of the surge residual $r(t)$ during the event — its maximum $r^{+}_{\max}$ for positive surges (peak), its minimum $r^{-}_{\min}$ for negative surges (trough) (m).
- the **skew surge**: for each tidal cycle, the difference between the simulated extreme water level and the nearest predicted astronomical extreme (high water for positive surges, low water for negative), aggregated over the event as the largest such difference (m).
- the **cumulative surge intensity**: the time integral of the surge residual's exceedance over the station-specific P97/P3 thresholds,

$$I^{+} = \int_{r(t)>r_{P97}} r(t)\,\mathrm{d}t, \qquad I^{-} = \int_{r(t)<r_{P3}} r(t)\,\mathrm{d}t,$$

  where r_{P97} and r_{P3} are the 97th and 3rd percentiles of the surge residual $r(t)$ over the full simulated period (m h). I^{+} is positive and I^{-} negative, by the sign of the residual they integrate.

Hydrograph descriptors. Within each window, the metrics above are complemented by three descriptors. The **duration** of the surge and of the drawdown is the time spent above r_{P97} and below r_{P3}. The **number of distinct surges** counts the separate exceedances of r_{P97}, two exceedances less than 12 h apart — one tidal cycle — being merged into one; distinct drawdowns are counted likewise below r_{P3}. The **phase** of the surge peak is the time between the maximum of the residual and the nearest predicted high water, and the phase of the trough the time between the minimum of the residual and the nearest predicted low water; both are negative when the extreme of the residual precedes the tidal extreme, as in Pupic Vurilj et al. (2025). Tidal extremes are taken from the harmonic prediction of Section 4.2.6.

Each hydrograph is finally assigned to one of six shape classes (Table 4.2). The classes follow explicit rules rather than a clustering, because 65 events are too few for a stable unsupervised classification: applied to this panel, the clustering of Pupic Vurilj et al. (2025) groups each event with itself at neighbouring gauges rather than with other events.

4.2.7 Statistical analysis

We test several hypotheses on our panel of events (overview in Table 6.3.1, Appendix 6.3.1). All analyses below operate on the panel assembled in

Table 4.2: Hydrograph shape classes, assigned to each event at each gauge from the exceedances of r_{P97} (surge) and r_{P3} (drawdown) within its window (Section 4.2.6). When both thresholds are crossed, the order of the maximum and the minimum of the residual sets the class. The classes do not involve the tidal phase, which is described separately (Section 4.3.6).

Class	Hydrograph
S1	a single surge above r_{P97}, no drawdown below r_{P3}
S2	two or more distinct surges, no drawdown
SD	a surge followed by a drawdown
DS	a drawdown followed by a surge
D	a drawdown only
M	moderate: neither threshold is crossed

Sections 4.2.4–4.2.4. Since every event was retained because it was extreme, the panel is not a random sample of future storms, and the storyline framing claims physical plausibility for each event rather than statistical representativeness of an ensemble (Shepherd et al., 2018). The significance tests are therefore not inferences about the future storm climate: they establish whether a contrast observed within the panel is systematic across the 65 events or carried by a handful of influential ones. Throughout this chapter, "significant" means robust within the panel, and the transfer of a result to the future climate rests on the physical plausibility claimed by the storyline framing, not on the p-values.

Three choices follow this. Because the metrics are not expected to be normally distributed within a small group, and normality could not be tested on the set of events for the same reason, non-parametric tests are used. All thresholds and percentiles are defined relative to the panel rather than to an unconditioned climatology (Section 4.4.6). And $\alpha = 0.05$ is used, with $0.05 < p < 0.10$ reported as marginal.

Two reductions of the panel are used. Event-level statistics take the worst-affected gauge per event, evaluated separately for each metric — the gauge carrying the deepest trough need not be the one carrying the highest peak. Zone contrasts instead pool the per-event values of every station in a zone, Scheldt estuary compared against North Sea. Because neighbouring stations record the same surge wave, the p-values of these zone contrasts describe the panel rather than give exact probabilities.

The statistical analysis can be described as:

- **Mann–Whitney** (U) asks whether the values of one group tend to rank above those of another, and is used here to test whether the estuary

responds more strongly than the open sea; it returns the direction of the contrast but says nothing about its size, which is why the difference of zone medians is reported alongside it.

- **Kruskal–Wallis (KW)** extends the same question as Mann–Whitney to more than two groups and is used to test whether the four track typologies produce different surges; a significant result establishes only *that* they differ, not *which* pair does; where it is significant, pairwise Mann–Whitney comparisons locate the contrast.

Holm's correction limits spurious results among the six pairwise typology contrasts of each metric. Exploratory century-scale tests on the order of the events are described and reported in Appendix 6.3.3; they are not used in the Results.

The hydrograph descriptors of Section 4.2.6 are analysed descriptively, without significance tests. To avoid counting an event once per gauge, each event contributes one value per zone: the median over the gauges of that zone for durations and intensities, and the class found at most gauges for the hydrograph shape. This zone class departs from Pupic Vurilj et al. (2025), who classify the hydrographs of each station separately, report the prevalence of each type per station, and count an event once per type when its peaks at different stations fall within two days of each other. With 65 events rather than several thousand, we instead summarise each event by one class per zone, so that the track types can be compared. For the hydrograph shape, the class of an event in a zone is the most frequent class among the gauges of that zone, which does not require a majority of the gauges. When two classes are found at the same number of gauges, which happens for 3 of the 65 events in the North Sea and 5 in the Scheldt, the class listed first in Table 4.2 is retained; this order favours a surge over a drawdown, and any threshold crossing over the moderate class M. A class M in a zone therefore means that most gauges of the zone cross neither threshold, not that none does. To show how well the class of a zone represents its gauges, we report the fraction of gauges that carry it (Section 4.3.5).

4.3 Results

This section first reports the selected driving model, the storm panel and the wind climate of the driving runs (Sections 4.3.1 and 4.3.2). It then examines the surge response along three axes: where along the continuum the surge is felt (Section 4.3.3), which storms produce it (Section 4.3.4), what shape and timing its hydrograph takes (Sections 4.3.5 and 4.3.6).

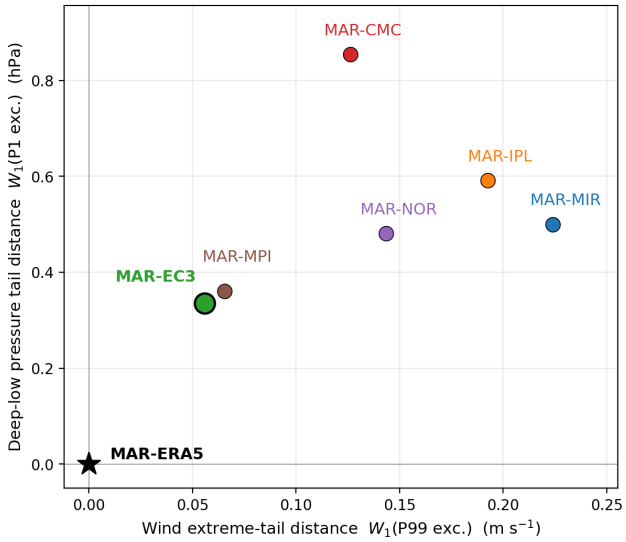

Figure 4.5: W_1 tail-fidelity comparison of the six MAR-ESM runs against MAR-ERA5, for the wind-speed P99 and pressure P1 exceedances.

4.3.1 ESM selection and panel characteristics

EC-Earth3-Veg is retained as the driving ESM, through its downscaled run MAR-EC3: against MAR-ERA5 over 1980–2010 it attains the best value in seven of the eight evaluation metrics, including both tail-fidelity distances (Fig. 4.5), and ranks first overall (Table 4.3). All results below therefore describe the response of the continuum to the MAR-EC3 atmospheric forcing.

The low-pressure tail is the more discriminating of the two forcing variables for separating the ensemble. On wind speed, MAR-EC3 and MAR-CMC are nearly indistinguishable over the full distribution (mean bias +0.16 for both, KS 0.019 vs. 0.022, PSS 0.981 vs. 0.975), and differ appreciably only in the W_1^{P99} tail metric (0.056 vs. 0.126 m s^{-1}). On sea-level pressure, by contrast, the two models diverge across every metric: MAR-CMC's mean bias is more than twice as large and of opposite sign (+1.38 vs. −0.51 hPa), its KS statistic is roughly double (0.056 vs. 0.027), its PSS is lower (0.944 vs. 0.959), and its W_1^{P1} tail distance is more than double (0.854 vs. 0.335 hPa) — the worst of the six-member ensemble. Pressure therefore reveals a model separation that wind speed alone would understate, which is why it is treated as the discriminating field in the ranking of Table 4.3.

MAR-MPI presents a different pattern of near-competitiveness: unlike MAR-CMC, it stays reasonably close to MAR-EC3 on both tail metrics

Table 4.3: Multi-metric ranking of the six MAR–ESM simulations against MAR-ERA5 (1980–2010), for 10 m wind speed and sea-level pressure. Metric definitions are given in Section 4.2.4; in each column the best value is in bold.

Model	Wind speed				Sea-level pressure				Rank
	$\Delta\mu$	KS	W_1^{P99}	PSS	$\Delta\mu$	KS	W_1^{P1}	PSS	
MAR-EC3	+0.16	**0.019**	**0.056**	**0.981**	**-0.51**	**0.027**	**0.335**	**0.959**	**1**
MAR-MPI	+0.27	0.031	0.065	0.969	-0.77	0.039	0.361	0.952	2
MAR-CMC	**+0.16**	0.022	0.126	0.975	+1.38	0.056	0.854	0.944	3
MAR-IPL	+0.16	0.020	0.192	0.979	-2.68	0.090	0.591	0.907	4
MAR-NOR	+0.27	0.038	0.143	0.962	+1.08	0.065	0.481	0.932	5
MAR-MIR	-0.70	0.092	0.224	0.908	-3.16	0.157	0.500	0.843	6

(W_1^{P99} = 0.065 m s^{-1} and W_1^{P1} = 0.361 hPa, against 0.056 and 0.335 for MAR-EC3) and on the full-distribution metrics alike. What separates the two models is therefore not a single discriminating field, as with MAR-CMC, but a small, consistent margin in MAR-EC3's favour across all eight metrics simultaneously — MAR-EC3 attains the better value on every one of them, without exception, though never by a large amount on any single metric.

The panel comprises sixty-five surge events, extracted from the SSP3–7.0 downscaling between November 2033 and December 2096 and each reconstructed at the same 26 tide gauges, from the open North Sea to the upper Scheldt estuary (Fig. 4.6). It combines the 31 events produced by the storms detected atmospherically (Step 1.2) with the 34 events re-admitted from the simulated response (Step 4), over 25 continuous simulation windows, so that some simulation windows contain multiple storm-surge events.

The panel holds many more events late in the projection, but this count is not a climatological occurrence rate. The number of events per decade rises from 3 in the 2030s to 20 in each of the 2060s and 2070s (Fig. 4.6), but it rests on a single driving model and a Xaver-anchored, point-scale criterion, and the 34 re-admitted events can only occur inside windows that already contain a detected storm. The frequency of the track types is conditioned in the same way: Jutland (n = 23) and Scandinavian (n = 22) events dominate, ahead of Skagerrak (n = 16), whereas the four Southern North Sea storms all fall in 2062 (Section 4.4.6).

4.3.2 Decadal evolution of the MAR wind fields

The strong winds weaken in summer, whereas no change emerges in winter, the season of most strong-wind events, or over the year. This result comes

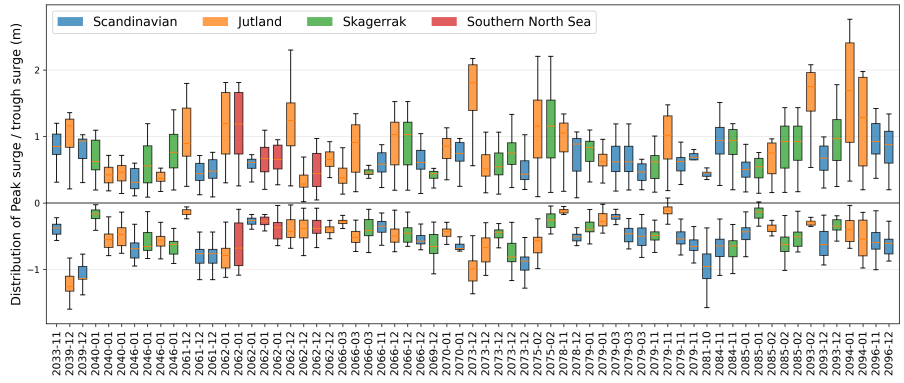

Figure 4.6: Distribution of the peak (upper part) and trough (lower part) surges across the 26 stations for each of the 65 surge events, ordered chronologically (2033–2096). Colour denotes track typology: blue: Scandinavian, orange: Jutland, green: Skagerrak, red: Southern North Sea. The figure illustrates the uneven distribution of events across typologies (from $n = 4$ for the Southern North Sea group to $n = 23$ for Jutland) and across decades (3 events in the 2030s against 20 each in the 2060s and 2070s) referenced in Section 4.4.6.

from the continuous hourly wind series of the six MAR-ESM runs under SSP3-7.0 at the Scheldt-mouth point (3.45° E, 51.45° N), which complement the discrete panel. For each run and each decade, the mean, the 90th (P90) and the 99th (P99) percentiles are computed on all hourly values of the decade, by season and over the year. The change of the six-run mean between the 2000s and each later decade d is divided by the standard deviation between the runs in the 2000s:

$$S/N(d) = \frac{\overline{X}(d) - \overline{X}(2000\text{s})}{\sigma_X(2000\text{s})},$$

where X is the mean, the P90 or the P99 of the wind speed in one run, $\overline{X}$ its mean over the six runs and σ_X its standard deviation between the runs. This signal-to-noise ratio exceeds one in absolute value when the change exceeds the disagreement between runs. The same ratio is computed for each run, with the change of that run in the numerator, to show how the runs spread around their mean (Fig. 4.7).

Only the summer extremes change beyond this spread. The summer P99 decreases from 12.5 to 11.8 $\mathrm{m\,s^{-1}}$ by the 2090s (−5.4 %, signal-to-noise ratio −1.2), in five of the six runs, MAR-IPL showing no change (Fig. 4.7d), and the summer P90 by 3.8 % (−0.6), so the weakening is strongest in the upper tail. Autumn winds weaken less (−3.3 % in the mean, −0.4). In winter, the P99

stays at 17.3 m s^{-1} (−0.1 %), and the P90 and the mean change by about −1 %, within ±0.4 of the inter-run spread throughout the century. The annual P99 does not change either (−0.3 %). It is set by the strongest hours of the year, which occur in winter and autumn, so the summer weakening, which takes place below it, does not affect it.

In winter, the runs disagree on the sign of the change. By the 2090s, the signal-to-noise ratio of the winter P99 ranges from −1.4 in MAR-MPI to +0.8 in MAR-EC3, around a six-run mean of zero (Fig. 4.7b). MAR-EC3, the run driving the panel, thus lies at the upper end of the ensemble. Its winter P99 rises from 17.2 to 18.2 m s^{-1} (+5.8 %) and its winter mean by 6.6 %, while its summer P99 falls by 11 %. A comparison of two decades from a single run is, however, strongly affected by internal variability.

Neither the duration nor the seasonal timing of strong-wind events changes detectably. An event is defined as a run of consecutive hours above each simulation's own 1980–2010 P99, merging gaps of up to 3 h. The mean event duration goes from 6.1 to 6.3 h: it increases in three of the six runs only. In MAR-EC3, it goes from 5.7 to 6.9 h. About 62 % of these events occur in winter in both periods.

4.3.3 Landward amplification of both surge signs

The estuary and the open sea respond differently to the same events. Five of the six metrics separate the two zones, with Scheldt values further from zero in both surge directions; only I^- shows no contrast (Fig. 4.9, Table 6.3.2).

The positive surge grows toward the estuary: taken event by event, the Scheldt-to-sea amplification factor for the peak surge has a median of 1.50 (Appendix 6.3.4). The peak surge is largest at the head of the estuary — an average of 1.19 m at Antwerp — and decays seaward to only 0.22 m at Aberdeen, the least exposed North Sea gauge. The single largest event of the panel, a peak surge residual of 2.76 m, would occur at Antwerp in January 2094 (Fig. 4.6). Reduced into the two zones, the Scheldt attains a mean positive peak of 0.94 m, nearly twice the North Sea mean of 0.49 m — a separation significant under the Mann–Whitney test, and shared by the cumulative positive intensity I^+ (Fig. 4.9, Table 6.3.2).

The negative surge shows the same contrast, with a smaller difference between the zones. Troughs are deeper in the Scheldt than in the North Sea (median −0.56 against −0.38 m, a ratio of about 1.5), and so is the low-water skew (−0.25 against −0.16 m). Both differences are significant (Table 6.3.2).

The estuary amplifies both surge signs, yet only the positive surge shows a matching increase in cumulative intensity: I^+ separates the two zones clearly, whereas I^- does not separate them at all (Fig. 4.9). This is the first

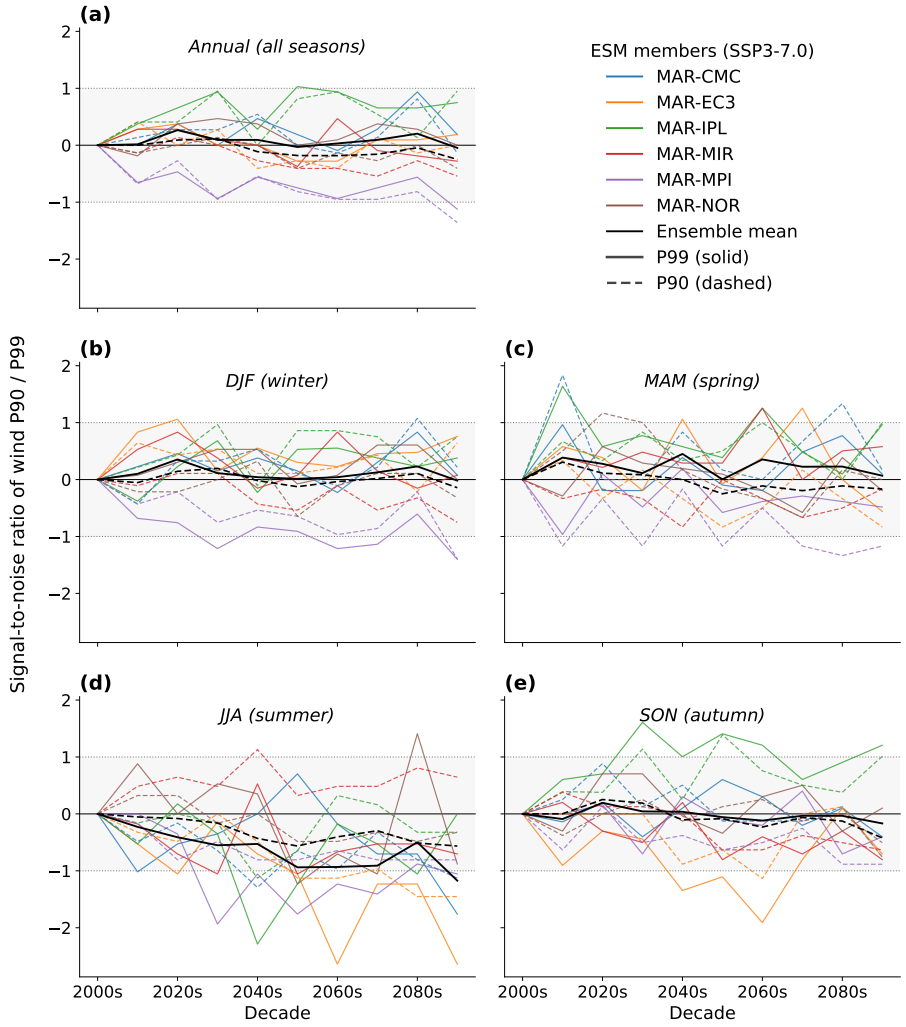

Figure 4.7: Only the six-run mean of the summer wind extremes changes beyond the spread between runs. Signal-to-noise ratio of the decadal P99 (solid) and P90 (dashed) of the hourly wind speed at the Scheldt-mouth point under SSP3-7.0, **(a)** over the year and **(b)–(e)** by season. Coloured lines: change of each MAR-ESM run since the 2000s; black lines: change of the six-run mean; both are divided by the standard deviation between the runs in the 2000s. The shaded band marks $|S/N| < 1$, where the change stays within the spread between runs. Percentiles are computed on all hourly values of each decade.

indication of the asymmetry between positive and negative surges that recurs throughout the results (Section 4.3.4).

The amplification is nearly the same for every track type. Event by event, the peak surge at Antwerp is 1.64 times that at Vlakte van de Raan, at the mouth of the estuary, for the Jutland and Scandinavian types, and 1.71 times for the Skagerrak type; the trough is deepened by a factor of 1.54 to 1.68 (Fig. 4.8). Only the four Southern North Sea storms depart from this range, with a factor of 2.0 on the peak. Whatever the event, the estuary thus multiplies both surge signs by a similar factor between its mouth and its head. This factor is computed on the surge residual. In this macrotidal estuary, where the tidal range also grows toward Antwerp, the residual carries part of the tide–surge interaction (Section 4.3.6), so the factor describes the amplification of the residual rather than that of the meteorological surge alone.

4.3.4 The track type orders the response but separates only the low-water skew

Track type does not separate the positive surge: none of the three metrics — peak, high-water skew, I^+ — separates the four typologies, either on the worst-affected gauge (all $p_{KW} \geq 0.19$) or at any individual station (Fig. 4.9, Table 6.3.2).

In the Scheldt, Jutland storms carry the largest median positive surge (Fig. 4.9). Jutland storms carry a median peak surge of 1.15 m (interquartile range 0.72 m to 1.42 m), against 0.86, 0.69 and 0.66 m for the Skagerrak, Scandinavian and Southern North Sea types, and a median I^+ of 4.9 m h, against 3.0 m h or less for the other types. The interquartile ranges overlap, so the panel can neither confirm nor exclude this contrast. In the North Sea, the four types carry similar peaks (medians of 0.35 to 0.45 m; Fig. 4.8).

Track type separates the negative surge on one metric only, the low-water skew. On the worst-affected gauge, the Scandinavian events produce the deepest median skew (−0.74 m) and differ significantly from the Skagerrak events (Table 6.3.2); resolved station by station, the typologies separate on this metric at 14 of the 26 gauges. Neither the trough surge nor the cumulative negative intensity shows such a dependence.

The Scandinavian type carries the deepest low-water skew in the North Sea, and the contrast fades landward. The typologies separate at 7 of the 11 North Sea gauges, and the Scandinavian type carries the deepest median skew at all seven (Fig. 4.10). The separation is strongest in the southern bight, where the spread between typologies reaches 0.53 m at Cromer and Lowestoft. In the Scheldt, the typologies still separate at the seven gauges from Vlakte van de Raan to Hansweert, but the Scandinavian and Southern North Sea types

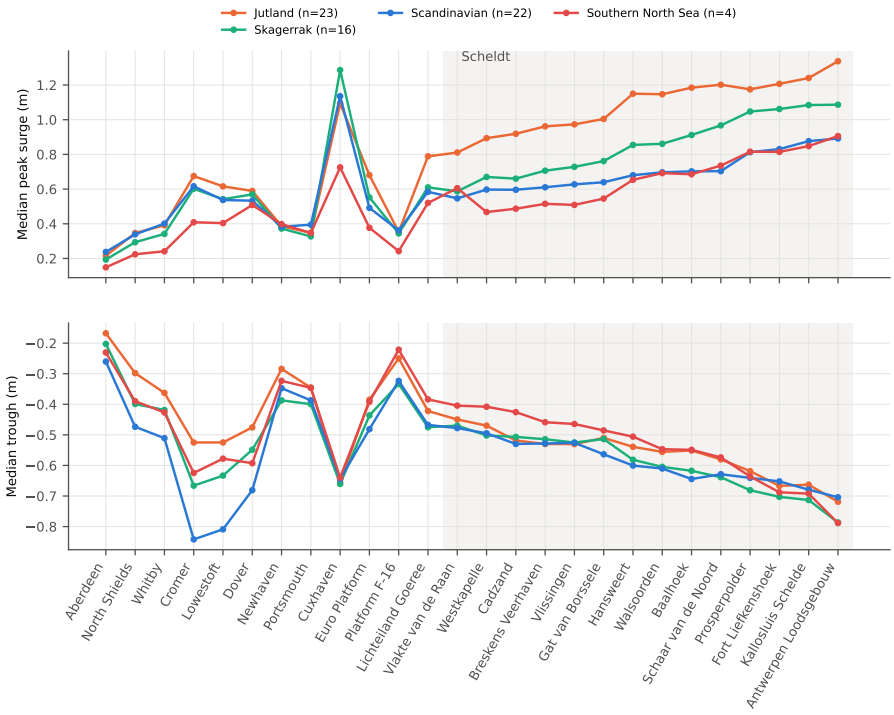

Figure 4.8: The estuary amplifies the surge of every track type alike. Median peak surge **(top)** and median trough surge **(bottom)** per track typology at each of the 26 gauges, ordered from the UK east coast to the head of the Scheldt; the shaded band marks the Scheldt zone, and Cuxhaven belongs to neither zone (Section 4.2.6). Lines join the gauges for readability only.

carry similar medians there (within 0.07 m), and the separation is no longer resolved from Walsoorden to Antwerp.

The drawdown lasts longest where it is deepest. At the North Sea gauges, Scandinavian storms keep the residual below r_{P3} for 3.5 h in median and carry the largest median I^- (−1.8 m h), whereas the median Jutland or Skagerrak storm does not cross r_{P3} at all (Fig. 4.9). In the Scheldt, the contrast between types fades, as it does for the low-water skew.

4.3.5 Surge and drawdown often follow each other within an event

The drawdown is a frequent part of the response. Both a surge above r_{P97} and a drawdown below r_{P3} characterise 21 of the 65 surge events in the Scheldt

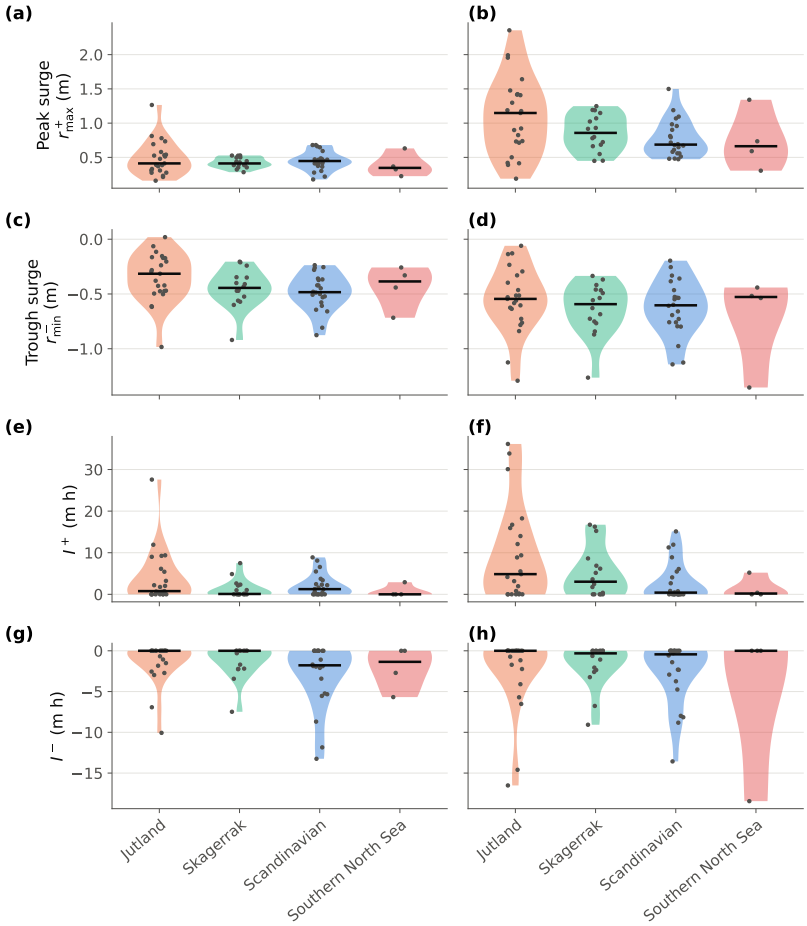

Figure 4.9: Jutland storms carry the largest positive surges in the Scheldt and Scandinavian storms the largest drawdowns in the North Sea, but the four track types overlap. Peak surge **(a, b)**, trough surge **(c, d)** and cumulative intensities I^{+} **(e, f)** and I^{-} **(g, h)** per track typology at the North Sea **(left: a, c, e, g)** and Scheldt **(right: b, d, f, h)** gauges. Each dot is one storm, summarised by the median over the gauges of the zone; black bars mark the median over storms. Kruskal–Wallis across typologies is non-significant for all four metrics on the worst-affected gauge (Table 6.3.2).

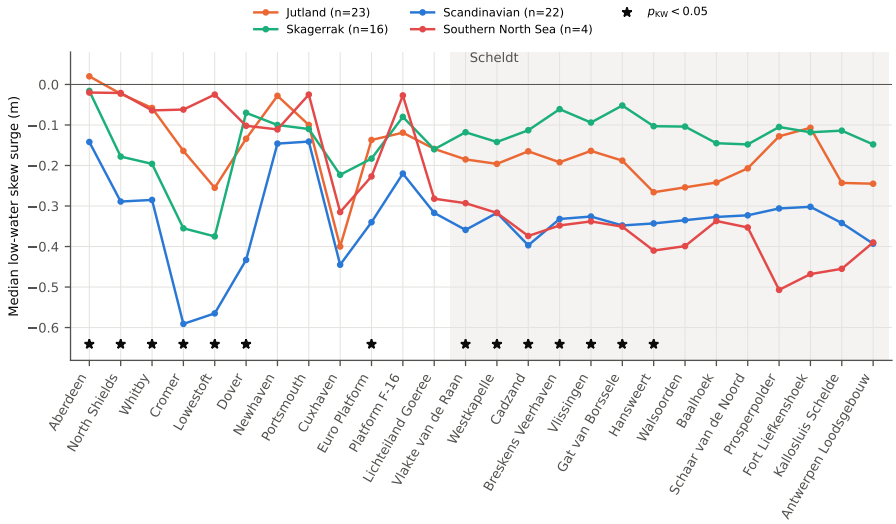

Figure 4.10: Scandinavian storms carry the deepest low-water skew in the North Sea, and the contrast between track types fades landward. Median low-water skew surge per track typology at each of the 26 gauges, ordered from the UK east coast to the head of the Scheldt, as in Fig. 4.8; the shaded band marks the Scheldt zone. Stars mark the gauges where the Kruskal–Wallis test separates the typologies ($p_{\mathrm{KW}} < 0.05$; 65 events). Lines join the gauges for readability only.

and 17 in the North Sea (Fig. 4.11). The drawdown usually comes first: the DS class outnumbers the SD class, by 14 to 7 in the Scheldt and 15 to 2 in the North Sea. A single surge (S1) characterises 14 events in each zone, and two or more distinct surges (S2) only 4 to 5.

The shape varies with the track type (Fig. 4.11). Scandinavian storms mostly lower the water level: in the North Sea, 13 of the 22 storms belong to the D or DS class, and none of them, in either zone, to the SD class. Jutland storms most often produce a single surge (7 of 23 storms in both zones) and only once a drawdown alone in the Scheldt. Three of the four Southern North Sea storms remain moderate in the Scheldt.

The class of a zone is robust in the Scheldt and less so in the North Sea. In the Scheldt, the retained class is found at a median of 93 % of the 14 gauges, and at no fewer than half of them for any event. In the North Sea, whose 11 gauges are spread over the open shelf, this fraction falls to a median of 64 %, and for 15 of the 65 events the class is carried by fewer than half of the gauges, down to 3. Breaking the ties the other way changes no class count

by more than three, and keeps the number of events that combine both signs between 16 and 17 in the North Sea and between 20 and 22 in the Scheldt.

The class M does not mean that the surge is absent. Most events classed M are episodes re-admitted from the simulated response (Section 4.2.4): 10 of the 16 in the North Sea, 15 of the 17 in the Scheldt, and 7 of the 9 events classed M in both zones. These episodes entered the panel because their residual crosses r_{P97} or r_{P3} at one or more gauges, but they fail the majority test of the zone class: the 7 re-admitted episodes classed M in both zones cross a threshold at only 2 to 9 of the 25 gauges.

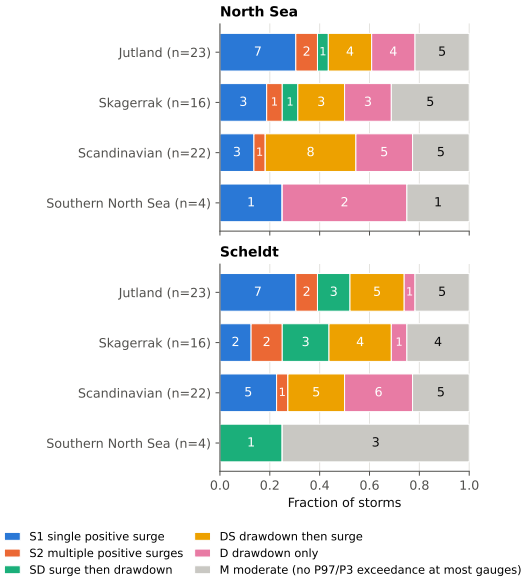

Figure 4.11: Scandinavian storms mostly lower the water level, Jutland storms most often raise it once. Fraction of the storms of each track typology in each hydrograph shape class (Table 4.2) at the North Sea **(top)** and Scheldt **(bottom)** gauges; numbers give the count of storms. Each storm takes the class found at most gauges of the zone (Section 4.2.7).

4.3.6 Surge peaks precede high water, troughs follow low water

Surge peaks occur preferentially before high water, on the rising tide (Fig. 4.12). Of the peaks exceeding r_{P97}, 66 % precede the nearest high water at the North Sea gauges and 74 % in the Scheldt, by 1.5 h and 2.1 h in median. Because the tidal phase at which a storm arrives is arbitrary in this panel

(Section 4.2.6), peaks would spread uniformly across the tidal cycle without tide–surge interaction; their clustering therefore reflects the interaction.

Troughs occur preferentially after low water, also on the rising tide. Of the troughs below r_{P3}, 66 % follow the nearest low water at the North Sea gauges, by 2.0 h in median, and 63 % in the Scheldt, by 0.7 h. Both extremes of the residual thus cluster on the rising tide, the peak before high water and the trough after low water.

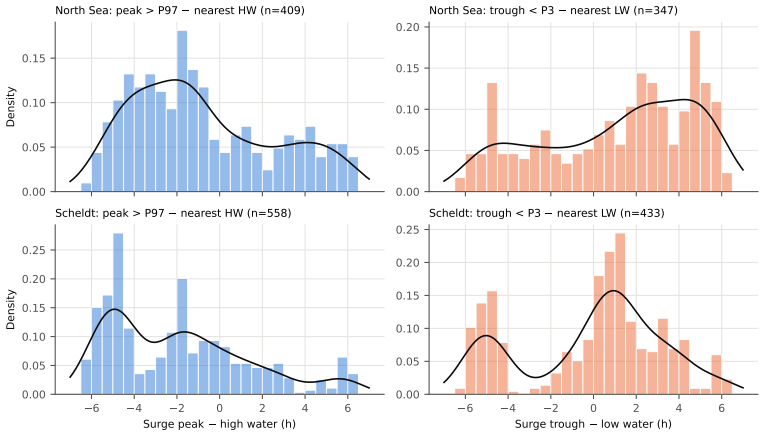

Figure 4.12: Surge peaks cluster before high water, troughs after low water. Probability density of the time between the surge peak (above r_{P97}) and the nearest predicted high water **(left)**, and between the trough (below r_{P3}) and the nearest predicted low water **(right)**, at the North Sea **(top)** and Scheldt **(bottom)** gauges. Bars show the empirical density in 0.5 h bins and lines a kernel density estimate; negative values denote an extreme of the residual that precedes the tidal extreme.

4.4 Discussion

The panel analysed here is one physically plausible realisation drawn from a much larger space of possible future storms, in the storyline sense of Section 4.2.2 (Shepherd et al., 2018; Sillmann et al., 2021). Read that way, it yields three results. The estuary amplifies both surge signs by a similar factor for every track type with more than four storms (Sections 4.4.1 and 4.4.2). The track type modulates the sign and the shape of the response more visibly than its amplitude, and surge and drawdown often follow each other within the same event (Section 4.4.2). Both extremes of the residual are timed relative to the tide as tide–surge interaction predicts, in agreement with observations

for the positive surge (Section 4.4.3). The section then discusses the future evolution of the winds that force the surge (Section 4.4.4) and what the analysis leaves open on total water levels (Section 4.4.5), before closing on the limitations that bound these results (Section 4.4.6).

4.4.1 Contrast along the continuum

The surge increases from the open North Sea to the head of the estuary for every track type (Section 4.3.3). This contrast is measured between groups of stations and does not by itself identify its cause. It resembles the growth of the astronomical tidal range toward Antwerp, which theory attributes to the balance between channel convergence and frictional dissipation (Friedrichs et al., 1994; Savenije et al., 2008), and projected extreme water levels in the Elbe also rise fastest in its upper estuary (Pein et al., 2023). Channel convergence is therefore a plausible candidate, but bathymetry, friction and intertidal storage were not varied here, and the simulations cannot separate their contributions. Part of the contrast may also come from tide–surge interaction: in the residual, a small shift in the phase of the tide produces a signal that grows with the tidal range, which increases toward Antwerp (Section 4.3.6). The per-event amplification factor is a ratio of two maxima and inherits their noise, but the zonal means show the same contrast (Section 4.3.3). The contrast also depends on the open-sea reference: with Cuxhaven, itself an estuary mouth, in the North Sea zone, the factor appeared to depend on the track type, a result that vanishes once it is excluded (Appendix 6.3.4).

The estuary deepens the troughs as well as raising the peaks, but does not treat them alike: only the peaks carry a matching increase in cumulative intensity, whereas I^- does not separate the two zones (Section 4.3.3). The estuary thus deepens the drawdown at its lowest point rather than over its whole duration, while the track type, which orders the drawdown at the North Sea gauges, matters less and less upstream (Section 4.3.4). Studies of negative surges have so far characterised where and when drawdowns occur in the North Sea, and which weather produces them (Geelhoed, 1973; Burlace, 1986; Jensen et al., 2022; Conte et al., 2013); this panel adds their landward evolution along an estuary. What these residuals imply for flood defences and navigation is discussed in Section 4.4.6.

4.4.2 Drivers of the surge response

Between the mouth and Antwerp, the peak surge grows by a factor of 1.6 to 1.7 and the trough by 1.5 to 1.7 for each of the three track types with more than four storms (Section 4.3.3), so the amplification hardly depends

on the track. The track types differ more in the surge that reaches the estuary, although mostly without statistical separation: the four types carry similar peaks in the North Sea, the median peak of Jutland storms is the largest in the Scheldt, and only the low-water skew separates the types (Section 4.3.4). This pattern fits the difference in scale between the storm and the estuary. An extratropical cyclone extends over about a thousand kilometres, the scale of the North Sea basin, whereas the estuary measures a few tens of kilometres. The surge is built mainly over the shelf, where the track sets the direction and duration of the wind, and the estuary transforms the surge that reaches its mouth (Section 1.2). In the Scheldt, this transformation depends on local features such as the size, elevation and location of the intertidal areas (Smolders et al., 2015) and the geometry of the marsh channels (Stark et al., 2015); in the German Bight, the same storms can affect neighbouring estuaries differently (Plüß et al., 2001). The separation between the two scales is not complete. The transformation of the surge in an estuary also depends on the time scale, amplitude and asymmetry of the incoming surge and on its phase relative to the tide (Familkhalili et al., 2020), which the track can modify; the amplification was not analysed against these properties here. The wind over the estuary can also add to the surge, as in Delaware Bay for tracks parallel to the coast (Deb et al., 2024). In the Scheldt, the peak surge of Storm Xaver in the estuary was sensitive to the resolution of the atmospheric forcing (Chapter 3), but the local wind was not separated from the incoming surge in the present simulations; a simulation without wind over the estuary would be needed to do so.

In this panel, the Scandinavian type carries the deepest low-water skew at every North Sea gauge where the track types differ. In the lower estuary, the types still differ, but the Scandinavian and Southern North Sea types carry similar medians, and from Walsoorden upstream the difference is no longer resolved (Section 4.3.4). This is consistent with the sustained offshore winds that push water out of the shallow southern North Sea during extreme low waters (Geelhoed, 1973; Burlace, 1986), but the wind direction was not analysed here. Jensen et al. (2022) relate the extreme low waters of the Elbe to strong south-easterly winds, using weather types defined by the pressure pattern rather than storm tracks. At Cuxhaven, the panel does not separate the track types ($p_{\mathrm{KW}} = 0.19$; Fig. 4.10), so the comparison with their result cannot be settled.

The shape classes add to the typology contrast without changing its interpretation. Scandinavian storms, whose tracks pass furthest north, mostly lower the water level, and none of them produces a surge followed by a drawdown, whereas Jutland storms most often produce a single surge (Section 4.3.5). In this panel, the track thus modulates whether a storm raises or lowers the water level, and in which order, more visibly than how high

it raises it. With 4 to 23 storms per type, this remains a description of the panel rather than a property of the track types. Unlike analyses of the positive surge alone (Pupic Vurilj et al., 2025), the panel thus shows the drawdown as a frequent part of the response, more often before the surge than after it.

4.4.3 Tide–surge interaction compared with observations

The tide–surge interaction depends on the depth and on the tide, which the simulations keep at their present-day values (Section 4.4.5); future storms of the panel should therefore obey the same interaction as observed storms, and comparing them tests the model chain rather than the future climate. Along the Dutch coast, observed surge peaks cluster during rising and low tides, and more so for peaks above 1 m (Pupic Vurilj et al., 2025). This clustering is a classical result for the North Sea, where a positive surge advances the tidal wave and so raises the residual on the rising tide (Horsburgh et al., 2007). The simulated surge peaks follow this interaction, more strongly in the Scheldt (74 % before high water) than in the open sea (66 %; Section 4.3.6), which supports the representation of tide–surge interaction in the model chain.

The troughs extend this result to the negative surge, for which no observed counterpart exists in the region. A drawdown delays the tidal wave instead of advancing it, so that the residual is most negative on the rising tide after low water (Horsburgh et al., 2007), which is where the simulated troughs cluster. The same interaction thus shapes both signs of the residual, with opposite phases relative to the tidal extremes.

4.4.4 Future wind extremes and surge

The winter winds that drive the surge show no detectable change in their extremes. In the continuous MAR series, only the summer extremes weaken beyond the spread between runs. In winter, when most storms occur, neither the mean, the P90 nor the P99 wind changes in the six-run mean, and the annual P99 does not change either. The runs disagree on the sign of the winter change, and MAR-EC3 shows the largest increase in winter extremes by the end of the century, but a two-decade comparison of a single run is dominated by internal variability (Section 4.3.2).

The panel cannot tell whether the surge itself changes over the century. Its 65 events are selected for their extreme character, unevenly spread over 2033–2096 and drawn from a single model, so the position of an event in time cannot be read as a century-scale evolution of the surge. Exploratory tests on the order of the events, reported in Appendix 6.3.3, leave no signal that withstands correction for multiple testing. These tests do not show that the surge climate is stationary, and a panel of this size cannot exclude a change

of moderate magnitude. What the chapter says about the future evolution therefore rests on the forcing of the surge, not on the surge itself.

The absence of change in the winter wind extremes agrees with ensemble projections over the North Sea. Twelve CMIP5 models project no change in the annual maximum wind speed or in rarer wind extremes over the basin, but more frequent extremes from westerly directions (de Winter et al., 2013). In CMIP6, the number of extreme cyclones increases by about 4 % in Northern-Hemisphere winter, whereas the maximum low-level wind speed changes little (Priestley et al., 2022a). Other studies project more frequent and more intense storms over central, western and northern Europe (Mölter et al., 2016; Little et al., 2023), consistent with the eastward extension of the winter storm track (Zappa et al., 2013; Harvey et al., 2020). The change in wind extremes thus depends on the region, the metric and the driving model, and a single driving model cannot settle it (Section 4.4.6).

Surge projections give the same picture: the meteorological component of North Sea surge change is consistently small, model-dependent, and hard to separate from internal variability. Early regional projections found end-of-century increases in German Bight surge heights (Woth, 2005; Woth et al., 2006); the single-model ensemble of Sterl et al. (2009) found no significant change along the Dutch coast; and Gaslikova et al. (2013) showed the sign and magnitude of the change to depend on the driving model. Basin-scale assessments attribute most projected extreme-sea-level change to mean sea-level rise, the meteorological contribution remaining secondary and uncertain (Vousdoukas et al., 2017).

The summer weakening agrees with CMIP projections of fewer North Atlantic cyclones in summer and of weaker summer cyclone winds in the Northern Hemisphere (Zappa et al., 2013; Priestley et al., 2022a). It does not imply a shift of storms between seasons, and the runs show none: about 62 % of the strong-wind events occur in winter in both periods (Section 4.3.2). Longer storms would matter for the surge, since it needs sustained forcing to develop (Reef et al., 2018), but the runs show no detectable change in the duration of strong-wind events: their mean duration goes from 6.1 to 6.3 h over the six runs and increases in only three of them, including MAR-EC3, from 5.7 to 6.9 h (Section 4.3.2). Whether the surge itself changes in duration or season would require a continuous simulation (Section 4.4.6). Conclusions on future changes are therefore limited to the atmospheric conditions that drive the surge; they do not extend to the surge itself.

4.4.5 Surge, tide and mean sea level

Extreme total water levels result from three factors: the atmospheric conditions, through the surge they drive, the phase and amplitude of the

tide, and the mean sea level. The highest levels arise when a severe storm coincides with a spring high tide, as during the 1953 flood (Gerritsen, 2005), and the timing of the surge relative to the tide is a well-documented control on extreme water levels (Horsburgh et al., 2007; Williams et al., 2016; Al Azad et al., 2018; Thomas et al., 2019). The panel reproduces the interaction between surge and tide (Section 4.4.3), but the tidal phase at which each storm arrives is arbitrary (Section 4.2.6), so the simulations do not represent the coincidence of a storm with a spring tide. The panel is also built on the first factor alone (Section 4.2.2): it is anchored on the wind speed of Storm Xaver rather than on its water level, which was raised by a spring tide. The chapter can therefore conclude on the atmospheric contribution to extreme water levels, but not on total water levels, on the frequency at which a given level would be exceeded, or on the probability that the three factors coincide.

For the mean sea level, the model chain carries only part of the change. The open boundary forces its regional, dynamic component, the **zos** field of the driving model, whose global mean is zero by construction (Gregory et al., 2019), and this slow signal is absorbed by the mean term of the per-event harmonic analysis rather than appearing in the surge residual (Section 4.2.6). The global-mean rise is absent. At Vlissingen, the median projection under SSP3-7.0 gives a relative rise of about 0.67 m by 2100 (IPCC, 2023; Garner et al., 2021), larger than the projected changes in the meteorological surge of the North Sea, which remain small and model-dependent (Section 4.4.4). Projections accordingly attribute most of the twenty-first-century increase in European extreme sea levels to mean-sea-level rise (Vousdoukas et al., 2017; Kirezci et al., 2020). To first order, this rise adds to the surge (Vousdoukas et al., 2017; Oppenheimer et al., 2019), but not exactly: in the northern German Bight, a rise of 0.54 m raises storm surge water levels by up to about 15 cm more than the rise itself, in the shallow areas of the Wadden Sea (Arns et al., 2015).

The tide itself will also change, because sea-level rise modifies its propagation, by amplification or damping depending on depth, friction and convergence (Khojasteh et al., 2021). On the European shelf, changes in high tide levels can reach ±15 % of the regional rise, with increases in the southern North Sea and the German Bight and decreases in the western English Channel (Pickering et al., 2012; Idier et al., 2017), that is up to about 10 cm for a rise of 0.67 m. Interactions between mean sea level, tide and surge can reach several tens of centimetres, positive or negative, depending on the environment (Idier et al., 2019), and in the Western Scheldt, sea-level rise makes the tidal wave more resonant (Röbke et al., 2025). A storm meeting a spring tide would therefore face a different tide from today.

Two sensitivity tests on a few events of the panel would be a first step towards total water levels. Shifting the tide so that the peak of the most severe

events coincides with the high water of a spring tide, as during Storm Xaver and as Grabemann et al. (2020) did for climate-model storms of the German Bight, would bound the total water level that a future event of the panel could produce, without giving the probability of the coincidence. Rerunning the most severe positive and negative surges with the mean sea level raised by about 0.67 m would quantify how much the surge residual changes on a higher mean level, and the interactions between mean sea level, tide and surge along the Scheldt. The continuous simulation of Section 4.4.6 would extend both to the full storm climatology.

4.4.6 Limitations and future work

Several limitations bound the results; each is stated together with how strongly it conditions the conclusions, ending with directions for future work.

Selection of the driving model

The panel describes one plausible, high-end trajectory, not a central estimate. It is driven by a single ESM, which sits at the upper end of the ensemble on two counts. EC-Earth3-Veg has the highest transient climate response of the six (2.62 K), a by-product of selecting on historical fidelity (Section 4.2.4) that adds to the high-end character of SSP3-7.0 (Section 4.2.3). MAR-EC3 also shows the largest increase in winter wind extremes of the six runs: by the 2090s, its winter P99 rises by 0.8 times the spread between runs, whereas the six-run mean does not change (Section 4.3.2).

The six MAR-ESM runs show how strongly the forcing depends on the driving model. In winter, the change in the P99 wind speed by the 2090s ranges from −1.4 to +0.8 times the spread between runs, so that the runs disagree on its sign; only the summer weakening is shared by five of the six runs (Section 4.3.2). This agrees with surge projections for the North Sea, in which differences between climate models outweigh the emission scenario and internal variability as a source of uncertainty, and single-model studies risk conveying a misleading impression of confidence (Woth, 2005; Woth et al., 2006; Sterl et al., 2009; Gaslikova et al., 2013). With one member per ESM, however, the spread between the six runs combines the differences between the models and the internal variability of each run, including decadal modes such as the NAO that modulate North Sea storminess. The two cannot be separated here.

Other sources of uncertainty are not sampled. The emission scenario is fixed to SSP3-7.0, and MAR is the only regional model used for the downscaling. None of these sources, nor the spread between the ESMs, is

propagated to the surge, since the hydrodynamic panel is driven by MAR-EC3 alone.

Two features of the pressure field are noted for transparency (Fig. 4.5, Table 4.3). MAR-EC3 is the closest of the six runs to MAR-ERA5 on every pressure metric, with a mean bias of −0.51 hPa; through the inverse barometer, a bias of this size changes the static surge by about half a centimetre, far below the wind-driven contribution. The six runs, however, differ appreciably in the deep low-pressure tail, with W_1^{P1} ranging from 0.335 to 0.854 hPa, so statistics of compound wind–pressure events depend on the choice of ESM.

The single-model design follows from the storyline framing, which claims physical plausibility for each event rather than a calibrated probability across models. An ensemble approach would run the same chain with several ESMs, or several members of one ESM, and show whether the results hold beyond MAR-EC3, while separating model uncertainty and internal variability from the response of the continuum. A single-model large ensemble has been used in this way for the low waters of the Elbe estuary: in 50 members of EC-Earth3, of which the driving model is a variant, the south-easterly gales that produce these low waters become significantly less frequent by 2071–2100 (Jensen et al., 2022). Such an ensemble separates the forced signal from internal variability, but not from the differences between models, and it was affordable because it used only the large-scale pressure fields of the global model. Applied to this chain, the same approach could screen a large ensemble for the atmospheric conditions of the panel at the scale of the global model, and downscale with MAR and simulate with SLIM only the selected events. Its cost would lie less in the computation, SLIM simulating a month in a few hours on GPUs (Chapter 2), than in the storage of its output: the full fields occupy about 24 GB per simulated month, about 0.7 TB for the 25 windows of this panel, so that 50 members selected in the same way would require about 35 TB. Writing the time series at gauges and along the continuum chosen in advance directly during the simulation, together with summary fields such as the extreme water levels at each element, would reduce this volume by orders of magnitude, as in other large surge simulations (Brown et al., 2012; Aleksandrova et al., 2025).

Sample size and panel design

The panel is small, conditioned on extreme character, and unevenly distributed. Every threshold, percentile and significance statement in this chapter is therefore defined with respect to the 65 retained events themselves, and not with respect to the unconditioned distribution of future weather: the r_{P97} and r_{P3} thresholds of Section 4.2.4, for instance, are percentiles of the

simulated storm windows, not of the future climate, in which events of this severity are by construction rare.

Group sizes range from 4 (Southern North Sea) to 23 (Jutland), a fourfold imbalance that is not a design choice but an emergent property of the detection and re-admission pipeline, shaped by the screening choices of stages **(i)**–**(iii)**. Concretely, the four Southern North Sea events all fall in 2062, so that class samples a single stretch of the simulated period. Whether west-to-east tracks near 52°N are genuinely infrequent under the simulated circulation, or merely under-detected by a Xaver-anchored, point-scale threshold at the Scheldt mouth, this panel cannot say. The events are also unevenly spread in time (3 in the 2030s against 20 each in the 2060s and 2070s).

The typology test has little power: with four events in the smallest group, a single event can shift a median. For the positive surge, the panel does not separate the track types. Jutland storms carry the largest median peak in the Scheldt, but the interquartile ranges overlap (Section 4.3.4), so the panel can neither confirm nor exclude a difference between the types. For the negative surge, Scandinavian storms carry a deeper low-water skew than Skagerrak storms on the worst-affected gauge (Section 4.3.4). Tested gauge by gauge, the low-water skew differs between the track types at 14 of the 26 gauges (Kruskal–Wallis, $p < 0.05$). The contrast is clearest in the southern bight and weakens along the Scheldt (Section 4.3.4).

Event selection criteria

Three limitations concern the criteria used to select the storms: the duration screen, the transit criterion, and the severity factors that the criteria leave out.

Duration screening threshold. The 3 h duration screen is deliberately conservative, and the surge-based re-admission partly offsets it. Two caveats attach to the bound (Section 4.2.4, stage **(ii)**). First, the 3 h to 4 h minimum reported by Reef et al. (2018) for a comparable shallow, semi-enclosed North Sea basin under a Xaver-like storm is the forcing duration below which the Wadden Sea surge fails to reach its maximum elevation, not one below which no surge forms; shorter episodes still drive a sub-maximal response, so the screen may discard events able to produce a partial yet locally relevant surge. Second, duration is measured here at the single Scheldt-mouth point, whereas Reef et al. (2018) impose a spatially uniform wind; since offshore winds are generally stronger than those near the coast, the point-scale duration underestimates the basin-scale forcing duration — the same point-versus-basin representativeness problem quantified by Befort et al. (2015). Neither

caveat is specific to the Scheldt, for which no dedicated surge response-time estimate is available. The historical test of Section 4.2.4 does not point to the duration screen as the limiting factor: Tilo (2007), the missed storm that matters for the Scheldt, never reaches the wind threshold at the Scheldt mouth, so a shorter screen would not retain it.

Storms excluded by the transit criterion. The panel characterises the surge response to basin-transiting storms specifically, not the full space of atmospheric configurations capable of producing an extreme surge. The full-transit criterion of stage **(iii)** discards storms that stall over the basin, remain locally confined, or complete only a partial transit — and these are precisely the configurations the grey-swan literature flags as worst-case candidates: a slow-moving or stalling depression prolongs the wind forcing over a fixed fetch, propagation speed being itself a first-order control on surge severity (Wei et al., 2019), and physically plausible but historically atypical tracks can generate surges far exceeding observed records (Horsburgh et al., 2021). The exclusion is therefore not neutral with respect to severity: it may remove configurations that the literature identifies as worst cases, so the panel is likely to underestimate the largest surge residuals.

The exclusion is nonetheless a deliberate trade-off, made with the classification in mind (stage **(iii)**). The typology of Section 4.2.5 identifies a storm by the latitude at which its track crosses the 8°E meridian; a system that never reaches that meridian has no class, and admitting it would pool into the track-type comparisons a transient, spatially confined forcing regime for which the classical scheme was not constructed (Petersen et al., 1991). The criterion thus buys the internal consistency of these comparisons at the cost of the completeness of the hazard estimate, a cost the surge-based re-admission of Section 4.2.4 cannot recover, since no simulation exists for an excluded storm. Quantifying it would require screening the full ESM record independently of the transit criterion, for instance with the grey-swan perturbation logic of Horsburgh et al. (2021) applied to stalling or slow-moving configurations.

Severity factors absent from the selection criteria. Another limitation of our selection is that it relies on the wind speed, its duration and the transit of the storm across the basin, but does not account for other factors known to modulate surge severity, such as the wind direction, the fetch, the translation speed of the storm or the timing of its peak relative to the tide (Wei et al., 2019; Horsburgh et al., 2007). A criterion favouring onshore winds would have excluded the offshore-wind storms that produce the deepest drawdowns; by using the wind speed alone, our selection retains storms capable of forcing

both signs of surge. In addition, 34 of the 65 events were re-admitted on their simulated response, whether it was a positive or a negative surge (Section 4.2.4). The timing relative to the tide was not included in the criteria, as it cannot be controlled in a storm catalogue. It still affects our results, since the peak, the trough and $I^{\pm}$ are computed on the surge residual, which carries part of the tide–surge interaction (Section 4.3.6). Future studies could include these factors explicitly in the selection, for instance through a wind stress projected onto the onshore or offshore direction and integrated over the southern North Sea, in order to target the most severe configurations more directly. Evaluating the first two stages at the Scheldt mouth retains the storms that are severe where the chapter analyses the surge, including the 1953 flood and the most severe windstorms of 1980–2010 (Section 4.2.4). It is less suited to storms whose surge builds up over the wider North Sea while the winds at the Scheldt mouth remain moderate, such as Tilo (2007), which raised the water at Vlissingen to one of its highest levels since 1900 (Rijkswaterstaat, 2007). The transit criterion and the re-admission of Step 4 add basin-scale information and the simulated response, but both apply to storms already detected at the Scheldt mouth. The panel therefore represents the storms that are severe at the Scheldt mouth, which is the aim of the storyline, rather than every configuration able to produce a high surge there.

River discharge stationarity

River inflow is prescribed from present-day climatological monthly means and held unchanged across the simulation period. This is a strong assumption: the Scheldt's discharge regime is itself expected to respond to the same SSP3-7.0 forcing that drives the storm projections analysed here, while that response is not propagated into the upstream boundary condition. Its effect on the surge is expected to be small. Zorndt et al. (2012) show for the Weser that peak water levels during storm events are governed predominantly by offshore meteorological forcing rather than by upstream discharge, and the long-term mean discharge of the Scheldt, about $104\,\mathrm{m^3\,s^{-1}}$ at Schelle, brings about $5\times10^6\,\mathrm{m^3}$ over a tidal cycle, less than 1 % of the flood volume of about $10^9\,\mathrm{m^3}$ at Vlissingen (Meire et al., 2005). The assumption matters more for questions where discharge-driven processes, salinity intrusion, sediment transport, or compound fluvial–coastal flooding, are the primary concern, none of which are addressed in this chapter.

Compound flooding from storm surge and river discharge is projected to become more frequent along the north-western European coast. The meteorological conditions that drive it become more frequent along parts of the northern European coast (Bevacqua et al., 2019; Bevacqua et al., 2020), and the number of compound flood days in northern and central Europe

increases, mostly because of the rise in mean sea level (Heinrich et al., 2023). These projections depend on the scenario and on the number of models used (Hermans et al., 2024). Under SSP3-7.0, the scenario of this chapter, the cyclonic westerly weather pattern associated with most compound events on the west-facing coasts of Europe is projected to become more frequent in winter (Heinrich et al., 2025). Such compound events have occurred in this region in the past (Paprotny et al., 2020), which makes them a relevant concern for the future of the Scheldt. Extending the present framework with a climate-responsive discharge boundary — and, more broadly, with an explicit treatment of compound surge–discharge interactions — is therefore a natural priority for follow-up work.

A continuous simulation with rising mean sea level

Two simplifications of our approach could be addressed in future work. First, MAR is downscaled over discrete 45-day windows around selected extreme events rather than continuously; second, the global-mean sea level is held fixed (Section 4.4.5). Both choices follow from the storyline approach and from the high computational cost of kilometre-scale downscaling. Future research could instead run a continuous MAR simulation over several decades and impose a mean sea-level rise following the SSP3-7.0 scenario. This would account for the full storm climatology, including the clustering and seasonality of events, and would let the surge develop on a higher baseline, which a simple addition of surge and sea-level rise does not capture.

Continuous surge simulations driven by climate projections already exist at coarser resolution. In the North Sea, transient simulations over 1961–2100 and a 17-member ensemble over 1950–2100 have been used to assess changes in extreme surges (Gaslikova et al., 2013; Sterl et al., 2009), and at the global scale, a ∼25 km climate-model ensemble covers 1950–2050 (Muis et al., 2023). These simulations do not resolve estuaries, and some do not include sea-level rise (Gaslikova et al., 2013), whereas its interaction with the tide and the surge is not additive (Arns et al., 2015; Idier et al., 2019).

The cost of such a simulation would lie mainly in the atmospheric downscaling, since MAR would have to run continuously over the whole North Sea domain rather than over the Belgium-centred domain of the existing ensemble (Section 4.2.4). On the hydrodynamic side, SLIM simulates a month in a few hours on GPUs (De Le Court et al., 2026), and the full fields of a century would occupy about 30 TB; as for the ensemble approach (Section 4.4.6), writing the time series at selected gauges and summary fields during the simulation would reduce this volume by orders of magnitude.

From surge residuals to impact

Finally, the surge residuals characterised here are only one input to a risk assessment, not the assessment itself. The port of Antwerp is one of the largest in Europe, and it sits in the upstream reach where the positive surge is among the largest of the continuum (Section 4.3.3) and where the drawdown reaches values comparable to the deepest anywhere in the panel. Translating these surge residuals into consequences for the port would require combining them with the tide and mean sea level, and coupling them to exposure and vulnerability information, following the port-city risk assessments pioneered by Hallegatte et al. (2011) for Copenhagen. Such an assessment would treat positive and negative surges as two distinct hazards: positive surges bear on flood defences, whereas negative surges bear on navigation — two loss channels that a single-hazard analysis would conflate. For navigation, the drawdowns matter most when they coincide with low water, when the depth available in the access channels to the port is smallest. The mean sea level acts on these low water levels in the opposite direction to flooding, increasing the water depth. In the Elbe estuary, the lowest water level of an extreme low-water event rose by 88 to 98 % of an imposed sea-level rise, so that a higher mean level makes such events less extreme and less frequent (Jensen et al., 2022). At Vlissingen, the median projected rise of about 0.67 m by 2100 (Section 4.4.5) would on this basis raise the lowest water levels by about 0.6 m, of the order of the median trough of the panel in the Scheldt. Morphological change can outweigh this effect: at Hamburg, low waters have fallen in the past despite the rising sea, through changes in the geometry of the estuary (Jensen et al., 2022). Whether the drawdowns become a greater or a lesser constraint on navigation therefore depends on the total water level and on the morphology, not on the surge residual alone.

4.5 Conclusion

This chapter asks what future extreme storms reveal about positive and negative storm surges along the Scheldt–North Sea continuum under a high-emission scenario. Sixty-five surge events, simulated under a high-end scenario with a single driving model, give three answers, on the evolution of the surge from the open sea to the head of the estuary, on the role of the storm track, and on how surge and drawdown combine.

First, the estuary amplifies both surge signs by a similar factor for every track type. The peak surge and the trough grow from the open sea to the head of the estuary, and between the mouth and Antwerp they are multiplied by a similar factor, 1.5 to 1.7, for every track type with more than four storms.

This factor applies to the surge residual, which in a macrotidal estuary also carries part of the tide–surge interaction. Channel convergence is a plausible candidate for this amplification, consistent with the landward amplification of long waves in convergent channels where convergence outweighs friction (Friedrichs et al., 1994; Savenije et al., 2008); the simulations do not separate its contribution from those of bathymetry, friction and intertidal storage, which would require experiments in which the configuration itself is varied.

Second, the track type modulates the sign and the shape of the response more visibly than its amplification. In this panel, Jutland storms carry the largest positive surges in the Scheldt and most often raise the water level once, whereas Scandinavian storms carry the deepest and longest drawdowns in the open sea, and none of them raises the water level before lowering it. Only the low-water skew separates the track types statistically, most clearly in the southern bight; the other contrasts describe the panel without establishing a difference between the types. These differences would therefore come from the surge that reaches the mouth. This is consistent with the scales involved: at the scale of an extratropical cyclone, the Scheldt estuary is close to a single point, although the contribution of the local wind over the estuary was not separated from that of the incoming surge.

Third, surge and drawdown are parts of the same hydrograph rather than separate events, yet they are not mirror images of one another. A quarter to a third of the events combine both signs, the drawdown usually coming first, and both extremes of the residual cluster on the rising tide, as tide–surge interaction predicts and as observations show for the positive surge on the Dutch coast. The two signs nevertheless differ: the estuary raises the cumulative intensity of the surge, but not that of the drawdown. Positive and negative surges should therefore be analysed together, along a single continuum.

These answers concern the response of the surge to the events of the panel, not a change in storminess: in the MAR runs, the winter wind extremes that drive the surge show no detectable change over the century (Section 4.4.4).

These results hold for the present-day morphology: because bathymetry and channel geometry are held fixed (Section 4.2.4), any future deepening or morphological change of the estuary could modify the amplification itself, as channel modification reshapes tidal and surge amplitudes together (Familkhalili et al., 2016; Talke et al., 2020; Röbke et al., 2025). Under sea-level rise, the marshes that attenuate the tide and the surge may keep pace through sedimentation or drown, which would maintain or reduce this attenuation (Temmerman et al., 2003; Stark et al., 2015; Temmerman et al., 2012). This geometry is itself shaped by management decisions: the navigation channel to the port of Antwerp is deepened and maintained by

dredging, while flood control areas and depoldered land return space to the tide, partly as compensation for these works (Vitale et al., 2025; Vikolainen et al., 2015; Smolders et al., 2020). These measures are decided jointly by Flanders and the Netherlands and can take decades to implement (Slinger, 2023; Vitale et al., 2025), so the future geometry of the estuary depends on these decisions as much as on natural evolution. The results also hold within stated bounds: a single driving model under a high-end pathway, a conditioned panel of 65 events, and the surge residual rather than total water levels. They open three lines of work: a continuous simulation with rising mean sea level (Section 4.4.6), which would resolve the full storm climatology and the interaction of surge, tide and mean level; the application of the chain to several driving models; and the analysis of total water levels for the events of the panel, by imposing a spring tide on the most severe ones or rerunning them with a raised mean sea level (Section 4.4.5).

Chapter 5

Conclusions and perspectives

5.1 Conclusion

In this thesis, we investigated how storm surges propagate along the Scheldt–North Sea continuum under present and future atmospheric forcing. To that aim, we needed a model covering scales that rarely meet in one configuration: the surge is generated over the shelf, over hundreds of kilometres, and amplified in estuarine channels a few tens of metres wide, while the atmosphere that drives it is usually known at scales far coarser than the estuary. We therefore configured the depth-averaged version of SLIM on a single unstructured mesh, from the shelf break to the tidal channels of the upper Scheldt. First, we evaluated this configuration over 2016–2020, forced by the CERRA reanalysis (Chapter 2). We then forced it with the regional atmospheric model MAR and examined how the resolution of this forcing affects the simulated surge of Storm Xaver (Chapter 3). Finally, we applied the model chain to future extreme storms under a high-emission scenario (Chapter 4).

We found that a single domain represents the tide and the surge from the open shelf to the lower estuary without the interface that nested configurations place at the mouth. With bottom roughness, the only free parameter, calibrated over a storm-free summer, the configuration reproduces

the M2 amplitude within 5.2 % from Vlakte van de Raan to Kallosluis, the non-tidal residual with RMSEs of 9 cm to 14 cm from the open shelf to Bath, and the peak of Storm Ciara within 1 to 11 cm. Low waters are reproduced as well as high waters, which made the analysis of negative surges possible. Upstream of Bath, the skill decreases: residual RMSEs reach 15 cm to 21 cm, where the roughness was calibrated on raw elevations only, which do not constrain phase errors, and where the flood control areas of the Sigma Plan are absent from the mesh. The tide also reaches Kallosluis about 20 minutes too early: the model leads the observed M2 phase by up to 10° at Kallosluis, mainly at low water. Since a uniform change of roughness would not correct this lead without damping amplitudes that are already right, it points instead to the effective channel depth or to the friction at low tide.

The next step was to determine which atmospheric forcing this configuration requires. For Storm Xaver, refining MAR from 30 km to 2 km improved the simulated peak water level by about 20 % at the upstream stations, whereas refining the forcing interval from 6 h to 15 min changed it by about 10 cm, and only at 2 km. This ranking, the opposite of that reported for broad-scale coastal dynamics (Agulles et al., 2024), reflects the scale of the system: a finer forcing better represents the coastline and the land–sea contrast around a narrow estuary, and reduces the underestimation of strong winds. Since 5 km differs from 2 km mostly by less than 10 cm for a quarter of the cost, it was adopted for Chapter 4. This ranking rests, however, on a single storm, on a forcing that inherits the ERA5 boundary conditions of MAR, and on a one-way coupling.

Building on these chapters, we followed a physical climate storyline approach (Shepherd et al., 2018): under SSP3-7.0, 25 periods driven by EC-Earth3-Veg were downscaled with MAR at 5 km and simulated with SLIM, yielding 65 extreme surge events over 2033–2096. Our simulations showed that the estuary amplifies both surge signs by a similar factor, 1.5 to 1.7 between the mouth and Antwerp, for every track type with more than four storms. The track type rather modulates the sign and the shape of the response: Jutland storms carry the largest positive surges in the Scheldt and Scandinavian storms the deepest drawdowns at the North Sea gauges, although only the low-water skew separates the types statistically. A quarter to a third of the events combine both signs, usually with the drawdown first, yet the two signs are not mirror images: the estuary raises the cumulative intensity of the surge but not that of the drawdown, so each must be assessed in its own right. Finally, the continuous wind series of the driving model show no detectable change in the winter wind extremes, whereas the panel itself, conditioned on extremes and unevenly spread over 2033–2096, cannot tell whether the surge changes over the century. These results concern the surge residual, not total water levels: the mean sea level and the morphology

were held fixed, the tidal phase of the surge was not imposed, and a single driving model was used, the one with the highest transient climate response of the six considered. The panel cannot estimate return levels either, and it excludes the stalling storms that the grey-swan literature flags as worst cases (Horsburgh et al., 2021).

At the end of this thesis, we can return to the research questions defined in the introduction (Chapter 1):

1. *How accurately does a single-domain configuration reproduce the height and the timing of the tide and the storm surge from the open North Sea to the upper Scheldt estuary?*

   From the open sea to Kallosluis, the configuration reproduces the levels of high and low waters within about a decimetre, with no loss of skill at the transition from sea to estuary. Heights are reproduced better than timing: the tide reaches Kallosluis about twenty minutes too early. The errors on the non-tidal residual grow by about half upstream of Bath, where the roughness was calibrated on raw elevations only. The surge peak was evaluated on a single storm, and wind waves are not represented.

2. *How does the spatial and temporal resolution of the atmospheric forcing affect the simulated storm surge along the continuum?*

   For Storm Xaver, the spatial resolution of the forcing controls the simulated surge inside the estuary: a 30 km-class forcing underestimates the peak there, and refining it to a few kilometres recovers most of it. The temporal resolution matters only once the grid is fine, at 2 km. Because it rests on one storm, this ranking is not yet a general rule.

3. *What do future extreme storms reveal about positive and negative storm surges along the Scheldt–North Sea continuum under a high-emission scenario?*

   In the 65 events of the panel, the estuary amplifies positive and negative surges alike, the storm track shapes the sign and the form of the surge that reaches the mouth, and surge and drawdown often follow each other within one storm. The winter wind extremes of the driving model show no detectable change over the century. Within the limits of a single model and a discrete panel, this suggests that the flood hazard is more likely to grow through the rise in mean sea level than through its atmospheric component, whereas the same rise would make extreme low waters less severe.

Taken together, these answers show that the overall objective of this thesis, representing storm surges through the full Scheldt–North Sea continuum under present and future atmospheric forcing, is reached for the present climate from the open shelf to Kallosluis, with larger errors on the surge residual upstream of Bath, and that the same configuration provides the basis to extend it to the head of the estuary. For the future, the panel gives a first description of how the continuum responds to extreme storms, for both surge signs, within the limits of a single driving model and of the surge residual; its amplification factor, computed up to Antwerp, inherits the larger errors of the upper estuary.

5.2 Contribution to the model development

Answering these questions required several developments in SLIM, many of them not mine: the thesis ran over a period of rapid change in the model, and much of my contribution was to test, debug and apply new code rather than to write it. First, I was among the first users to beta-test and debug the multi-GPU version of SLIM in two dimensions on a multi-scale, multi-year problem; earlier applications to the Scheldt (de Brye et al., 2010; Gourgue et al., 2009) ran on CPU-bound set-ups that could not sustain such runs. Second, I helped integrate the implicit wetting–drying algorithm of Le et al. (2020), whose parameters proved hard to tune over this domain, and then debugged the explicit scheme that replaced it, developed within the team, the Scheldt being one of its first demanding applications. Third, I kept the tidal-analysis routines (UTide; Codiga 2011) and the coupling to river-discharge products (GEOGloWS; Hales et al. 2025) compatible with the new code. Finally, I built the coupling between SLIM and MAR. This thesis is the first to force SLIM with a high-resolution regional atmospheric model and to use it for projections driven by climate-model output, and its configuration is now the base set-up for subsequent SLIM projects on the Scheldt–North Sea system.

5.3 Perspectives for future works

Each limitation identified above opens a direction for future work. We outline five of them.

5.3.1 Improving the hydrodynamic model

The phase lead and the upstream errors of Chapter 2 call for sensitivity runs on the effective channel depth and the friction at low tide, and for a

recalibration of the roughness of the upper reaches on the tidal phase and on individual constituents rather than on raw elevations. Two processes are also missing there. The flood control areas of the Sigma Plan are the flats that the plan restores and floods on purpose (Smolders et al., 2015; Temmerman et al., 2013), and Storm Xaver gave real-scale evidence that they attenuate the surge upstream (Smolders et al., 2020). Representing them and their sluices would let the configuration test where additional storage is most effective, over all 65 events rather than a single storm. Vegetation, now represented through an increased bottom friction that underestimates the drag where the water is shallower than the canopy, would require a depth-dependent drag (Baptist et al., 2007). Finally, surface waves are omitted. Wave set-up raises extreme coastal water levels (Marcos et al., 2019), and coupling a wave model increased the surge of Storm Xaver in the German Bight by about 30 % (Stanev et al., 2016; Staneva et al., 2016).

5.3.2 Atmospheric forcing and couplings

The resolution experiment of Chapter 3 should be repeated on storms with other tracks and translation speeds before its ranking is used as a rule. A two-way atmospheric coupling would capture the feedback of the sea surface on the wind and let the resolution question be revisited in that setting (Colle et al., 2015). River discharge, held at present-day climatology, would likewise need a two-way coupling for compound events, which the North Sea is projected to experience more often (Bevacqua et al., 2019; Bormann et al., 2024; Feng et al., 2024).

5.3.3 Sea-level rise and estuarine morphology

If future storms carry no robust intensification, the hazard would grow through two other routes: the rise in mean sea level and the geometry of the estuary. We excluded the former from Chapter 4 so that the atmospheric forcing varies alone, but neither route can be added afterwards by simple superposition. A higher mean level modifies tidal propagation and frictional dissipation (Idier et al., 2019): on the European shelf, it changes high-tide levels by up to ±15 % of the rise (Pickering et al., 2012; Idier et al., 2017); in the German Bight, a rise of 0.54 m changed storm surge water levels by up to about 15 cm beyond the rise itself (Arns et al., 2015); and in the Western Scheldt, it makes the tidal wave more resonant (Röbke et al., 2025). A higher mean level would not only raise the water but reorganise the circulation of the estuary. Flats that now dry at low tide would stay submerged longer, which would shift the balance between channels and shoals, the flood–ebb asymmetry of the tide and the residual circulation (Khojasteh et al., 2021;

Talke et al., 2020), and with them the storage that attenuates the surge upstream. Whether the intertidal flats and marshes keep pace with the rising sea, through sediment accretion, or drown will determine whether their attenuation of the surge is maintained (Temmerman et al., 2003; Stark et al., 2015); its loss would increase the positive surge propagating upstream (Temmerman et al., 2012). The amplification factor of Chapter 4 is likewise a property of the present-day geometry, whereas channel deepening and dredging reshape tidal range and surge amplitude together (Familkhalili et al., 2016; Ralston et al., 2019; Talke et al., 2020; Wang et al., 2019). We therefore suggest running the panel again at raised mean levels, starting from the median SSP3-7.0 projection of about 0.67 m at Vlissingen by 2100 (IPCC, 2023; Garner et al., 2021), close to the 60 cm assumed in the cost–benefit analysis of the updated Sigma Plan (Broekx et al., 2011), on an evolved bathymetry, and with a spring tide imposed on the most severe events to obtain total water levels.

5.3.4 Event selection for drawdowns and storm sequences

The panel was selected on atmospheric severity, anchored on Storm Xaver, an archetype of positive surge. That the two signs differ even in such a selection makes a catalogue built for drawdowns worth pursuing, as Jensen et al. (2022) did for the Elbe by conditioning the selection on the meteorological configurations that generate extreme low waters. Their drivers differ from ours: they relate extreme low waters to strong south-easterly winds, whereas in our panel the deepest low-water skew follows Scandinavian tracks, and the track types are not separated at Cuxhaven. Extending their approach to the whole southern North Sea would show whether these drivers belong to the basin or to each estuary. Additional driving models (Muis et al., 2023) and a grey-swan perturbation of the stalling storms (Horsburgh et al., 2021) would address the other limits of the panel.

Such a catalogue would also allow storm sequences to be studied. In 1953, drawdowns halted navigation two days before the surge that flooded the estuary (Burlace, 1986), and a quarter to a third of our events combine both signs. Whether a drawdown followed by a refill leaves a signature on salinity and stratification, as positive surges and barrier closures do (Zorndt et al., 2012; Chen et al., 2023b), a depth-averaged model cannot say. Since wetting and drying makes three-dimensional schemes costly and fragile over such domains (Chen et al., 2008; Choudhary et al., 2025), a 2D–3D coupling with SLIM3D (Vallaeys et al., 2018; Alaerts et al., 2022), keeping the depth-averaged scheme over the intertidal flats, would be the logical next step.

5.3.5 Beyond the Scheldt: other estuaries, port and management

Applying the same chain to two or three contrasting estuaries would test whether the amplification factor can be predicted from convergence length, depth and friction, as long-wave theory suggests (Friedrichs et al., 1994; Savenije et al., 2008), and whether the resolution rule of Chapter 3 holds outside the Scheldt. A positive answer would turn a site-specific result into a screening rule for estuaries that will not be explicitly modelled for years. In the Scheldt, the configuration delivers the water-level side of assessments for the port of Antwerp, whose access channel operates within narrow depth margins (Wang et al., 2019). Turning these levels into consequences would require exposure and vulnerability data (Hallegatte et al., 2011), and modelling sediment transport (Gourgue et al., 2013) would first require a wider evaluation of the currents, which Chapter 2 compared at three stations only, with a tidal ellipse 11 % too weak at Bol van Heist. Finally, flood planning on this transboundary continuum rests on Belgian–Dutch coordination around a shared model (Broekx et al., 2011; Slinger, 2023), whereas SSP3-7.0 assumes eroding international cooperation (O'Neill et al., 2017): under this scenario, physical forcing and adaptive capacity move in opposite directions (Oppenheimer et al., 2019). This is not a result of this thesis, but it is the condition under which its results would be used.

5.4 Final thoughts

Throughout this work, the scale at which the system is resolved emerged repeatedly as the control on what a model can see: the mesh must reach the tidal channels where the amplification accumulates, and the atmospheric forcing must be refined to a few kilometres before the estuarine surge is reproduced. Most estuary–sea systems are still modelled as an estuary or as a shelf sea rather than as one continuum (Muis et al., 2016; Vousdoukas et al., 2017), although unstructured meshes and GPU-accelerated solvers now make the alternative affordable (Lambrechts et al., 2008; De Le Court et al., 2026). The Scheldt shares its defining features with many macrotidal estuaries deepened for navigation and bordered by ports, such as the Elbe and the Weser (Talke et al., 2021; Jensen et al., 2022), and estuaries host more than fifteen percent of the world's population on barely two percent of the land (McGranahan et al., 2007). Resolving the continuum as a single domain is therefore not only a modelling choice but a requirement for projecting how these systems respond to a changing climate, and for supporting the adaptation decisions that depend on it.

Chapter 6

Appendices

6.1 Appendix to Chapter 2: Multiscale hydrodynamic modeling of the Scheldt–North Sea continuum

6.1.1 Wetting and drying

This section details the WD algorithm summarised in Section 2.1.2. Several WD schemes have been developed and tested within SLIM over the years, spanning both explicit and implicit time-integration approaches (Gourgue et al., 2009; Kärnä et al., 2011; Le et al., 2020).

Explicit schemes compute fluxes directly from the known state at time level n and advance the solution in a single step. They handle the wet–dry front naturally and conserve mass to machine precision, but their stability is governed by the CFL condition: the time step must be short enough that information does not travel more than one grid cell per step. In drying areas, by contrast, the gravity-wave speed $\sqrt{gH}$ decreases and relaxes this wave-speed limit, but two other difficulties arise: as $H \to 0$ the velocity recovered as $\mathbf{u} = (H\mathbf{u})/H$ can grow very large and violate the CFL condition locally, and an element can lose more water in a single step than it contains, producing negative depths (Gourgue et al., 2009).

Implicit schemes solve for the state at time level $n+1$ simultaneously across all elements, which relaxes the CFL constraint and allows much larger

time steps. Early versions of SLIM used a fully implicit WD method that modifies the bathymetry in drying areas so that the total water depth never vanishes, bypassing the singularity at $H = 0$ (Kärnä et al., 2011). A subsequent improvement introduced a *thin-film* approach in which a minimum water depth H_{thin} is always maintained everywhere, so that dry elements are never truly removed but are instead kept artificially wet with a negligible film of water (Medeiros et al., 2013). This conserves mass, though it requires careful tuning of H_{thin} to balance numerical stability against physical realism.

The present implementation combines the thin-film method with an explicit time-stepping scheme made feasible by recent GPU-based optimisations of SLIM, which dramatically reduce wall-clock times and thus offset the CFL-induced time-step penalty (De Le Court et al., 2026). The minimum depth H_{thin} is imposed at every mesh node at all times, guaranteeing $H > 0$ throughout the domain. The WD algorithm then corrects the raw numerical solution at each time step through three successive steps.

Step 1 – Prevent excessive water loss. An element can only export as much water as it actually contains above the thin-film level (H_{thin}). Without this control, a nearly dry element could, in a single time step, export more water than it holds, driving H below zero and causing a numerical blow-up.

The temporal scheme advances the free-surface elevation as

$$\eta^{n+1} = \eta^n + \Delta t\, M^{-1} F(\eta^*, \mathbf{u}^*), \tag{6.1}$$

where F is the flux operator and M is the mass matrix. The outgoing volume of an element over the time step is

$$\Delta V = \sum_{j \in \text{edges}} F_j^{\text{ext,out}}, \tag{6.2}$$

where the sum runs over all edges and only the outgoing part of each edge flux contributes, so that $\Delta V \leq 0$, with $\Delta V < 0$ as soon as water leaves the element. The maximum volume that can safely leave the element — that is, the volume above the thin-film level — is

$$\tilde{V} = \frac{J}{6} \sum_{i \in \text{nodes}} \tilde{H}_i, \qquad \tilde{H}_i = \eta_i + h_i - H_{\text{thin}}, \tag{6.3}$$

where J is the element Jacobian and $\tilde{H}_i$ is the headroom above the thin-film level at node i.

Four distinct situations can arise, illustrated in Fig. 6.1.1:

(a) the element does not contain enough water to sustain any outflow;

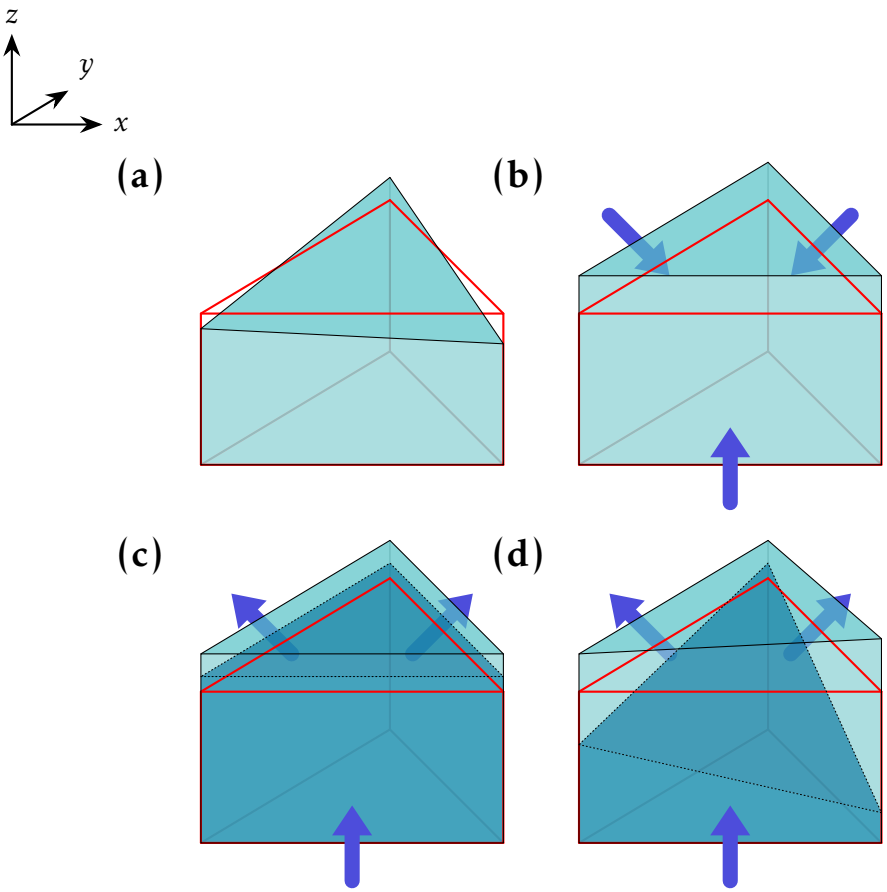

Figure 6.1.1: Schematic representation of the four possible states for determining the flux-limiting WD coefficient, C^F_{WD}. The light blue triangular prisms represent the water level at the beginning of the time step; the red-framed prisms indicate the volume that can be safely removed ($\tilde{V}$); the dark blue prisms with dotted edges show the water level at the end of the time step after applying the outgoing fluxes; and the blue arrows indicate the net flux direction through each edge. (a) The element was already at or below thin-film level, no outflow permitted: $C^F_{WD} = 0$, (b) no outflow; no limiting needed $C^F_{WD} = 1$, (c) outflow does not threaten the thin-film level $C^F_{WD} = 1$, and (d) outflow would exceed safe threshold; fluxes are proportionally scaled back $C^F_{WD} = \frac{\tilde{V}}{|\Delta V|}$. Figure adapted from Alaerts (2025) where a slight variant of the WD algorithm described here is considered.

(b) the element contains sufficient water and no water leaves it;

(c) $\tilde{V} > 0$, $\Delta V < 0$, and $\Delta V \geq -\tilde{V}$: water leaves the element but the outgoing volume does not deplete it below the safe threshold;

(d) $\tilde{V} > 0$, $\Delta V < 0$, and $\Delta V < -\tilde{V}$: the outgoing flux would remove too much water;

which lead to the summary of the flux-limiting coefficient:

$$C^F_{\mathrm{WD}} = \begin{cases} 0 & \text{if } \tilde{V} \leq 0, \\ 1 & \text{if } \tilde{V} > 0 \text{ and } \Delta V = 0 \quad (Fig.\ 6.1.1.b), \\ & \text{or if } \tilde{V} > 0,\ \Delta V < 0, \text{ and } \Delta V \geq -\tilde{V} \quad (Fig.\ 6.1.1.c) \\ \dfrac{\tilde{V}}{|\Delta V|} & \text{otherwise} \quad (Fig.\ 6.1.1.d) \end{cases} \tag{6.4}$$

Once C^F_{WD} is determined for each element, all outgoing edge fluxes from that element are multiplied by its coefficient:

$$F^{\mathrm{ext}}_j \leftarrow F^{\mathrm{ext}}_j C^F_{\mathrm{WD},j}, \qquad \forall j \in \text{edges}. \tag{6.5}$$

Step 2 – Nodal redistribution: smooth out sub-element dry patches. Even after the flux-limiting step, the free-surface elevation can vary significantly within a single triangular element. Because SLIM2D uses linear basis functions, the water depth is interpolated linearly across each triangle, so one or two nodes can become locally dry (i.e. $H_i < H_{\mathrm{thin}}$) even when the element-averaged depth remains positive. The purpose of this step is to detect such sub-element dry patches and redistribute mass internally, within the triangle and without exchanging water with neighboring elements, so that every node satisfies $H_i \geq H_{\mathrm{thin}}$.

The redistribution is governed by the coefficient:

$$C^H_{\mathrm{WD}} = \begin{cases} 1 & \text{if } H_{\mathrm{mean}} \leq H_{\mathrm{thin}}, \\ \dfrac{H_{\mathrm{thin}} - H_{\mathrm{min}}}{H_{\mathrm{mean}} - H_{\mathrm{min}} + \epsilon} & \text{if } H_{\mathrm{min}} < H_{\mathrm{thin}} < H_{\mathrm{mean}}, \\ 0 & \text{otherwise}, \end{cases} \tag{6.6}$$

where H_{min} and H_{mean} are the minimum and mean nodal water depths within the element, and ϵ is a machine precision positive floating-point number (added to prevent division by zero). When every node is above H_{thin}, no redistribution is needed ($C^H_{\mathrm{WD}} = 0$). Otherwise, two possible situations can

occur (Fig. 6.1.2). The first case ($H_{\text{mean}} \leq H_{\text{thin}}$) handles elements that are entirely, or almost entirely, dry: setting $C^H_{\text{WD}} = 1$ forces the free surface to be perfectly flat at the element mean, which is the most stable representation of a nearly dry element (Fig. 6.1.2.a). The second case ($H_{\text{min}} < H_{\text{thin}}$) handles partially dry elements where the element mean is above the threshold but at least one node is below it: C^H_{WD} is chosen so that the driest node is lifted just to H_{thin}, while wetter nodes lose a proportional amount of water to compensate (Fig. 6.1.2.b). The free-surface elevation at each node is then adjusted as

$$\eta_i \leftarrow \eta_i + C^H_{\text{WD}} \, (H_{\text{mean}} - H_i), \tag{6.7}$$

which pulls all nodal elevations towards the element mean by the fraction C^H_{WD}.

Step 3 – Momentum limiting: suppress supercritical flow in shallow water The third and final step ensures that velocities remain physically realistic as elements transition between wet and dry states. Even after the two previous steps have kept H positive, very shallow water depths can still produce unrealistically large velocities if the momentum $\mathbf{m} = H\mathbf{u}$ inherited from the previous time step is large relative to the current water column. In the extreme case, such velocities become supercritical (Froude number > 1), which is physically inconsistent with the sub-critical tidal and storm-surge flows that dominate shallow shelf seas and estuaries, and can seed numerical instabilities in subsequent time steps. The momentum $\mathbf{m} = H\mathbf{u}$ is limited to prevent supercritical flow. For each node i, the effective usable depth and the momentum magnitude are

$$\hat{H}_i = \max(0, \, H_i - H_{\text{thin}}), \qquad |\mathbf{m}_i| = \sqrt{(Hu_i)^2 + (Hv_i)^2}, \tag{6.8}$$

and the maximum allowable momentum is defined by a Froude-number constraint,

$$m_{i,\max} = \hat{H}_i \sqrt{g \hat{H}_i} \, \text{Fr}_{\max}, \qquad \text{Fr}_{\max} = 1. \tag{6.9}$$

Where $|\mathbf{m}_i| > m_{i,\max}$, the momentum is rescaled while its direction is preserved:

$$\mathbf{m}_i \leftarrow \mathbf{m}_i \, \frac{m_{i,\max}}{|\mathbf{m}_i|}. \tag{6.10}$$

The three steps together guarantee that, at the end of every time step, the water depth is everywhere positive, sub-element dry patches are smoothed out, and velocities are physically bounded — providing a robust and mass-conservative treatment of the wetting-and-drying dynamics that characterise intertidal and floodplain areas.

6.1.2 Bathymetry dataset

The computational mesh is mapped onto a composite high-resolution bathymetric dataset. As detailed in the main text, this dataset merges regional coastal surveys with specific estuarine sounding data to ensure an accurate representation of the shallow water topography across the domain (Fig. 6.1.3).

6.1.3 Validation of the semi-diurnal tidal components

Table 6.1.1 gives the observed and modelled amplitudes and phases of the M2 and S2 constituents at the tide gauges of the domain, from the offshore platforms to the upper estuary, discussed in Section 2.3.1.

Table 6.1.1: Observed (A^o) and modelled (A^m) amplitudes (m) and phases (φ^o, φ^m, degrees) of the M2 and S2 constituents along the continuum (2016–2020). The last row gives the mean and standard deviation of the amplitude error (%) and absolute phase error (degrees).

	M2				S2			
Station	A^o	A^m	φ^o	φ^m	A^o	A^m	φ^o	φ^m
Platform A12 (NS)	0.27	0.27	131.0	130.1	0.08	0.08	173.8	170.7
F3 platform (NS)	0.23	0.24	185.7	192.8	0.06	0.06	235.7	238.7
Platform F16-A (NS)	0.50	0.55	180.5	180.7	0.15	0.17	232.5	231.0
K13a platform (NS)	0.52	0.58	178.6	175.8	0.19	0.20	233.8	229.7
Euro Platform (NS)	0.73	0.70	23.9	19.6	0.18	0.17	79.6	74.2
Lichteiland Goeree (NS)	0.85	0.84	37.4	35.4	0.21	0.21	94.2	91.8
Vlakte van de Raan (NS)	1.48	1.43	16.6	11.8	0.42	0.40	70.8	65.2
Cadzand (NS)	1.66	1.58	19.4	16.1	0.47	0.44	74.6	70.8
Westkapelle (NS)	1.52	1.44	23.7	18.9	0.42	0.40	78.8	72.9
Breskens Veerhaven (LSE)	1.72	1.63	28.4	23.3	0.47	0.45	85.0	79.0
Vlissingen (LSE)	1.72	1.66	30.5	25.9	0.47	0.45	87.2	81.9
Gat van Borssele (LSE)	1.80	1.76	36.9	31.2	0.49	0.48	94.6	88.6
Hansweert (LSE)	1.97	1.96	51.2	44.2	0.52	0.52	112.1	105.0
Walsoorden (LSE)	2.00	2.01	53.9	46.2	0.52	0.54	115.4	107.6
Baalhoek (LSE)	2.06	2.07	58.0	49.5	0.54	0.55	119.9	111.7
Schaar van de Noord (LSE)	2.08	2.10	60.5	52.0	0.54	0.56	122.9	114.9
Bath (LSE)	2.10	2.12	62.4	53.6	0.55	0.56	124.9	116.7
Prosperpolder (USE)	2.11	2.16	64.0	55.7	0.55	0.57	127.2	119.2
Fort Liefkenshoek (USE)	2.16	2.19	66.5	57.0	0.55	0.58	132.5	121.0
Kallosluis schelde (USE)	2.19	2.23	68.1	58.2	0.58	0.60	132.7	122.4
Antwerpen Loodsgebouw (USE)	2.23	2.41	73.4	61.6	0.56	0.65	137.6	127.8
Mean error and std	$3.2 \pm 3.0\%$		$5.7 \pm 2.9°$		$3.9 \pm 2.0\%$		$6.1 \pm 2.6°$	

6.1.4 Validation of the non-linear tidal components

To evaluate the model's capacity to resolve shallow-water tidal distortion and estuarine asymmetry, the non-linear quarter-diurnal (M_4) and sixth-diurnal (M_6) constituents are analyzed along the domain. Table 6.1.2 summarizes the observed and modelled amplitudes and phases, alongside the mean relative errors and standard deviations. Amplitude errors are largest offshore, where M4 and M6 are only a few centimetres; the relative phase $2\varphi_{M2} - \varphi_{M4}$ is discussed in Section 2.3.1.

Table 6.1.2: Observed (A^o) and modelled (A^m) amplitudes (m) and phases (φ^o, φ^m, degrees) of the M4 and M6 constituents along the continuum (2016–2020). The last row gives the mean and standard deviation of the amplitude error (%) and phase error (degrees).

		M4				M6			
No	**Station**	A^o	A^m	φ^o	φ^m	A^o	A^m	φ^o	φ^m
1	Platform A12 (NS)	0.04	0.04	345.6	342.6	0.01	0.01	33.7	53.3
2	F3 platform (NS)	0.05	0.05	321.0	321.1	0.02	0.02	29.6	32.8
3	Platform F16-A (NS)	0.04	0.05	284.8	290.1	0.02	0.02	325.1	313.6
4	K13a platform (NS)	0.02	0.03	149.6	147.2	0.03	0.03	156.5	127.0
5	Euro Platform (NS)	0.10	0.12	71.9	74.5	0.04	0.03	5.2	353.4
6	Lichteiland Goeree (NS)	0.15	0.17	82.2	81.9	0.06	0.04	17.3	358.4
7	Vlakte van de Raan (NS)	0.13	0.12	31.3	30.0	0.08	0.07	337.1	339.7
8	Cadzand (NS)	0.12	0.11	32.5	28.0	0.10	0.08	343.9	355.6
9	Westkapelle (NS)	0.14	0.14	38.0	37.9	0.09	0.08	352.4	356.8
10	Breskens Veerhaven (LSE)	0.14	0.12	52.2	50.0	0.09	0.08	16.2	23.7
11	Vlissingen (LSE)	0.13	0.12	59.9	58.2	0.09	0.08	21.3	31.4
12	Gat van Borssele (LSE)	0.12	0.12	70.5	76.0	0.09	0.08	43.8	52.9
13	Hansweert (LSE)	0.11	0.13	99.5	110.5	0.09	0.09	113.8	120.4
14	Walsoorden (LSE)	0.12	0.13	109.7	115.4	0.10	0.10	134.5	132.7
15	Baalhoek (LSE)	0.11	0.13	117.8	120.0	0.11	0.10	151.8	151.1
16	Schaar van de Noord (LSE)	0.11	0.12	121.0	124.6	0.11	0.11	163.1	163.6
17	Bath (LSE)	0.10	0.12	115.5	122.3	0.12	0.12	168.1	170.4
18	Prosperpolder (USE)	0.11	0.11	119.2	123.9	0.13	0.13	180.0	184.8
19	Fort Liefkenshoek (USE)	0.11	0.10	122.8	123.0	0.14	0.14	192.7	193.9
20	Kallosluis Schelde (USE)	0.10	0.09	122.1	127.3	0.14	0.15	199.9	206.4
21	Antwerpen Loodsgebouw (USE)	0.11	0.12	127.8	162.9	0.13	0.12	223.9	244.6
	Mean error and std	$12.0 \pm 11.8\%$		$3.4 \pm 2.7°$		$12.8 \pm 12.1\%$		$8.2 \pm 7.5°$	

6.1.5 Current velocities validation

The simulated along-axis velocities correlate with the observations at 0.98 at the coastal stations and 0.90 in the estuary (Fig. 6.1.4). The current directions are bipolar, alternating between ebb and flood, and the model matches the dominant occurrence sectors within 22.5° at all sites. While overall velocity distributions match observations up to the third quartile, the upper tail is

systematically truncated, with the 99th percentile underestimated by 8% to 13% across the domain. In the estuary, this narrowed distribution reflects an under-represented tidal asymmetry, as the model partitions the flow too evenly between the ebb and flood cycles. Although this dampening of peak currents limits the resolution of extreme bed shear stresses for sediment transport, it remains a physically acceptable approximation for the barotropic storm surge application for this thesis.

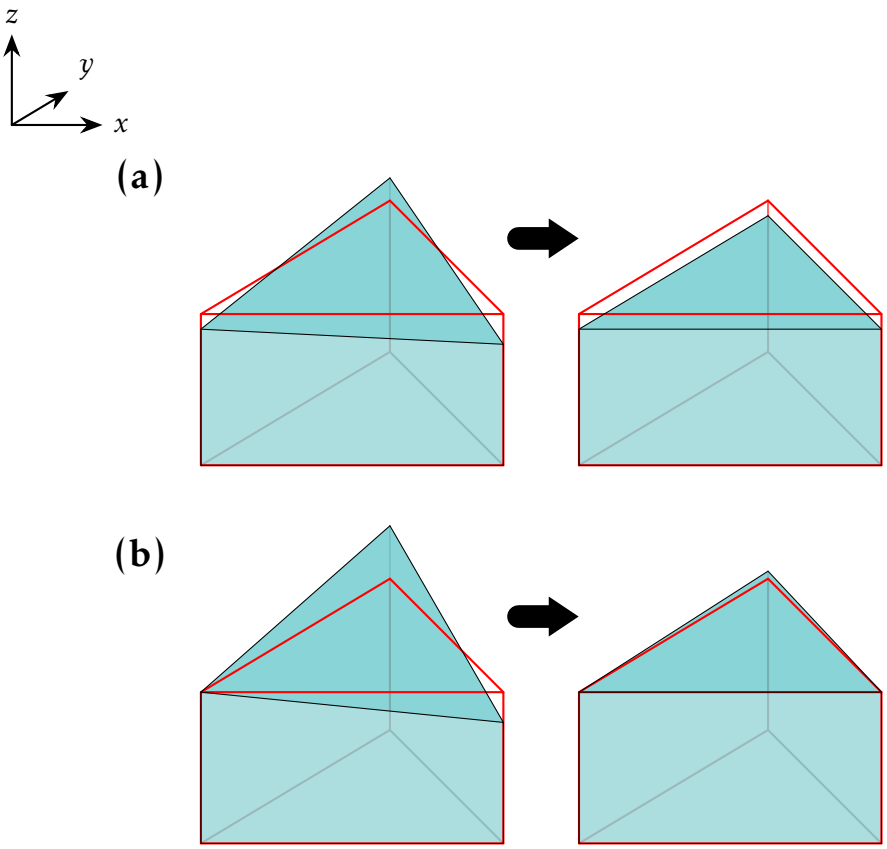

Figure 6.1.2: Schematic representation of the two possibilities for mass redistribution within each triangle: the left prisms represent the state at the beginning of the time step and the right prisms the state after mass redistribution. The light blue triangular prisms represent the volume with the water level H; the red-framed prisms delimit the volume with the minimum safe water level H_{thin}. (a) Fully or predominantly dry elements ($H_{\text{mean}} \leq H_{\text{thin}}$) (b) Partially dry elements ($H_{\text{mean}} > H_{\text{thin}}$) . Figure adapted from Alaerts (2025) where a slight variant of the WD algorithm described here is considered.

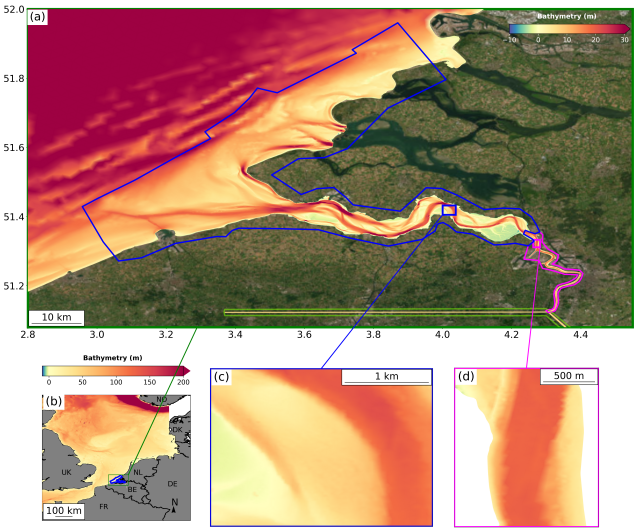

Figure 6.1.3: Interpolated bathymetry and source distribution across the model domain. Colored regions in panel **(a)** highlight the extent of the high-resolution bathymetric data sources used for the coastal area and lower Scheldt estuary from Rijkswaterstaat (2021) *in blue*, for the upper Scheldt estuary from AGENTSCHAP MDK (2021) *in magenta*, and the schematized freshwater tidal network with constant bathymetry in green, with Esri World Imagery as basemap (ESRI, 2025). Over the continental shelf, outside these areas, the bathymetry comes from EMODnet (2021). The lower panels illustrate the interpolated bathymetry mapped onto the computational mesh at **(b)** a large-scale view of the North Sea, and **(c-d)** close-up views of two specific locations within the Scheldt estuary. Panels on the estuary (a,c and d) share the same colorbar and panel on the North Sea (b) has its own.

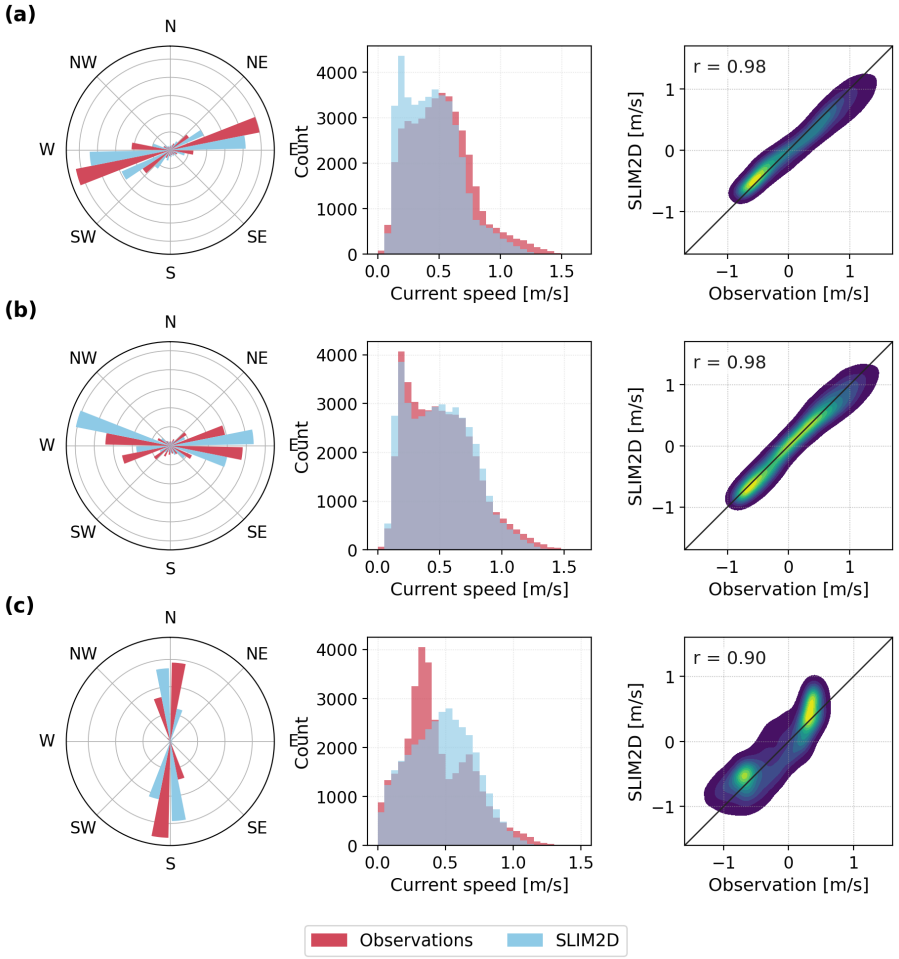

Figure 6.1.4: Validation of SLIM2D currents against the Waterinfo/Meetnet measuring piles at (a) Bol van Heist (MP3), (b) Scheur Wielingen (MP4) and (c) Lillo Meetpaal. In each row, from left to right: occurrence rose of the current direction in $22.5°$ sectors; distribution of the hourly current speed [m/s]; and density of the simulated against the observed along-axis velocity, obtained by projecting the horizontal velocity onto the major axis of the observed M_2 tidal ellipse, with the 1:1 line and the correlation coefficient. Positive along-axis values are directed towards the bearing of the major axis, which differs between sites. Correlations are computed over 2016–2020.

6.2 Appendix to Chapter 3: Atmospheric forcing resolution impacts on storm surge modeling

6.2.1 Atmospheric model validation

The linear regression analysis across all spatial and temporal resolutions (Table 6.2.1) consistently reveals a regime shift in wind speed behavior, characterized by a systematic transition from overestimation to underestimation. This crossover pattern appears in all modeled resolutions, confirming that the identified shift is not limited to any specific resolution. The 5 km spatial and 15 min temporal resolution produces the steepest regression slopes (reaching 0.74) and the highest crossover values (up to 8.3 m/s), indicating better alignment with observed wind speeds across both low and high wind regimes. As spatial resolution becomes coarser, both the slope and crossover value decline (down to 0.66 and 5.59 m/s, respectively), signaling a reduced ability of the model to capture stronger wind events. Temporal resolution has a smaller impact: coarsening the forcing from 15 min to 6 h lowers the slope by 0.04 to 0.05 and the crossover by 0.6 to 1.0 m/s, depending on the spatial resolution.

Table 6.2.1: Linear regression equations from the density distribution (like in Fig. 3.4) of wind speed for all the spatial and temporal resolutions of the MAR simulations, where y = modeled wind speed (m/s) and x = observed wind speed (m/s), and their crossover values.

MAR resolutions	Linear regression equation	Crossover (m/s)
2km, 15min	$y = 0.73x + 2.15$	7.99
2km, 1h	$y = 0.72x + 2.19$	7.85
2km, 3h	$y = 0.69x + 2.34$	7.46
2km, 6h	$y = 0.68x + 2.33$	7.22
5km, 15min	$y = 0.74x + 2.13$	8.29
5km, 1h	$y = 0.73x + 2.18$	8.17
5km, 3h	$y = 0.70x + 2.34$	7.75
5km, 6h	$y = 0.70x + 2.22$	7.30
10km, 15min	$y = 0.72x + 2.19$	7.93
10km, 1h	$y = 0.71x + 2.25$	7.87
10km, 3h	$y = 0.68x + 2.39$	7.54
10km, 6h	$y = 0.67x + 2.32$	7.07
20km, 15 min	$y = 0.72x + 1.87$	6.76
20km, 1h	$y = 0.71x + 1.94$	6.77
20km, 3h	$y = 0.68x + 2.08$	6.59
20km, 6h	$y = 0.68x + 1.91$	5.99
30km, 15 min	$y = 0.70x + 1.88$	6.21
30km, 1h	$y = 0.69x + 1.95$	6.26
30km, 3h	$y = 0.66x + 2.12$	6.19
30km, 6h	$y = 0.66x + 1.92$	5.59

The wind speed analysis of the weather stations (Table 6.2.2) shows that the performance gains from high-resolution data vary markedly by regions. Coastal stations such as Cadzand and Hoofdplaat show larger improvements in correlation and RMSE reduction compared to inland stations such as Westdorpe. This supports the hypothesis that finer spatial and temporal resolution is especially beneficial in coastal or topographically heterogeneous regions, where dynamics vary more rapidly in space and time. Moreover, at West Sole Oil Platform, located offshore, high correlation values (up to 0.932) are already achieved at coarser resolutions, with limited benefit from further refinement. The other oil platforms show no significant improvement with higher spatial resolution either. This suggests that over open water, where variability is smoother, coarse model resolution may already suffice.

Across nearly all locations, refining the temporal resolution of the atmospheric model MAR from 6-hourly to 15-minute consistently improves model performance (Table 6.2.2). RMSE and NRMSE generally decrease with finer temporal resolution, while correlation coefficients increase. For example, in Hansweert, RMSE drops from 1.401 at 6-hourly (30 km) to 1.195 at 1-hourly resolution, with a corresponding rise in correlation from 0.904 to 0.935. This suggests the model benefits from capturing higher-frequency variability in the observed data. Spatial resolution shows a more complex, location-dependent pattern. In general, the correlation improves as the resolution becomes finer from 30 to 10 km, especially near the Scheldt estuary (e.g., Hoofdplaat, Cadzand). The RMSE does not decrease at every station: at Marollegat, Hoofdplaat, Hansweert and Westdorpe, the 30 km run has a lower RMSE than the 5 and 2 km runs. At Cadzand, RMSE decreases from 2.4 (30 km, 6h) to 1.9 (5 km, 15 min), and correlation improves from 0.7 to 0.8. However, further refinement from 5 km to 2 km often leads to increased RMSE and decreased correlation—an effect most visible in Hansweert and Marollegat. When comparing MAR and ERA5 wind fields against observations, we find that MAR tends to underperform relative to ERA5 at stations located near the coast. However, at offshore locations such as the Hoorn-A Helipad and the West Sole Oil Platform, which lie closer to the open boundary and to the core of Storm Xaver's track, MAR shows a clear advantage. In these offshore settings, the added spatial detail provided by MAR's downscaling improves the representation of wind intensity and variability compared to ERA5, which is known to smooth large wind gradients (Molina et al., 2021).

6.2.2 Timing of the peak water levels

Figure 6.2.1 complements Fig. 3.12 for the temporal resolution of the atmospheric forcing: with the spatial resolution fixed at 2 km, the timing

Table 6.2.2: Statistics for wind speed of ERA5 and of the different MAR spatial and temporal resolutions for all the stations of Fig. 3.2, except ZDI the most western weather station on Fig. 3.2.b already presented in the main text, from November 25 to December 20, 2013.

Forcing	RMSE (m/s)	NRMSE (-)	Correlation (-)
Tyra E Helideck (lat = 55.7215°,lon = 4.8021°)			
ERA5	2.6	8.05	0.917
MAR			
30km, 6h	3.855	12.05	0.766
30km, 3h	3.628	11.34	0.810
30km, 1h	3.527	11.02	0.829
30km, 15 min	3.501	10.94	0.834
20km, 6h	3.622	11.32	0.777
20km, 3h	3.377	10.55	0.820
20km, 1h	3.278	10.25	0.838
20km, 15 min	3.259	10.18	0.842
10km, 6h	3.542	11.07	0.783
10km, 3h	3.276	10.24	0.826
10km, 1h	3.180	9.94	0.842
10km, 15 min	3.165	9.89	0.845
5km, 6h	3.501	10.94	0.779
5km, 3h	3.205	10.02	0.826
5km, 1h	3.108	9.71	0.841
5km, 15 min	3.098	9.68	0.841
2km, 6h	3.562	11.13	0.779
2km, 3h	3.277	10.24	0.823
2km, 1h	3.200	10.00	0.833
2km, 15 min	3.206	10.02	0.829
A12-CPP HELIPAD Oil Platform (lat = 55.4167°,lon = 3.8167°)			
ERA5	2.5	8.35	0.928
MAR			
30km, 6h	3.566	11.73	0.826
30km, 3h	3.326	10.94	0.868
30km, 1h	3.218	10.58	0.887
30km, 15 min	3.192	10.50	0.892
20km, 6h	3.406	11.20	0.821
20km, 3h	3.145	10.35	0.865
20km, 1h	3.034	9.98	0.883
20km, 15 min	3.010	9.90	0.888
10km, 6h	3.333	10.96	0.820
10km, 3h	3.050	10.03	0.866
10km, 1h	2.944	9.68	0.881
10km, 15 min	2.926	9.62	0.884
5km, 6h	3.222	10.60	0.820
5km, 3h	2.924	9.62	0.865
5km, 1h	2.800	9.21	0.881
5km, 15 min	2.782	9.15	0.882
2km, 6h	3.316	10.91	0.817
2km, 3h	3.028	9.96	0.860
2km, 1h	2.928	9.63	0.872
2km, 15 min	2.914	9.58	0.872

Forcing	RMSE (m/s)	NRMSE (-)	Correlation (-)
D15-FA-1 HELIPAD Oil Platform (lat = 53.8167°,lon = 2.95°)			
ERA5	2.7	8.50	0.922
MAR			
30km, 6h	3.661	12.25	0.804
30km, 3h	3.409	11.40	0.850
30km, 1h	3.304	11.05	0.871
30km, 15 min	3.279	10.97	0.877
20km, 6h	3.493	11.68	0.814
20km, 3h	3.218	10.76	0.859
20km, 1h	3.124	10.45	0.876
20km, 15 min	3.101	10.37	0.881
10km, 6h	3.452	11.54	0.806
10km, 3h	3.137	10.49	0.856
10km, 1h	3.031	10.14	0.873
10km, 15 min	3.010	10.07	0.877
5km, 6h	3.443	11.52	0.800
5km, 3h	3.086	10.32	0.855
5km, 1h	2.943	9.84	0.876
5km, 15 min	2.922	9.77	0.879
2km, 6h	3.571	11.94	0.791
2km, 3h	3.218	10.76	0.847
2km, 1h	3.098	10.36	0.865
2km, 15 min	3.087	10.33	0.865
J6-A HELIPAD Oil Platform (lat = 52.3667°,lon = 3.35°)			
ERA5	2.5	9.00	0.867
MAR			
30km, 6h	3.385	10.61	0.869
30km, 3h	3.209	10.06	0.888
30km, 1h	3.139	9.84	0.896
30km, 15 min	3.105	9.73	0.899
20km, 6h	3.352	10.51	0.849
20km, 3h	3.173	9.95	0.868
20km, 1h	3.108	9.74	0.875
20km, 15 min	3.086	9.67	0.879
10km, 6h	3.260	10.22	0.847
10km, 3h	3.063	9.60	0.868
10km, 1h	2.985	9.36	0.876
10km, 15 min	2.974	9.32	0.878
5km, 6h	3.201	10.03	0.843
5km, 3h	2.989	9.37	0.864
5km, 1h	2.907	9.11	0.872
5km, 15 min	2.903	9.10	0.873
2km, 6h	3.331	10.44	0.839
2km, 3h	3.127	9.80	0.860
2km, 1h	3.048	9.56	0.867
2km, 15 min	3.047	9.55	0.867

Table 6.2.2: (continued)

Forcing	RMSE (m/s)	NRMSE (-)	Correlation (-)
P11-B / De Ruyter (lat = 52.9167°,lon = 4.15°)			
ERA5	2.4	8.46	0.946
MAR			
30km, 6h	2.708	9.74	0.865
30km, 3h	2.560	9.21	0.883
30km, 1h	2.558	9.20	0.884
30km, 15 min	2.586	9.30	0.878
20km, 6h	2.521	9.07	0.871
20km, 3h	2.384	8.58	0.886
20km, 1h	2.392	8.60	0.886
20km, 15 min	2.421	8.71	0.882
10km, 6h	2.491	8.96	0.870
10km, 3h	2.338	8.41	0.888
10km, 1h	2.347	8.44	0.886
10km, 15 min	2.388	8.59	0.880
5km, 6h	2.455	8.83	0.871
5km, 3h	2.275	8.18	0.891
5km, 1h	2.268	8.16	0.891
5km, 15 min	2.339	8.41	0.882
2km, 6h	2.468	8.88	0.878
2km, 3h	2.293	8.25	0.896
2km, 1h	2.316	8.33	0.891
2km, 15 min	2.392	8.60	0.880
Hoorn-A Helipad Oil Platform (lat = 57.2833°,lon = 1.65°)			
ERA5	3.7	10.70	0.962
MAR			
30km, 6h	3.115	11.20	0.889
30km, 3h	2.903	10.44	0.917
30km, 1h	2.834	10.19	0.926
30km, 15 min	2.850	10.25	0.927
20km, 6h	3.084	11.09	0.887
20km, 3h	2.860	10.29	0.915
20km, 1h	2.801	10.07	0.921
20km, 15 min	2.772	9.97	0.922
10km, 6h	3.067	11.03	0.877
10km, 3h	2.813	10.12	0.908
10km, 1h	2.737	9.85	0.915
10km, 15 min	2.741	9.86	0.914
5km, 6h	2.926	10.53	0.880
5km, 3h	2.662	9.58	0.909
5km, 1h	2.598	9.34	0.914
5km, 15 min	2.598	9.35	0.912
2km, 6h	3.099	11.15	0.868
2km, 3h	2.857	10.28	0.893
2km, 1h	2.803	10.08	0.895
2km, 15 min	2.805	10.09	0.892

Forcing	RMSE (m/s)	NRMSE (-)	Correlation (-)
Marnock Oil Platform (lat = 54.0167°,lon = 1.1°)			
ERA5	2.3	7.95	0.883
MAR			
30km, 6h	4.462	12.97	0.842
30km, 3h	4.247	12.35	0.878
30km, 1h	4.185	12.17	0.891
30km, 15 min	4.168	12.12	0.892
20km, 6h	4.475	13.01	0.837
20km, 3h	4.286	12.46	0.865
20km, 1h	4.209	12.24	0.879
20km, 15 min	4.185	12.17	0.883
10km, 6h	4.283	12.45	0.847
10km, 3h	4.080	11.86	0.875
10km, 1h	3.996	11.62	0.888
10km, 15 min	3.966	11.53	0.892
5km, 6h	4.286	12.46	0.838
5km, 3h	4.074	11.84	0.866
5km, 1h	3.981	11.57	0.877
5km, 15 min	3.969	11.54	0.877
2km, 6h	4.453	12.95	0.830
2km, 3h	4.257	12.38	0.853
2km, 1h	4.167	12.11	0.864
2km, 15 min	4.132	12.01	0.864
Ravenspurn N Oil Platform (lat = 54.3167°,lon = 2.9333°)			
ERA5	2.3	7.95	0.883
MAR			
30km, 6h	2.751	9.52	0.816
30km, 3h	2.585	8.94	0.842
30km, 1h	2.521	8.72	0.853
30km, 15 min	2.493	8.63	0.857
20km, 6h	2.752	9.52	0.801
20km, 3h	2.576	8.91	0.829
20km, 1h	2.486	8.60	0.844
20km, 15 min	2.480	8.58	0.846
10km, 6h	2.646	9.16	0.811
10km, 3h	2.484	8.60	0.836
10km, 1h	2.387	8.26	0.851
10km, 15 min	2.375	8.22	0.853
5km, 6h	2.593	8.97	0.816
5km, 3h	2.428	8.40	0.841
5km, 1h	2.318	8.02	0.857
5km, 15 min	2.313	8.00	0.859
2km, 6h	2.601	9.00	0.819
2km, 3h	2.436	8.43	0.843
2km, 1h	2.338	8.09	0.857
2km, 15 min	2.332	8.07	0.859

Table 6.2.2: (continued)

Forcing	RMSE (m/s)	NRMSE (-)	Correlation (-)
Marollegat (lat = 51.483°,lon = 4.2°)			
ERA5	2.4	13.31	0.931
MAR			
30km, 6h	2.000	11.11	0.860
30km, 3h	1.840	10.22	0.892
30km, 1h	1.783	9.91	0.902
30km, 15 min	1.753	9.74	0.903
20km, 6h	1.826	10.14	0.870
20km, 3h	1.663	9.24	0.898
20km, 1h	1.619	8.99	0.904
20km, 15 min	1.653	9.18	0.903
10km, 6h	1.665	9.25	0.875
10km, 3h	1.502	8.34	0.904
10km, 1h	1.500	8.33	0.906
5km, 6h	1.839	10.22	0.870
5km, 3h	1.714	9.52	0.899
5km, 1h	1.744	9.69	0.898
5km, 15 min	1.816	10.09	0.896
2km, 6h	1.959	10.88	0.871
2km, 3h	1.901	10.56	0.891
2km, 1h	1.949	10.83	0.890
2km, 15 min	2.003	11.13	0.887
Woensdrecht (lat = 51.4491°,lon = 4.342°)			
ERA5	1.2	7.79	0.898
MAR			
30km, 6h	2.007	12.54	0.806
30km, 3h	1.929	12.05	0.847
30km, 1h	1.897	11.86	0.867
30km, 15 min	2.006	12.54	0.872
20km, 6h	1.832	11.45	0.816
20km, 3h	1.766	11.04	0.850
20km, 1h	1.754	10.96	0.861
20km, 15 min	1.655	10.35	0.862
10km, 6h	2.340	14.63	0.837
10km, 3h	2.314	14.46	0.871
10km, 1h	2.331	14.57	0.882
10km, 15 min	2.215	13.85	0.881
5km, 6h	1.889	11.81	0.826
5km, 3h	1.844	11.52	0.860
5km, 1h	1.863	11.65	0.864
5km, 15 min	1.767	11.05	0.862
2km, 6h	1.777	11.11	0.804
2km, 3h	1.730	10.81	0.836
2km, 1h	1.750	10.94	0.842
2km, 15 min	1.986	12.41	0.841

Forcing	RMSE (m/s)	NRMSE (-)	Correlation (-)
Cadzand (lat = 51.383°,lon = 3.383°)			
ERA5	1.7	9.09	0.862
MAR			
30km, 6h	2.378	12.52	0.683
30km, 3h	2.276	11.98	0.715
30km, 1h	2.188	11.52	0.740
30km, 15 min	2.123	11.18	0.758
20km, 6h	2.364	12.44	0.707
20km, 3h	2.262	11.91	0.740
20km, 1h	2.198	11.57	0.760
20km, 15 min	2.125	11.18	0.770
10km, 6h	2.360	12.42	0.730
10km, 3h	2.244	11.81	0.769
10km, 1h	2.189	11.52	0.787
10km, 15 min	2.225	11.71	0.795
5km, 6h	2.073	10.91	0.775
5km, 3h	1.948	10.25	0.808
5km, 1h	1.900	10.00	0.822
5km, 15 min	1.868	9.83	0.829
2km, 6h	2.124	11.18	0.756
2km, 3h	1.985	10.45	0.789
2km, 1h	1.927	10.14	0.803
2km, 15 min	1.892	9.96	0.813
Hoofdplaat (lat = 51.367°,lon = 3.667°)			
ERA5	1.6	10.15	0.900
MAR			
30km, 6h	1.973	12.33	0.759
30km, 3h	1.808	11.30	0.801
30km, 1h	1.696	10.60	0.827
30km, 15 min	1.636	10.22	0.841
20km, 6h	1.867	11.67	0.791
20km, 3h	1.710	10.69	0.827
20km, 1h	1.638	10.24	0.844
20km, 15 min	1.599	9.99	0.851
10km, 6h	1.986	12.41	0.780
10km, 3h	1.846	11.54	0.819
10km, 1h	1.788	11.18	0.835
10km, 15 min	1.769	11.06	0.841
5km, 6h	1.917	11.98	0.800
5km, 3h	1.763	11.02	0.843
5km, 1h	1.733	10.83	0.855
5km, 15 min	1.650	10.31	0.866
2km, 6h	2.010	12.56	0.791
2km, 3h	1.897	11.85	0.828
2km, 1h	1.881	11.76	0.840
2km, 15 min	1.847	11.55	0.841

Table 6.2.2: (continued)

Forcing	RMSE (m/s)	NRMSE (-)	Correlation (-)
Hansweert (lat = 51.446°,lon = 3.998°)			
ERA5	1.8	10.55	0.935
MAR			
30km, 6h	1.401	8.24	0.904
30km, 3h	1.242	7.31	0.928
30km, 1h	1.195	7.03	0.935
30km, 15 min	1.294	7.61	0.933
20km, 6h	1.259	7.41	0.909
20km, 3h	1.127	6.63	0.928
20km, 1h	1.115	6.56	0.931
20km, 15 min	1.149	6.76	0.927
10km, 6h	1.669	9.82	0.907
10km, 3h	1.617	9.51	0.927
10km, 1h	1.643	9.66	0.927
10km, 15 min	1.696	9.97	0.924
5km, 6h	1.667	9.80	0.895
5km, 3h	1.624	9.55	0.913
5km, 1h	1.672	9.83	0.911
5km, 15 min	1.683	9.90	0.904
2km, 6h	1.923	11.31	0.884
2km, 3h	1.881	11.07	0.906
2km, 1h	1.935	11.38	0.904
2km, 15 min	2.040	12.00	0.899
Westdorpe (lat = 51.233°,lon = 3.867°)			
ERA5	1.0	6.32	0.923
MAR			
30km, 6h	1.792	11.20	0.817
30km, 3h	1.662	10.39	0.860
30km, 1h	1.584	9.90	0.884
30km, 15 min	1.558	9.74	0.891
20km, 6h	1.850	11.56	0.828
20km, 3h	1.726	10.78	0.873
20km, 1h	1.666	10.41	0.892
20km, 15 min	1.659	10.37	0.896
10km, 6h	1.847	11.54	0.830
10km, 3h	1.735	10.84	0.874
10km, 1h	1.704	10.65	0.889
10km, 15 min	1.712	10.70	0.893
5km, 6h	1.784	11.15	0.842
5km, 3h	1.670	10.44	0.887
5km, 1h	1.660	10.37	0.899
5km, 15 min	1.658	10.36	0.899
2km, 6h	1.799	11.24	0.827
2km, 3h	1.694	10.59	0.873
2km, 1h	1.695	10.59	0.884
2km, 15 min	1.704	10.65	0.880

Forcing	RMSE (m/s)	NRMSE (-)	Correlation (-)
West Sole Oil Platform (lat = 53.7°,lon = 1.1333°)			
ERA5	2.5	9.88	0.968
MAR			
30km, 6h	3.034	12.04	0.884
30km, 3h	2.828	11.22	0.915
30km, 1h	2.768	10.99	0.925
30km, 15 min	2.791	11.07	0.927
20km, 6h	2.801	11.12	0.889
20km, 3h	2.576	10.22	0.920
20km, 1h	2.495	9.90	0.931
20km, 15 min	2.491	9.89	0.931
10km, 6h	2.693	10.69	0.889
10km, 3h	2.441	9.69	0.921
10km, 1h	2.353	9.34	0.931
10km, 15 min	2.362	9.37	0.929
5km, 6h	2.580	10.24	0.890
5km, 3h	2.307	9.15	0.922
5km, 1h	2.205	8.75	0.932
5km, 15 min	2.225	8.83	0.930
2km, 6h	2.694	10.69	0.883
2km, 3h	2.432	9.65	0.914
2km, 1h	2.333	9.26	0.924
2km, 15 min	2.356	9.35	0.921
VLISSINGEN (lat = 51.45°,lon = 3.6°)			
ERA5	1.9	9.01	0.907
MAR			
30km, 6h	1.664	7.71	0.880
30km, 3h	1.509	6.99	0.904
30km, 1h	1.452	6.72	0.913
30km, 15 min	1.589	7.36	0.910
20km, 6h	1.556	7.20	0.886
20km, 3h	1.437	6.65	0.903
20km, 1h	1.441	6.67	0.903
20km, 15 min	1.476	6.83	0.898
10km, 6h	1.612	7.46	0.883
10km, 3h	1.432	6.63	0.909
10km, 1h	1.442	6.68	0.907
10km, 15 min	1.508	6.98	0.902
5km, 6h	1.603	7.42	0.884
5km, 3h	1.503	6.96	0.904
5km, 1h	1.518	7.03	0.905
5km, 15 min	1.603	7.42	0.899
2km, 6h	1.690	7.83	0.867
2km, 3h	1.528	7.08	0.897
2km, 1h	1.530	7.08	0.900
2km, 15 min	1.540	7.10	0.890

of the peak water level stays within ±10 min of that of the 15 min simulation over most of the domain.

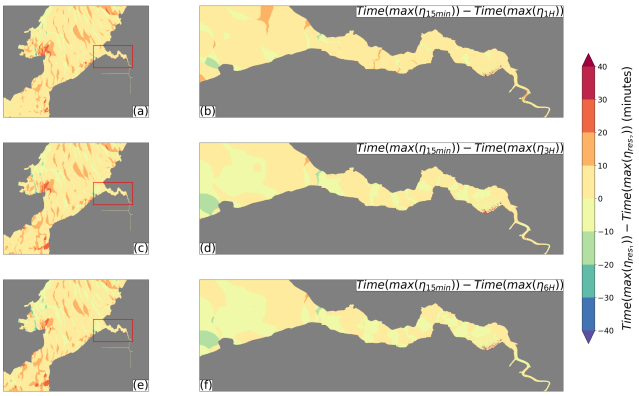

Figure 6.2.1: Timing differences in peak water levels during the storm surge between the reference simulation with 2 km resolution and 15 min atmospheric forcing, and simulations with coarser temporal resolution: (a-b) 1 h, (c-d) 3 h, and (e-f) 6 h intervals. The color scale indicates the deviation in peak timing from the reference, measured in minutes. The left panels depict the coastal North Sea, while the right panels present close-up views of the Scheldt estuary.

6.3 Appendix to Chapter 4: Future storm surges in the Scheldt–North Sea continuum

6.3.1 Statistical analysis

The tests are defined as follows.

Group contrasts. The two-group (zone) contrast is tested with the Mann–Whitney U test (Mann et al., 1947). The test pools the values of both groups, ranks them together, and asks whether the values of one group tend to rank systematically higher than those of the other; the statistic U counts, over all pairs formed of one Scheldt and one North Sea value, how often the first exceeds the second. Because only ranks enter the computation, the test makes no assumption on the shape of the underlying distributions and is insensitive to outliers. A small p-value indicates an ordering of the two zones too systematic to arise from the internal variability of the panel alone.

Table 6.3.1: Overview of the statistical analysis of Chapter 4: the question asked, how the panel is reduced to answer it, the test, and how multiple testing is handled. Test definitions are given in Section 4.2.7 and below.

Question	Reduction	Test	Multiple testing
Does the estuary respond differently from the open sea?	Pooled by zone	Mann–Whitney U	None; descriptive, with the difference of zone medians
Does the track typology discriminate the response?	Worst-affected gauge	Kruskal–Wallis, then pairwise Mann–Whitney	Holm, over the six pairwise contrasts of each metric
Where along the continuum does the typology matter?	Per gauge	Kruskal–Wallis	None; descriptive spatial pattern
Exploratory, Appendix 6.3.3			
Does the response intensify over the century?	Worst-affected gauge	OLS and Theil–Sen with Mann–Kendall	Holm, over the twelve zone-level tests

The four-group (typology) contrast is tested with the Kruskal–Wallis test (Kruskal et al., 1952), the extension of the Mann–Whitney test to more than two groups. A significant result establishes that the typologies differ, not which pair differs; where it is significant, pairwise Mann–Whitney comparisons locate the contrast. Because six pairwise tests are then run per metric, each carrying its own 5 % false-positive risk, the family of p-values is adjusted with the sequential correction of Holm (1979), which keeps the probability of even one spurious rejection across the whole family below α; only Holm-adjusted p-values are reported as significant. Under the conditional reading of Section 4.2.7, this correction separates contrasts robust within the panel from those carried by one or two influential events — a distinction that matters given that the smallest typology comprises only four storms.

Table 6.3.2 synthesises the tests reported in the Results and the exploratory trend tests of Appendix 6.3.3: five of the six surge metrics separate the two zones, one typology contrast survives correction, and no trend survives the rank-based test.

Table 6.3.2: Synthesis of the statistical analyses for each surge metric ($n = 65$ storms; test definitions and notation: Section 4.2.7). **Zone contrast**: direction of the difference between the Scheldt and the North Sea reference zone (Cuxhaven excluded), with the difference of zone medians in the units of the metric, and the Mann–Whitney p-value. Because neighbouring stations record the same surge wave, these pooled p-values are read as descriptive of the panel rather than as exact probabilities (Section 4.2.7); they are reported against a threshold for that reason. **Typology**: Kruskal–Wallis p-value across the four track typologies, one value per storm (worst-affected gauge per metric). **Century-scale trends**, per zone on identical series (worst-affected gauge per storm): ordinary least-squares slope per decade with p_{OLS} in parentheses (slopes with $p_{\mathrm{OLS}} \leq 0.05$ in bold), and Theil–Sen slope per decade with the Holm-adjusted Mann–Kendall p-value (family of twelve zone-level tests). No Theil–Sen slope carries $p_{\mathrm{Holm}} < 0.05$: the least-squares slopes do not survive the rank-based, corrected test on the same series. Pooled across all gauges, the peak-surge OLS slope is $+0.068$ m per decade ($p_{\mathrm{OLS}} = 0.080$). The per-typology and per-station tests are reported in Appendix 6.3.3.

	Zone contrast			Typology	Trend, Scheldt (per dec.)		Trend, North Sea (per dec.)	
Metric	Direction	Δ median	p_U	p_{KW}	OLS	Theil–Sen	OLS	Theil–Sen
Positive surge								
$r^{+}_{\max}$	Scheldt higher	+0.46 m	< 0.001	0.29	**+0.087** m (0.016)	+0.074 (p_{Holm}=0.37)	+0.050 m (0.054)	+0.045 (p_{Holm}=0.41)
Skew surge HW	Scheldt higher	+0.20 m	< 0.001	0.19	**+0.076** m (0.045)	+0.063 (p_{Holm}=0.65)	**+0.055** m (0.038)	+0.045 (p_{Holm}=0.37)
I^{+}	Scheldt higher	+3.45 m h	< 0.001	0.34	**+1.73** m h (0.026)	+1.32 (p_{Holm}=0.27)	+0.73 m h (0.24)	+0.81 (p_{Holm}=0.97)
Negative surge								
$r^{-}_{\min}$	Scheldt deeper	−0.18 m	< 0.001	0.15	+0.021 m (0.41)	+0.020 (p_{Holm}=1)	+0.025 m (0.33)	+0.003 (p_{Holm}=1)
Skew surge LW [a]	Scheldt deeper	−0.09 m	< 0.001	**0.007**	+0.022 m (0.43)	+0.023 (p_{Holm}=1)	+0.016 m (0.52)	−0.008 (p_{Holm}=1)
I^{-} [b]	no contrast	—	0.49	0.65	+0.50 m h (0.17)	+0.01 (p_{Holm}=1)	+0.12 m h (0.79)	−0.09 (p_{Holm}=1)

[a] Holm-significant pairwise contrast: Scandinavian vs. Skagerrak, $p_{\mathrm{Holm}} = 0.0022$.
[b] I^{-} is negative by the sign of the residual it integrates (Section 4.2.6), so a positive slope denotes a weakening of the cumulative drawdown.

6.3.2 Retained storm-surge event catalogue

Table 6.3.3 lists the 65 surge events of the panel in chronological order, together with the track descriptors used for their dynamical classification and the resulting typology.

Table 6.3.3: Catalogue of the **65 surge events** constituting the panel, listed chronologically. The panel combines the 31 events produced by the storms detected atmospherically (stages (i)–(iii)) and the 34 events re-admitted from the simulated response (Section 4.2.4); each event is assigned one of the four track typologies of Section 4.2.5 (Fig. 4.3). **Start** is the onset of the basin-scale surge response (UTC); **Dur.** is the North Sea transit duration; φ_0 is the track-onset latitude; Δlon and Δlat are the net zonal (eastward +) and meridional (northward +) track displacements — final minus initial track position — used for classification (Section 4.2.5).

N°	Start (UTC)	Dur. (h)	φ_0 (°N)	Δlon (°)	Δlat (°)	Storm typology
1	2033-11-23 05:37	12.50	58.22	9.90	2.60	Scandinavian
2	2039-12-24 03:52	15.75	61.33	4.19	−2.79	Jutland
3	2039-12-27 08:37	18.00	59.86	10.98	3.30	Scandinavian
4	2040-01-04 05:07	27.00	56.88	12.04	0.29	Skagerrak
5	2040-01-09 21:22	27.75	59.95	13.12	−4.95	Jutland
6	2040-01-11 03:22	13.50	60.65	15.10	−7.76	Jutland
7	2046-01-04 08:07	12.00	59.33	9.75	2.11	Scandinavian
8	2046-01-13 15:07	3.75	57.26	1.80	1.15	Skagerrak
9	2046-01-22 08:37	20.50	55.69	13.57	−0.11	Jutland
10	2046-01-25 21:22	63.00	58.93	10.81	−1.65	Skagerrak
11	2061-12-19 13:22	26.00	62.21	13.64	−10.63	Jutland
12	2061-12-28 08:07	21.00	57.82	4.61	5.03	Scandinavian
13	2061-12-29 07:07	15.50	52.63	5.96	6.32	Scandinavian
14	2062-01-03 15:07	16.75	57.43	8.64	−2.73	Jutland
15	2062-01-05 05:52	17.00	50.70	12.27	1.97	Southern North Sea
16	2062-01-10 20:07	12.50	55.99	10.22	3.90	Scandinavian
17	2062-01-15 01:07	18.50	51.96	10.30	1.33	Southern North Sea
18	2062-01-19 17:52	9.25	52.73	5.32	−0.24	Southern North Sea
19	2062-12-14 23:37	57.75	56.45	12.73	0.34	Jutland
20	2062-12-17 18:52	20.25	57.81	11.22	−4.93	Jutland

continued on next page

Table 6.3.3 (continued)

Nº	Start (UTC)	Dur. (h)	φ_0 (°N)	Δlon (°)	Δlat (°)	Storm typology
21	2062-12-19 13:22	3.75	52.56	4.70	−0.39	Southern North Sea
22	2062-12-23 20:52	10.00	57.51	3.63	−1.70	Jutland
23	2066-03-12 13:07	4.75	56.56	5.11	0.63	Jutland
24	2066-03-19 00:07	21.75	56.49	14.73	0.47	Jutland
25	2066-03-27 13:22	12.00	60.00	11.15	0.47	Skagerrak
26	2066-11-29 14:22	12.00	60.74	11.53	2.28	Scandinavian
27	2066-12-07 09:22	17.75	54.97	14.35	0.88	Jutland
28	2066-12-08 03:22	13.00	58.22	4.91	−1.54	Skagerrak
29	2066-12-14 13:07	8.25	57.09	7.03	4.27	Scandinavian
30	2069-12-31 13:22	6.50	62.73	8.75	−0.78	Skagerrak
31	2070-01-04 09:37	13.25	53.18	12.20	0.56	Jutland
32	2070-01-07 02:37	39.75	60.95	11.20	2.29	Scandinavian
33	2073-12-09 18:37	36.00	57.09	12.04	−2.27	Jutland
34	2073-12-14 07:37	6.50	56.47	7.39	−0.17	Jutland
35	2073-12-16 09:07	16.50	60.78	11.93	−1.20	Skagerrak
36	2073-12-18 12:37	26.75	57.81	9.96	−0.80	Skagerrak
37	2073-12-23 14:07	31.75	50.58	2.37	12.30	Scandinavian
38	2075-02-15 15:07	16.25	62.14	13.16	−4.77	Jutland
39	2075-02-17 07:37	8.75	62.83	2.79	−0.98	Skagerrak
40	2078-11-28 10:37	15.75	59.31	3.15	−6.85	Jutland
41	2078-12-12 08:22	18.00	56.86	10.86	6.43	Scandinavian
42	2079-01-01 01:22	4.50	59.07	2.46	−1.24	Skagerrak
43	2079-01-05 00:07	5.25	53.96	4.14	−0.67	Jutland
44	2079-03-21 03:52	10.25	58.27	8.10	2.51	Scandinavian
45	2079-03-22 19:37	10.00	59.73	7.79	3.36	Scandinavian
46	2079-03-24 01:07	27.00	54.05	8.56	7.09	Scandinavian

continued on next page

Table 6.3.3 (continued)

N°	Start (UTC)	Dur. (h)	φ_0 (°N)	Δlon (°)	Δlat (°)	Storm typology
47	2079-11-19 10:22	16.50	62.21	9.27	1.06	Skagerrak
48	2079-11-20 20:07	13.50	54.96	13.93	−0.40	Jutland
49	2079-11-27 15:07	16.00	57.28	8.93	4.31	Scandinavian
50	2079-11-30 00:52	19.00	57.38	10.93	2.29	Scandinavian
51	2081-10-31 10:52	20.00	50.01	9.82	9.53	Scandinavian
52	2084-11-04 06:52	24.00	53.42	12.05	4.57	Scandinavian
53	2084-11-09 03:07	14.25	60.61	11.94	−0.54	Skagerrak
54	2085-01-16 20:37	16.25	53.32	9.96	5.54	Scandinavian
55	2085-01-18 22:22	41.00	61.47	−8.45	−3.46	Skagerrak
56	2085-02-19 07:07	8.25	54.31	7.10	0.13	Jutland
57	2085-02-24 22:37	23.00	58.36	12.15	−1.88	Skagerrak
58	2085-02-26 19:07	45.75	56.61	14.92	0.27	Skagerrak
59	2093-02-03 11:37	12.50	60.03	16.13	−4.19	Jutland
60	2093-12-28 16:22	23.25	56.38	11.32	2.34	Scandinavian
61	2093-12-30 17:22	15.25	59.00	9.67	−1.58	Skagerrak
62	2094-01-08 19:22	14.25	55.22	12.85	−0.14	Jutland
63	2094-01-10 16:52	14.00	56.07	3.26	0.75	Jutland
64	2096-11-29 19:22	22.75	52.53	13.94	5.51	Scandinavian
65	2096-12-03 19:52	6.75	48.50	6.62	2.40	Scandinavian

6.3.3 Exploratory century-scale tests

Method. These tests are exploratory. The panel is a sample of discrete events selected for their extreme character and unevenly spread in time, not a continuous series, so their results are not used in the Results of Chapter 4 (Section 4.4.4). Whether the surge metrics change across 2033–2096 is examined per zone, on the worst-affected gauge of each storm, with two estimators of different sensitivity applied to the same series. Ordinary least squares (OLS) gives the standard linear slope; because each event enters through its squared deviation from the mean date, a few severe events in a densely sampled decade can dominate it. The rank-based counterpart combines the Mann–Kendall test (Mann, 1945; Kendall et al., 1962), which counts over all pairs of events whether the later value is higher or lower than the earlier one, with the Theil–Sen slope (Theil, 1950; Sen, 1968), the median of all pairwise slopes; this pairing is routinely applied to trend detection in marine extremes (e.g., Wang et al., 2021; Bagnasco et al., 2026). A trend is treated as robust only if it survives the Mann–Kendall test after Holm correction (Appendix 6.3.1), applied to the twelve zone-level tests (six metrics × two zones). The same test is repeated for each typology and each station.

Results. No century-scale change in the surge withstands this test. OLS fits nominally significant positive slopes in the Scheldt, steepest for the peak surge (+0.087 m per decade, $p_{\mathrm{OLS}} = 0.016$), and offshore for the high-water skew surge alone. On the same series, the Mann–Kendall test retains none of them: the lowest adjusted value, for the Scheldt cumulative intensity, is $p_{\mathrm{Holm}} = 0.27$, and the Theil–Sen slopes of the positive-surge metrics are lower than their least-squares counterparts, except for the North Sea cumulative intensity (Table 6.3.2). For each typology, every adjusted p-value is 1. Station by station, 17 of the 26 stations reach nominal significance under least squares, and none survives the corrected rank-based test. No trough, low-water skew or I^- slope is significant in either zone, even under least squares. The disagreement between the two estimators reflects the uneven sampling of the century — three events in the 2030s against twenty in each of the 2060s and 2070s (Section 4.3.1) — and the weight that least squares gives to the late 2093–2096 cluster, not a monotonic rise of the surge.

6.3.4 Sensitivity to the North Sea zone reference definition

A single sensitivity control reversed two results that first pointed toward estuary-specific dynamics: the exclusion of Cuxhaven from the North Sea zone (Section 4.3.3). Cuxhaven is itself an estuary mouth and dominated the reference-zone maximum in 77 % of storms. With it included, the

amplification factor appeared typology-dependent ($p = 0.017$) and Δlat appeared correlated with the amplification ($r = -0.31$). That Cuxhaven behaves estuarine rather than open-sea is well established: its water levels carry the Elbe's own funnelling amplification and have long served as the reference for German Bight storm-tide reconstruction (Meyer et al., 2023; Grabemann et al., 2019; Pein et al., 2023) — precisely what disqualifies it as an open-shelf baseline here.

With Cuxhaven excluded, the amplification factor behaves as a near-constant multiplier: it remains close to its panel median across all four typologies and shows no significant typology dependence (Fig. 6.3.1), and none of the storm-type contrasts survives on the other surge metrics either, with the single exception of low-water skew surge (Table 6.3.2). In any estuary-versus-open-sea comparison, the reference zone is therefore a result-critical choice, to be tested before any conclusion about estuary-specific dynamics is drawn — the spatial analogue of the proxy-point sensitivity that Befort et al. (2015) document for the atmospheric side.

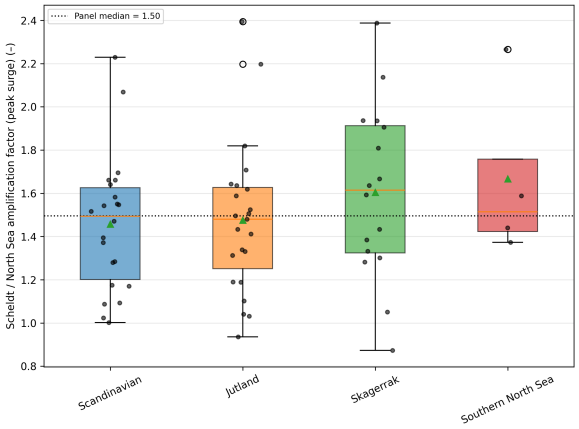

Figure 6.3.1: Per-storm Scheldt / North Sea reference amplification factor for peak surge, by storm typology. The factor is close to its panel median of 1.50 (dotted line) across all types and does not depend significantly on typology (Kruskal–Wallis $p = 0.53$).

Bibliography

Agulles, M., M. Marcos, A. Amores, and T. Toomey (2024). "Storm surge modelling along European coastlines: The effect of the spatio-temporal resolution of the atmospheric forcing". In: *Ocean Modelling* 192, p. 102432.

Al Azad, A. S. M. A., K. S. Mita, M. W. Zaman, M. Akter, T. Z. Asik, A. Haque, M. A. Hussain, and M. M. Rahman (2018). "Impact of tidal phase on inundation and thrust force due to storm surge". en. In: *Journal of Marine Science and Engineering* 6.4, p. 110.

Alaerts, L. (2025). "Multiscale hydrodynamic modelling of the Danube delta". Anglais. phd. Université catholique de Louvain / Université de Liège.

Alaerts, L., T. Dobbelaere, P. M. Gravinese, and E. Hanert (2022). "Climate change will fragment Florida stone crab communities". In: *Frontiers in Marine Science* 9.

Aleksandrova, N., J. Veenstra, and S. Muis (2025). *Global dataset of storm surges and extreme sea levels for 1950–2024 based on the ERA5 climate reanalysis*.

Alexandru, A., R. De Elia, and R. Laprise (2007). "Internal Variability in Regional Climate Downscaling at the Seasonal Scale". en. In: *Monthly Weather Review* 135.9, pp. 3221–3238.

Arndt, S., G. Lacroix, N. Gypens, P. Regnier, and C. Lancelot (2011). "Nutrient dynamics and phytoplankton development along an estuary–coastal zone continuum: A model study". In: *Journal of Marine Systems* 84.3-4, pp. 49–66.

Arns, A., T. Wahl, S. Dangendorf, and J. Jensen (2015). "The impact of sea level rise on storm surge water levels in the northern part of the German Bight". In: *Coastal Engineering* 96, pp. 118–131.

Arns, A., T. Wahl, C. Wolff, A. T. Vafeidis, I. D. Haigh, P. Woodworth, S. Niehüser, and J. Jensen (2020). "Non-linear interaction modulates global extreme sea levels, coastal flood exposure, and impacts". en. In: *Nature Communications* 11.1, p. 1918.

Ayyad, M., M. R. Hajj, and R. Marsooli (2022). "Machine learning-based assessment of storm surge in the New York metropolitan area". en. In: *Scientific Reports* 12.1, p. 19215.

Baeyens, W. (1998). "General description of the Scheldt estuary". en. In: *Trace Metals in the Westerschelde Estuary: A Case-Study of a Polluted, Partially Anoxic Estuary*. Dordrecht: Springer Netherlands, pp. 1–14. ISBN: 978-90-481-5062-5 978-94-017-3573-5.

Bagnasco, T., A. Stocchino, M. I. Vousdoukas, and J. Wang (2026). "Characterization of significant wave height trends in the South China Sea based on wave hindcast results: A non-stationary extreme value approach". In: *Applied Ocean Research* 173, p. 105153.

Baldissera Pacchetti, M., L. Coulter, S. Dessai, T. Shepherd, J. Sillmann, and B. Hurk (2023). "Varieties of approaches to constructing physical climate storylines: A review". In: *Wiley Interdisciplinary Reviews: Climate Change* 15.

Baptist, M., V. Babovic, J. Rodríguez Uthurburu, M. Keijzer, R. Uittenbogaard, A. Mynett, and A. Verwey (2007). "On inducing equations for vegetation resistance". In: *Journal of Hydraulic Research* 45.4, pp. 435–450.

Barbier, E. B., S. D. Hacker, C. Kennedy, E. W. Koch, A. C. Stier, and B. R. Silliman (2011). "The value of estuarine and coastal ecosystem services". en. In: *Ecological Monographs* 81.2, pp. 169–193.

Baulenas, E., G. Versteeg, M. Terrado, J. Mindlin, and D. Bojovic (2023). "Assembling the climate story: use of storyline approaches in climate-related science". en. In: *Global Challenges* 7.7, p. 2200183.

Befort, D. J., M. Fischer, G. C. Leckebusch, U. Ulbrich, A. Ganske, G. Rosenhagen, and H. Heinrich (2015). "Identification of storm surge events over the German Bight from atmospheric reanalysis and climate model data". English. In: *Natural Hazards and Earth System Sciences* 15.6, pp. 1437–1447.

Benoit, M., D. Aelbrecht, G. Bellue, M. Luck, and D. Violeau (2002). "Propagation des houles et des surcotes extrêmes vers les côtes

et estuaires apports de la modélisation numérique". In: *La Houille Blanche* 88.2, pp. 86–89.

Bevacqua, E., D. Maraun, M. I. Vousdoukas, E. Voukouvalas, M. Vrac, L. Mentaschi, and M. Widmann (2019). "Higher probability of compound flooding from precipitation and storm surge in Europe under anthropogenic climate change". In: *Science Advances* 5.9, eaaw5531.

Bevacqua, E., M. I. Vousdoukas, G. Zappa, K. Hodges, T. G. Shepherd, D. Maraun, L. Mentaschi, and L. Feyen (2020). "More meteorological events that drive compound coastal flooding are projected under climate change". en. In: *Communications Earth & Environment* 1.1, p. 47.

Bijl, W (1997). "Impact of a wind climate change on the surge in the southern North Sea". en. In: *Climate Research* 8, pp. 45–59.

Boer, G. J. and M. Lazare (1988). "Some Results Concerning the Effect of Horizontal Resolution and Gravity–Wave Drag on Simulated Climate". EN. In: *Journal of Climate* 1.8, pp. 789–806.

Bormann, H., J. Kebschull, L. Gaslikova, and R. Weisse (2024). "Model-based assessment of climate change impact on inland flood risk at the German North Sea coast caused by compounding storm tide and precipitation events". English. In: *Natural Hazards and Earth System Sciences* 24.7, pp. 2559–2576.

Bouwer, L. M. and S. N. Jonkman (2018). "Global mortality from storm surges is decreasing". en. In: *Environmental Research Letters* 13.1, p. 014008.

Brajkovic, J., X. Fettweis, B. Noël, H. V. D. Vyver, N. Ghilain, P. Archambeau, M. Pirotton, and S. Doutreloup (2025). "Increased intensity and frequency of extreme precipitation events in Belgium as simulated by the regional climate model MAR". In: *Journal of Hydrology: Regional Studies* 59, p. 102399.

Breitburg, D., L. A. Levin, A. Oschlies, M. Grégoire, F. P. Chavez, D. J. Conley, V. Garçon, D. Gilbert, D. Gutiérrez, K. Isensee, G. S. Jacinto, K. E. Limburg, I. Montes, S. W. A. Naqvi, G. C. Pitcher, N. N. Rabalais, M. R. Roman, K. A. Rose, B. A. Seibel, M. Telszewski, M. Yasuhara, and J. Zhang (2018). "Declining oxygen in the global ocean and coastal waters". In: *Science* 359.6371, eaam7240.

Broekx, S., S. Smets, I. Liekens, D. Bulckaen, and L. De Nocker (2011). "Designing a long-term flood risk management plan for the Scheldt estuary using a risk-based approach". en. In: *Natural Hazards* 57.2, pp. 245–266.

Brown, J. M., J. Wolf, and A. J. Souza (2012). "Past to future extreme events in Liverpool Bay: model projections from 1960–2100". en. In: *Climatic Change* 111.2, pp. 365–391.

Burlace, M. I. (1986). "The negative North Sea surge of the 19th December 1982". en. In: *Hydrographic Journal* 39, pp. 11–15.

Calafat, F. M., T. Wahl, M. G. Tadesse, and S. N. Sparrow (2022). "Trends in Europe storm surge extremes match the rate of sea-level rise". en. In: *Nature* 603.7903, pp. 841–845.

Camus, P., I. D. Haigh, N. Quinn, T. Wahl, T. Benson, B. Gouldby, A. A. Nasr, M. M. Rashid, A. R. Enríquez, S. E. Darby, R. J. Nicholls, and N. C. Nadal-Caraballo (2024). "Tracking the spatial footprints of extreme storm surges around the coastline of the UK and Ireland". In: *Weather and Climate Extremes* 44, p. 100662.

Carstensen, J., R. Klais, and J. E. Cloern (2015). "Phytoplankton blooms in estuarine and coastal waters: Seasonal patterns and key species". In: *Estuarine, Coastal and Shelf Science*. Special Issue: Global Patterns of Phytoplankton Dynamics in Coastal Ecosystems 162, pp. 98–109.

Carter, G. S. and M. A. Merrifield (2007). "Open boundary conditions for regional tidal simulations". In: *Ocean Modelling* 18.3, pp. 194–209.

Chen, C., H. Liu, and R. C. Beardsley (2003). "An Unstructured Grid, Finite-Volume, Three-Dimensional, Primitive Equations Ocean Model: Application to Coastal Ocean and Estuaries". EN. In: *Journal of Atmospheric and Oceanic Technology* 20.1, pp. 159–186.

Chen, C., J. Qi, C. Li, R. C. Beardsley, H. Lin, R. Walker, and K. Gates (2008). "Complexity of the flooding/drying process in an estuarine tidal-creek salt-marsh system: An application of FVCOM". en. In: *Journal of Geophysical Research: Oceans* 113.C7.

Chen, F., Z. Li, K. Ding, Z. Sun, and H. Zhou (2023a). "Assessment and integration of ERA5 Reanalysis and Fujita-Takahashi models for storm surge prediction in the East China sea". en. In: *Applied Sciences* 13.19, p. 10658.

Chen, Z. and P. M. Orton (2023b). "Effects of Storm Surge Barrier Closures on Estuary Saltwater Intrusion and Stratification". en. In: *Water Resources Research* 59.3, e2022WR032317.

Cheng, J. and P. Wang (2019). "Unusual beach changes induced by Hurricane Irma with a negative storm surge and poststorm recovery". In: *Journal of Coastal Research* 35.6, p. 1185.

Choudhary, G. K., C. J. Trahan, L. Pettey, M. Farthing, C. Berger, G. Savant, E. Inanc, C. Dawson, and M. Loveland (2025). "Strongly Coupled 2D and 3D Shallow Water Models: Theory and Verification". en. In: *Journal of Hydraulic Engineering* 151.1, p. 04024049.

Cid, A., M. Menéndez, S. Castanedo, A. J. Abascal, F. J. Méndez, and R. Medina (2016). "Long-term changes in the frequency, intensity and duration of extreme storm surge events in southern Europe". en. In: *Climate Dynamics* 46.5, pp. 1503–1516.

Cockburn, B., G. E. Karniadakis, and C.-W. Shu (2000). "The Development of Discontinuous Galerkin Methods". en. In: *Discontinuous Galerkin Methods*. Ed. by B. Cockburn, G. E. Karniadakis, and C.-W. Shu. Berlin, Heidelberg: Springer, pp. 3–50. ISBN: 978-3-642-59721-3.

Codiga, D. (2011). *Unified tidal analysis and prediction using the UTide Matlab functions*.

Coles, S. (2001). "A point process characterization of extremes". en. In: *An Introduction to Statistical Modeling of Extreme Values*. Ed. by S. Coles. London: Springer, pp. 124–141. ISBN: 978-1-4471-3675-0.

Colle, B. A., M. J. Bowman, K. J. Roberts, M. H. Bowman, C. N. Flagg, J. Kuang, Y. Weng, E. B. Munsell, and F. Zhang (2015). "Exploring water level sensitivity for Metropolitan New York during Sandy (2012) using ensemble storm surge simulations". en. In: *Journal of Marine Science and Engineering* 3.2, pp. 428–443.

Conte, D. and P. Lionello (2013). "Characteristics of large positive and negative surges in the Mediterranean Sea and their attenuation in future climate scenarios". In: *Global and Planetary Change* 111, pp. 159–173.

Corkan, R. H. (1948). *Storm surges in the North Sea*. Tech. rep. 15072.

Cosby, A. G., V. Lebakula, C. N. Smith, D. W. Wanik, K. Bergene, A. N. Rose, D. Swanson, and D. E. Bloom (2024). "Accelerating growth of human coastal populations at the global and continent levels: 2000–2018". en. In: *Scientific Reports* 14.1, p. 22489.

Costanza, R., R. de Groot, P. Sutton, S. van der Ploeg, S. J. Anderson, I. Kubiszewski, S. Farber, and R. K. Turner (2014). "Changes in the global value of ecosystem services". In: *Global Environmental Change* 26, pp. 152–158.

Cox, T., T. Maris, P. De Vleeschauwer, T. De Mulder, K. Soetaert, and P. Meire (2006). "Flood control areas as an opportunity to restore estuarine habitat". In: *Ecological Engineering* 28.1, pp. 55–63.

Cucco, A., G. Quattrocchi, and S. Zecchetto (2019). "The role of temporal resolution in modeling the wind induced sea surface transport in coastal seas". In: *Journal of Marine Systems* 193, pp. 46–58.

Curcic, M. and B. K. Haus (2020). "Revised estimates of ocean surface drag in strong winds". en. In: *Geophysical Research Letters* 47.10, e2020GL087647.

Cushman-Roisin, B. and J.-M. Beckers (2011). *Introduction to Geophysical Fluid Dynamics - Physical and Numerical Aspects*. en. Vol. 101. International Geophysics. Elsevier. ISBN: 978-0-12-088759-0.

De Brye, B., A. de Brauwere, O. Gourgue, T. Kärnä, J. Lambrechts, R. Comblen, and E. Deleersnijder (2010). "A finite-element, multi-scale model of the Scheldt tributaries, river, estuary and ROFI". en. In: *Coastal Engineering* 57.9, pp. 850–863.

De Vries, H., M. Breton, T. de Mulder, Y. Krestenitis, J. Ozer, R. Proctor, K. Ruddick, J. C. Salomon, and A. Voorrips (1995). "A comparison of 2D storm surge models applied to three shallow European seas". en. In: *Environmental Software* 10.1, pp. 23–42.

De Winter, R. C., A. Sterl, and B. G. Ruessink (2013). "Wind extremes in the North Sea Basin under climate change: An ensemble study of 12 CMIP5 GCMs". en. In: *Journal of Geophysical Research: Atmospheres* 118.4, pp. 1601–1612.

De Le Court, M., V. Legat, A. P. Ishimwe, C. Scherpereel, E. Hanert, and J. Lambrechts (2026). "An efficient multi-GPU implementation for the Discontinuous Galerkin ocean model SLIM". In: *ArXiv Preprint*.

Deb, M., J. J. Benedict, N. Sun, Z. Yang, R. D. Hetland, D. Judi, and T. Wang (2024). "Estuarine hurricane wind can intensify surge-dominated extreme water level in shallow and converging coastal systems". English. In: *Natural Hazards and Earth System Sciences* 24.7, pp. 2461–2479.

Deb, S., H. Xue, and S. Rao (2020). "Storm surge inundation modeling of five winter storms in Saco-Casco Bays: A FVCOM based numerical study". In: *IGARSS 2020 - 2020 IEEE International Geoscience and Remote Sensing Symposium*, pp. 5745–5748.

Debreu, L., P. Marchesiello, P. Penven, and G. Cambon (2012). "Two-way nesting in split-explicit ocean models: Algorithms, implementation and validation". en. In: *Ocean Modelling* 49-50, pp. 1–21.

Deppermann, C. E. (1947). "Notes on the origin and structure of Philippine typhoons". In: *Bulletin of the American Meteorological Society* 28.9, pp. 399–404.

Dinapoli, M. G., C. G. Simionato, and D. Moreira (2020). "Development and validation of a storm surge forecasting/hindcasting modelling system for the extensive Rio de la Plata Estuary and its adjacent Continental Shelf". en. In: *Natural Hazards* 103.2, pp. 2231–2259.

Done, J. M., M. Ge, G. J. Holland, I. Dima-West, S. Phibbs, G. R. Saville, and Y. Wang (2020). "Modelling global tropical cyclone wind footprints". English. In: *Natural Hazards and Earth System Sciences* 20.2, pp. 567–580.

Donelan, M. A., B. K. Haus, N. Reul, W. J. Plant, M. Stiassnie, H. C. Graber, O. B. Brown, and E. S. Saltzman (2004). "On the limiting aerodynamic roughness of the ocean in very strong winds". en. In: *Geophysical Research Letters* 31.18.

Dong, B., B. Huang, C. Tan, J. Xia, K. Lin, S. Gao, and Y. Hu (2025). "Multi-GPU parallelization of shallow water modelling on unstructured meshes". In: *Journal of Hydrology* 657, p. 133105.

Dronkers, J. (1986). "Tidal asymmetry and estuarine morphology". In: *Netherlands Journal of Sea Research* 20.2, pp. 117–131.

Dube, S. K., T. S. Murty, J. C. Feyen, R. Cabrera, B. A. Harper, J. D. Bales, and S. Amer (2010). "Storm surge modeling and applications in coastal areas". en. In: *World Scientific Series on Asia-Pacific Weather*

and Climate. Vol. 4. World Scientific, pp. 363–406. ISBN: 978-981-4293-47-1 978-981-4293-48-8.

Dullaart, J. C. M., S. Muis, H. de Moel, P. J. Ward, D. Eilander, and J. C. J. H. Aerts (2023). "Enabling dynamic modelling of coastal flooding by defining storm tide hydrographs". English. In: *Natural Hazards and Earth System Sciences* 23.5, pp. 1847–1862.

Egbert, G. D., A. F. Bennett, and M. G. G. Foreman (1994). "TOPEX/POSEIDON tides estimated using a global inverse model". en. In: *Journal of Geophysical Research: Oceans* 99.C12, pp. 24821–24852.

Familkhalili, R. and S. A. Talke (2016). "The effect of channel deepening on tides and storm surge: A case study of Wilmington, NC". en. In: *Geophysical Research Letters* 43.17, pp. 9138–9147.

Familkhalili, R., S. A. Talke, and D. A. Jay (2020). "Tide-Storm Surge Interactions in Highly Altered Estuaries: How Channel Deepening Increases Surge Vulnerability". en. In: *Journal of Geophysical Research: Oceans* 125.4, e2019JC015286.

Familkhalili, R., S. A. Talke, and D. A. Jay (2022). "Compound flooding in convergent estuaries: insights from an analytical model". English. In: *Ocean Science* 18.4, pp. 1203–1220.

Feng, D., Z. Tan, D. Engwirda, J. D. Wolfe, D. Xu, C. Liao, G. Bisht, J. J. Benedict, T. Zhou, H.-Y. Li, and L. R. Leung (2024). "Simulation of Compound Flooding Using River-Ocean Two-Way Coupled E3SM Ensemble on Variable-Resolution Meshes". en. In: *Journal of Advances in Modeling Earth Systems* 16.6, e2023MS004054.

Fenoglio-Marc, L., R. Scharroo, A. Annunziato, L. Mendoza, M. Becker, and J. Lillibridge (2015). "Cyclone Xaver seen by geodetic observations". en. In: *Geophysical Research Letters* 42.22, pp. 9925–9932.

Ferrarin, C., A. Roland, M. Bajo, G. Umgiesser, A. Cucco, S. Davolio, A. Buzzi, P. Malguzzi, and O. Drofa (2012). "Tide-surge-wave modelling and forecasting in the Mediterranean Sea with focus on the Italian coast". In: *Ocean Modelling* 61.

Fettweis, X., B. Franco, M. Tedesco, J. H. van Angelen, J. T. M. Lenaerts, M. R. van den Broeke, and H. Gallée (2013). "Estimating the Greenland ice sheet surface mass balance contribution to future

sea level rise using the regional atmospheric climate model MAR". English. In: *The Cryosphere* 7.2, pp. 469–489.

Flambard, J., Y. Amirat, G. Feld, M. Benbouzid, and N. Ruiz (2019). "River and estuary current power overview". en. In: *Journal of Marine Science and Engineering* 7.10, p. 365.

Flather, R. (1976). *Results from a storm surge prediction model of the north-west European continental shelf for April, November and December, 1973*. Tech. rep. 24. Institute of Oceanographic Sciences.

— (2001). "Storm Surges". In: *Encyclopedia of Ocean Sciences*, pp. 2882–2892. ISBN: 978-0-12-227430-5.

Flather, R. A. (1984). "A numerical model investigation of the storm surge of 31 January and 1 February 1953 in the North Sea". en. In: *Quarterly Journal of the Royal Meteorological Society* 110.465, pp. 591–612.

Friedrichs, C. T. and D. G. Aubrey (1988). "Non-linear tidal distortion in shallow well-mixed estuaries: a synthesis". en. In: *Estuarine, Coastal and Shelf Science* 27.5, pp. 521–545.

— (1994). "Tidal propagation in strongly convergent channels". en. In: *Journal of Geophysical Research: Oceans* 99.C2, pp. 3321–3336.

Gallée, H. and G. Schayes (1994). "Development of a three-dimensional meso-gamma primitive equation model: Katabatic winds simulation in the area of Terra Nova Bay, Antarctica". en. In: *Monthly Weather Review* 122, pp. 671–685.

Garner, G. G., T. Hermans, R. E. Kopp, A. B. A. Slangen, T. L. Edwards, A. Levermann, S. Nowicki, M. D. Palmer, C. Smith, B. Fox-Kemper, H. T. Hewitt, C. Xiao, G. Aðalgeirsdóttir, S. S. Drijfhout, N. R. Golledge, M. Hemer, G. Krinner, A. Mix, D. Notz, I. S. Nurhati, L. Ruiz, J.-B. Sallée, Y. Yu, L. Hua, T. Palmer, and B. Pearson (2021). *IPCC AR6 Sea Level Projections*.

Garzon, J. L. and C. M. Ferreira (2016). "Storm surge modeling in large estuaries: sensitivity analyses to parameters and physical processes in the Chesapeake Bay". en. In: *Journal of Marine Science and Engineering* 4.3, p. 45.

Gaslikova, L., I. Grabemann, and N. Groll (2013). "Changes in North Sea storm surge conditions for four transient future climate realizations". en. In: *Natural Hazards* 66.3, pp. 1501–1518.

Geelhoed, P. T. (1973). "Negative surges in the Southern North Sea". en. In: *The International Hydrographic Review*.

Gerber, M., A. Ganske, S. Müller-Navarra, and G. Rosenhagen (2016). "Categorisation of meteorological conditions for storm tide episodes in the German Bight". In: *Meteorologische Zeitschrift* 25, pp. 447–462.

Gerritsen, H. (2005). "What happened in 1953? The Big Flood in the Netherlands in retrospect". en. In: *Philosophical Transactions of the Royal Society A: Mathematical, Physical and Engineering Sciences* 363.1831, pp. 1271–1291.

Geuzaine, C. and J.-F. Remacle (2009). "GMSH: A 3-D finite element mesh generator with built-in pre- and post-processing facilities". en. In: *International Journal for Numerical Methods in Engineering* 79.11, pp. 1309–1331.

Giorgi, F. and X. Bi (2000). "A study of internal variability of a regional climate model". en. In: *Journal of Geophysical Research: Atmospheres* 105.D24, pp. 29503–29521.

Gourgue, O., W. Baeyens, M. S. Chen, A. de Brauwere, B. de Brye, E. Deleersnijder, M. Elskens, and V. Legat (2013). "A depth-averaged two-dimensional sediment transport model for environmental studies in the Scheldt Estuary and tidal river network". en. In: *Journal of Marine Systems* 128, pp. 27–39.

Gourgue, O. (2011). "Finite element modeling of sediment dynamics in the Scheldt". en. PhD thesis. Université catholique de Louvain.

Gourgue, O., R. Comblen, J. Lambrechts, T. Kärnä, V. Legat, and E. Deleersnijder (2009). "A flux-limiting wetting–drying method for finite-element shallow-water models, with application to the Scheldt Estuary". en. In: *Advances in Water Resources* 32.12, pp. 1726–1739.

Gourgue, O., B. B. Sishah, J. Vanlede, H. Komijani, and M. Chen (2015). "Modelling tides and storm surges on the European continental shelf". en. In: *21st Telemac Mascaret user conference*, pp. 21–26.

Grabemann, I., L. Gaslikova, T. Brodhagen, and E. Rudolph (2019). *Very severe storm tides in the German Bight (North Sea) and their potential for enhancement*.

— (2020). "Extreme storm tides in the German Bight (North Sea) and their potential for amplification". English. In: *Natural Hazards and Earth System Sciences* 20.7, pp. 1985–2000.

Grailet, J.-F., R. J. Hogan, N. Ghilain, D. Bolsée, X. Fettweis, and M. Grégoire (2025). "Inclusion of the ECMWF ecRad radiation scheme (v1.5.0) in the MAR (v3.14), regional evaluation for Belgium, and assessment of surface shortwave spectral fluxes at Uccle". English. In: *Geoscientific Model Development* 18.6, pp. 1965–1988.

Gregory, J. M., S. M. Griffies, C. W. Hughes, J. A. Lowe, J. A. Church, I. Fukimori, N. Gomez, R. E. Kopp, F. Landerer, G. L. Cozannet, R. M. Ponte, D. Stammer, M. E. Tamisiea, and R. S. W. van de Wal (2019). "Concepts and Terminology for Sea Level: Mean, Variability and Change, Both Local and Global". en. In: *Surveys in Geophysics* 40.6, pp. 1251–1289.

Haidvogel, D., E. Curchitser, S. Danilov, and B. Fox-Kemper (2017). "Numerical modelling in a multiscale ocean". In: *Journal of Marine Research* 75.6.

Hales, R. C., E. J. Nelson, M. Souffront, A. L. Gutierrez, C. Prudhomme, S. Kopp, D. P. Ames, G. P. Williams, and N. L. Jones (2025). "Advancing global hydrologic modeling with the GEOGloWS ECMWF streamflow service". en. In: *Journal of Flood Risk Management* 18.1, e12859.

Hallegatte, S., N. Ranger, O. Mestre, P. Dumas, J. Corfee-Morlot, C. Herweijer, and R. M. Wood (2011). "Assessing climate change impacts, sea level rise and storm surge risk in port cities: a case study on Copenhagen". en. In: *Climatic Change* 104.1, pp. 113–137.

Harrison, P. A., R. W. Dunford, I. P. Holman, G. Cojocaru, M. S. Madsen, P.-Y. Chen, S. Pedde, and D. Sandars (2019). "Differences between low-end and high-end climate change impacts in Europe across multiple sectors". en. In: *Regional Environmental Change* 19.3, pp. 695–709.

Harvey, B. J., P. Cook, L. C. Shaffrey, and R. Schiemann (2020). "The Response of the Northern Hemisphere Storm Tracks and Jet Streams to Climate Change in the CMIP3, CMIP5, and CMIP6 Climate Models". en. In: *Journal of Geophysical Research: Atmospheres* 125.23, e2020JD032701.

Hasan, G. M. J., D. S. van Maren, and S. K. Ooi (2016). "Hydrodynamic modeling of Singapore's coastal waters: Nesting and model accuracy". In: *Ocean Modelling* 97, pp. 141–151.

Hausfather, Z. and G. P. Peters (2020). "RCP8.5 is a problematic scenario for near-term emissions". en. In: *Proceedings of the National Academy of Sciences* 117.45, pp. 27791–27792.

Heaps, N. S. (1969). "A two-dimensional numerical sea model". In: *Philosophical Transactions of the Royal Society of London, Series A: Mathematical and Physical Sciences* 265.1160, pp. 93–137.

Heinrich, P., S. Hagemann, and R. Weisse (2025). "Automated classification of atmospheric circulation types for compound flood risk assessment: CMIP6 model analysis utilising a deep learning ensemble". In: *Environmental Research Letters* 20.7, p. 074018.

Heinrich, P., S. Hagemann, R. Weisse, and L. Gaslikova (2023). "Changes in compound flood event frequency in northern and central Europe under climate change". English. In: *Frontiers in Climate* 5.

Hermans, T. H. J., J. J. M. Busecke, T. Wahl, V. Malagón-Santos, M. G. Tadesse, R. A. Jane, and R. S. W. van de Wal (2024). "Projecting Changes in the Drivers of Compound Flooding in Europe Using CMIP6 Models". en. In: *Earth's Future* 12.5, e2023EF004188.

Hersbach, H., B. Bell, P. Berrisford, S. Hirahara, A. Horányi, J. Muñoz-Sabater, J. Nicolas, C. Peubey, R. Radu, D. Schepers, A. Simmons, C. Soci, S. Abdalla, X. Abellan, G. Balsamo, P. Bechtold, G. Biavati, J. Bidlot, M. Bonavita, G. De Chiara, P. Dahlgren, D. Dee, M. Diamantakis, R. Dragani, J. Flemming, R. Forbes, M. Fuentes, A. Geer, L. Haimberger, S. Healy, R. J. Hogan, E. Hólm, M. Janisková, S. Keeley, P. Laloyaux, P. Lopez, C. Lupu, G. Radnoti, P. de Rosnay, I. Rozum, F. Vamborg, S. Villaume, and J.-N. Thépaut (2020). "The ERA5 global reanalysis". en. In: *Quarterly Journal of the Royal Meteorological Society* 146.730, pp. 1999–2049.

Hervouet, J.-M. (2007). *Hydrodynamics of Free Surface Flows: Modelling with the Finite Element Method*. en. John Wiley & Sons. ISBN: 978-0-470-03558-0.

Holland, G. (1980). "An analytic model of the wind and pressure profiles in hurricanes". In: *Mon. Weather Rev.* 108, pp. 1212–1218.

Holm, S. (1979). "A Simple Sequentially Rejective Multiple Test Procedure". In: *Scandinavian Journal of Statistics* 6.2, pp. 65–70.

Holt, J. and R. Proctor (2008). "The seasonal circulation and volume transport on the northwest European continental shelf: A fine-resolution model study". en. In: *Journal of Geophysical Research: Oceans* 113.C6, 2006JC004034.

Holthuijsen, L. H., M. D. Powell, and J. D. Pietrzak (2012). "Wind and waves in extreme hurricanes". en. In: *Journal of Geophysical Research: Oceans* 117.C9.

Hong, S.-Y. and M. Kanamitsu (2014). "Dynamical downscaling: Fundamental issues from an NWP point of view and recommendations". en. In: *Asia-Pacific Journal of Atmospheric Sciences* 50.1, pp. 83–104.

Horsburgh, K. J. and C. Wilson (2007). "Tide-surge interaction and its role in the distribution of surge residuals in the North Sea". en. In: *Journal of Geophysical Research: Oceans* 112.C8, 2006JC004033.

Horsburgh, K., I. D. Haigh, J. Williams, M. De Dominicis, J. Wolf, A. Inayatillah, and D. Byrne (2021). ""Grey swan" storm surges pose a greater coastal flood hazard than climate change". en. In: *Ocean Dynamics* 71.6, pp. 715–730.

Hsiao, S.-C., W.-S. Chiang, J.-H. Jang, H.-L. Wu, W.-S. Lu, W.-B. Chen, and Y.-T. Wu (2021). "Flood risk influenced by the compound effect of storm surge and rainfall under climate change for low-lying coastal areas". In: *Science of The Total Environment* 764, p. 144439.

Hu, K., Q. Chen, and H. Wang (2015). "A numerical study of vegetation impact on reducing storm surge by wetlands in a semi-enclosed estuary". In: *Coastal Engineering* 95, pp. 66–76.

Hurrell, J. W. and C. Deser (2009). "North Atlantic climate variability: The role of the North Atlantic Oscillation". In: *Journal of Marine Systems* 78.1, pp. 28–41.

Hussain, M. A., Y. Tajima, M. A. Hossain, and P. Das (2017). "Impact of cyclone track features and tidal phase shift upon surge characteristics in the Bay of Bengal along the Bangladesh Coast". en. In: *Journal of Marine Science and Engineering* 5.4, p. 52.

Huybrechts, N, C Villaret, and J.-M. Hervouet (2010). "Comparison between 2D and 3D modelling of sediment transport: application to the dune evolution". en. In: *River Flow* 4, pp. 887–893.

Idier, D., F. Paris, G. Le Cozannet, F. Boulahya, F. Dumas, G. Le Cozannet, F. Boulahya, and F. Dumas (2017). "Sea-level rise impacts on the tides of the European Shelf". en. In: *Continental Shelf Research* 137, pp. 56–71.

Idier, D., X. Bertin, P. Thompson, and M. D. Pickering (2019). "Interactions between mean sea level, tide, surge, waves and flooding: Mechanisms and contributions to sea level variations at the coast". en. In: *Surveys in Geophysics* 40.6, pp. 1603–1630.

Ionita, M., V. Nagavciuc, R. Kumar, and O. Rakovec (2020). "On the curious case of the recent decade, mid-spring precipitation deficit in central Europe". en. In: *npj Climate and Atmospheric Science* 3.1, p. 49.

IPCC (2021). *Climate Change 2021 – The Physical Science Basis: Working Group I Contribution to the Sixth Assessment Report of the Intergovernmental Panel on Climate Change*. Cambridge: Cambridge University Press.

— (2023). *Climate Change 2021 – The Physical Science Basis: Working Group I Contribution to the Sixth Assessment Report of the Intergovernmental Panel on Climate Change*. 1st ed. Cambridge University Press. ISBN: 978-1-009-15789-6.

Ivanov, E., A. Capet, A. Barth, E. J. Delhez, K. Soetaert, and M. Grégoire (2020). "Hydrodynamic variability in the Southern Bight of the North Sea in response to typical atmospheric and tidal regimes. Benefit of using a high resolution model". en. In: *Ocean Modelling* 154, p. 101682.

Jacob, B. and E. V. Stanev (2017). "Interactions between wind and tidally induced currents in coastal and shelf basins". en. In: *Ocean Dynamics* 67.10, pp. 1263–1281.

Jay, D. A. (1991). "Green's law revisited: Tidal long-wave propagation in channels with strong topography". en. In: *Journal of Geophysical Research: Oceans* 96.C11, pp. 20585–20598.

Jelgersma, S., M. J. F. Stive, and L. van der Valk (1995). "Holocene storm surge signatures in the coastal dunes of the western Netherlands". In: *Marine Geology* 125.1, pp. 95–110.

Jensen, C., T. Mahavadi, N. H. Schade, I. Hache, and T. Kruschke (2022). "Negative storm surges in the Elbe Estuary—Large-scale

meteorological conditions and future climate change". en. In: *Atmosphere* 13.10, p. 1634.

Jonkman, S. N. and I. Kelman (2012). "Deaths during the 1953 North Sea Storm Surge". EN. In: pp. 749–758.

Kapetsky, J. (1984). "Coastal lagoon fisheries around the world: Some perspectives on fishery yields, and other comparative fishery characteristics". In: *Management of Coastal Lagoon Fisheries* 61, pp. 97–139.

Kendall, M. G. and J. D. Gibbons (1962). *Rank correlation methods*. 4th ed. Griffin London.

Kendon, M., M. McCarthy, S. Jevrejeva, A. Matthews, and T. Legg (2019). "State of the UK climate 2018". en. In: *International Journal of Climatology* 39.S1, pp. 1–55.

Kendon, M., M. McCarthy, S. Jevrejeva, A. Matthews, T. Sparks, and J. Garforth (2021). "State of the UK Climate 2020". en. In: *International Journal of Climatology* 41.S2, pp. 1–76.

Kettle, A. J. (2018). "The North Sea surge of 31 October–1 November 2006 during Storm Britta". English. In: *Advances in Geosciences*. Vol. 45. Copernicus GmbH, pp. 273–279.

Khanal, S., N. Ridder, H. de Vries, W. Terink, and B. van den Hurk (2019). "Storm Surge and Extreme River Discharge: A Compound Event Analysis Using Ensemble Impact Modeling". English. In: *Frontiers in Earth Science* 7.

Khojasteh, D., S. Chen, S. Felder, V. Heimhuber, and W. Glamore (2021). "Estuarine tidal range dynamics under rising sea levels". en. In: *PLOS ONE* 16.9, e0257538.

Kirezci, E., I. R. Young, R. Ranasinghe, S. Muis, R. J. Nicholls, D. Lincke, and J. Hinkel (2020). "Projections of global-scale extreme sea levels and resulting episodic coastal flooding over the 21st Century". en. In: *Scientific Reports* 10.1.

Klein, Y. L., J. P. Osleeb, and M. R. Viola (2004). "Tourism-generated earnings in the coastal zone: a regional analysis". In: *Journal of Coastal Research* 20.4 (204), pp. 1080–1088.

Klerk, W. J., H. C. Winsemius, W. J. van Verseveld, A. M. R. Bakker, and F. L. M. Diermanse (2015). "The co-incidence of storm surges and extreme discharges within the Rhine–Meuse Delta". en. In: *Environmental Research Letters* 10.3, p. 035005.

Kohno, N., S. K. Dube, M. Entel, S. H. M. Fakhruddin, D. Greenslade, M.-D. Leroux, J. Rhome, and N. B. Thuy (2018). "Recent progress in storm surge forecasting". In: *Tropical Cyclone Research and Review* 7.2, pp. 128–139.

Kolokythas, G., De Maerschalck, B., Wang, L, Fonias, S., Breugem, A, Vanlede, J, and Mostaert, F (2021). *Modelling Belgian Coastal zone and Scheldt mouth area*. en. Tech. rep. 12. Flanders Hydraulics Research: Antwerp.

Koopmann, G. (1962). "Wasserstandserhöhungen in der Deutschen Bucht infolge von Schwingungen und Schwallerscheinungen und deren Bedeutung bei der Sturmflut vom 16./17. Februar 1962". de. In: *Deutsche Hydrografische Zeitschrift* 15.5, pp. 181–198.

Kruskal, W. H. and W. A. Wallis (1952). "Use of Ranks in one-criterion variance analysis". In: *Journal of the American Statistical Association*.

Kwadijk, J., N. W. Arnell, C. Mudersbach, M. de Weerd, A. Kroon, and M. Quante (2016). "Recent change-river flow". In: *North Sea Region Climate Change Assessment*. 1st ed. Regional Climate Studies. Springer Cham, pp. 137–146. ISBN: 978-3-319-39743-6.

Kärnä, T. (2012). "Development of a Baroclinic Discontinuous Galerkin Finite Element Model for Estuarine and Coastal Flows". en. PhD thesis.

Kärnä, T., B. de Brye, O. Gourgue, J. Lambrechts, R. Comblen, V. Legat, and E. Deleersnijder (2011). "A fully implicit wetting-drying method for DG-FEM shallow water models, with an application to the Scheldt Estuary". en. In: *Computer Methods in Applied Mechanics and Engineering* 200.5-8, pp. 509–524.

Lambrechts, J., E. Hanert, E. Deleersnijder, P.-E. Bernard, V. Legat, J.-F. Remacle, and E. Wolanski (2008). "A multi-scale model of the hydrodynamics of the whole Great Barrier Reef". en. In: *Estuarine, Coastal and Shelf Science* 79.1, pp. 143–151.

Lapetina, A. and Y. P. Sheng (2015). "Simulating complex storm surge dynamics: Three-dimensionality, vegetation effect, and onshore sediment transport". en. In: *Journal of Geophysical Research: Oceans* 120.11, pp. 7363–7380.

Le, H.-A., J. Lambrechts, S. Ortleb, N. Gratiot, E. Deleersnijder, and S. Soares-Frazão (2020). "An implicit wetting–drying algorithm for the discontinuous Galerkin method: application to the Tonle Sap,

Mekong River Basin". en. In: *Environmental Fluid Mechanics* 20.4, pp. 923–951.

Lesser, G. R., J. A. Roelvink, J. A. T. M. van Kester, and G. S. Stelling (2004). "Development and validation of a three-dimensional morphological model". In: *Coastal Engineering*. Coastal Morphodynamic Modeling 51.8, pp. 883–915.

Lewis, H. W., J. Siddorn, J. M. Castillo Sanchez, J. Petch, J. M. Edwards, and T. Smyth (2019). "Evaluating the impact of atmospheric forcing and air–sea coupling on near-coastal regional ocean prediction". English. In: *Ocean Science* 15.3, pp. 761–778.

Little, A. S., M. D. K. Priestley, and J. L. Catto (2023). "Future increased risk from extratropical windstorms in northern Europe". en. In: *Nature Communications* 14.1, p. 4434.

Lorenz, M. and U. Gräwe (2023). "Uncertainties and discrepancies in the representation of recent storm surges in a non-tidal semi-enclosed basin: a hindcast ensemble for the Baltic Sea". English. In: *Ocean Science* 19.6, pp. 1753–1771.

Loridan, T., S. Khare, E. Scherer, M. Dixon, and E. Bellone (2015). "Parametric modeling of transitioning cyclone wind fields for risk assessment studies in the Western North Pacific". EN. In: *Journal of Applied Meteorology and Climatology* 54.3, pp. 624–642.

Lubbock, J. W. (1836). "On the tides at the port of London". In: *Philosophical Transactions of the Royal Society of London* 126, pp. 217–266.

Lucas-Picher, P., D. Caya, R. de Elía, and R. Laprise (2008). "Investigation of regional climate models' internal variability with a ten-member ensemble of 10-year simulations over a large domain". en. In: *Climate Dynamics* 31.7, pp. 927–940.

Luettich Richard, J. and J. Westerink (1999). "Implementation of the Wave Radiation Stress Gradient as a Forcing for the ADCIRC Hydrodynamic Model: Upgrades and Documentation for ADCIRC Version 34.12". In.

Mann, H. B. and D. R. Whitney (1947). "On a test of whether one of two random variables is stochastically larger than the other". In: *The Annals of Mathematical Statistics* 18.1, pp. 50–60.

Mann, H. B. (1945). "Nonparametric tests against trend". In: *Econometrica* 13.3, p. 245.

Marchesiello, P., J. McWilliams, and A. Shchepetkin (2001). "Open boundary conditions for long-term integration of regional oceanic models". In: *Ocean Modelling* 3, pp. 1–20.

Marcos, M., J. Rohmer, M. I. Vousdoukas, L. Mentaschi, G. Le Cozannet, and A. Amores (2019). "Increased extreme coastal water levels due to the combined action of storm surges and wind waves". en. In: *Geophysical Research Letters* 46.8, pp. 4356–4364.

Marta-Almeida, M., R. D. Hetland, and X. Zhang (2013). "Evaluation of model nesting performance on the Texas-Louisiana continental shelf". en. In: *Journal of Geophysical Research: Oceans* 118.5, pp. 2476–2491.

Mastenbroek, C., G. Burgers, and P. a. E. M. Janssen (1993). "The Dynamical Coupling of a Wave Model and a Storm Surge Model through the Atmospheric Boundary Layer". en. In.

McGranahan, G., D. Balk, and B. Anderson (2007). "The rising tide: assessing the risks of climate change and human settlements in low elevation coastal zones". EN. In: *Environment & Urbanization* 19.1, pp. 17–37.

Medeiros, S. C. and S. C. Hagen (2013). "Review of wetting and drying algorithms for numerical tidal flow models". en. In: *International Journal for Numerical Methods in Fluids* 71.4, pp. 473–487.

Meire, P., T. Ysebaert, T. Ysebaert, S. Van Damme, S. Van Damme, E. Van den Bergh, E. Van den Bergh, E. Van den Bergh, T. Maris, Eric Struyf, and E. Struyf (2005). "The Scheldt estuary: a description of a changing ecosystem". In: *Hydrobiologia* 540.1, pp. 1–11.

Menéndez, M. and P. L. Woodworth (2010). "Changes in extreme high water levels based on a quasi-global tide-gauge data set". en. In: *Journal of Geophysical Research: Oceans* 115.C10.

Merkens, J.-L., L. Reimann, J. Hinkel, and A. T. Vafeidis (2016). "Gridded population projections for the coastal zone under the Shared Socioeconomic Pathways". In: *Global and Planetary Change* 145, pp. 57–66.

Meyer, E. M. I. and L. Gaslikova (2023). "Investigation of historical severe storms and storm tides in the German Bight with century reanalysis data". en. In: *Natural Hazards and Earth System Sciences* 24.2, pp. 481–499.

Milliman, J. D. and K. L. Farnsworth (2011). *River discharge to the coastal ocean: a global synthesis*. en. 1st ed. Cambridge University Press. ISBN: 978-0-521-87987-3 978-0-511-78124-7 978-1-107-61218-1.

Mizuta, R., A. Murata, M. Ishii, H. Shiogama, K. Hibino, N. Mori, O. Arakawa, Y. Imada, K. Yoshida, T. Aoyagi, H. Kawase, M. Mori, Y. Okada, T. Shimura, T. Nagatomo, M. Ikeda, H. Endo, M. Nosaka, M. Arai, C. Takahashi, K. Tanaka, T. Takemi, Y. Tachikawa, K. Temur, Y. Kamae, M. Watanabe, H. Sasaki, A. Kitoh, I. Takayabu, E. Nakakita, and M. Kimoto (2017). "Over 5,000 years of ensemble future climate simulations by 60-km global and 20-km regional atmospheric models". en. In.

Mohammed, R. and M. Scholz (2018). "Critical review of salinity intrusion in rivers and estuaries". en. In: *Journal of Water and Climate Change* 9.1, pp. 1–16.

Molina, M. O., C. Gutiérrez, and E. Sánchez (2021). "Comparison of ERA5 surface wind speed climatologies over Europe with observations from the HadISD dataset". en. In: *International Journal of Climatology* 41.10, pp. 4864–4878.

Morris, R. L., T. M. Konlechner, M. Ghisalberti, and S. E. Swearer (2018). "From grey to green: Efficacy of eco-engineering solutions for nature-based coastal defence". en. In: *Global Change Biology* 24.5, pp. 1827–1842.

Muis, S., J. C. J. H. Aerts, J. A. Antolínez, J. C. Dullaart, T. M. Duong, L. Erikson, R. J. Haarsma, M. I. Apecechea, M. Mengel, D. Le Bars, A. O'Neill, R. Ranasinghe, M. J. Roberts, M. Verlaan, P. J. Ward, and K. Yan (2023). "Global projections of storm surges using high-resolution CMIP6 climate models". en. In: *Earth's Future* 11.9, e2023EF003479.

Muis, S., M. Verlaan, H. C. Winsemius, J. C. J. H. Aerts, and P. J. Ward (2016). "A global reanalysis of storm surges and extreme sea levels". en. In: *Nature Communications* 7.1, p. 11969.

Muller, H., L. Pineau-Guillou, D. Idier, and F. Ardhuin (2014). "Atmospheric storm surge modeling methodology along the French (Atlantic and English Channel) coast". en. In: *Ocean Dynamics* 64.11, pp. 1671–1692.

Mölter, T., D. Schindler, A. T. Albrecht, and U. Kohnle (2016). "Review on the Projections of Future Storminess over the North Atlantic European Region". en. In: *Atmosphere* 7.4, p. 60.

Nguyen, T. T., J. Staneva, A. Bonaduce, B. Jacob, and J. Pein (2025). "Seamless integration of the land–ocean continuum: the complex interplay of wave-induced processes and estuarine influences". en. In: *Ocean Dynamics* 75.6, p. 58.

Nicholls, R. J., P. P. Wong, V. Burkett, J. Codignotto, J. Hay, R. McLean, S. Ragoonaden, C. Woodroffe, P. Abuodha, J. Arblaster, B. Brown, D. Forbes, J. Hall, S. Kovats, J. Lowe, K. McInnes, S. Moser, S. Rupp-Armstrong, and Y. Saito (2007). "Coastal systems and low-lying areas". en. In.

Nicholls, R. J. (2006). "Storm surges in Coastal Areas". In: *Natural Disaster Hotspots Case Studies*. Vol. 6. World Bank Publications, pp. 79–108.

Nihoul, J. C. J., F. C. Ronday, J. J. Peters, and A. Sterling (1978). "Hydrodynamics of the Scheldt Estuary". en. In: *Elsevier Oceanography Series*. Ed. by J. C. J. Nihoul. Vol. 23. Hydrodynamics of Estuaries and Fjords. Elsevier, pp. 27–53.

Nudds, S., Y. Lu, S. Higginson, S. P. Haigh, J.-P. Paquin, M. O'Flaherty-Sproul, S. Taylor, H. Blanken, G. Marcotte, G. C. Smith, N. B. Bernier, P. MacAulay, Y. Wu, L. Zhai, X. Hu, J. Chanut, M. Dunphy, F. Dupont, D. Greenberg, F. J. M. Davidson, and F. Page (2020). "Evaluation of structured and unstructured models for application in operational ocean forecasting in nearshore waters". en. In: *Journal of Marine Science and Engineering* 8.7, p. 484.

Oppenheimer, M., B. Glavovic, J. Hinkel, v. Roderik, A. Magnan, A. Abd-Elgawad, C. Rongshu, M. Cifuentes, D. Robert, T. Ghosh, J. Hay, M. Ben, B. Meyssignac, Z. Sebesvari, S. A.J., S. Dangendorf, and T. Frederikse (2019). "Sea level rise and implications for low lying islands, coasts and communities". In: pp. 321–445.

Orton, P. M., E. W. Sanderson, S. A. Talke, M. Giampieri, and K. MacManus (2020). "Storm tide amplification and habitat changes due to urbanization of a lagoonal estuary". English. In: *Natural Hazards and Earth System Sciences* 20.9, pp. 2415–2432.

OSPAR Commission, ed. (2000). *Region 2: Greater North Sea*. en. Quality status report 2000 : region ... / OSPAR Commission for the protection of the marine environment of the North-East Atlantic 2. London. ISBN: 978-0-946956-48-7.

Otto, L., J. T. F. Zimmerman, G. K. Furnes, M. Mork, R. Saetre, and G. Becker (1990). "Review of the physical oceanography of the North Sea". In: *Netherlands Journal of Sea Research* 26.2, pp. 161–238.

O'Neill, B. C., E. Kriegler, K. L. Ebi, E. Kemp-Benedict, K. Riahi, D. S. Rothman, B. J. van Ruijven, D. P. van Vuuren, J. Birkmann, K. Kok, M. Levy, and W. Solecki (2017). "The roads ahead: Narratives for shared socioeconomic pathways describing world futures in the 21st century". In: *Global Environmental Change* 42, pp. 169–180.

Paprotny, D. (2025). *HANZE v2.4 flood impact model input data*.

Paprotny, D., M. I. Vousdoukas, O. Morales-Nápoles, S. N. Jonkman, and L. Feyen (2020). "Pan-European hydrodynamic models and their ability to identify compound floods". en. In: *Natural Hazards* 101.3, pp. 933–957.

Patil, A. R., F. F. Perez, J. Lambrechts, I. Draoui, and E. Deleersnijder (2024). "A multiscale 1D-2D coupled model of the Scheldt estuary rivers and the European continental shelf". en. In: *CoastLab 2024: Physical Modelling in Coastal Engineering and Science*.

Pein, J., J. Staneva, B. Mayer, M. D. Palmer, and C. Schrum (2023). "A framework for estuarine future sea-level scenarios: Response of the industrialised Elbe estuary to projected mean sea level rise and internal variability". English. In: *Frontiers in Marine Science* 10.

Petersen, M. and H. Rohde (1991). *Sturmflut–Die gro{β}en Fluten an den Küsten Schleswig-Holsteins und in der Elbe*. Wachholtz.

Pickering, M. D., N. C. Wells, K. J. Horsburgh, and J. A. M. Green (2012). "The impact of future sea-level rise on the European Shelf tides". In: *Continental Shelf Research* 35, pp. 1–15.

Plancke, Y., J. Stark, D. Meire, and M. Schrijver (2020). "Complex flow patterns in the Scheldt estuary: Field measurements and validation of a hydrodynamic model". EN. In: *Journal of Hydraulic Engineering* 146.7, p. 05020004.

Plüß, A, E Rudolph, and D Schrödter (2001). "Characteristics of storm surges in German estuaries". en. In: *Climate Research* 18, pp. 71–76.

Pope, V. and R. Stratton (2002). "The processes governing horizontal resolution sensitivity in a climate model". en. In: *Climate Dynamics* 19.3, pp. 211–236.

Powell, M. D., P. J. Vickery, and T. A. Reinhold (2003). "Reduced drag coefficient for high wind speeds in tropical cyclones". en. In: *Nature* 422.6929, pp. 279–283.

Prandle, D. and J. Wolf (1978). "Surge-Tide Interaction in the Southern North Sea". In: *Hydrodynamics of Estuaries and Fjords*.

Priestley, M. D. K. and J. L. Catto (2022a). "Future changes in the extratropical storm tracks and cyclone intensity, wind speed, and structure". English. In: *Weather and Climate Dynamics* 3.1, pp. 337–360.

— (2022b). "Improved representation of extratropical cyclone structure in HighResMIP models". en. In: *Geophysical Research Letters* 49.5, e2021GL096708.

Pringle, W. J., J. Wang, K. J. Roberts, and V. R. Kotamarthi (2021). "Projected changes to cool-season storm tides in the 21st century along the northeastern United States coast". en. In: *Earth's Future* 9.7, e2020EF001940.

Proudman, J. and A. T. Doodson (1924). "The principal constituent of the tides of the North Sea". In: *Philosophical Transactions of the Royal Society of London. Series A, Containing Papers of a Mathematical or Physical Character* 224.616-625, pp. 185–219.

Prügel, H. (1942). *Die Sturmflutschäden an der schleswig-holsteinischen Westküste in ihrer meteorologischen und morphologischen Abhängigkeit*. Christian-Albrechts-Universitat zu Kiel. Vol. 11.

Pugh, D. T. (1987). *Tides, surges and mean sea level*. en. Chichester: Wiley. ISBN: 978-0-471-91505-8.

Pupic Vurilj, M., J. A. A. Antolínez, S. Muis, and O. Morales Napoles (2025). "Storm surge hydrographs from historical observations of sea level along the Dutch North Sea coast". en. In: *Natural Hazards*.

Ralston, D. K., S. Talke, W. R. Geyer, H. A. M. Al-Zubaidi, and C. K. Sommerfield (2019). "Bigger tides, less flooding: Effects of eredging on barotropic dynamics in a highly modified estuary". en. In: *Journal of Geophysical Research: Oceans* 124.1, pp. 196–211.

Randresihaja, N. R., O. Gourgue, L. Alaerts, X. Fettweis, J. Lambrechts, M. De Le Court, M. Grégoire, and E. Hanert (2026). "How atmospheric forcing resolution impacts storm surge model results: Insights from Storm Xaver in the North Sea-Scheldt estuary continuum". In: *Regional Studies in Marine Science* 96, p. 104919.

Reef, K. R. G., G. Lipari, P. C. Roos, and S. J. M. H. Hulscher (2018). "Time-varying storm surges on Lorentz's Wadden Sea networks". en. In: *Ocean Dynamics* 68.8, pp. 1051–1065.

Rego, J. L. and C. Li (2010). "Nonlinear terms in storm surge predictions: Effect of tide and shelf geometry with case study from Hurricane Rita". en. In: *Journal of Geophysical Research: Oceans* 115.C6.

Ridder, N., H. de Vries, S. Drijfhout, H. van den Brink, E. van Meijgaard, and H. de Vries (2018). "Extreme storm surge modelling in the North Sea". en. In: *Ocean Dynamics* 68.2, pp. 255–272.

Rijkswaterstaat (2007). *Stormvloedrapport 88 van 9 november 2007*. Tech. rep. Den Haag: Stormvloedwaarschuwingsdienst (SVSD), Rijkswaterstaat.

Roberts, J. F., A. J. Champion, L. C. Dawkins, K. I. Hodges, L. C. Shaffrey, D. B. Stephenson, M. A. Stringer, H. E. Thornton, and B. D. Youngman (2014). "The XWS open access catalogue of extreme European windstorms from 1979 to 2012". English. In: *Natural Hazards and Earth System Sciences* 14.9, pp. 2487–2501.

Roberts, M. J., J. Camp, J. Seddon, P. L. Vidale, K. Hodges, B. Vannière, J. Mecking, R. Haarsma, A. Bellucci, E. Scoccimarro, L.-P. Caron, F. Chauvin, L. Terray, S. Valcke, M.-P. Moine, D. Putrasahan, C. D. Roberts, R. Senan, C. Zarzycki, P. Ullrich, Y. Yamada, R. Mizuta, C. Kodama, D. Fu, Q. Zhang, G. Danabasoglu, N. Rosenbloom, H. Wang, and L. Wu (2020). "Projected future changes in tropical cyclones using the CMIP6 HighResMIP multimodel ensemble". en. In: *Geophysical Research Letters* 47.14, e2020GL088662.

Rossiter, J. R. (1954). "The North Sea storm surge of 31 January and 1 February 1953". In: *Philosophical Transactions of the Royal Society of London. Series A, Mathematical and Physical Sciences* 246.915, pp. 371–400.

Rucińska, D. (2019). "Describing Storm Xaver in disaster terms". In: *International Journal of Disaster Risk Reduction* 34, pp. 147–153.

Russell, M., A. Hakami, P. A. Makar, A. Akingunola, J. Zhang, M. D. Moran, and Q. Zheng (2019). "An evaluation of the efficacy of very high resolution air-quality modelling over the Athabasca oil sands region, Alberta, Canada". English. In: *Atmospheric Chemistry and Physics* 19.7, pp. 4393–4417.

Röbke, B. R., H. Elmilady, M. A. Chaves, M. Taal, and M. van der Wegen (2025). "The relative impact of sea level rise and dredging strategies on the morphodynamic evolution of the Western Scheldt estuary (The Netherlands)". In: *Coastal Engineering*, p. 104750.

Saint-Amand, A., J. Lambrechts, C. J. Thomas, and E. Hanert (2023). "How fine is fine enough? Effect of mesh resolution on hydrodynamic simulations in coral reef environments". In: *Ocean Modelling* 186, p. 102254.

Salomon, J.-c., M. Breton, and P. Guegueniat (1993). "Computed residual flow through the Dover Strait". en. In: *Gauthier-villars* 16.5-6, pp. 449–455.

Sampurno, J., V. Vallaeys, R. Ardianto, and E. Hanert (2022). "Modeling interactions between tides, storm surges, and river discharges in the Kapuas River delta". English. In: *Biogeosciences* 19.10, pp. 2741–2757.

Sanuy, M., J. A. Jiménez, M. I. Ortego, and A. Toimil (2020). "Differences in assigning probabilities to coastal inundation hazard estimators: Event versus response approaches". en. In: *Journal of Flood Risk Management* 13.S1, e12557.

Savenije, H. H. G., M. Toffolon, J. Haas, and E. J. M. Veling (2008). "Analytical description of tidal dynamics in convergent estuaries". en. In: *Journal of Geophysical Research: Oceans* 113.C10.

Schaffer, L., A. Boesch, J. Baehr, and T. Kruschke (2025). "Development of a wind-based storm surge model for the German Bight". English. In: *Natural Hazards and Earth System Sciences* 25.6, pp. 2081–2096.

Schimanke, S., M. Ridal, P. Le Moigne, L. Berggren, P. Undén, R. Randriamampianina, U. Andrea, E. Bazile, A. Bertelsen, P. Brousseau, P. Dahlgren, L. Edvinsson, A. El Said, M. Glinton, S. Hopsch, L. Isaksson, R. Mladek, E. Olsson, A. Verrelle, and Z. Q. Wang (2021). *CERRA sub-daily regional reanalysis data for Europe on model levels from 1984 to present*. dataset.

Screen, J. A. and I. Simmonds (2010). "The central role of diminishing sea ice in recent Arctic temperature amplification". en. In: *Nature* 464.7293, pp. 1334–1337.

Sen, P. K. (1968). "Estimates of the regression coefficient based on Kendall's Tau". In: *Journal of the American Statistical Association* 63.324, pp. 1379–1389.

Shaw, T. A., M. Baldwin, E. A. Barnes, R. Caballero, C. I. Garfinkel, Y.-T. Hwang, C. Li, P. A. O'Gorman, G. Rivière, I. R. Simpson, and A. Voigt (2016). "Storm track processes and the opposing influences of climate change". en. In: *Nature Geoscience* 9.9, pp. 656–664.

Shepherd, T. G., E. Boyd, R. A. Calel, S. C. Chapman, S. Dessai, I. M. Dima-West, H. J. Fowler, R. James, D. Maraun, O. Martius, C. A. Senior, A. H. Sobel, D. A. Stainforth, S. F. B. Tett, K. E. Trenberth, B. J. J. M. van den Hurk, N. W. Watkins, R. L. Wilby, and D. A. Zenghelis (2018). "Storylines: an alternative approach to representing uncertainty in physical aspects of climate change". en. In: *Climatic Change* 151.3, pp. 555–571.

Shiogama, H., S. Fujimori, T. Hasegawa, M. Hayashi, Y. Hirabayashi, T. Ogura, T. Iizumi, K. Takahashi, and T. Takemura (2023). "Important distinctiveness of SSP3–7.0 for use in impact assessments". en. In: *Nature Climate Change* 13.12, pp. 1276–1278.

Sillmann, J., T. G. Shepherd, B. van den Hurk, W. Hazeleger, O. Martius, J. Slingo, and J. Zscheischler (2021). "Event-based storylines to address climate risk". en. In: *Earth's Future* 9.2, e2020EF001783.

Simpson, J., W. Bos, F. Schirmer, A. Souza, T. Rippeth, S. Jones, and D. Hydes (1993). "Periodic stratification in the rhine ROFI in the north-sea". In: *Oceanologica Acta* 16.1, pp. 23–32.

Simpson, J. (2012). *Introduction to the physical and biological oceanography of shelf seas*. eng. Ed. by J. Sharples. Cambridge: Cambridge University Press. ISBN: 978-1-139-03409-8.

Slinger, J. H. (2023). "Developing the transboundary long term vision of the Scheldt estuary – an untold story". In: *Water International* 48.8, pp. 1046–1067.

Smagorinsky, J. (1963). "General circulation experiments with the primitive equations: I. The basic experiment". EN. In: *Monthly Weather Review* 91.3, pp. 99–164.

Smith, S. D. and E. G. Banke (1975). "Variation of the sea surface drag coefficient with wind speed". en. In: *Quarterly Journal of the Royal Meteorological Society* 101.429, pp. 665–673.

Smith, S. D. (1988). "Coefficients for sea surface wind stress, heat flux, and wind profiles as a function of wind speed and temperature". In: *Journal of Geophysical Research: Oceans*.

Smolders, S (2016). "Integraal Plan Bovenzeeschelde". en. In: p. 508.

Smolders, S., Y. Plancke, S. Ides, P. Meire, and S. Temmerman (2015). "Role of intertidal wetlands for tidal and storm tide attenuation along a confined estuary: a model study". English. In: *Natural Hazards and Earth System Sciences* 15.7, pp. 1659–1675.

Smolders, S., M. João Teles, A. Leroy, T. Maximova, P. Meire, and S. Temmerman (2020). "Modeling storm surge attenuation by an integrated nature-based and engineered flood defense system in the Scheldt estuary (Belgium)". en. In: *Journal of Marine Science and Engineering* 8.1, p. 27.

Sobolowski, S., S. Somot, J. Fernandez, G. Evin, D. Maraun, S. Kotlarski, M. Jury, R. E. Benestad, C. Teichmann, O. B. Christensen, B. Katharina, E. Buonomo, E. Katragkou, C. Steger, S. Sørland, G. Nikulin, C. McSweeney, A. Dobler, T. Palmer, R. Wilke, J. Boé, L. Brunner, A. Ribes, S. Qasmi, P. Nabat, F. Sevault, T. Oudar, and S. Brands (2023). "EURO-CORDEX GCM Selection & Ensemble Design: Implementation Framework". eng. In: *Selection & Ensemble Design: Implementation Framework*.

Stanev, E. V., R. Al-Nadhairi, J. Staneva, J. Schulz-Stellenfleth, and A. Valle-Levinson (2014). "Tidal wave transformations in the German Bight". en. In: *Ocean Dynamics* 64.7, pp. 951–968.

Stanev, E. V., J. Schulz-Stellenfleth, J. Staneva, S. Grayek, S. Grashorn, A. Behrens, W. Koch, and J. Pein (2016). "Ocean forecasting for the German Bight: from regional to coastal scales". en. In: *Ocean Science* 12.5, pp. 1105–1136.

Staneva, J., K. Wahle, W. Koch, A. Behrens, L. Fenoglio-Marc, and E. V. Stanev (2016). "Coastal flooding: impact of waves on storm surge during extremes - a case study for the German Bight". English. In: *Natural Hazards and Earth System Sciences* 16.11, pp. 2373–2389.

Stark, J., S. Smolders, P. Meire, and S. Temmerman (2017). "Impact of intertidal area characteristics on estuarine tidal hydrodynamics: A modelling study for the Scheldt Estuary". In: *Estuarine, Coastal and Shelf Science* 198, pp. 138–155.

Stark, J., T. Van Oyen, P. Meire, and S. Temmerman (2015). "Observations of tidal and storm surge attenuation in a large tidal marsh". en. In: *Limnology and Oceanography* 60.4, pp. 1371–1381.

Sterl, A., H. van den Brink, H. de Vries, R. Haarsma, and E. van Meijgaard (2009). "An ensemble study of extreme storm surge related water levels in the North Sea in a changing climate". English. In: *Ocean Science* 5.3, pp. 369–378.

Sutton-Grier, A. E., K. Wowk, and H. Bamford (2015). "Future of our coasts: The potential for natural and hybrid infrastructure to enhance the resilience of our coastal communities, economies and ecosystems". In: *Environmental Science & Policy* 51, pp. 137–148.

Sündermann, J. and T. Pohlmann (2011). "A brief analysis of North Sea physics". pl. In: *Oceanologia* 53.3, pp. 663–689.

Tadesse, M. G., T. Wahl, and A. Cid (2020). "Data-driven modeling of global storm surges". English. In: *Frontiers in Marine Science* 7.

Talke, S. A., R. Familkhalili, and D. A. Jay (2021). "The influence of channel deepening on tides, river discharge effects, and storm surge". en. In: *Journal of Geophysical Research: Oceans* 126.5, e2020JC016328.

Talke, S. A. and D. A. Jay (2020). "Changing tides: The role of natural and anthropogenic factors". fr. In: *Annual Review of Marine Science* 12.Volume 12, 2020, pp. 121–151.

Tasnim, K., T. Shibayama, M. Esteban, H. Takagi, K. Ohira, and R. Nakamura (2014). "Field observation and numerical simulation of past and future storm surges in the Bay of Bengal: case study of cyclone Nargis". In: *Natural Hazards* 75.

Temmerman, S. and Wartel, S. (2003). "Sedimentation on tidal marshes in the Scheldt estuary: a field and numerical modelling study". PhD thesis. KUL. Faculteit Wetenschappen. Departement Geografie-Geologie.

Temmerman, S., M. B. De Vries, and T. J. Bouma (2012). "Coastal marsh die-off and reduced attenuation of coastal floods: A model analysis". In: *Global and Planetary Change* 92-93, pp. 267–274.

Temmerman, S., P. Meire, T. J. Bouma, P. M. J. Herman, T. Ysebaert, and H. J. De Vriend (2013). "Ecosystem-based coastal defence in the face of global change". en. In: *Nature* 504.7478, pp. 79–83.

Theil, H. (1950). "A rank-invariant method of linear and polynomial regression analysis". In: 12.85, p. 173.

Thomas, A., J. Dietrich, T. Asher, M Bell, B. Blanton, J. Copeland, A. Cox, C. Dawson, J. Fleming, and R. Luettich (2019). "Influence of storm timing and forward speed on tides and storm surge during Hurricane Matthew". In: *Ocean Modelling* 137, pp. 1–19.

Tinker, J., J. A. Polton, P. E. Robins, M. J. Lewis, and C. K. O'Neill (2022). "The influence of tides on the North West European shelf winter residual circulation". English. In: *Frontiers in Marine Science* 9.

Turner, R., N. Rabalais, D. Justic', and Q. Dortch (2003). "Global patterns of dissolved N, P and Si in large rivers". en. In: *Biogeochemistry* 64.3, pp. 297–317.

Vallaeys, V., T. Kärnä, P. Delandmeter, J. Lambrechts, A. M. Baptista, E. Deleersnijder, and E. Hanert (2018). "Discontinuous Galerkin modeling of the Columbia River's coupled estuary-plume dynamics". en. In: *Ocean Modelling* 124, pp. 111–124.

Van Buuren, A., L. Gerrits, and G. R. Teisman (2010). "Understanding and managing the Westerschelde – synchronizing the physical system and the management system of a complex estuary". English. In: *Hydrology and Earth System Sciences* 14.11, pp. 2243–2257.

Van Damme, S., E. Struyf, T. Maris, T. Ysebaert, F. Dehairs, M. Tackx, C. Heip, and P. Meire (2005). "Spatial and temporal patterns of water quality along the estuarine salinity gradient of the Scheldt estuary (Belgium and The Netherlands): results of an integrated monitoring approach". In: *Hydrobiologia* 540, pp. 29–45.

Vanderborght, J.-P., I. M. Folmer, D. R. Aguilera, T. Uhrenholdt, and P. Regnier (2007). "Reactive-transport modelling of C, N, and O2 in a river–estuarine–coastal zone system: Application to the Scheldt estuary". In: *Marine Chemistry*. Special issue: Dedicated to the memory of Professor Roland Wollast 106.1, pp. 92–110.

Vanlede, J., S. Smolders, T. Maximova, and M. J. Teles (2015). "The unstructured Scaldis model: A new 3D high resolution model for hydrodynamics and sediment transport in the tidal Scheldt". en. In.

Vemuri, A., S. Buckingham, W. Munters, J. Helsen, and J. van Beeck (2022). "Sensitivity analysis of mesoscale simulations to physics parameterizations over the Belgian North Sea using weather research and forecasting – advanced research WRF (WRF-ARW)". English. In: *Wind Energy Science* 7.5, pp. 1869–1888.

Vikolainen, V., A. van Buuren, J. Warnen, K. Lulofs, and H. Bressers (2015). "Negotiated Space for the River Scheldt in Flanders. A longitudinal reconstruction of the policy debate to realize multifunctional retention capacity". en. In: *International Journal of Water Governance*.

Vissio, G., V. Lembo, V. Lucarini, and M. Ghil (2020). "Evaluating the performance of climate models based on Wasserstein distance". en. In: *Geophysical Research Letters* 47.21, e2020GL089385.

Vitale, C., A. Crabbé, S. Meijerink, C. Fletcher, M. Nijamdeen, and M. Wiering (2025). "Understanding Flood Governance in the Dutch-Flemish Scheldt Estuary: An Evolutionary Governance Perspective". en. In: *Ocean and Society* 2.0.

Von Storch, H. and K. Woth (2008). "Storm surges: perspectives and options". en. In: *Sustainability Science* 3.1, pp. 33–43.

Vousdoukas, M. I., L. Mentaschi, E. Voukouvalas, M. Verlaan, and L. Feyen (2017). "Extreme sea levels on the rise along Europe's coasts". en. In: *Earth's Future* 5.3, pp. 304–323.

Vousdoukas, M. I., L. Mentaschi, E. Voukouvalas, M. Verlaan, S. Jevrejeva, L. P. Jackson, and L. Feyen (2018). "Global probabilistic projections of extreme sea levels show intensification of coastal flood hazard". en. In: *Nature Communications* 9.1, p. 2360.

Vousdoukas, M. I., E. Voukouvalas, A. Annunziato, A. Giardino, and L. Feyen (2016). "Projections of extreme storm surge levels along Europe". en. In: *Climate Dynamics* 47.9, pp. 3171–3190.

Wadey, M. P., I. D. Haigh, R. J. Nicholls, J. M. Brown, K. Horsburgh, B. Carroll, S. L. Gallop, T. Mason, and E. Bradshaw (2015). "A comparison of the 31 January–1 February 1953 and 5–6 December 2013 coastal flood events around the UK". English. In: *Frontiers in Marine Science* 2.

Wahle, K., B. E. V. Stanev, and J. Staneva (2022). "Detecting anomalous sea-level states in North Sea tide gauge data using an autoassociative neural network". en. In.

Wamsley, T. V., M. A. Cialone, J. M. Smith, J. H. Atkinson, and J. D. Rosati (2010). "The potential of wetlands in reducing storm surge". en. In: *Ocean Engineering* 37.1, pp. 59–68.

Wang, J., J. Liu, Y. Wang, Z. Liao, and P. Sun (2021). "Spatiotemporal variations and extreme value analysis of significant wave height in the South China Sea based on 71-year long ERA5 wave reanalysis". In: *Applied Ocean Research* 113, p. 102750.

Wang, Z. B., W. Vandenbruwaene, M. Taal, and H. Winterwerp (2019). "Amplification and deformation of tidal wave in the Upper Scheldt Estuary". en. In: *Ocean Dynamics* 69.7, pp. 829–839.

Warder, S. C., K. J. Horsburgh, and M. D. Piggott (2021). "Adjoint-based sensitivity analysis for a numerical storm surge model". In: *Ocean Modelling* 160, p. 101766.

Watson, I. and C. W. F. Jr. (1990). "State of the art in storm-surge protection: The Netherlands Delta Project". In: *Journal of Coastal Research* 6.3, pp. 739–764.

Weaver, R. J. and J. Luettich (2009). "2D vs. 3D storm surge sensitivity in ADCIRC: Case study of Hurricane Isabel". EN. In: *Estuarine and Coastal Modeling*, pp. 762–779.

Weaver, R. J., P. Taeb, S. Lazarus, M. Splitt, B. P. Holman, and J. Colvin (2016). "Sensitivity of modeled estuarine circulation to spatial and temporal resolution of input meteorological forcing of a cold frontal passage". en. In: *Estuarine, Coastal and Shelf Science* 183, pp. 28–40.

Wei, X., J. M. Brown, J. Williams, P. D. Thorne, M. E. Williams, and L. O. Amoudry (2019). "Impact of storm propagation speed on coastal flood hazard induced by offshore storms in the North Sea". In: *Ocean Modelling* 143, p. 101472.

Weisberg, R. H. and L. Zheng (2006). "Hurricane Storm Surge Simulations for Tampa Bay". In: *Estuaries and Coasts* 29.6, pp. 899–913.

Weisse, R., H. v. Storch, and F. Feser (2005). "Northeast Atlantic and North Sea storminess as simulated by a regional climate model during 1958–2001 and comparison with observations". EN. In: *Journal of Climate* 18.3, pp. 465–479.

Weisse, R., H. von Storch, H. D. Niemeyer, and H. Knaack (2012). "Changing North Sea storm surge climate: An increasing hazard?"

In: *Ocean & Coastal Management*. Special Issue on the Wadden Sea Region 68, pp. 58–68.

Welander, P. (1961). "Numerical prediction of storm surges". In: *Advances in Geophysics*.

Westerink, J. J., R. A. Luettich, J. C. Feyen, J. H. Atkinson, C. Dawson, H. J. Roberts, M. D. Powell, J. P. Dunion, E. J. Kubatko, and H. Pourtaheri (2008). "A Basin- to Channel-Scale Unstructured Grid Hurricane Storm Surge Model Applied to Southern Louisiana". EN. In: *Monthly Weather Review* 136.3, pp. 833–864.

Williams, J., K. J. Horsburgh, J. A. Williams, and R. N. F. Proctor (2016). "Tide and skew surge independence: New insights for flood risk". en. In: *Geophysical Research Letters* 43.12, pp. 6410–6417.

Williams, J. J. and L. S. Esteves (2017). "Guidance on Setup, Calibration, and Validation of Hydrodynamic, Wave, and Sediment Models for Shelf Seas and Estuaries". en. In: *Advances in Civil Engineering* 2017.1, p. 5251902.

Woth, K. (2005). "North Sea storm surge statistics based on projections in a warmer climate: How important are the driving GCM and the chosen emission scenario?" en. In: *Geophysical Research Letters* 32.22.

Woth, K., R. Weisse, and H. von Storch (2006). "Climate change and North Sea storm surge extremes: an ensemble study of storm surge extremes expected in a changed climate projected by four different regional climate models". en. In: *Ocean Dynamics* 56.1, pp. 3–15.

Xu, H., J. H. Chow, X. Xu, and P. Tkalich (2024). "Storm surge model for Singapore strait and south China Sea using Delft3d FM". en. In: American Society of Mechanical Engineers Digital Collection.

Yang, Z., T. Wang, L. Castrucci, and I. Miller (2020). "Modeling assessment of storm surge in the Salish Sea". In: *Estuarine, Coastal and Shelf Science* 238, p. 106552.

Yasuda, T., N. Katahira, N. Mori, and H. Mase (2014). "Projection of future changes in storm surge risk in Japan using Regional Climate Model output". en. In: *Vulnerability, Uncertainty, and Risk*. Liverpool, UK: American Society of Civil Engineers, pp. 2724–2733. ISBN: 978-0-7844-1360-9.

Ye, F., Y. J. Zhang, H. Yu, W. Sun, S. Moghimi, E. Myers, K. Nunez, R. Zhang, H. V. Wang, A. Roland, K. Martins, X. Bertin, J. Du, and Z. Liu (2020). "Simulating storm surge and compound flooding events with a creek-to-ocean model: Importance of baroclinic effects". In: *Ocean Modelling* 145, p. 101526.

Zappa, G., L. C. Shaffrey, K. I. Hodges, P. G. Sansom, and D. B. Stephenson (2013). "A Multimodel Assessment of Future Projections of North Atlantic and European Extratropical Cyclones in the CMIP5 Climate Models". EN. In: *Journal of Climate* 26.16, pp. 5846–5862.

Zhang, Y. J., T. Fernandez-Montblanc, W. Pringle, H.-C. Yu, L. Cui, and S. Moghimi (2023). "Global seamless tidal simulation using a 3D unstructured-grid model (SCHISM v5.10.0)". English. In: *Geoscientific Model Development* 16.9, pp. 2565–2581.

Zhang, Y. J., F. Ye, E. V. Stanev, and S. Grashorn (2016). "Seamless cross-scale modeling with SCHISM". In: *Ocean Modelling* 102, pp. 64–81.

Zheng, L., R. Weisberg, Y. Huang, R. Luettich, J. Westerink, P. Kerr, A. Donahue, G. Crane, L. Akli, Zheng, J. Luettich Richard, J Westerink, P Kerr, and G Crane (2013). "Implications from comparisons two and three dimensional model simulations for the storm surge of Hurricane Ike". In: *Journal of Geophysical Research, Oceans* 118, pp. 3350–3369.

Zijl, F., M. Verlaan, and H. Gerritsen (2013). "Improved water-level forecasting for the Northwest European Shelf and North Sea through direct modelling of tide, surge and non-linear interaction". en. In: *Ocean Dynamics* 63.7, pp. 823–847.

Zimmerman, J. T. F. (1978). "Topographic generation of residual circulation by oscillatory (tidal) currents". In: *Geophysical & Astrophysical Fluid Dynamics* 11.1, pp. 35–47.

Zorndt, A. C., T. Schlurmann, and I. Grabemann (2012). "The influence of extreme events on hydrodynamics and salinities in the weser estuary in the context of climate impact research". In: *Coastal Engineering Proceedings* 33, p. 50.